DESIGN-DEVELOP-TEST A LOW HEAD HYDRAULIC TURBINE USING NEW THEORY FOR THE STANDARD MODULAR HYDROPOWER TECHNOLOGY

By

Jinbo Chen

A DISSERTATION

Submitted to
Michigan State University
in partial fulfillment of the requirements
for the degree of

Mechanical Engineering – Doctor of Philosophy

2020

ABSTRACT

DESIGN-DEVELOP-TEST A LOW HEAD HYDRAULIC TURBINE USING NEW THEORY FOR THE STANDARD MODULAR HYDROPOWER TECHNOLOGY

By

Jinbo Chen

Hydropower has been considered as a great renewable energy resource for decades and provides enormous clean and renewable energy every year. In terms of generation, hydropower is the primary source of renewable energy in the United States, delivering 48% of total renewable electricity sector generation in 2015, and roughly 62% of total cumulative renewable generation over the past decade (2006-2015). However, recently, the large hydropower project is questioned because of the concerns of the large reservoir, dam, and the water channel on the local environment. Due to the smaller scale, short development time, and low environmental impact, the low-head small hydropower system gains increasing attention from the industrial and academic community.

The low-head hydropower has the potential to generate a significant amount of electricity from rivers that traditionally were unsuitable for developing hydraulic power plants and supporting the resiliency of the U.S electricity system. Based on the 2016 Hydropower Vision Report, across the U.S, approximately 65.5GW of new stream-reach hydropower capacities are available. These new stream-reach resources are characterized by low-head, varying flows, and highly valued river functions, including fish preservation, sediment transport, and recreational usage. The development of those resources could be possible only if the technologies for low-head hydropower that balance efficiency, economics, and environmental sustainability were developed. The traditional hydropower design method was limited to the new challenges of the low-head application. Therefore, a new ***Standard Modular Hydropower Technology (SMH)*** was proposed

by the U.S. Department of Energy (DOE) in 2017. This new concept offers a new perspective for small hydropower technology developments based on the premise that standardization, modularity, and preservation of stream functionality must become essential and fully realized features of next-generation hydropower technologies and project designs, and consists of three major modules: ***Generation Module, Passage Modules, Foundation Modules***.

Based on the needs for the new design method suitable for the ***SMH***, this research focuses on developing a new design methodology for the ***Generation Module,*** which is a low impact, damless Kaplan turbine system, suitable for the low-head new stream-reach sites application. With extensive numerical simulation results and flexible geometrical configuration methods, the new design methodology can balance the performance, economics, and environmental sustainability and provide new perspectives for the future low-head hydropower system designs and developments.

To this endless, meaningless, and joyful life that I attempt to make better.

ACKNOWLEDGEMENTS

To my supported advisor Dr. Abraham Engeda for this amazing project and opportunity.

To my helpful and kind committee members, Dr. Norbert Müeller, Dr. Andre Benard, and Dr. Wei Liao, for being part of this journey and providing the crucial advice that necessary for my success.

To all my friends and colleagues, Zhangrui Zhou, Mekuannint Messele, Huixiang Chen, Jintong Gu, Leilei Wang, Xu Tan, and others for supporting my works.

To my parents for letting me do things freely without any restraints.

TABLE OF CONTENTS

LIST OF TABLES

LIST OF FIGURES

KEY TO SYMBOLS

Abbreviations

CAE	Computer-Aided Engineering
CFD	Computational Fluid Dynamic
CFT	Crossflow Turbine
DOE	Department of Energy, U.S.
DNS	Direct Numerical Simulation
LES	Large Eddy Simulation
NACA	National Advisory Committee for Aeronautics
NS	Navier-Stokes
RANS	Reynolds Averaging Navier Stokes
SMH	Standard Modular Hydropower Technology
SA	Spalart Allmaras
SST	Shear Stress Transport

Symbols

A	Turbine Cross-sectional Area
a_0, a_1, a_2, a_3, a_4	Blade thickness distribution coefficients
B(t)	Bezier curve function
CL	Blade Chord length
C	Absolute Velocity [m/s]
C_{rsa}	Runner Stagger-angle setting constant
C_{ssa}	Stator Stagger-angle setting constant
C_1, C_2	Bezier Curve Control points

D	Turbine Diameter [m]
g	Standard Gravity Constant [m/s^2]
H	Design Head [m]
K	Vortex Constant
$\dot{m}$	Mass Flow rate [kg/s]
n_s	Specific Rotation Speed
P_1, P_2, P_3, P_4	Bezier Curve set of points
Q_{11}	Unite Flow Rate [m$^{1/2}$/s]
R_T/S_T	Runner Relative Blade Thickness/Stator relative Blade Thickness
r	Radius location [m]
S	Blade Spacing
W	Relative Velocity [m/s]
ΔW_T	Turbine Specific Work [J/kg]
U	Radial rotational velocity [m/s]
W_T	Turbine Work [J]
y_t	Blade thickness distribution function
Greek Symbols	
α	Absolute Velocity Angle [degree]
β	Relative Velocity Angle/ Blade angle [degree]
Γ	Blade Blockage ratio
γ	Stagger-angle
η_t	Turbine Overall Hydraulic Efficiency
θ	General Inclined Angle [degree]

μ_r	Blade Pitch Angle [degree]
σ	Blade Solidity
ρ	Fluid Density [kg/m^3]
φ	Auxiliary angle
Ω	Rotational Speed [RPM]
Ω_s	Specific Rotation Speed
ω	Rotational Speed [rad]

Subscripts

a/x	Axial Direction
Tip/Hub	Tip Location/Hub Location
r	Runner/Radial Direction
s	Stator
u	Circumferential direction
1,2,3	Stator Inlet; Runner Inlet; Runner Outlet, respectively

CHAPTER I: INTRODUCTION

This chapter summaries some basic histories, categories, and applications for the hydraulic turbine. Also, the new technologies for low head micro-hydraulic applications are briefly covered too.

1.1. History of hydropower and hydraulic turbines

Hydropower is the longest established source for the generation of electricity, which started in 1880 as a small DC generating plant in Wisconsin, United States. [1] Since 1880, hydropower has been utilized for more than a hundred years, and undoubtedly is the most efficient and confident source of renewable energy. [2] Hydropower contributes to 19% of the total global output of electricity by the end of 1999, which produced 2650-Terawatt hour (TWh) [3]; and later produced almost 3100 TWh at the beginning of 2009 and is expected to reach 3606 TWh in 2020. [4]

Compared to other power plant applications, large hydropower plants require significantly higher initial investments; however, the overall maintenance and operating cost are lower. Raabe (1985) listed the various advantages and disadvantages of hydropower plants, and a summary of these is given in **Table 1.1**.

The critical component of a hydraulic power system, undoubtedly, is the hydraulic turbine, which has a long period of development; the oldest version of it was the waterwheel, first used in ancient Greece and other cultures for processing agricultural. In 1830, a French engineer, Benoit Fourneyron, developed the first commercially successful hydraulic turbine. Later, the American engineer James B. Francis designed the first radial-inflow hydraulic turbine (Francis Turbine) that became widely used until now. In the late 19th century, American inventor, Lester A. Pelton invented the first impulse turbine, the Pelton wheel turbine, in which water is piped at high pressure to a nozzle where it expands completely to atmospheric pressure. Viktor Kaplan introduced the first turbine concept, the Kaplan turbine, for the small head application in 1913. Later, he improved his concept with swiveling blades to improve the efficiency of various flow and head conditions.

Table 1.1. *Key Features of hydroelectric power plants [1]*

Advantages	Disadvantages
• Technology is relatively simple and proven.	• The number of favorable sites limited and available only in some countries.
• High efficiency, long useful life.	• Problems with cavitation and water hammer.
• No thermal phenomena apart from those in bearings and generator.	• High initial cost, especially for low head power plants, compared with thermal power plants
• Small operating, maintenance, and replacement costs	• Inundation of the reservoirs and displacement of the population, loss of arable land.
• No air pollution. No thermal pollution of water	• Facilitates sedimentation upstream and erosion downstream of a barrage

Pelton, Francis, and Kaplan turbines are the three most popular turbine types worldwide for the traditional hydraulic power system, and **Table 1.2** summaries the normal operating conditions for all three types of turbines.

Table 1.2. *The operating ranges of the three most popular turbine for traditional hydraulic systems [1]*

	Pelton Turbine	Francis Turbine	Kaplan Turbine
Specific speed [rad]	0.005-0.4	0.4-2.2	1.8-5.0
Head [m]	100-1770	20-90	6-70
Maximum power [MW]	500	800	300
Optimum Hydraulic efficiency [%]	90	95	94

Table 1.2 *(Cont'd)*

	Pelton Turbine	Francis Turbine	Kaplan Turbine
Regulation method	Needle valve and deflector plate	Stagger-angle of guide vanes	Stagger-angle of rotor blades

(Note: Values shown in the table may subject to change)

1.2. Small hydropower and its application (A literature review)

Generally, a large, and high-capital-cost dam equipped with a large turbine is required to produce sufficient power supply. However, low-head, small hydropower stations present an attractive and efficient way for electricity generation in rural, remote, and hilly areas because of the increment in the level of greenhouse gas emissions and fuel prices in these sites, and they have become increasingly popular for application at small rivers. [5] Micro-hydropower schemes can be used to generate enough electrical power for home, farm, and plantation or small village. [6] They can also be used in mechanical end-uses like agriculture processing, textiles fabrication, ice cream production, cooling, and drying. [7] The main advantages of the low-head micro-power system are that it is predictable if enough water supply is available and possesses a positive environmental impact. [8,9] Therefore, the system has become the leading interest for future hydro-developments in Europe, where large-scale stations have indeed been utilized but in return give adverse effects on the environment. [9,10] Most low-head, small hydropower plants generate power less than 100kW, but there are also other categories with classification below 500kW and less than the ten-meter head. [5] Recent publications raise the importance of using the simple and existing turbines to achieve minimum cost to produce power. [11] Installation of large and medium hydropower plants with dams, vast reservoirs, large turbines, electrical equipment, and controllers have been proven very expensive, and have an uneconomical and negative environmental impact. [5] Though intended as a clean and cheap source of energy generation, many developing countries that need rural electrification are instead exposed to economic problems when installing this costly hydro-equipment. [12]

Using micro-hydropower with new design and arrangement of these equipment leading to, especially the turbines, can be the perfect solution to overcome the economic and operational problems and reduce the total cost of hydropower plants. [5] Since the micro-turbine can generate very reliable power with relativity simple designs and fabrications, it has recently gained rapid growth in the power generation field, especially in rural areas, as their power is needed to feed both baseload and peak demand requirements of grid supply. [5]

Table 1.3. *A general classification of hydropower turbines and their applicable head ranges.*

Classifications of Turbine		Turbine types	Head Range [m]
Impulse Turbine		Pelton	50-1300
		Turgo	3-150
		Crossflow	3-250
Reaction Turbine	Axial Flow Turbine	Bulb Turbine	2-20
		Straflo Turbine	2-40
		Tube Turbine	5-30
		Kaplan Turbine	2-40
	Other Turbines	Francis Turbine	10-350
		Kinetic Energy Turbine	No head needed
		Archimedes Screw Turbine	As low as 1 meter

1.2.1. **Classification of hydro-turbines and related low head applications**

Hydropower turbines are categorized into two types: impulse and reaction turbines. **Table 1.3** shows the general classification and the applicable head range for each type of turbine.

1.2.2. Impulse Turbines

Impulse turbines have a simple design and are inexpensive. There are three major types of impulse turbines: Turgo, Crossflow, and Pelton. Those types are commonly used for high and medium heads. [13] Recently, they have been applied for lower head micro-sites, and their proven effectiveness has allowed them to become an accepted alternative practice in many countries. [14]

- Energy System & Design Ltd. [15] has produced a **Turgo turbine**, which can be used for head between 3m and 150m. The water is applied on one side, usually at an angle of about 20°, goes across the blades, and exits on the other side (**Fig. 1.1**). In the previous researches, Williamson et al. [16, 17] optimized **Turgo turbine** models in micro-project and pico-project, by altering the location of low heads from 3.5 m down to 1m to improve the turbine performance. For one specific model, the Turgo turbine has an experimental efficiency of 91% at 3.5m head and 87% at 1m head. [16]

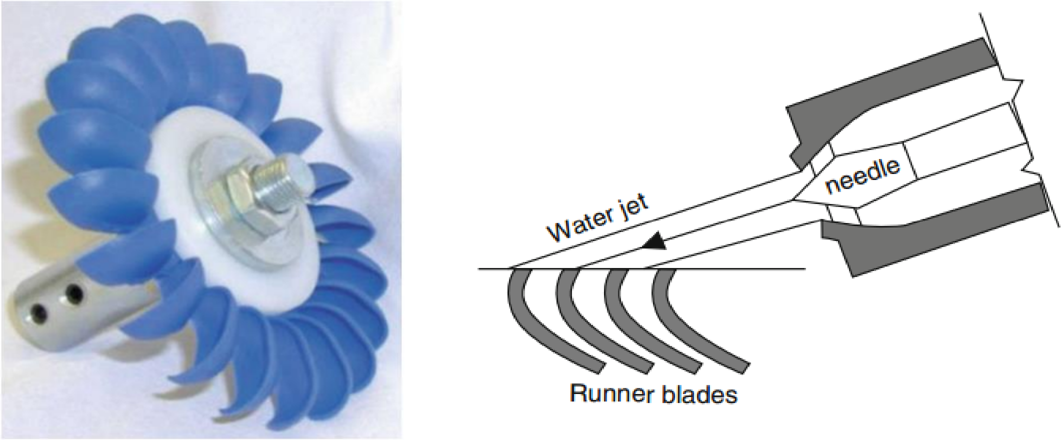

Figure 1.1. *A low-head Turgo wheel turbine developed by Energy System & Design Ltd [23]*

- **The Pelton turbine** has one or multi-jets (**Fig. 1.2**). Pelton wheels are suitable for a large head and low-flow sites (The Turgo turbine wheel is a modified version of Pelton wheels for low head application). [5] Recently, Pelton turbines have been used for small and micro-hydropower configurations, using a single jet. [18, 19] Generally, a Pelton turbine has a maximum efficiency between 70-90%. [19]

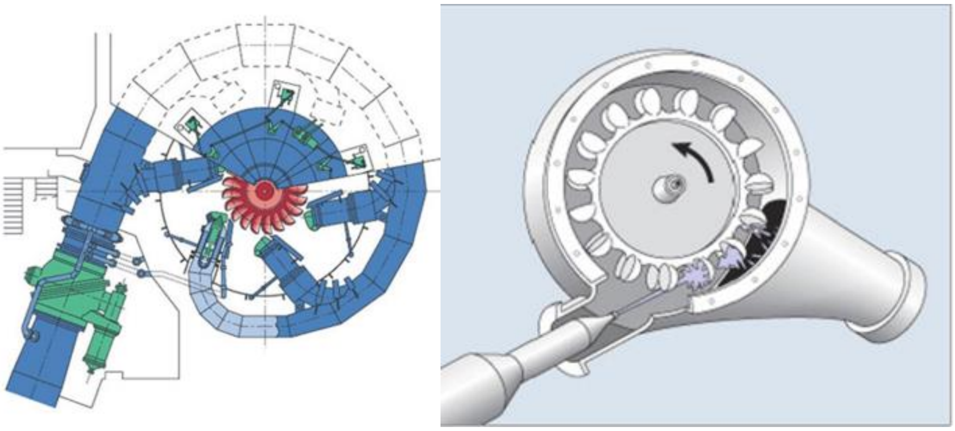

Figure 1.2. *A crosssection of a low-head six jet Pelton turbine (Right), and a single jet Pelton turbine (Left) [24,25]*

- A **Crossflow turbine** (CFT) is another significant impulse turbine for low-head applications. It is commonly applied in horizontal and vertical configurations [5] **(Fig. 1.3**). The crossflow turbine allows the water to flow through the blades twice. During the first pass, water flows from the outside of the blades to the inside; the second pass is from the inside back out (**Fig. 1.3**). [5] This type of turbine is usually used at a higher flow rate and lower head than the Pelton and Turgo turbines. [20] The average efficiency of CFT turbines is usually 80% for small and micro-power outputs but can reach up to 86% in the case of medium and large units. [21]

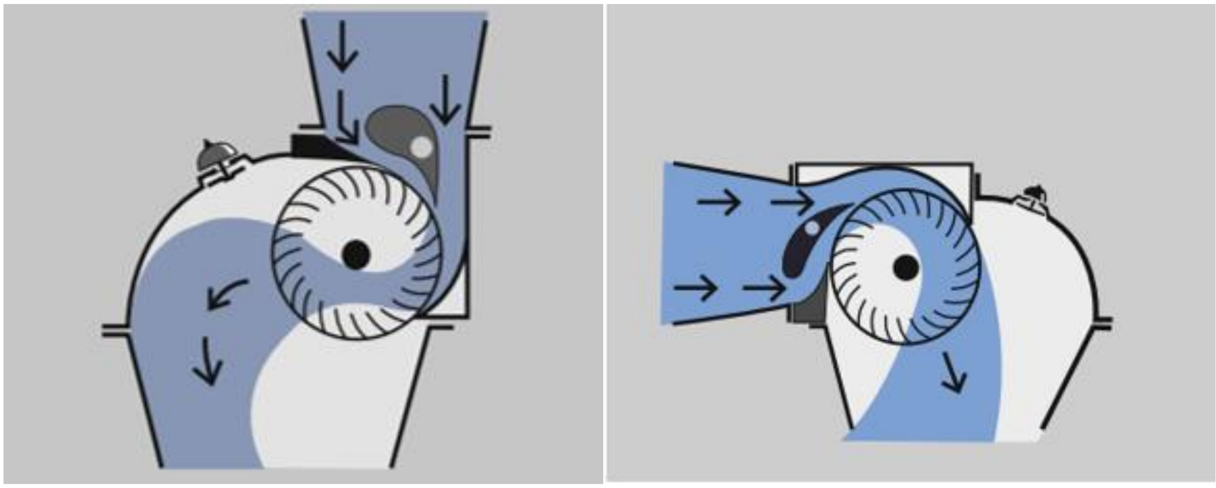

Figure 1.3. *Low-head crossflow turbine in the vertical position (Left), horizontal position (Right) [26]*

1.2.3. Reaction Turbines

A reaction turbine generates power from the combined action of pressure and moving water. The runner is placed directly in the water stream flowing over the blades rather than striking each individually. [20] Compared to impulse turbines, reaction turbines have a better performance in low head and high flow rate conditions. [20] At lower operation speeds, the efficiency of reaction turbines is usually higher than the impulse turbines. [22] Most reaction turbines are classified as the **axial flow turbines**, as shown in **Table 1.3**, and this type of turbine is indeed practical, indicating excellent efficiency, simplicity, and cost-effectiveness (More detailed descriptions for axial turbine will present in the next section). [27] Other reaction turbines include the Francis turbine and the Kinetic Energy turbine.

- A **Francis turbine** is the most common turbine at hydropower stations. The Francis turbine is typically used in a large-head condition; however, recent research shows it could apply to the low-head site too. This turbine has a radial or mixed flow runner, which is equipped with guide buckets. Water is introduced just above the runner and all around it and then falls through, causing it to spin. Besides the runner, the other components are the scroll case, wicket gates, and a draft tube. [20] A cross-sectional of a Francis turbine is shown in **Fig 1.4**.

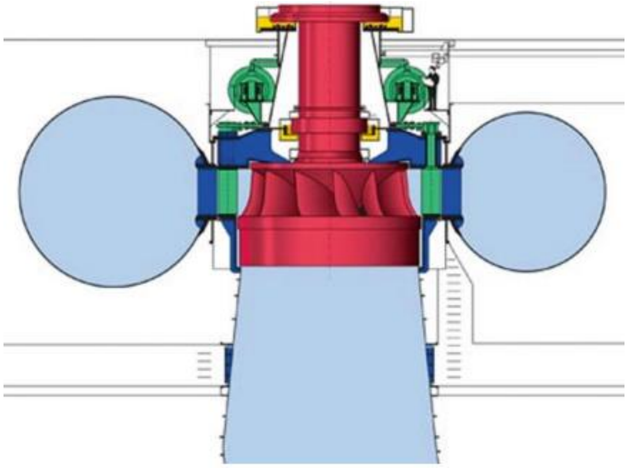

***Figure 1.4.** Cross-section of a low head Francis turbine with scroll case, wicket gates and draft tube [28]*

- The **kinetic energy turbines**, also called free-flow turbines, generate electricity from the kinetic energy present in flowing water rather than the potential energy from the head. [20] The system may operate in rivers, manmade channels, tidal waters, or ocean currents. [20] Since kinetic turbines utilize the water stream's natural pathway, the diversion of water through the manmade channel, riverbeds, or pipes is not required. [20] These systems do not require large civil works; instead, existing structures such as bridges, tailraces, and channels are sufficient for these turbines. [20] The basic structure of a kinetic turbine is shown in **Fig 1.5.**

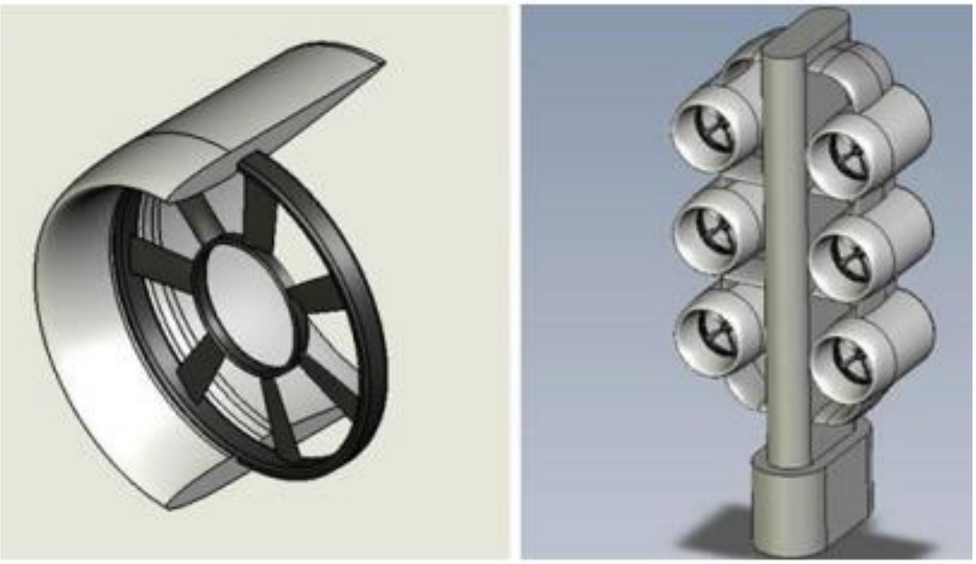

Figure 1.5. *Basic structure of a kinetic turbine with multiple unit configurations [29]*

- The **Archimedes screw turbine** has become a more attractive option for some lower head sites, as its heads can be set as low as 1 meter and is especially suited for sites with large flows. [5] Western renewable energy [30] and Landustries [31] have developed the Archimedean screw as a relatively novel method to generate electrical energy from a low-head source. This turbine is being used as one of a few systems that are able to maintain or even improve the wildlife in and around the river, which is the key feature for it. [31] A water flow geometry in the Archimedes screw is shown in **Fig 1.6.**

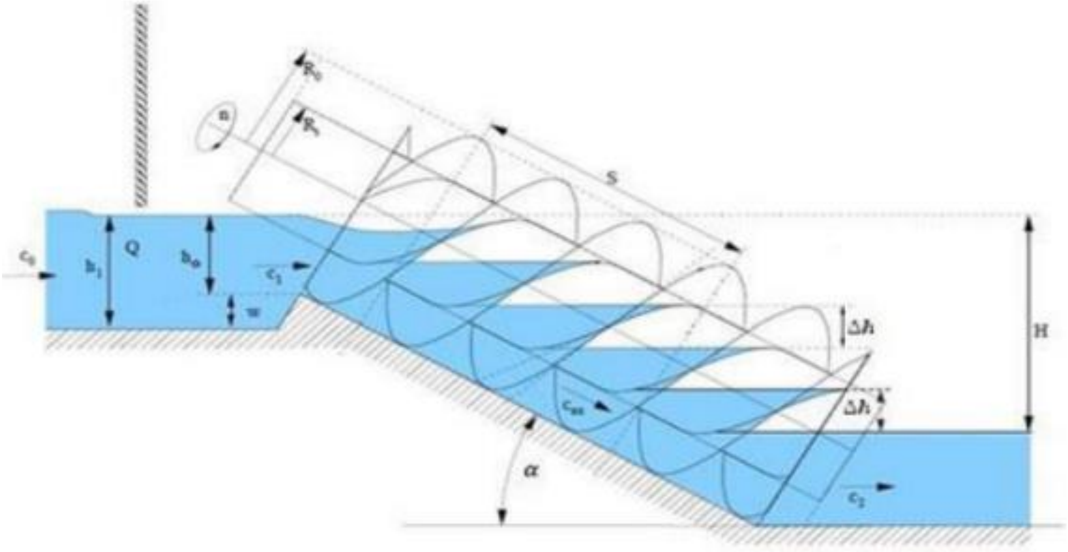

Figure 1.6. *Water flow geometry in a low-head Archimedes screw turbine [32]*

1.2.4. **The Axial hydro-turbine for low head application**

As shown in **Table 1.3**, most of the reaction turbines are the axial type of turbines. An axial type turbine generally has a runner with three to six blades in which water impinges continuously at a constant rate. [20] The pitch of the blades may be fixed or adjustable, and the major components besides the runner are a scroll case, wicket gates, and a draft tube. [20] Generally speaking, the axial hydro-turbine has four major types: Bulb turbine, Straflo turbine, tube turbine, and Kaplan turbine.

- The **Bulb turbine** has the turbine and generator sealed and placed directly in the water stream. [20] The near-straight design of the water passage provides both size and cost advantages. Bulb turbines can also operate in a reverse flow direction. Bulb turbines are available for power output in the range of 10-100MW. [20] A typical bulb turbine is shown in **Fig 1.7**. This type of turbine is suitable for low-heads applications, namely below 25m; for very low heads, an extra set of gears is used to increase the rpm of the generator. [20]

- The **Straflo turbine** is a registered brand name that stands for straight-flow. The key feature of the Straflo turbine is the combination of the turbine and generator since the generator is attached directly to the perimeter of the turbine. [20] A Straflo turbine also consists of a group of axial turbines with a concentrically arranged generator outside of the flow channel. [20] Various components of a Straflo turbine are shown in **Fig 1.8**.

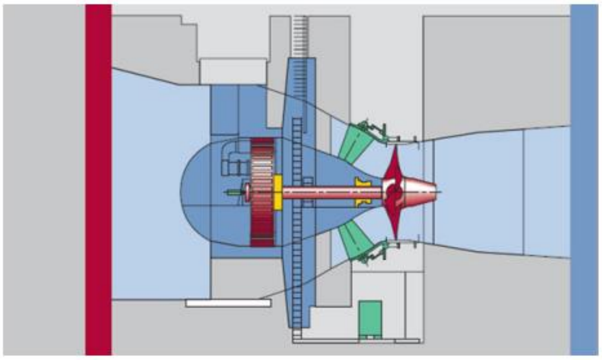

Figure 1.7. *Cross-section of a horizontal bulb turbine and generator for low-head power station [33]*

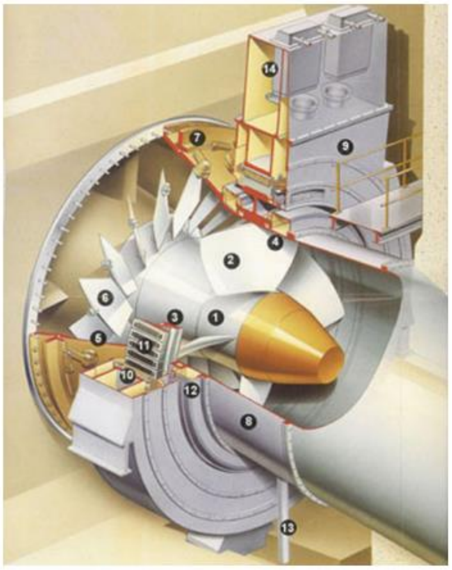

Figure 1.8. *An example layout of the Straflo turbine for low head application [34]*

- In a **Tube Turbine**, the penstock bends just before or after the runner, allowing a straight-line connection to the generator. The power output from tube turbines ranges from 20 to 700 kW. **Figure 1.9** shows the main components of a tube turbine. These types of turbines have a direct drive configuration where the turbine and the generator are on the same shaft having common bearings and seals. There are five main features of the tube turbine [20]: 1. Compact structure, turbine, and generator with bearings and seals in one unit, 2. The installation angle for the unit may vary from vertical to horizontal, 3. Stainless steel structure, 4. Long service intervals, 5. Heads range from 5 to 30 m which are sufficient for most applications

- The **Kaplan turbine** has adjustable blades and the wicket gates, allowing for a broader range of operation. The runner-blade is attached to the turbine shaft and the generator directly at various speeds to generate electricity at the optimum efficiency. Typically, the Kaplan turbine is equipped with the double regulation method: adjustable blades and wicket gates. However, a recent development in various speed generator technology allows a third regulation method for the Kaplan turbine, which further improves the overall performance. The basic components of a Kaplan turbine are shown in **Fig 1.10.**

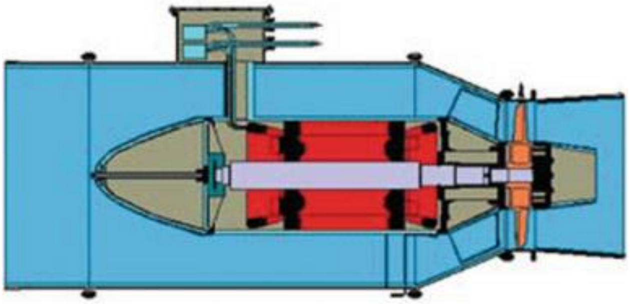

Figure 1.9. *A horizontal tube turbine configuration for low-head hydropower plant [20]*

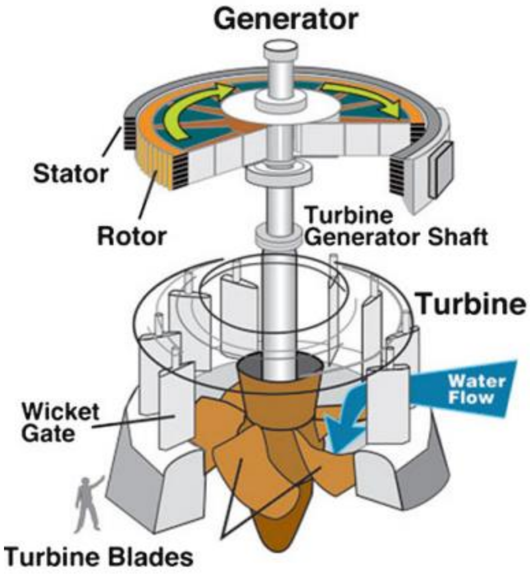

Figure 1.10. *Basic components of a traditional Kaplan turbine power station [35]*

With different configurations, the Bulb turbine and Kaplan turbine are the two most commonly used turbines for low-head applications; and **Table. 1.4** shows some current low head turbine configurations and corresponding features.

Currently, there are many turbine types suitable for low head hydropower applications on the market, and **Table 1.5** is a summary of the current low-head turbines and their suppliers with corresponding performance characteristic features.

Table 1.4. *Current configurations of axial turbines for low head applications (Adapted from [36])*

	Turbine configuration	Features
Kaplan turbine	Inclined axis, very low head Kaplan gear turbine	Inclined at an angle of 15 to 45 degrees; Very low head application between 2 and 8 meters; Maximum power capacity is about 2.6MW
	Horizontal axis "S" type Kaplan turbine	Runner sizes range from 1.0m up to 4m; Heads range from 5m to 25m; Power output about 12MW
	Vertical axis small Kaplan turbine with elbow draft tube	Avoiding the use of draft tube gates
	Horizontal axis pit type propeller turbine	Fixed blade angle; Peaked efficiency curve; Suited for constant flow and head condition
Bulb Turbine	Belt driven bulb turbine	Short installation time; Compact powerhouse structure; Up to 4m head; Up to 600kW power output
	Bevel Gear bulb turbine	High-speed generator; Up to 12m head; Up to 2600kW power output;
	Axial Bulb turbine	Direct driven synchronous generator; Horizontal or inclined axis; Short installation time; Low noise level; Up to 6m head; Up to 5000kW power output

***Table 1.5**. Current turbines on the market suitable for low head applications (Adapted from [37])*

Turbine type	Supplier	Flow range [m^3/s]	Head range [m]	Power output [kW]
Pelton	Powerspout	0.008-0.01	3-100	<1.6
Cross-flow	IREM	0.01-1.0	5-60	<100
	Ossberger	0.04-13	2.5-200	15-3000
	Wasserkraft Volk	1.5-150	Not given	<2000
Archimedean Screw	Andritz	<10	<10	<500
	Hydro Coil	<10	4-20	2-8
	3 Helix Power	0.2-10	1-10	1.4-700
Kaplan (Axial and bulb included)	Ossberger	1.5-60	1.5-20	20-3500
	Mavel	0.3-150	1.5-35	30-20000
	Voith	Not given	3-95.0	100-400000
	Energy systems and Design	0.03-0.06	0.5-3.0	0.09-1
	Power Pal	0.04-0.13	1.5	0.1-1
	Wasserkraft Volk	Not given	1-40	Not given
	Gugler	0.2-50	1-100	3-10000
	Alstom	0.3-150	2-30.0	<130000
	Voith	2-30.0	Not given	1000-80000
	Voith (Minihydro)	1-14.0	2-10.0	Not given
	Tamanini	1.0-15	5-20	50-2000
	Hydrolink	Not given	1.5-25	Not given
Hydrokinetic	Alternate Hydro	>0.8m/s	>0.6	1-4.0
	New Energy Corporation	2.4-3m/s	Not given	5-25.0
	Alden	<2.6m/s	25	Not given
	Hydrovolots	1.5-3m/s	0.15	1.5-12
Vortex	Zotloterer	0.05-20	0.7-2	0.5-160
Francis	Wasserkraft Volk	Not given	<300	<20000
	Mavel	0.1-30	15-440	20-30000
	Gilkes	0.05-40	<400	<20000
	Voith	Not given	3-95	5-10000000
	Gugler	0.03-25	2-500	3-10000
	Tamanini	0.2-10	15-300	20-5000
	Hydrolink	Not given	20-120	Not given
	Newmills Engineering. LTD	Not given	10-350	1-820
	Kossler	0.8-60	15-250	500-15000

1.3. Standard Modular Hydropower Technology (SMH)

Across the U.S., there are more than 65.5GW of new stream-reach hydropower capacities that can be used for hydropower development. [38] Those riverine resources are very functionally and geographically diverse and characterized by low-head, varying flows, and highly valued river function. Because of those features, low-head hydropower and hydrokinetic technologies are best-suited technology for those sites for their versatility and low impact on the environment. However, a complex and uncertain aspect of the new low-head hydropower development that is targeted explicitly to the new stream-reach sites is the balancing of performance, environmental impact, and project cost. Moreover, small, low-head sites, in particular, are challenging to design and develop with acceptable performance and cost.

Because of those hydropower potentials and associated challenges in 2017, the U.S. Department of Energy (DOE) proposed a new **Standard Modular Hydropower Technology (SMH)** concept that can enable hydropower technology to deploy and operate in a new stream-reach site with minimal environmental impacts and greater public acceptance at a reduced cost. This new design paradigm has three basic principles for a low-cost, environmentally sustainable hydropower growth strategy and Logistics as the following [39]:

- **Standardization:** Guidelines, rules, and specifications (i.e., standards) to maximize compatibility, acceptance, interoperability, quality, safety, and repeatability while minimizing environmental disturbance. In a hydropower context, standardization of design, review, regulation, manufacturing, operations, maintenance, and other features are intended to reduce site-specificity and project costs.
- **Modularity:** The physical or virtual organization of a hydropower facility is divided into discrete functional units, known as modules. In SMH, the entire facility is envisioned

as a modular structure, with the generation, passage, and foundation modules assembled to deliver energy and environmental benefits at many different sites.

- **Environmental Compatibility:** Siting and developing hydropower facilities with an understanding that streams provide valuable environmental benefits that must be preserved. SMH development must embody an understanding of how coupled stream-hydropower systems can minimize disturbances to landscape features, water quantity, connectivity, geomorphology, water quality, and biota.

The first concept of modularity refers to the use of different module types to assemble an entire SMH facility. The **SMH** has three primary modules with several sub-modules for the application to different sites; **Fig 1.11** shows the conceptual schematic of this Modularity concept, and **Table 1.6** summaries the basic function of each module [39]. All those modules can be assembled to form an SMH facility that matches the scale, environmental attributes, and watershed context of the site selected for development [39].

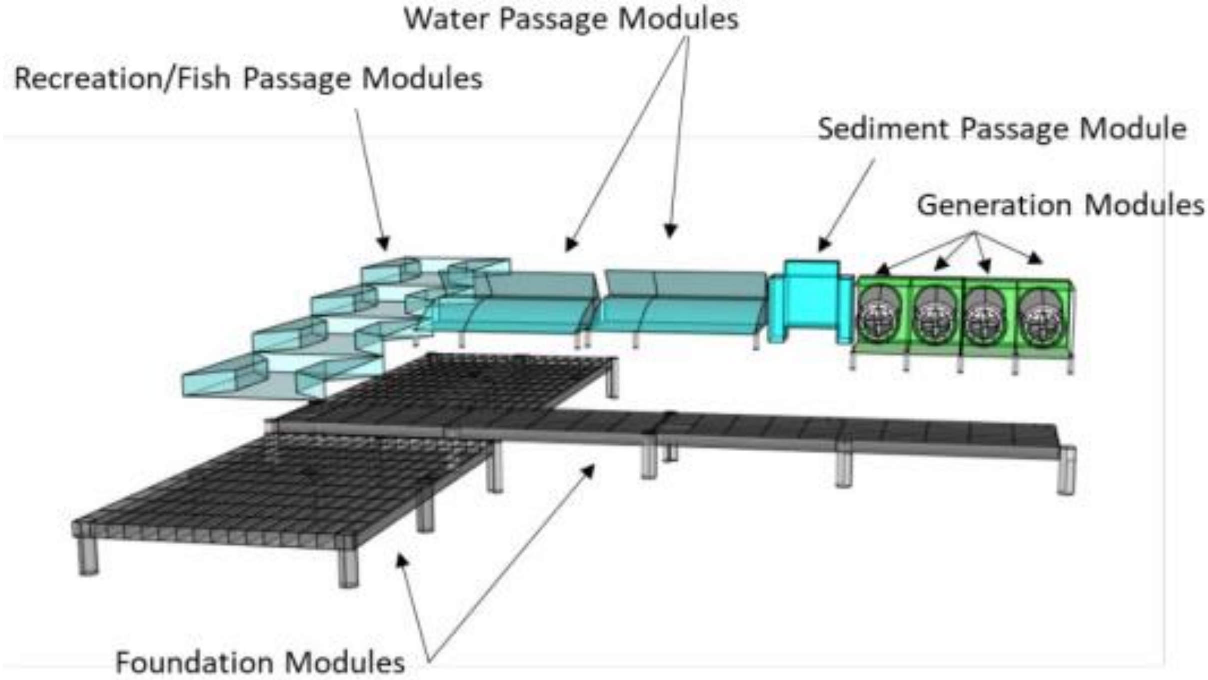

Figure 1.11. *Conceptual schematic showing the primary modules of an SMH facility design [39]*

The second concept of modularity refers to scalability at many sites through multiple modules of the same type. For example, an upstream fish passage module may be applicable at many sites with a watershed region; a cost-optimized, compact generation module designed with broad operational flexibility could be applied at multiple sites throughout the country [39].

Table 1.6. *The basic functions for the SMH modules and their sub-modules*

Major Modules	Basic Function
Generation Module (Including Turbine Rotor Module, Generator Module)	Encompasses all hydraulic and electric machines, equipment, and systems necessary for hydroelectric power generation.
Passage Module (Including Fish Passage Module, Sediment Passage Module, Recreation Passage Module, Water Passage Module)	Allow fish, sediment, water, and recreational craft to pass the facility safely.
Foundation Module	Provides structural resistance and reliably interface with the streambed to support generation and passage modules

Based on the initial investigation, a successful **SMH** facility should have six features [39]:

- Predictable and somewhat regular production of electricity.
- Minimal alteration of the inflow hydrograph and minimal impoundment of inflow water.
- Environmental mitigation technology (functionality) inherent within and integral to the facility design (including fish passage, water quality, and sediment management design).

- Minimal disruption to the aesthetics of the natural stream and stream-scape, and do not occupy the full width of the river.
- Minimal fluctuations of water surface elevation.
- Enabling of safe recreational passage through and activity around the project.

1.3.1. SMH Generation Module

As the most critical module for SMH technology, the Generation Module is envisioned as an integrated water-to-wire module that contains a hydraulic water turbine, generator, controls, and electrical equipment within a single unit [39]. The overall design goal of the generation module is to balance the performance, economic, and environmental sustainability, so it is appealing for developers.

- *Performance Considerations*

The traditional hydraulic system is often equipped with a large reservoir that helps the system maintain the optimum operating head condition. However, the SMH system for the new stream-reach sites requires minimal water impoundment. Additionally, one major characteristic of the new stream-reach development sites is the high variability in flow rate. To demonstrate this high flow rate variability and **Fig. 1.12** shows an example of an average daily flow rate of one selected new stream-reach development site for the past 50 years. Furthermore, at most low-head new stream-reach sites, the tailwater elevation generally rises twice as fast as headwater elevation when river flow increases, leading to a significant reduction in the available gross head [40]. As a result, the low-head new stream-reach sites with high variability in flow and head often result in operating beyond the acceptable performance and efficiency limits for the traditional turbine. This variability requires a different deployment of regulation methods and presents a significant design challenge for the generation module design.

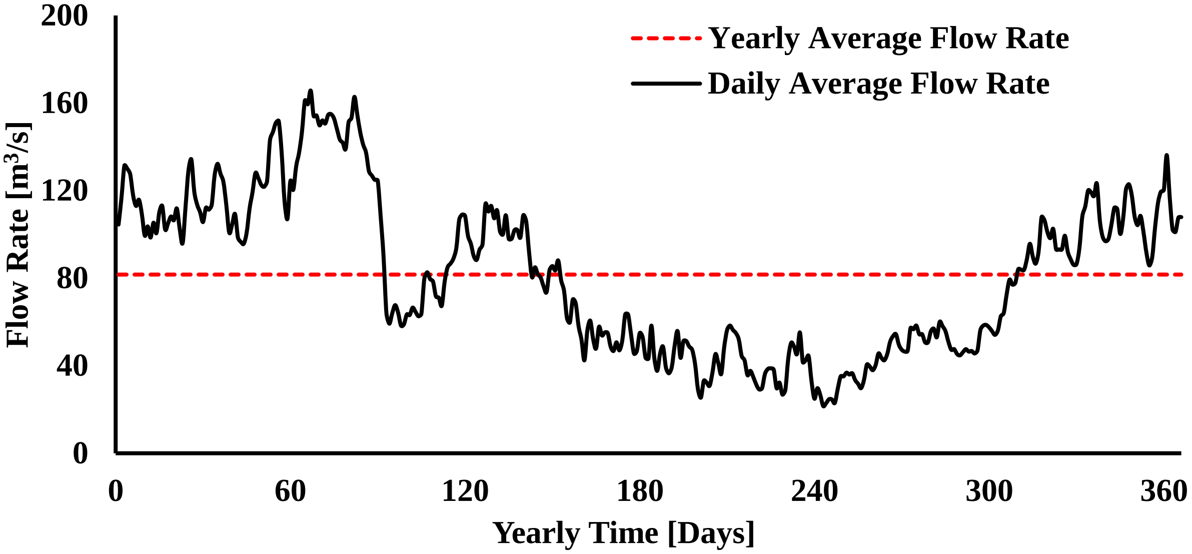

Figure 1.12. *Daily average flow rate for a selected new Stream-reach site for the past 50-years. (Data extrapolated from Oak Ridge National Laboratory SMH Explorer website: https://smh.ornl.gov/explorer/)*

- *Economics Considerations*

The immediate installed cost target for an SMH project is under \$6,000/kW, including all necessary modules [39]. Over time, this number should be reduced as the module deployment increases. Conventionally, there are six main cost sectors for developing a small hydro project: 1. Installation Cost, 2. Planning Cost, 3. Civil work, 4. Infrastructure and Logistics, 5. Electrical connection/Construction, 6. Equipment Cost. Among those sectors, the civil work normally represents 40%-50% of the total project cost for a hydro-power project [41]. This civil work cost is normally high because of the construction of the dam for creating a necessary head and the water channel for diverting the river to the turbine. However, for low-head, new stream-reach sites, which feature with minimal water impoundment and run-of-river type operation, the traditional dam structure is not a necessity.

Therefore, a damless concept for the generation module, which means the size of the generation module can be large enough for creating enough low head conditions, will significantly reduce the overall cost, but at the same time, creates new design challenges for the turbine designs.

- *Environmental Sustainability Considerations*

The preservation of stream functionality is one of the most instrumental premises for SMH technology, and there are three primary environmental considerations for the new stream-reach sites: 1. Fish Preservation, 2. Sediment Preservation, 3. Recreation Activities Preservation. Among all those three, there is one primary consideration that is critical for the generation module design: fish preservation. The new stream-reach sites' river often has high-valued native fish species (anadromous, catadromous, and amphidromous), and hydropower facilities can work as barriers for them. Therefore, the low-head hydro-system needs to have maximum protection for fish migrations. There are two ways to achieve this fish protection: introducing advanced fish passage design for overall facility construction and introducing the fish-friendly turbine design concept that allows fish to pass the generation module safely.

1.3.2. **Design Specifications for SMH Generation Module**

Because of the performance, economics, and environmental considerations, the DOE has five specific design specifications for the SMH generation module [39]:

- Must be fully immersed in water, which necessitates the use of the reaction-type of the turbine.
- Must encompass all equipment and systems for safe and reliable operation.
- The design flow rate is less than 113m^3/s, and the design head is less than 9m per unit.
- Run-of-river type operation is preferred, which means the sum of inflows into the upstream region of the facility must equal the sum of outflows into the downstream reach of the facility.
- Minimal environmental disturbance, including low fish mortality rate and low noise level, etc.

1.4. Research Objectives

Because of the need for new and innovative design methods for **SMH** technology suitable for potential new stream-reach sites, this dissertation uses physical, theoretical, numerical and analytical modeling techniques to design, develop and test a low impact, low-head turbine generation module. The main goal of this dissertation is to introduce a new design methodology for the **SMH** generation module that is suitable for low-head hydraulic conditions with flexible geometry configurations, optimum overall performance, and a wide operating range.

The design and development process of this low-head generation module consists of the following three steps: 1. Runner hydrodynamic design and development of the 3-D geometric models and interfaces; 2. Numerical design methods development; and 3. CFD simulations and analysis.

CHAPTER II: BASIC MECHANICS AND PHYSICS FOR HYDRAULIC TURBINE SYSTEM

This chapter summarizes the basic physical and thermodynamics laws and develops them into a form that suitable for the study of the hydraulic turbine. The essential laws and theories for developing hydraulic turbine covered in this chapter include:

- The continuity laws of a control volume.
- The first law of thermodynamics and the steady flow energy equation.
- The conservation of momentum equations and Euler equations.
- Definitions of hydraulic turbine efficiency and loss.

2.1. Main Conservation Equations

2.1.1. The Continuity Equation

In a flow system, the mass flow rate $\dot{m}$ is related to the flow density ρ, fluid absolute velocity C, and the cross-sectional area A of the system. If the fluid with a constant density ρ, through the finite area dA of the system during a finite time dt, the elementary mass is $dm = \rho C dt dA \cos\theta$, where the C is the absolute fluid velocity, and θ is the angle between fluid velocity and the normal direction of the area, referring in **Figure 2.1.**

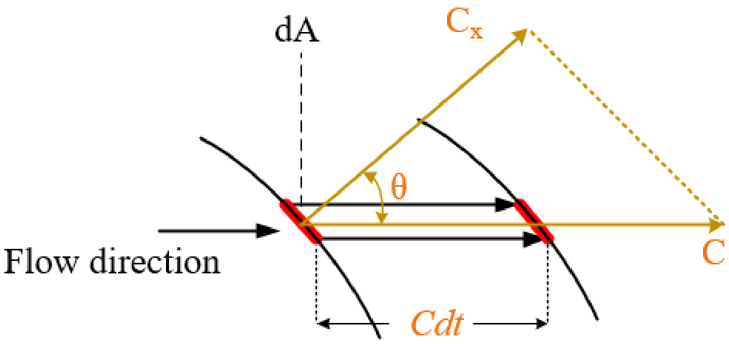

Figure 2.1. *Demonstration of an elementary mass across an area element (dA) with an absolute fluid velocity (C) and an angle θ*

The velocity component perpendicular to the area dA is $C_x = C\cos\theta$, and $dm = \rho C_x dAdt$. The elementary rate of mass flow rate is

$$d\dot{m} = \frac{dm}{dt} = \rho C_x dA, \text{ where } C_x \text{ is axial velocity} \tag{2-1}$$

Most 1-D analyses in this chapter are limited to the incompressible steady flows, where the axial velocity and density are considered as constant across each section of the turbine. If A_1 and A_2 are the cross-section area at station 1 and 2 along a turbine passage the system has no accumulation of fluid within the control volume and has the mass flow rate as

$$\dot{m} = \rho_1 C_{x1} A_1 = \rho_2 C_{x2} A_2 = \rho C_x A \tag{2-2}$$

2.1.2. First Law of Thermodynamics for Hydraulic Turbine

The First Law of Thermodynamics reveals that if a system is taken through a complete cycle during which the heat is transferred, and work is done, then [1]

$$\oint (dQ - dW) = 0 \tag{2-3}$$

where $\oint dQ$ represents the heat transfer to the system during the cycle, and $\oint dW$is the work done by the system during this cycle. During the change from state-1 to state-2, there is a change in the property of internal energy

$$E_2 - E_1 = \int_1^2 (dQ - dW) \tag{2-4}$$

For an infinitesimal change of state

$$dE = dQ - dW \tag{2-5}$$

Where dE is the change in energy per unit mass, this term includes internal, kinetic, and potential energy

$$dE = d(E + \frac{C^2}{2} + gZ) \tag{2-6}$$

Now consider the steady flow of fluid through a control volume representing a turbomachine system; the fluid passes at a steady mass flow rate $\dot{m}$, entering at station-1 and leaving at station-2. Energy is transferred from the fluid to the turbomachinery blades and positive work being done via the blade at the rate $\dot{W}_x$. In the general case, positive heat transfer takes place at the rate $\dot{Q}$ from the surroundings to the control volume. Thus, the steady-flow energy equation is

$$\dot{Q} - \dot{W}_x = m\left[(h_2 - h_1) + \frac{1}{2}(C_2^2 - C_1^2) + g(Z_2 - Z_1)\right] \tag{2-7}$$

where h is the specific enthalpy, $\frac{1}{2}C^2$ is the kinetic energy per unit mass, and gZ is the potential energy per unit mass. Now defining stagnation enthalpy by $h_0 = h + \frac{1}{2}C^2 + gZ$, **Eqn (2-7)** becomes

$$\dot{Q} - \dot{W}_x = \dot{m}(h_{01} - h_{02}) \tag{2-8}$$

Moreover, for incompressible flow, **Eqn (2-8)** could be rewritten in the following form, which P_0 is called the ‘stagnation pressure’ where $P_0 = P + \frac{1}{2}\rho c^2$

$$\dot{Q} - \dot{W}_x = \dot{m}(P_{01} - P_{02}) + \dot{m}(Z_1 - Z_2) \tag{2-9}$$

2.1.3. The Momentum Equation and Newton’s Second Law of Motion

One of the most fundamental and critical principles in mechanical Engineering is **Newton’s Second Law of Motion**. The momentum equation relates the sum of the external forces acting on a fluid element to its acceleration, or to the rate of change of momentum in the direction of the resultant external force [1].

Considering a system of a mass of m, the sum of all the body and surface forces acting on m along some arbitrary direction x is equal to the time rate of change of the total $x - momentum$ of the system, i.e. [1].

$$\sum F_x = \frac{d}{dt}(mC_x) \tag{2-10}$$

For a steady-state control volume where fluid enters at a uniform velocity C_{x1} and leaves with a uniform velocity C_{x2}, then

$$\sum F_x = \dot{m}(C_{x2} - C_{x1}) \tag{2-11}$$

Equation (2-11) is the one-dimensional form of the steady-flow, momentum equation.

Now, considering a rotation system of mass m for the turbomachinery. The sum of the moments of all external forces acting on the system about some arbitrary axis (‘A’ axis) that fixed in space is equal to the time rate of change of angular momentum of the system. In other word, torque τ must be supplied through the shaft to the rotor in order to change the tangential momentum of mass m of fluid from station-1 to station-2 as [42]

$$\tau_A = \frac{d}{dt}(mrC_u) \tag{2-12}$$

where r is the distance of the mass center from the axis of rotation measured along the normal to the axis, and C_u is the velocity perpendicular to both the axial and radius direction [42]. For one-dimensional steady flow, **Eqn (2-12)** could be rewritten in the following form

$$\tau_A = \dot{m}(r_2C_{u2} - r_1C_{u1}) \tag{2-13}$$

2.1.4. **Euler’s Equation and Velocity triangle**

For a pump or turbine rotor running at angular velocity Ω, the rate at which the rotor does work on the fluid is

$$W_c = \tau_A\Omega = \dot{m}(U_2C_{u2} - U_1C_{u1}) \tag{2-14}$$

where the blade circumferential speed is $\mathrm{U} = \Omega\mathrm{r}$, thus the specific work done on the fluid is

$$\Delta\mathrm{W_c} = \frac{\dot{\mathrm{W}}_\mathrm{c}}{\dot{\mathrm{m}}} = \frac{\tau_\mathrm{A}\Omega}{\dot{\mathrm{m}}} = \mathrm{U_2C_{u2}} - \mathrm{U_1C_{u1}} > 0 \tag{2-15}$$

This equation is referred to as **Euler's Pump Equations**. And for a turbine, the fluid does work on the rotor, and the sign for work is then reversed. Thus, the specific work is

$$\Delta W_t = \frac{\dot{W}_t}{\dot{m}} = \frac{\tau_A \Omega}{\dot{m}} = U_1 C_{u1} - U_2 C_{u2} > 0 \tag{2-16}$$

This equation is referred to as **Euler's Turbine Equation**.

For a rotating system in turbomachinery, it is essential to define the velocity component correctly. Considering a fluid passing through the runner, by definition, C is the absolute velocity that tangential to the absolute path, W is the relative velocity tangential to the blade, or the relative path, and U is the blade velocity. For every instant during the particle movement through the runner, the following velocity relationship remains true:

$$\vec{C} = \vec{U} + \vec{W} \tag{2-17}$$

Also, **Fig 2.2** shows a velocity triangle for a generalized turbine system.

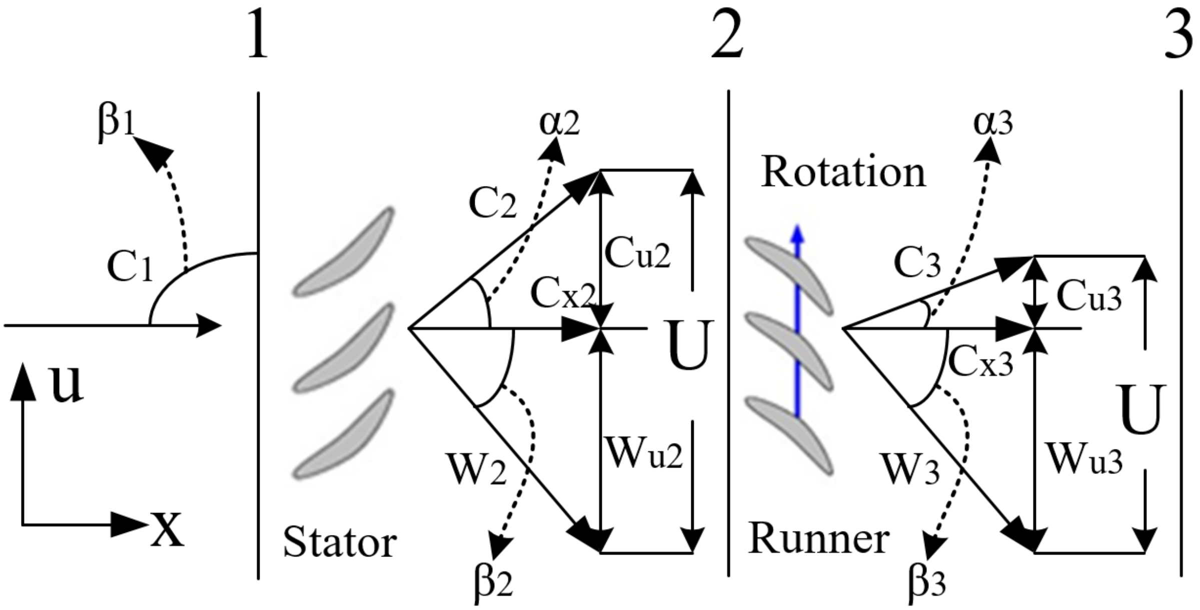

Figure 2.2. *The velocity triangle for a generalized turbine system that shows each velocity component at each turbine station: Station-1 is the Turbine inlet, Station-2 is the Stator Outlet, Station-3 is the Runner Outlet*

2.2. Definitions of Efficiency and Loss Estimation

Turbines are designed to convert the available energy in a flowing fluid into useful mechanical work to the shaft. The efficiency of this process, the $overall\ efficiency\ \eta_0$, is a performance factor of considerable interest to both the designer and user of the turbine. Thus [1]

$$\eta_0 = \frac{mechanical\ energy\ available\ at\ coupling\ of\ output\ shaft\ in\ unit\ time}{maximum\ energy\ difference\ possible\ for\ the\ fluid\ in\ unit\ time} \tag{2-18}$$

Mechanical energy losses occur between the turbine runner and the output shaft coupling as a result of the work done against friction at the bearings or other mechanical devices. The magnitude of this kind of loss is difficult to estimate as it varies with size and manufactured skills. So, another efficiency $turbine\ efficiency\ \eta_t$, or $hydraulic\ efficiency\ \eta_h$ were widely used as

$$\eta_h\ or\ \eta_t\ = \frac{mechanical\ energy\ supplied\ to\ the\ runner\ in\ unit\ time}{maximum\ energy\ difference\ possible\ for\ the\ fluid\ in\ unit\ time} \tag{2-19}$$

From above definitions, it is easily deduced that the $mechanical\ efficiency\ \eta_m$, which is simply the ratio of the shaft power to the rotor power, as

$$\eta_m = \frac{\eta_0}{\eta_h} \tag{2-20}$$

For the hydraulic turbines, the turbine hydraulic efficiency η_h (or the turbine total to static efficiency η_{ts}), is defined as the work supplied by the rotor in unit time divided by the maximum hydrodynamic energy difference of the fluid per unit time, as [1]

$$\eta_h\ or\ \eta_{ts} = \frac{\Delta W_x}{g\Delta H_{total}} \tag{2-21}$$

The losses for hydraulic turbine are modeled as $\Delta H = k\frac{(velocity)^2}{2g}$ (where k is loss coefficient), and could be classified into several different categories which are shown in **Table 2.1**.

Table 2.1. *Loss models for axial hydraulic turbines (Adapted from [43]).*

Loss Mechanism	Loss model
Guide vane profile loss (skin friction loss at the stator) [44]	$\Delta H_{gvpl} = \frac{\xi_s C_2^2}{2g}$ $\xi = \left(\frac{10^5}{Re}\right)^{\frac{1}{4}} \left[(1+\xi_1)\left(0.975+\frac{0.075b}{B}\right)-1\right]$ $\xi_1 = \xi_0 e^{0.01053\varepsilon},\ \xi_0 = 0.04{\sim}0.06$ $\varepsilon = flow\ turning\ angle$ $\frac{B}{b} = \frac{blade\ height}{chord\ length} = cascade\ aspect\ ratio$
Incidence loss [43]	$\Delta H_{il} = \frac{\lambda w_{inc}^2}{2g}$ $w_{inc} = \left(\frac{C_{x2}}{\tan\gamma_{blade}} + \frac{C_{x2}}{\tan(90-\alpha_2)}\right) - u$ $\lambda = 0.5 - 0.7$
Runner-blade profile loss [44]	$\Delta H_{rbpl} = \frac{\xi_b W_3^2}{2g}$
Mechanical Loss [44]	$\eta_{mec} = 0.95 - 0.99$
Losses in the flow passage between the guide vanes and runner [45]	$\Delta H_{gvr} = \frac{k_2 H_t Q}{D^2 (g H_t)^{0.5}}$ $k_2 = 0.002 - 0.005; H_t = Total\ head;$ $D = guide\ vanes\ diameter$ $Q = volumetric\ flow\ rate$

Now the total head required could express as following

$$\Delta H_{total} = \Delta H_{Effective} + \sum \Delta H_{losses} \tag{2-22}$$

The effective head could be determined from the design specification

$$\Delta H_{effective} = \frac{W_T}{\dot{m}g} \tag{2-23}$$

Finally, the hydraulic efficiency could be expressed as

$$\eta_h \; or \; \eta_{ts} = \frac{W_T}{\dot{m}g\Delta H_{total}} \tag{2-24}$$

Another important definition of efficiency is total-to-total efficiency (η_{tt}) which could express as,

(P_i is the inlet total pressure; P_o is the outlet total pressure)

$$\eta_{tt} = \frac{W_T}{Q(P_i - P_o)} \tag{2-25}$$

CHAPTER III: DESIGN METHODOLOGY DEVELOPMENTS

In general, the hydraulic turbine design process has three critical steps: 1. general size and operation design, 2. blade profile design, 3. blade configuration design. In order to solve the challenges that associate with the new SMH technologies, unconventional design method and configurations must be developed and tested. Therefore, this chapter presents a comprehensive design methodology with a detailed theoretical background and in-depth geometrical considerations.

3.1. Turbine selection and current development status

Currently, there are two paths to utilize the potential energy of the low head or new stream-reach sites: 1. Low-head Hydropower Application, and 2. River Current Application. For the low-head hydropower application, five major types of turbines are widely used: 1. Open-flume Francis turbines, 2. Kaplan turbine, 3. Tubular turbines, 4. Crossflow turbine, 5. Archimedes screw turbines. **Table 3.1** summaries some advantages and disadvantages of those types of turbines.

For the River-current application, the hydro-kinetic turbine is commonly used. This type of turbine uses ultra-low or zero head conditions and is driven by the free-flow stream. This technology has two advantages: Multi-unit arrays can be deployed for maximum power production like the wind farm, and the structural requirements are low; thus, the civil cost will be limited. However, this technology still suffers from some significant drawbacks, including 1. relatively low efficiency, 2. high installation cost, 3. high maintenance difficulties.

Based on the DOE's design specifications mentioned in ***section 1.3.2***, only the reaction turbine is allowed for SMH applications. Furthermore, since the high flow rate and head variability, among all turbine types, the Kaplan turbine (or its variants) is the best option for the

SMH technology. However, the new design method needs to be developed for the challenges associated with the new SMH technology.

Therefore, the proposed generation module is an open flume, damless Kaplan turbine system, and has eight major components. **Figure 3.1** shows a complete layout of this generation module. This Generation Module has a fixed stator, and an adjustable runner, the geometry of the stator and runner can be optimized for better performance.

Table 3.1. *Five major types of turbines for low-head applications. (Adapted from [46])*

Turbine Type	Advantages	Disadvantages
Open-flume Francis Turbine	High efficiency on the design condition	Narrow operation range, expensive to manufacture
Kaplan Turbine	High efficiency over a wide range.	The regulation method can be complex
Tubular Turbine	High efficiency, and various configurations for a low hydraulic loss.	Need straight passage through the turbine, can increase the civil cost.
Crossflow Turbine	Wide operation range (head and flow).	Relatively low efficiency
Archimedes Screw Turbine	Wide operation range, high tolerance for debris, and fish friendly.	Relatively large for transportation, and technology still immature.

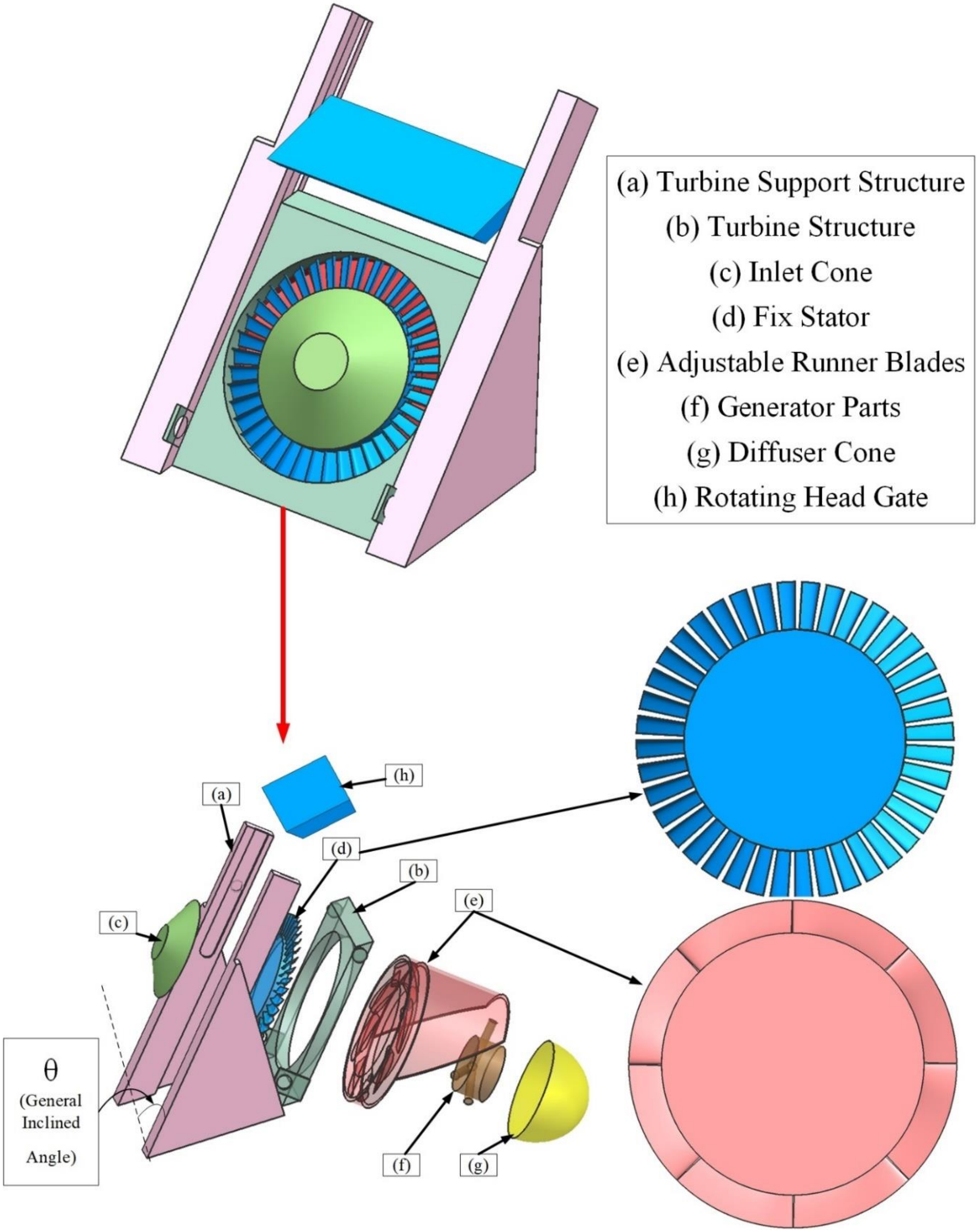

Figure 3.1. *The proposed generation module's configuration for SHM technology. (Top: Total Assembly Model; Bottom: Close-up for each component)*

3.2. Design methodology developments

3.2.1. Additional design considerations

In addition to the DOE SMH generation module design specifications, there are four crucial design considerations for developing a successful SMH generation module.

- For the SMH generation module, since the head condition is ultra-low, traditional dam structure is not a necessity. Instead, the reinforced Kaplan turbine structure (Part-B in **Fig 3.1**) is considered as a dam that provides the low head condition for the turbine. This configuration can reduce the cost and complexity of the civil works, and also, means the overall turbine structure size and the position are related to the head condition and performance.
- Since the SMH generation module is directly installed into the water system, it must be fish-friendly, which means larger turbine areas for fish migration and low rotational speed for avoiding unnecessary fish damage.
- The low head, relatively low flow rate, and relatively large blade area natures of this design mean no draft tube or tiny draft tube is needed to recover the end water kinetic energy since it is already minimal. The water exits the turbine system and can directly discharge to the river or atmosphere, which means less piping and water guiding structure costs.
- Typically, the new stream-reach sites have various flow conditions from season to season; this means the proposed generation module system must at least have one regulated feature for different flow conditions. Therefore, the blades and speed regulation methods are the two traditional ways to regulate the system for different flow conditions economical-effectively. However, since the general turbine structure serves as a dam for this design, a rotating head-gate (Part-H in **Fig 3.1**) could be considered as a new regulated method for regulating the head conditions.

3.2.2. **Generation module initial size and operation condition design**

- *Generation module overall size and positioning*

Initial size design is the first challenge for developing a low-head hydraulic turbine. Traditionally, a specification map is used for determining the basic turbine characteristics, including head, rating power, and rotational speed for optimum performance. **Figure 3.2** shows a typical specification map between the specific speed and specific diameter for various turbine types. **Figure 3.3** shows a similar specification map for the Kaplan turbine. Those charts come from years of surveys from the major hydro station and often provide an accurate initial size design for the traditional hydro-system. However, for low head conditions, those charts can result in a smaller size and higher rotational speed, which are preferential features for high efficiency. Those features are contradicted with the concept of SMH since it requires a large turbine area and less fish damage.

This proposed turbine uses its turbine structure (Part-A in **Fig 3.1**) to provide the low-head condition; therefore, the initial turbine size is related to the designed head and the positioning of the turbine structure. For the low-head application turbine, the turbine structure is often positioned in water with a general-inclined angle (refer as θ in **Fig 3.1**), and this angle is generally from $15° - 45°$ [47]. A larger inclined angle requires a more extended turbine structure and is more subject to the tailwater elevation, and a smaller inclined angel can have a shorter turbine structure, which means a smaller turbine area. Turbine structure minimum length can be calculated as

$$Turbine\ structure\ minimum\ structure\ length \approx \frac{Design\ Head}{cos\theta} \tag{3-1}$$

This minimum length gives a guideline for the initial size of the turbine (Turbine Overall Diameter), and addition head-gate (Part-H in **Fig 3.1**) can be equipped for more headspace for the off-design condition.

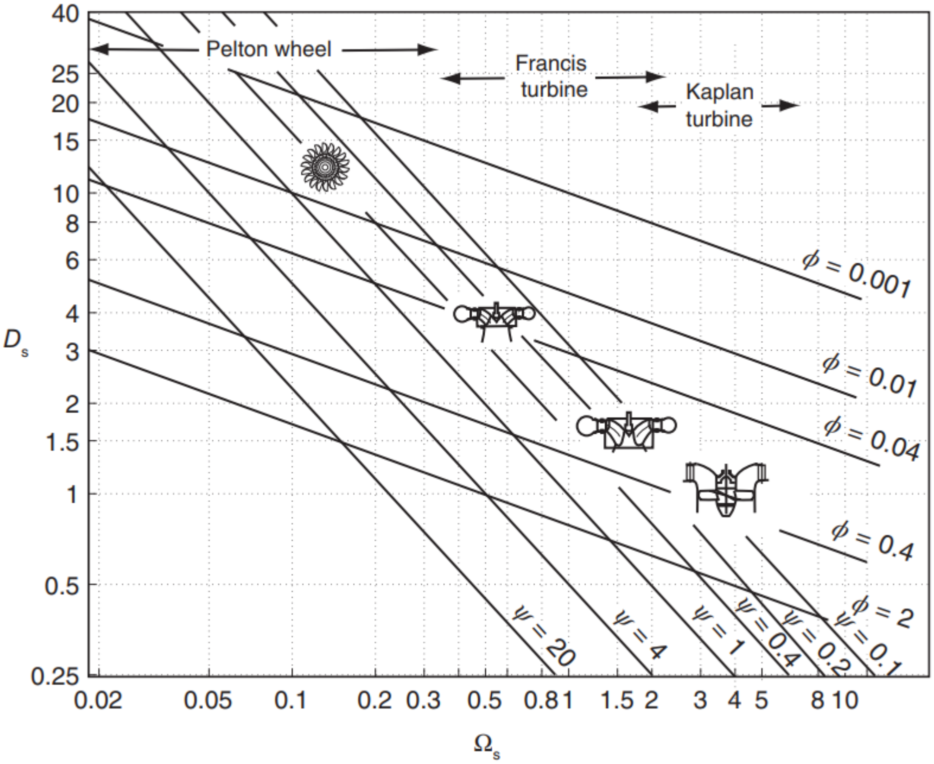

Figure 3.2. *A typical specification map for different turbine types [48]*

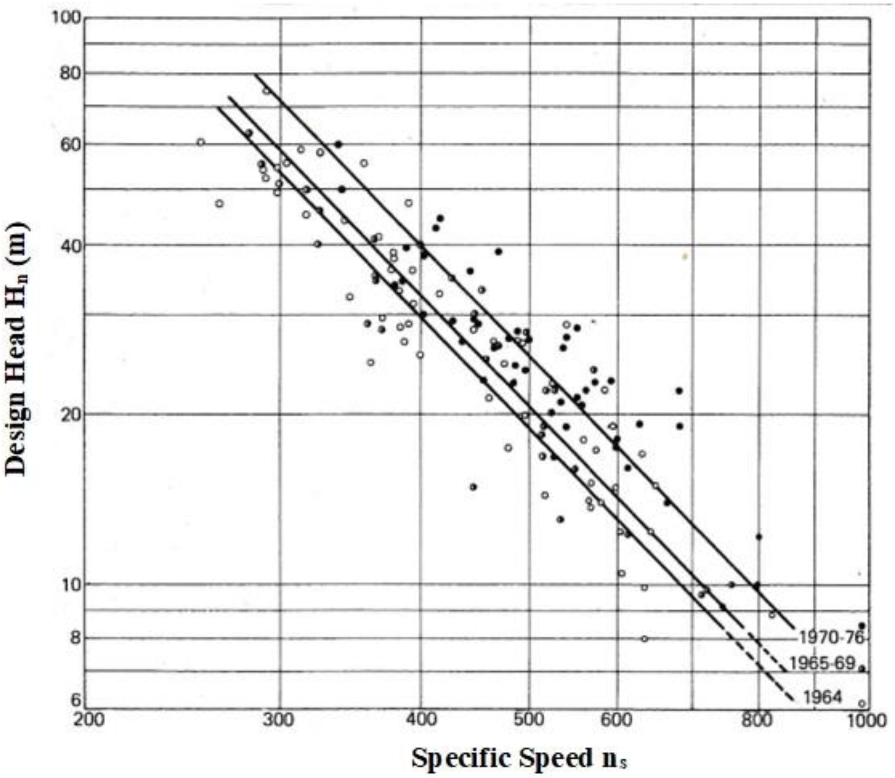

Figure 3.3. *A conventional Kaplan turbine specification map using for initial design [49]*

- *Generation module hub diameter*

After determining the overall diameter, the turbine hub diameter is the next parameter that needs to be considered with care. For the SMH generation module, the hub volume must contain the generator and control components; this means the hub diameter and its impact on turbine performance should be studied thoroughly for future generator selections and designs. Additionally, depending on which 1-D design method is used for the turbine runner, the hub diameter has a significant impact on the turbine runner shape, which is covered in ***section 3.2.3***. For traditional Kaplan turbine, two empirical equations can be used for determining the hub-tip ratio for optimum performance

$$\frac{D_{hub}}{D_{tip}} = 0.8 - 0.1\Omega_s \text{ [48]} \qquad (3\text{-}2)$$

$$\frac{D_{hub}}{D_{tip}} = 0.25 + \frac{94.64}{n_s} \text{ [49]} \qquad (3\text{-}3)$$

Those equations can only be useful for the initial guess, and the different hub-to-tip ratio must be studied for low-head applications. Different hub-to-tip ratios between 0.68-0.8 were studied, and the results were shown in ***section 5.1***.

- *Generation module operation condition*

For the initial design stage, the rotational speed is the only operational condition that needs to be considered. The criteria for determining the rotational speed comes from environmental considerations. The high rotational speed is typically required for a low head application that can have a high risk for the fish population. DOE developed ten criteria for designing a fish-friendly hydraulic turbine system in 1999 [50] (The full list of these criteria is in **Appendix-A**). According to those criteria, the peripheral runner speed should have less than 12.24m/s (preferably 6.12m/s) for a fish-friendly turbine, and this criterion limits the maximum rotational speed for the SMH generation module.

3.2.3. **1-D Vortex analysis for axial turbine**

All turbine design starts with a 1-D velocity calculation, so it is essential to define the velocity component, which shown in **Figure 2.2**. For the initial 1-D Kaplan turbine design, there are two steps to calculate the velocity at each radial span location: 1. Determining the mean velocity value and 2. Determining other span velocities with appropriate assumptions. Determining the mean velocity value is simplified by using three fundamental conservation equations mentioned in ***Chapter 2***. Then, the next step is determining the velocity component at each radial span location, which is the most critical part of the 1-D design. Conventionally, the free vortex assumption is widely used for initial velocity calculation.

The free vortex assumption is an inviscid and ideal case which includes four parts: 1. Flow upstream of the runner is assumed to be free of the vortex, 2. Flow has uniform axial velocity (C_x) distribution, 3. Flow has zero radial velocity (C_r) across all span locations, and 4. Flow at each radial location has a constant rC_u value, namely

$$[rC_u]_{mean} = [rC_u]_{tip} = [rC_u]_{hub} \tag{3-4}$$

This equation comes directly from analyzing the radial equilibrium of the blade and considering a radial fluid element in **Fig 3.4**. The equilibrium of this fluid element in the radial direction is given by Newton's second law, which states as

$$\sum F_r = ma_r\,, a_r = -\frac{C_u^2}{r} \tag{3-5}$$

The net force along the r direction could be written as

$$\sum F_r = pd\theta dz - \left(p + \frac{\partial p}{\partial r}dr\right)d\theta dz = -\rho d\theta dzdr\frac{C_u^2}{r} \tag{3-6}$$

where,

$$\frac{\partial p}{\partial r} = \frac{\rho C_u^2}{r} \tag{3-7}$$

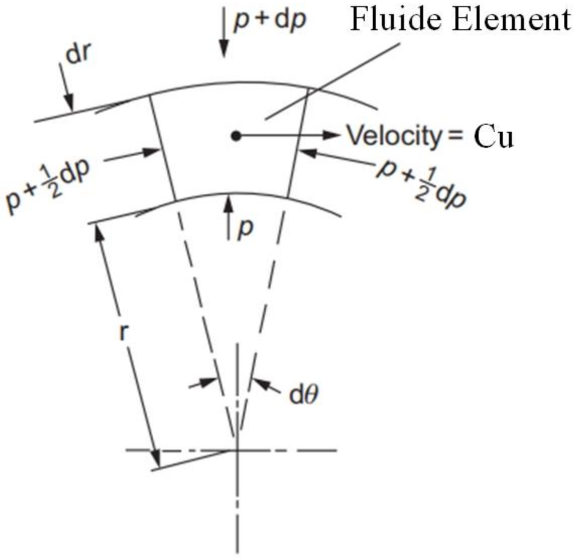

Figure 3.4. *A radial fluid element in a typical axial turbomachinery system.*

Considering the stagnation enthalpy h_0 as constant for every particle and keep it constant along a plane perpendicular on the axis

$$h_0 = h + \frac{C_u^2}{2} + \frac{C_x^2}{2} = Constant \tag{3-8}$$

In a differential form

$$\frac{dh_0}{dr} = \frac{dh}{dr} + C_u\frac{dC_u}{dr} + C_x\frac{dC_x}{dr} \tag{3-9}$$

$$since\ Tds = dh - \frac{dp}{\rho} \quad \rightarrow \quad T\frac{ds}{dr} = \frac{dh}{dr} - \frac{1}{\rho}\frac{dp}{dr} \quad \rightarrow \quad \frac{dh}{dr} = T\frac{ds}{dr} + \frac{1}{\rho}\frac{dp}{dr} \tag{3-10}$$

Substituting the above equation into **Eqn (3-8)** as

$$\frac{C_u^2}{r} + C_u\frac{dC_u}{dr} + C_x\frac{dC_x}{dr} = 0 \tag{3-11}$$

Equation (3-11) can be written to describe blade geometry variation from mean to hub and tip as

$$\frac{d}{dr}(C_x^2) + \frac{1}{r^2}\frac{d}{dr}(rC_u)^2 = 0 \tag{3-12}$$

For inviscid and steady flow, assume C_x is uniform in r direction, then

$$\frac{d}{dr}(rC_u) = 0 \tag{3-13}$$

The above equation is known as the **free vortex condition**.

Two other assumptions could also be used for initial velocity calculation: Force vortex assumption and Constant vortex. Force vortex means that: $C_u = Kr$, where K is vortex constant. And constant vortex means: $C_u = constant$. **Figure 3.5** shows examples of runner-blade geometries designed with three different vortex assumptions. Previous research [51] has shown that different vortex assumptions trend to have similar hydraulic performance, and the only difference was the pressure distribution pattern across the blade, which may result in different deformation behavior of the blades. This paper mainly uses the free vortex assumption for initial velocity calculation.

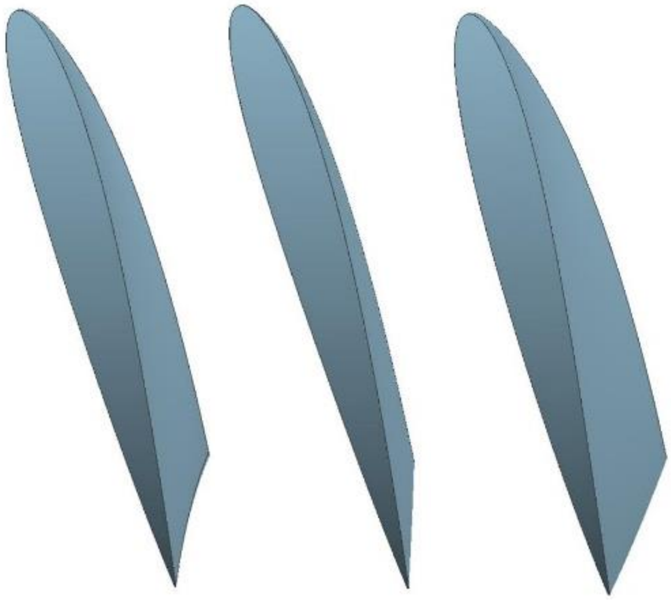

Figure 3.5. *Three example runner-blades configurations with different vortex assumptions. (From left to right: Free vortex, Force Vortex, Constant Vortex)*

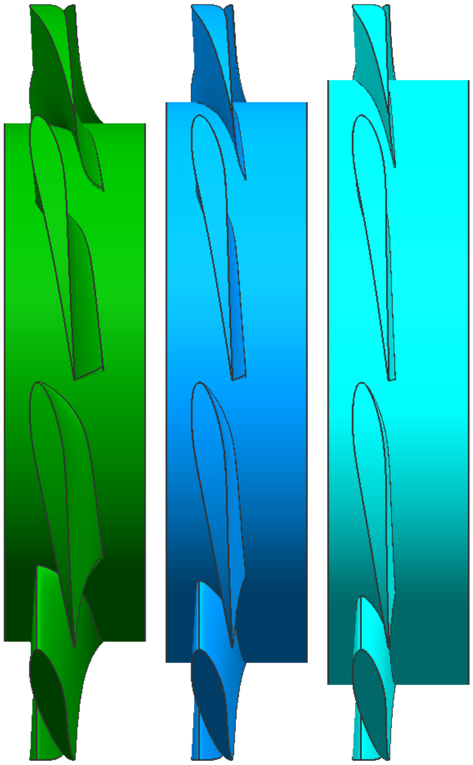

Figure 3.6. *Three example runner-blade configurations with different hub diameter settings. (From left to right: hub-to-tip ratios (D_{hub}/D_{tip}) =0.685, 0.743, 0.8.)*

Because of the relatively low rotational speed, when utilizing the free vortex assumption for designing runner-blade, small hub diameter can result in a large C_{u2} velocity and small U velocity, and this can cause a negative β_2 value. This negative β_2 value at specific radial span location can cause a larger twist angle of the blade, and the **Fig.3.6** shows three geometries of the blade with three hub diameters. A large, twist-angle blade can increase the complexity and the manufacturing cost of the blade. Therefore, it is crucial to define a minimum hub-to-tip ratio for preventing a large blade twist angle. When using the free vortex assumption, the minimum hub-to tip ratio is defined when $\beta_2 = 0$, and can be calculated as

$$\frac{D_{hub}^2}{D_{tip}} = \frac{4\eta_t g \cos\theta}{\omega^2} \tag{3-14}$$

3.2.4. 1-D Blade geometry construction

There are some previous researches focus on designing the hydraulic turbine blade profile. Ferro et al. [52] used the through-flow analysis approach and streamline curvature method to design a mini hydraulic bulb turbine rotor; Stuikno et al. [53] used the minimum pressure coefficient and free vortex method to design a low-head turbine; Anagnostopoulos et al. [54] used the Lagrangian approach to develop and optimize a Turgo turbine; Höfler et al. [55] used the stream curvature method to design the runner blade row of the Saxo-type turbine. This thesis focuses on a geometry-based design methodology for a low-head hydraulic turbine system.

By using the calculated velocity values from the vortex assumption, blade geometry can be constructed by two steps: 1. blade camberline construction, and 2. blade thickness distribution. The proposed generation module has two blade profiles: one is the stator-blade, and the other one is the runner-blade. Those two blade profiles share the same design process. Here is a general process for designing a runner-blade geometry (for stator-blade geometry, replace the runner-blade angle values with stator angle values). Based on **Eqn (2-16)**, the power delivered by the turbine runner-blade is only dependent on the blade inlet and outlet velocity conditions. Therefore, for general 1-D considerations, the blade camberline can be any shape of curves, as long as its inlet and outlet match the velocity condition (namely velocity direction). However, the blade geometry has a significant effect on the overall hydraulic performance. Therefore, the blade camberline construction method needs to meet two main requirements: 1. need to match inlet and outlet velocity conditions, and 2. need to have the flexibility to control the blade general curve shape for further optimization. Based on those considerations, a new blade construction method, five-point Bezier curve method, is invented to create and optimize the blade camberline geometry.

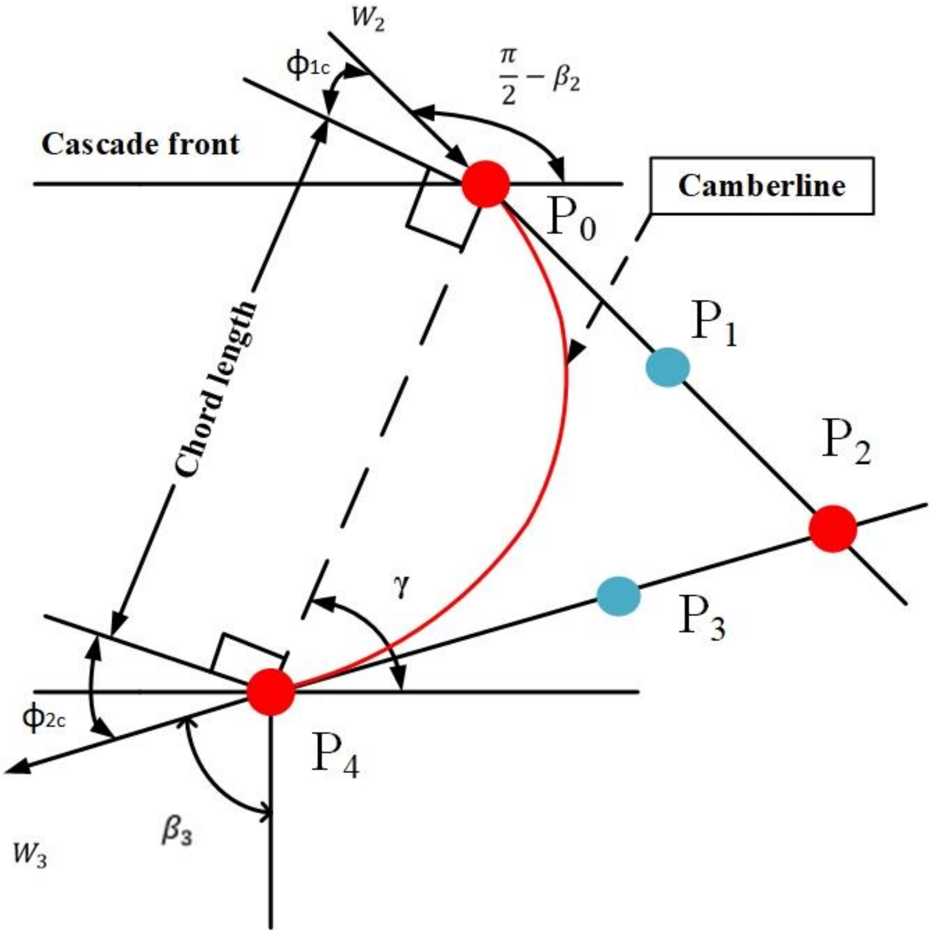

Figure 3.7. *A standard unit runner-blade profile for the proposed turbine system*

Bezier curve is a parametric curve constructed by a set of control points (P_i and $i \geq 3$). For constructing the blade camberline, two points are fixed, one is at the beginning of the camberline, and the other one is at the endpoint of the camberline. The rest of the points are located outside the camberline to control the camberline-overall geometry. The general nth order Bezier curve state as

$$B(t) = \sum_{i=0}^{n} \binom{n}{i} (1-t)^{n-i} t^i P_i \tag{3-15}$$

where $\binom{n}{i}$ is the binomial coefficient, P_i is the set of points. So, the fourth-order Bezier curve is

$$B(t) = (1-t)^4 P_0 + 4(1-t)^3 t P_1 + 6(1-t)^2 t^2 P_2 + 4(1-t) t^3 P_3 + t^4 P_4 \tag{3-16}$$

For a standard unit runner-blade camberline shown in **Fig 3.7**, P_0 is the inlet point, P_4 is the outlet point: $P_0 = (0,0), P_4 = (1,0)$. Then, to match the velocity direction, drawing two lines that are both tangential to the curve at inlet and outlet. The intersection point of two lines is the P_2,

$$P_2 = \left(\frac{1}{1 + \frac{\cot \phi_{1c}}{\cot \phi_{2c}}}, \frac{\cot \phi_{1c}}{1 + \frac{\cot \phi_{1c}}{\cot \phi_{2c}}} \right) \tag{3-17}$$

where, ϕ_{1c} and ϕ_{2c} are auxiliary angles, that come from the velocity triangle

$$\phi_{1c} = \gamma_r + \beta_2 \tag{3-18}$$

$$\phi_{2c} = 180° - \gamma_r - \beta_3 \tag{3-19}$$

where, γ_r is the stagger-angle of the runner-blade (γ_s is for stator), for a continuous curve

$$90° - \beta_3 < \gamma_r < 90° - \beta_2 \tag{3-20}$$

And, the γ_r can be defined as

$$\gamma_r = (90° - \beta_3) + C_{rsa}(\beta_3 - \beta_2) \tag{3-21}$$

where, C_{rsa} is the runner-blade stagger-angle setting constant, and C_{rsa} is between 0 and 1 (For stator-blade, stator-blade stagger-angle setting constant refer as C_{ssa} , and can be defined the same way with stator-blade angle β_1 and β_2). This stagger-angle, setting constant is critical for turbine blade design and has a significant influence on the turbine overall hydraulic performance. **Figure 3.8** shows a series of runners and stators blade with different stagger-angle setting constants, and detailed numerical results were shown in ***sections 5.2.1 and 5.3.1***.

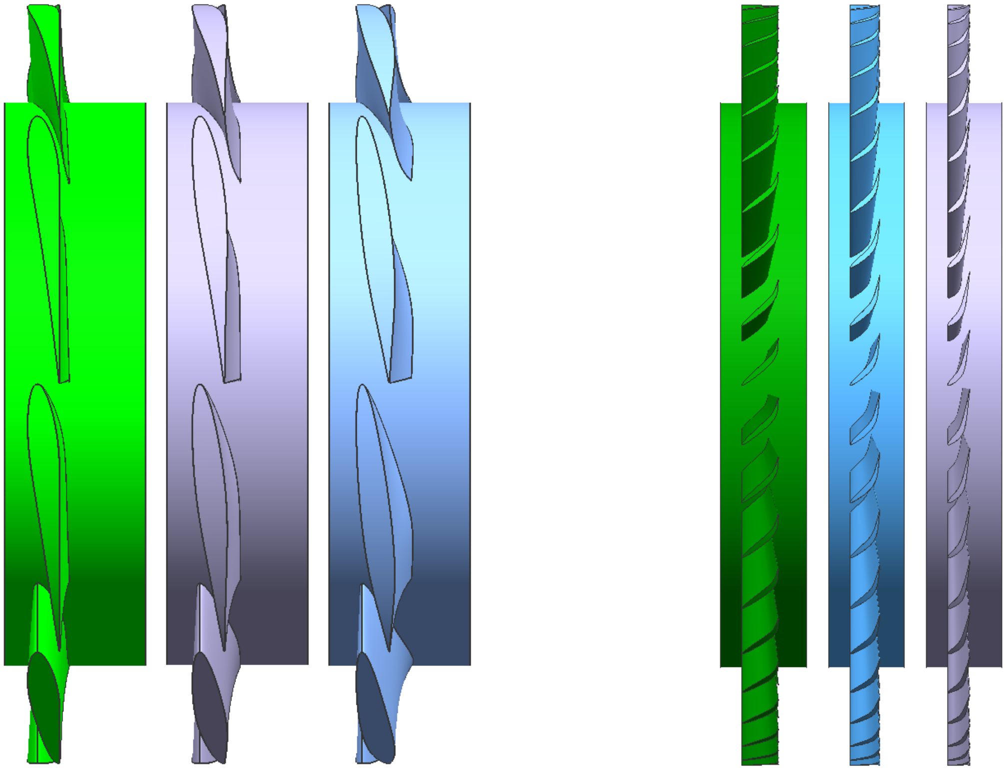

(a) Runner-blade with various Stagger-angle setting Constants. From left to right: $C_{rsa} = 0.3; 0.5; 0.7.$

(b) Stator-blade with various Stagger-angle setting Constants. From left to right: $C_{ssa} = 0.3; 0.5; 0.7.$

Figure 3.8. *Runner-blade and Stator-blade with different stagger-angle setting constants*

Conventionally, three points (P_0, P_2, P_4) Bezier curve method is enough to construct a blade camberline for the right velocity conditions. However, a three-point Bezier curve (second-order Bezier curve) has one disadvantage: for a given velocity condition (which means β_2 and β_3 are given), the blade profile is only controlled by the stagger-angle (γ_r). This limitation means, for a fixed stagger-angle, the blade profile cannot be changed, which can cause less fixable control for further optimization. So instead of a three-point Bezier curve, the five-point Bezier curve is used by adding two more points to construct the blade camberline. One point (P_1) is on the straight line P_0P_2

$$P_1 = (c_1 P_{2x}, c_1 P_{2y}) \tag{3-22}$$

Another point (P_3) is on the straight line P_2P_4

$$P_3 = (1-(1-P_{2x})c_2, c_2P_{2y}) \tag{3-23}$$

C_1 and C_2 are two Bezier curve control points. By adding those two points, this method not only meets the velocity conditions but also increase the flexibility for further optimization. Therefore, the general fourth-order Bezier curve point coordinate for the runner-blade camberline is

$$\begin{aligned} B(x) = {} & [4c_2 - 3 + P_{2x}(6 - c_1 - 4c_2)]x^4 + [4 - 4c_2 + P_{2x}(12c_1 + 4c_2 - 12)]x^3 \\ & + P_{2x}(6 - 12c_1)x^2 + 4P_{2x}c_1x \end{aligned} \tag{3-24}$$

$$\begin{aligned} B(y) = {} & P_{2y}(24 - 16c_1 - 16c_2)x^4 + \left[4 - 4c_2 + P_{2y}(12c_1 + 4c_2 - 12)\right]x^3 \\ & + P_{2y}(6 - 12c_1)x^2 + 4P_{2y}c_1x \end{aligned} \tag{3-25}$$

After carefully constructing the blade camberline using the above method, the last step for constructing a blade profile is to have a thickness distribution function for the camberline. For this paper, the NACA-4 series profile is used and can be stated as

$$\frac{y_t}{R_{Lc}\ or\ S_{Lc}} = \frac{R_T\ or\ S_T}{0.2}(a_0x^{0.5} + a_1x + a_2x^2 + a_3x^3 + a_4x^4) \tag{3-26}$$

where, R_{LC} and S_{LC} are the runner and stator-blade chord length; and R_T and S_T are the runner and stator-blade relative maximum thickness as

$$\mathrm{R}_T = \frac{R_{Tm}}{R_{Lc}};\ S_T = \frac{S_{Tm}}{S_{Lc}} \tag{3-27}$$

where, R_{TM} and S_{TM} are the runner and stator-blade maximum thickness. In **Eqn (3-25)**, the a_0 to a_4 are prescribed coefficients

$$\begin{gathered} a_0 = 0.2969;\ a_1 = -0.126;\ a_2 = -0.3516;\ a_3 = 0.2843 \\ a_4 = -0.1015\ or - 0.1036\ \text{ for a closed trailing edge} \end{gathered} \tag{3-28}$$

The superposition method, which superimposes the thickness onto the camberline, is needed for this last step. **Figure 3.9** shows an example of this superimposed method. By using some points located at the camberline (x_c, and y_c in **Fig 3.9**), this superimposes method aims to calculate the blade's suction and pressure side surface point coordination. Then by connecting those points, the blade profile can be created. On the suction side of the blade, the blade surface point coordination (x_s, y_s) can be calculated as

$$x_s = x_c - (y_t)sin\vartheta; \; y_s = y_c + (y_t)cos\vartheta \tag{3-29}$$

On the pressure side of the blade (x_p, y_p)

$$x_p = x_c + (y_t)sin\vartheta; \; y_p = y_c - (y_t)cos\vartheta \tag{3-30}$$

where ϑ is the camberline tangential angle at each chosen point.

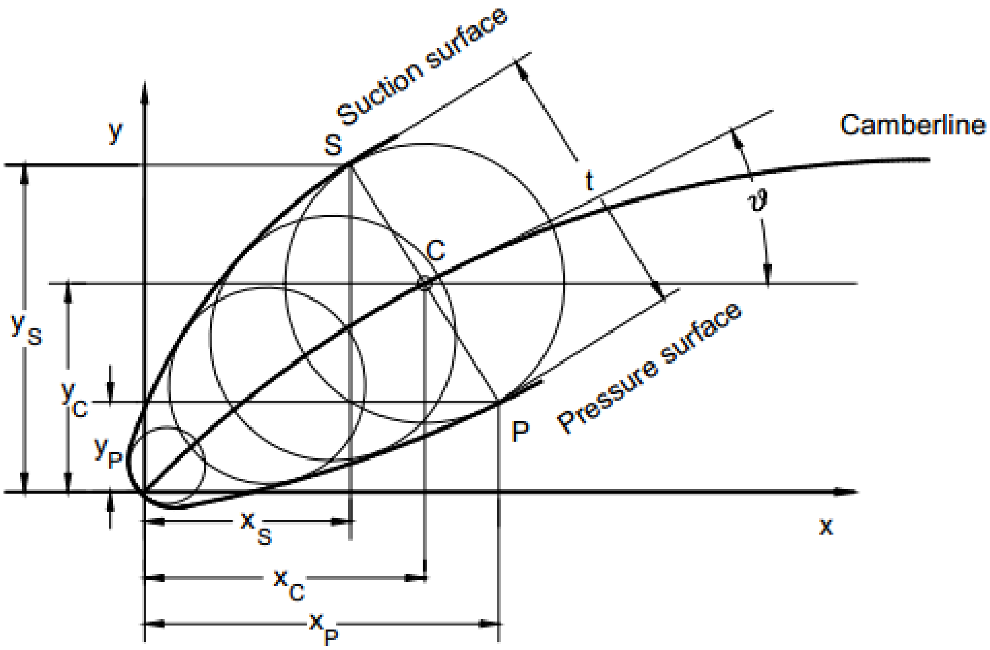

Figure 3.9. *Superimposition method using the thickness distribution function to construct a blade profile [56]*

3.2.5. **Summaries of 1-D blade design**

By using the above method, the blade profile for each span location can be determined; then, by using standard CAE software, which connects each span's blade profile, the final blade geometry can be constructed. The above method has great flexibility for designing an SMH generation module; for example, by using 11 radial-span locations, the runner-blade has a total of 33 parameters for modifying runner-blade geometry, which is good for future pressure distribution, stress and performance optimization. In a nutshell, there are four fundamental steps for constructing a blade profile.

- Construct the camber lines profile by the Bezier curve method from the calculated velocity.
- Chose a base profile, a relative thickness, and the stagger-angle setting constant for the blade.
- Calculate the suction surface and pressure surface coordinate from **Eqn (3-29), (3-30)**.
- Smooth the profile and make sure there is no discontinuity and waviness on the surface.

3.3. Generation module’s blade configuration design

Obtaining the blade profile is the first step for constructing an excellent turbine blade system. Seven fundamental blade configuration parameters can further affect the blade geometry and eventually influence the overall performance. **Table 3.2** lists all seven parameters, and this section will comprehensively explain all those parameters.

Table 3.2. *Seven blade configuration parameters for stator and runner blade*

Stator-blade	Stator Inlet Angle Stator Solidity Stator-blade Number Stator Thickness	Runner-blade	Runner-blade Number Runner-blade Solidity Runner-blade Thickness

3.3.1. Stator Inlet Angle

The Stator-blade inlet angle is referred to as β_1 in **Fig. 2.2**. Since the SMH generation module is positioned in the water with a general-inclined angle θ; theoretically, this stator, the inlet-flow angle is related to the general-inclined angle as

$$\beta_{1\,flow} = \frac{\pi}{2} + \theta \tag{3-31}$$

However, the inflow water trends to have a constant 90° inflow angle ($\beta_{1\,flow}$) for different general inclined angle configuration (Detail results were shown in ***section 5.2.2***). Therefore, the stator-inlet **blade-angle** ($\beta_{1\,blade}$) can be set differently to the stator inlet-flow angle ($\beta_{1\,flow}$) to achieve a better overall hydraulic performance. **Figure 3.10** shows five stator examples with a different $\beta_{1\,blade}$ between 55° and 130°. Different $\beta_{1\,blade}$ angles can completely alter the stator geometry and influence the overall hydraulic performance. The detailed numerical results were shown in ***section 5.2.2.***

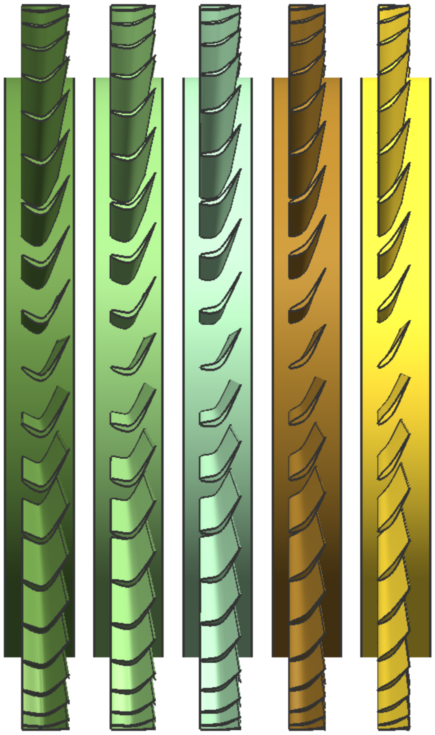

Figure 3.10. *Five stator-blades with different inlet blade angles (β_{1blade}). (From left to right: β_{1blade} = 55°, 70°, 90°, 110°,130°)*

3.3.2. **Stator-blade Number**

The purpose of the stator is to guide and pre-rotate the flow to the runner-blade. High stator counts can result in better flow guidance, but the thickness of the stator can also increase the blockage loss. Also, high stator count can decrease the inlet area, which can cause additional damage to larger fish. Therefore, it is vital to find a balance between stator number and overall hydraulic performance. **Figure 3.11** shows five stator examples with different stator-blade numbers counts between 20 and 60. The detailed numerical results were shown in ***section 5.2.3.1***.

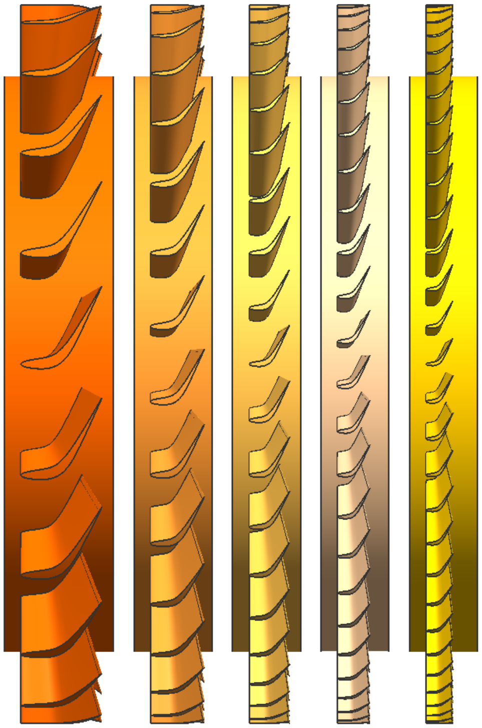

Figure 3.11. *Five stator models with different stator number. (From left to right: Stator Number = 20, 30, 40, 50 ,60)*

3.3.3. **Runner-blade Number**

Just like the stator-blade number, the runner-blade number is another critical parameter that can affect the overall hydraulic performance. Since the proposed SMH generation module has an adjustable runner-blade mechanism, the less runner-blade count can decrease the complexity of the control system and the overall module cost. Therefore, it is crucial to study how the runner-blade number affects the overall hydraulic performance. **Figure 3.12** shows five runner examples with different runner-blade numbers count between 4 and 12. Although the runner-blades number also has a profound influence on vibration, the only focus here is on the effect on overall hydraulic performance. The detailed numerical results were shown in ***section 5.3.2.1***.

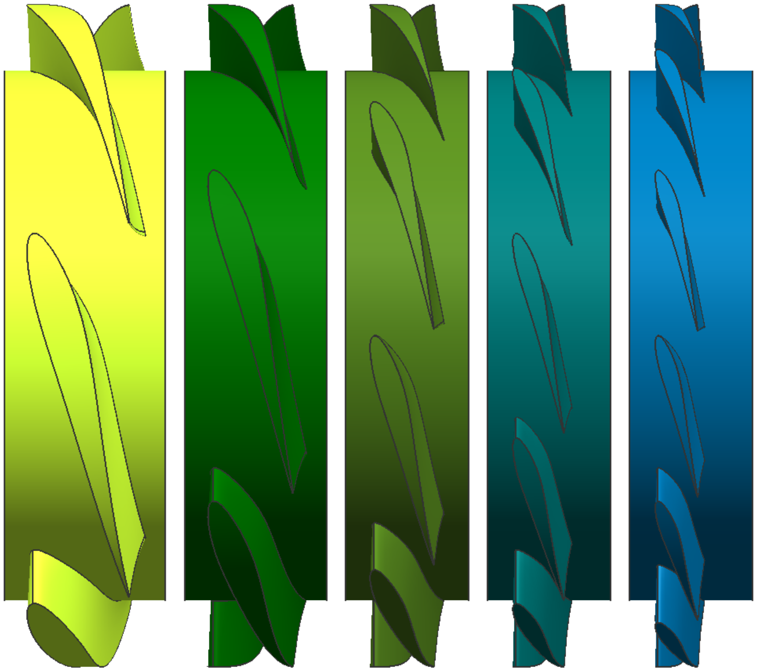

Figure 3.12. *Five runner-blades with different runner-blade number. (From left to right: Runner Number = 5, 6, 8, 10, 12)*

3.3.4. Stator and Runner blade Solidity

The solidity of a blade is defined as

$$\sigma = \frac{CL}{S} \tag{3-32}$$

where CL is the blade chord length, S is the blade spacing, can be defined as

$$S = \frac{\pi d_{span}}{N} \tag{3-33}$$

where d_{span} is the diameter at each blade span location, N is the blade number.

The runner-blade cascade solidity has significant influences on the flow behavior, especially on the blade profile losses (ζ). The runner-blade profile loss has two parts

$$\zeta = \zeta_{friction} + \zeta_{seperation} \tag{3-34}$$

With a defined spacing, there is an equilibrium between the separation and friction losses. Based on previous research, the corresponding solidity ratio has an optimum when $\sigma = 1$, which is shown in **Fig 3.13**.

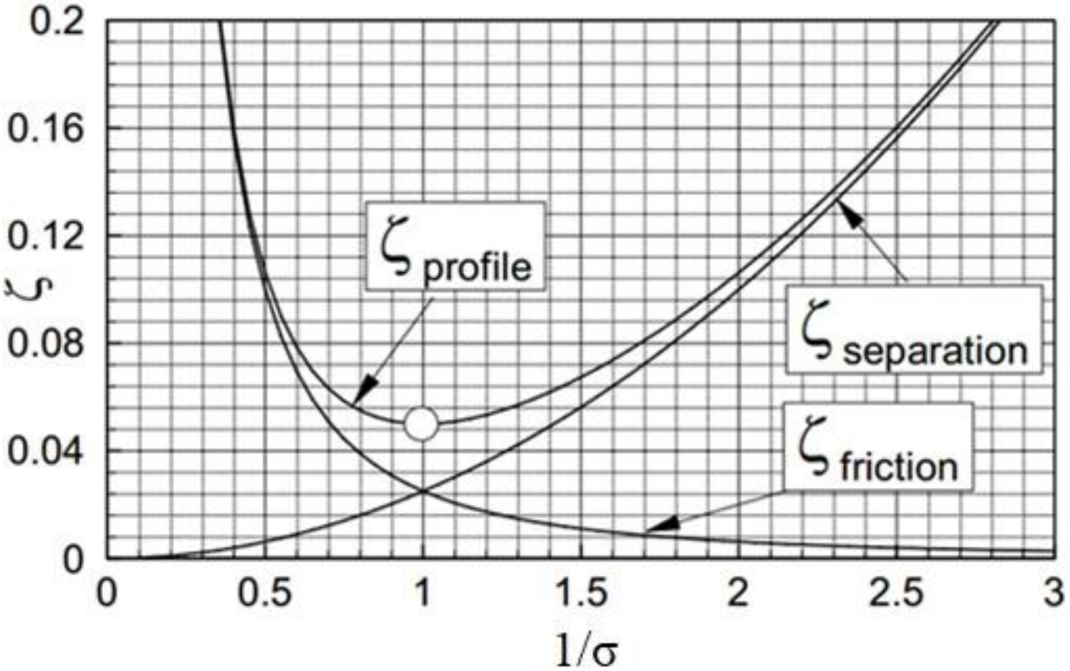

Figure 3.13. *The runner-blade profile loss as a function of the invert of solidity [56] (The circle marks the optimum value)*

For the SMH generation module, the runner-blade solidity can determine the runner-blade size, which has a profound effect on the efficiency and costs; therefore, different runner-blade solidity values must be tested. **Figure 3.14** shows six runner-blade examples with various solidity number, and detailed numerical results were shown in ***section 5.3.2.2***.

The stator-blade solidity, on the other hand, does not have an optimum value. However, the stator profile is also influential for the SMH generation module, since it helps to prevent the runner-blade being damaged by inlet trash, and also provide a correct guide for the inlet flow and fishes to the runner-blade; therefore, different stator-blade solidity values need to be tested. **Figure 3.15** shows ten stator-blade examples with various solidity number, and detailed numerical results were shown in ***section 5.2.3.2***.

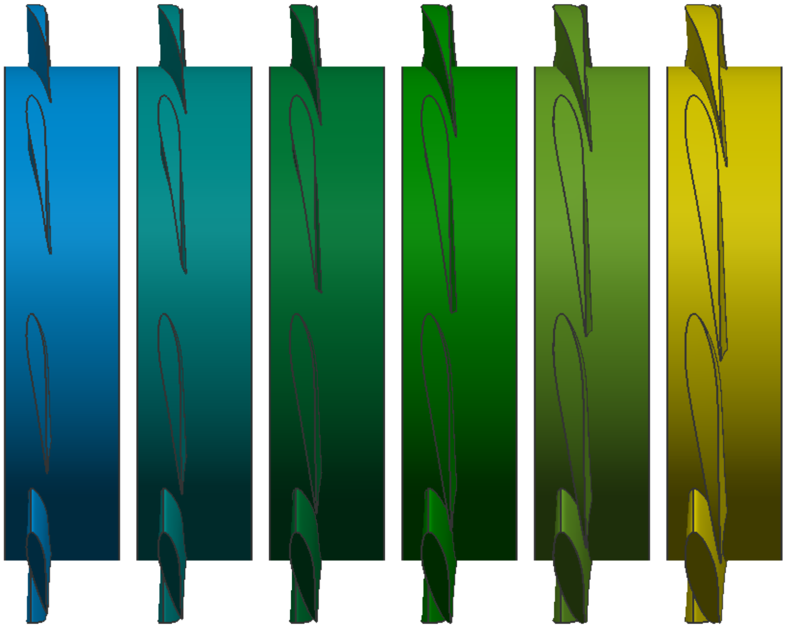

Figure 3.14. *Various Runner-blades with different solidity values. (Form left to right: σ_r=0.7,0.8,0.9,1,1.1,1.2)*

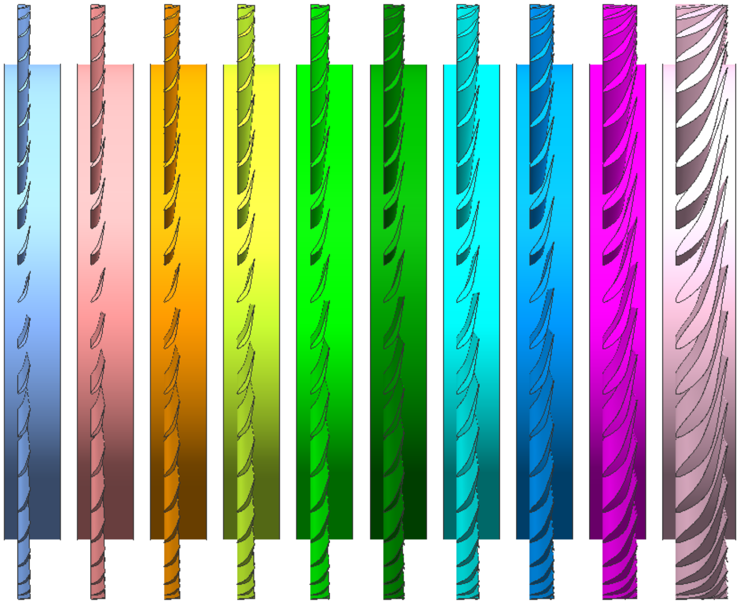

Figure 3.15. *Various stator-blades with different solidity values. (From left to right: σ_s=0.7, 0.8, 0.9, 1, 1.1, 1.2, 1.3, 1.4, 2.0, 3.0.)*

3.3.5. **Stator and Runner blade Thickness**

As shown in **Eqn (3-26)**, the relative blade thickness is the ratio of the maximum blade thickness and the chord length. This value has a significant impact on blade blockages, flow behaviors, deformation, and stress performance. In the hydraulic turbine, the thickness of the runner-blade can block the annulus passage area over the entire runner-blade zone. This runner blockage can be defined as the runner-blade maximum-blockage ratio (Γ_{RM}) or inlet blockage ratio (Γ_{inlet}) as

$$\Gamma_{RM} = \frac{R_{TM}}{S_R \cos \beta_2}; or\ \Gamma_{inlet} = \frac{R_T * \sigma}{\cos \beta_2};\ R_{TM} = R_T * CL_R \tag{3-35}$$

Where R_{TM} is the maximum runner thickness, R_T is the runner-blade relative thickness, CL_R is the runner-blade chord length, S_R is the runner-blade spacing, σ is the blade solidity, and β_2 is the runner-blade angle. **Fig. 3.16** shows a schematic diagram of this blockage definition. Since at each span location the β_2 is different, the Γ_{RM} is also a function of span location, and the mean maximum-blockage ration is defined at the mean span location.

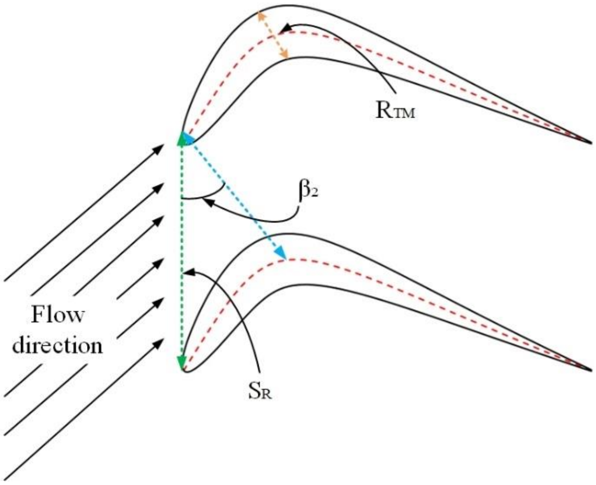

__Figure 3.16.__ The definition of the blockage at the runner-blade inlet

There are some previous studies related to the effect of the blade thickness on turbomachinery performance. Mu et al. [57], Tao et al. [58], and Yang et al. [59] studied how blade thickness affects the centrifugal pump performance; and Kim et al. [60] studied the effect of blade thickness on a Francis hydraulic turbine's performance. Generally, the turbine runner-blade has a R_T value around 15%-18%. [56] However, since this proposed SMH generation module has a large and irregular size, different blade thickness values have to be tested for hydraulic performance. **Figure 3.17** shows five runner-blade examples with different relative thicknesses, and the numerical simulation results were shown in ***section 5.3.2.3***.

Since the SMH generation module has to be fish-friendly, the stator-blade, relative thickness needs special consideration. Small stator thickness may have poor flow guidance; large stator thickness may induce substantial blockage loss and cause damage to large fish species; therefore, different stator relative thickness values were tested, **Fig. 3.18** shows five different stator-blade examples with various relative thickness. Detailed numerical results were shown in ***section 5.2.3.3***.

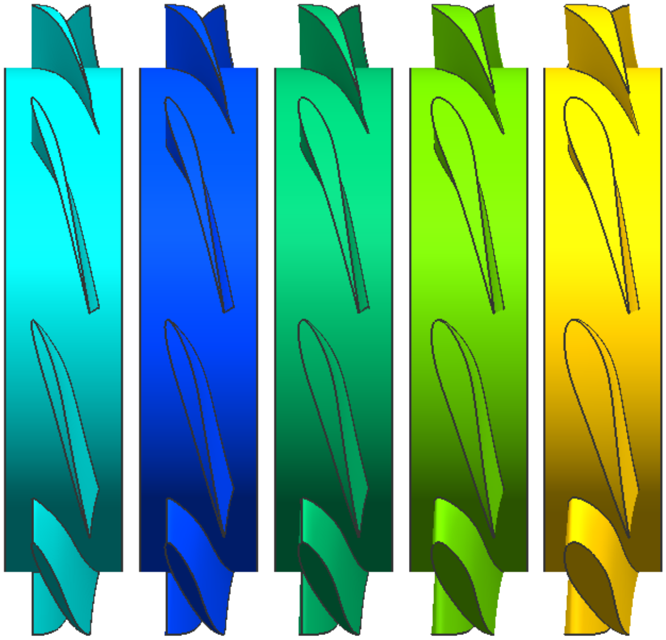

Figure 3.17. *Five runner-blades with different relative thickness values. (From left to right:* R_T*=5%, 7.5%, 10%, 12.5%, 15%.)*

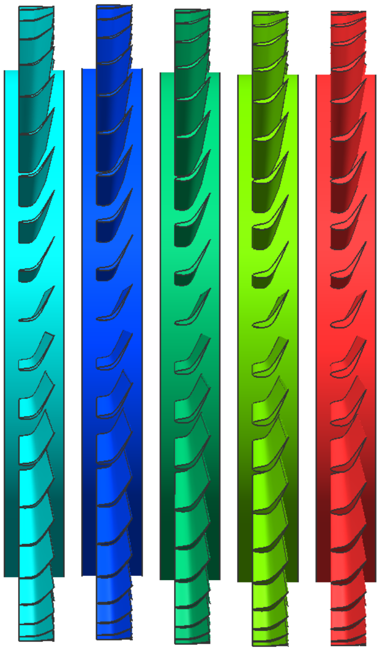

Figure 3.18. *Five stator-blade with different relative thickness values. (From left to right:* S_T*=5%, 7.5%, 10%, 12.5%, 15%)*

3.4. Summary

Appendix-B shows all initial design parameters with descriptions and initial recommend setting values.

CHAPTER IV: NUMERICAL METHODS

In this chapter, the basic computational fluid dynamic (CFD) methods' backgrounds are covered. A successful and accurate numerical simulation depends on a series of steps:

- Computational domain definition and construction
- Turbulence Modeling selection
- Boundary Condition setting.

Each step was discussed comprehensively in this section. The widely available commercial computational fluid dynamics software ANSYS FLUENT 2018 was used for this research.

4.1. General governing equations

For more than 20 years, the computational fluid dynamic has become a powerful tool for evaluating the turbomachinery system's performance and flow physics. Significant progress has been made, which ensures a more accurate prediction of the performance and flow behaviors in the turbomachinery.

The general governing equations for computational fluid dynamics are the Navier-Stokes (N-S) equations. The N-S equations for incompressible isothermal flow through a turbomachinery system can be written as

$$\frac{\partial u_i}{\partial x_i} = 0;\ \frac{\partial u_i}{\partial t} + u_j \frac{\partial u_i}{\partial x_j} = -\frac{1}{\rho}\frac{\partial p}{\partial x_i} + \upsilon \frac{\partial^2 u_i}{\partial x_j \partial x_j} \tag{4-1}$$

where u_i is the velocity vector, p is the pressure, ρ is the density of the fluid, and υ is the kinematic viscosity of the fluid. Generally, the hydraulic system could be considered as an isothermal system, which means no heat addition or removal in this fluid system. Since there is no general solution for the non-linear equation, the N-S equation needs to be solved numerically with specific boundary conditions and initial conditions. With complex geometries, solving the N-S equation for turbomachinery is numerically costly. When predicting the general performance of the turbomachinery, the averaged flow values are usually the properties of interest at the beginning of the design process. Therefore, RANS (Reynolds Averaging Navier Stokes method) is normally used. This method is obtained by time-averaging the Navier-Stoke equation for the averaged values of the flow properties over a sufficient time period, and are written as

$$\frac{\partial U_i}{\partial x_i} = 0; \qquad \frac{\partial U_i}{\partial t} + U_j \frac{\partial U_i}{\partial x_j} = -\frac{1}{\rho}\frac{\partial P}{\partial x_i} + \frac{\partial}{\partial x_j}\left[\upsilon\left(\frac{\partial U_j}{\partial x_i} + \frac{\partial U_i}{\partial x_j}\right) - \overline{u_i' u_j'}\right] \tag{4-2}$$

where U_i is the time-averaged velocity vector, u_i' is the velocity fluctuation due to turbulence and $-\overline{u_i' u_j'}$ is the Reynolds shear stress. The basic concept of the RANS method is to decompose the flow velocity u_i into two parts: time-averaged value U_i, and the fluctuating value u_i' as

$$u_i = U_i + u_i' \tag{4-3}$$

In **Eqn (4-2)**, the Reynolds shear stress part could not be solved directly and must to be modeled with different turbulent models, which will be covered in ***section 4.2.2***.

4.2. Numerical method developments

A successful and effective numerical simulation requires three parts: a sufficient computational domain, correct turbulence model selection, and appropriate boundary conditions setting. This section covers all those three parts.

4.2.1. Computational domain construction

Mesh represents the geometric domain for the CFD computation that has a significant impact on the simulation’s accuracy and cost. A suitable mesh is a premise for a successful numerical simulation. For turbomachinery applications, the structured hexahedral mesh is preferred since it is mostly aligned to the main flow direction. [61] However, a structured hexahedral mesh is challenging and time-consuming for a complex turbomachinery geometry. An unstructured hybrid mesh scheme has been used for simulating the turbomachinery flow physics recently, which means different mesh schemes are used in different flow regions, for example, hexahedral mesh near the wall region and unstructured mesh in the other region. In this research, the hybrid meshes scheme is used.

In order to generate the mesh, different geometry models were first defined and cleaned (any geometric errors or in-continuity) in the computer-aided design (CAD) software. Then this clean geometrical model was imported into ANSYS Mesh software. Different mesh criteria were utilized for smoothing and refinement to avoid any numerical errors.

In order to capture the boundary conditions and flow behaviors near the blades, at least 10 layers were needed on the wall of the blades. The dimensionless wall distance $y^+ (y^+ = \frac{\mu_T y}{\nu})$ is one critical indication for turbulent boundary layer accuracy. For example, for the $SST\ k - \omega$ turbulence model, the $y^+ < 1$ is required to capture the near-wall region flow behaviors [61]. However, the $SST\ k - \omega$ model has a wall function that enables a smooth switch between the near-wall region and the central flow region [62]. This wall function allows the use of some coarse grids without a significant penalty in simulation [63].

As this research proposed a new design methodology for the Kaplan turbine, which needs a number of CFD simulations to test the geometric setting parameters, only general performance, and basic properties were focused. So, in order to balance the computational cost and accuracy, different mesh sizes were used. There are three computational domains for this proposed turbine system: inlet water channel, stator, and runner, and each part has a unique meshing scheme for better computational performance. **Figure 4.1 (a)-(d)** shows those three parts and their meshing scheme.

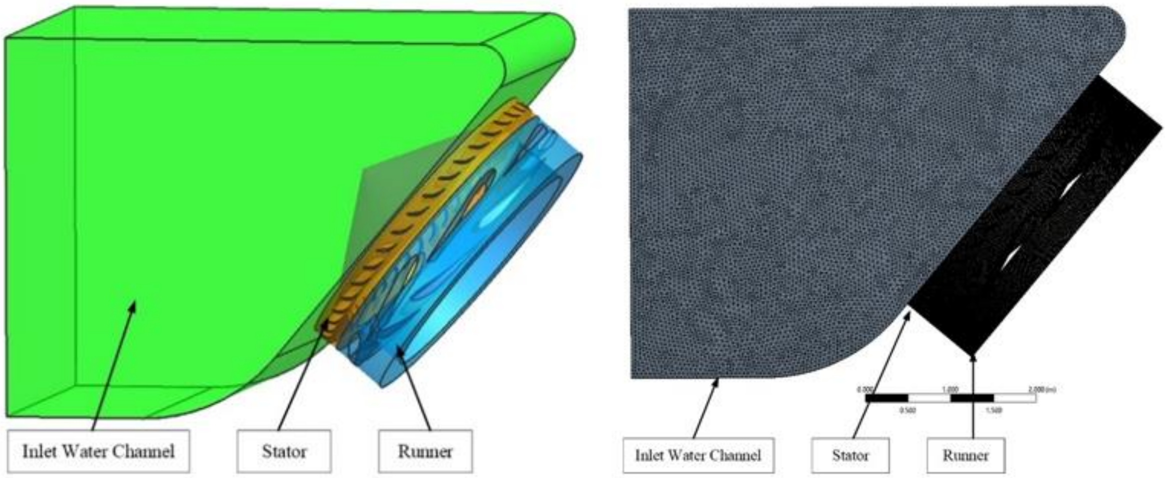

(a) Three computational domains (b) Overall mesh for the generation module

(c) Mesh for the stator blade

(d) Mesh for the runner blade

Figure 4.1. *The numerical grids for the three computational fluid domains.*

Generally, more elements mean more accurate results, but with a higher computational cost. Therefore, it is necessary to demonstrate how different mesh sizes influence the overall prediction of the performance. Five different mesh schemes were selected for one example model. **Table 4.1** shows the detail mesh information for each scheme, and **Figure 4.2** shows the mesh quality and performance relation.

Table 4.1. *Detail mesh information for the five selected mesh schemes*

	Mesh-1	Mesh-2	Mesh-3	Mesh-4	Mesh-5
Mesh size [m]	0.015	0.01	0.0075	0.006	0.005
Mesh Type	Tetrahedrons Mesh + 10 layer near the wall				
Total element number [million]	13.6	33.3	70.8	178.4	304.5

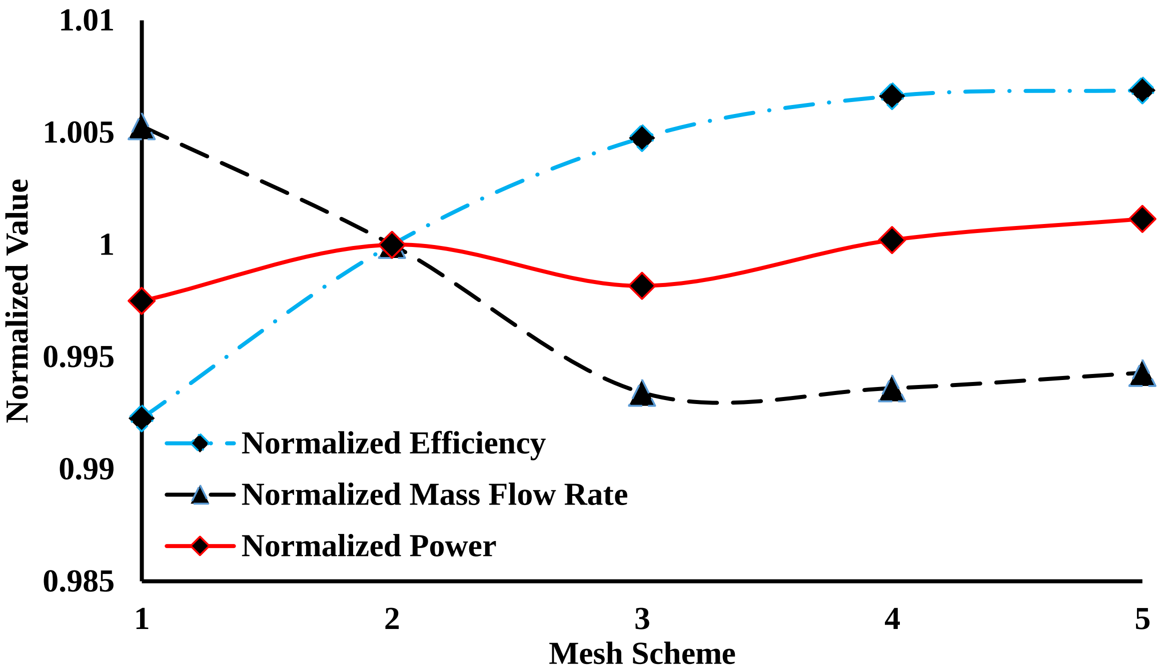

Figure 4.2. *The mesh quality and normalized performance relation for the five selected schemes.*

All values in **Fig 4.2** were normalized with respect to the scheme-2 values. The results show that with a finer mesh, the efficiency increases by around 0.68%, the mass flow rate decreases around 0.57%, and the power increases by around 0.12%. Mesh-5 would provide more accurate results; however, the computational cost was too substantial. By using the same computing power, mesh-5 required 45 times more computational time than mesh-2. This methodology needs hundreds of simulations to verify the geometry settings and other parameters; therefore, Mesh-2 was considered sufficiently reliable for predicting the overall hydraulic performance and was mainly used in this paper.

4.2.2. **Turbulence model selection**

Turbulence modeling is an essential part of any turbomachinery design and has a significant impact on design outcomes. Current approaches for turbulence modeling have four main types: 1) RANS based simulation, 2) Large-eddy simulation (LES), 3) Direct numerical simulation (DNS), 4) Hybrid RANS-LES.

- As mention before, RANS is a time-average method; mean velocity, pressure, and other turbulence's properties were computed with some appropriate modeling scheme. RANS simulations with different modeling methods have been widely used for turbomachinery design because of its cost advantage and accuracy satisfaction.
- LES simulation is another promising method, Navier-Stokes equations are solved in large-eddy scale, and small-scale eddy needs to be modeled in LES. LES simulation requires more significant computational resources and finner mesh scheme then the RANS method, so it is less practical than the RANS method due to the cost for turbomachinery applications.
- The DNS method is the most accurate method which numerically solves the Navier-Stokes equations in any fluid domain. However, the enormous computational cost makes DNS an impractical method and only for elementary geometry.
- The hybrid method combines both the RANS and LES method to achieve a more accurate prediction of flow patterns. Nera the wall region, the Spalart-Allmaras (SA) turbulence model

(one-equation RANS model) is used, and outside the boundary layer, the LES model is applied. This method is good for capturing the flow patterns around the walls, but it is still too computationally expensive for this research.

In this research, $SST\ k-\omega$ turbulence model is used, which has better performance for turbomachinery applications [61]. The $SST\ k-\omega$ turbulence model is a two-equation RANS model that has two equations, one for turbulence kinetic energy k and one for specific dissipation rate ω, which consists of blending the $k-\omega$ model and $k-\epsilon$ model based on the proximity to the walls. Due to the over-prediction of the shear stress in the adverse pressure gradient boundary layer of the original $k-\omega$ model, in 1994, Menter first proposed the $SST\ k-\omega$ model [64]. In the $SST\ k-\omega$ model, to account for the transport of the turbulence shear stress, a limiter function is used and modified, which shows better predictions of separation and streamline curvature [64]. Because of those features, the $SST\ k-\omega$ model is considered as a better model for the turbomachinery application than the standard two-equation models.

In the $SST\ k-\omega$ model, the Bousinessq approximation is used to calculate the Reynolds stress for the turbulence viscosity models as

$$\overline{-\rho u_i' u_j'} = \frac{2}{3}\rho k \delta_{ij} - \mu_i \left(\frac{\partial U_i}{\partial x_j} + \frac{\partial U_j}{\partial x_i}\right);\ k = \overline{\frac{1}{2} u_k' u_k'} \tag{4-4}$$

For $k-\epsilon$ model, the transport equation for the turbulent kinetic energy k can be written as

$$\frac{\partial k}{\partial t} + \frac{\partial U_j k}{\partial x_j} = \frac{\partial}{\partial x_j}\left[\left(\nu + \frac{\nu_t}{\sigma_k}\right)\frac{\partial k}{\partial x_j}\right] + P_k - \epsilon \tag{4-5}$$

where, P_k is the production of turbulence kinetic energy and can be defined as

$$P_k = \overline{u_i' u_j'} \frac{\partial U_i}{\partial x_j} \tag{4-6}$$

Additionally, the transport equation for the turbulence dissipation rate ϵ is

$$\frac{\partial \epsilon}{\partial t}+\frac{\partial U_j \epsilon}{\partial x_j}=\frac{\partial}{\partial x_j}\left[\left(\nu+\frac{\nu_t}{\sigma_\epsilon}\right)\frac{\partial \epsilon}{\partial x_j}\right]+\frac{\epsilon}{k}(P_k C_{\epsilon 1}-C_{\epsilon 2}\epsilon)P_k=\overline{u_i' u_j'}\frac{\partial U_i}{\partial x_j} \tag{4-7}$$

$$C_{\epsilon 1}=1.44,\, C_{\epsilon 2}=1.92,\, \sigma_\epsilon=1.3,\, C_\mu=0.09, \sigma_k=1$$

And ν_t is given by [65]

$$\nu_t=C_\mu\frac{k^2}{\epsilon} \tag{4-8}$$

Similarly, for the $k-\omega$ model, the transport equation for turbulent kinetic energy k can be written as

$$\frac{\partial k}{\partial t}+\frac{\partial U_i k}{\partial x_i}=\frac{\partial}{\partial x_j}\left[\left(\nu+\frac{\nu_t}{\sigma_k}\right)\frac{\partial k}{\partial x_j}\right]+P_k-\beta' k\omega \tag{4-9}$$

And, the transport equation for the specific dissipation rate ω is

$$\frac{\partial \omega}{\partial t}+\frac{\partial U_i \omega}{\partial x_i}=\frac{\partial}{\partial x_j}\left[\left(\nu+\frac{\nu_t}{\sigma_\epsilon}\right)\frac{\partial \omega}{\partial x_j}\right]+\alpha\frac{\omega}{k}P_k-\beta\omega^2;\ \upsilon_t=\frac{k}{\omega}, \epsilon=\frac{C_\mu k}{\omega} \tag{4-10}$$

$$\beta'=0.09,\, \sigma_k=2.0,\, \sigma_\omega=2.0,\, \alpha=5/9\ ,\, \beta=0.075$$

Away from the wall, the $SST\ k-\omega$ model transforms into the standard $k-\epsilon$ model due to the better performance in the free shear layers, which solves the disadvantage of the $k-\omega$ model. The suggested boundary condition is: [64]

$$\omega=\frac{60\nu}{\beta y^2} \tag{4-11}$$

where y is the distance from the wall to the first-cell center. Since the $SST\ k-\omega$ model using the blending functions, the $k-\omega$ transport function is rewritten as

$$\frac{\partial \omega}{\partial t}+\frac{\partial U_i \omega}{\partial x_i}=\frac{\partial}{\partial x_j}\left[\left(\nu+\frac{\nu_t}{\sigma_\epsilon}\right)\frac{\partial \omega}{\partial x_j}\right]+\alpha\frac{\omega}{k}P_k-\beta\omega^2+2(1-F_1)\sigma_{\omega 2}\frac{1}{\omega}\frac{\partial k}{\partial x_j}\frac{\partial \omega}{\partial x_j} \tag{4-12}$$

Where the blending function is given by

$$F_1=\tan^{-1}(\arg_1^4) \tag{4-13}$$

$$\arg_1 = \min\left[\max\left(\frac{\sqrt{k}}{\beta'\omega y}, \frac{500\nu}{y^2\omega}\right), \frac{4\rho k}{CD_{kw}\sigma_{\omega 2}y^2}\right] \tag{4-14}$$

where CD_{kw} is written as

$$CD_{kw} = \max\left(2\rho\frac{1}{\sigma_{\omega 2}\omega}\frac{\partial k}{\partial x_j}\frac{\partial \omega}{\partial x_j}, 1.0 \times 10^{-10}\right) \tag{4-15}$$

The turbulent viscosity ν_t is expressed as

$$\nu_t = \frac{\alpha_1 k}{\max(\alpha_1\omega, SF_2)};\ F_2(Second\ blending\ function) = \tan^{-1}(arg_2^2) \tag{4-16}$$

$$\arg_2 = \max\left(\frac{2\sqrt{k}}{\beta'\omega y}, \frac{500\nu}{y^2\omega}\right) \tag{4-17}$$

$$S = \sqrt{2S_{ij}S_{ij}}, S_{ij} = \frac{1}{2}\left(\frac{\partial U_i}{\partial U_j} + \frac{\partial U_j}{\partial U_i}\right) \tag{4-18}$$

4.2.3. **Boundary conditions setting**

Numerical simulations of any flow system require the specification of all boundary conditions in the whole computational domains.

- *Inlet boundary condition*

For the Kaplan turbine, two inlet boundary condition types are normally used, either the total pressure or the velocity (which is equal as mass flow rate for incompressible flow). Those two boundary conditions represent two design parameters: total pressure, which represents the design head, and the velocity, which represents the total mass flow rate. In the 1-D design phase, both design parameters must be specified. However, in CFD, those two parameters are highly dependent on each other and other geometry settings. This means only one parameter could be fixed and another one must float. If the turbine geometry is designed appropriately, the float value should be close to the designed value, but irregular geometry settings may cause huge loss and influence the mass flow rate and head values. Additionally, a 5% turbulence intensity was assumed at the inlet, and the inlet flow is assumed unaffected from the downstream flow.

- *Outlet boundary condition*

There are two boundary conditions options for the outlet boundary: pressure and velocity. Generally, two combinations of boundary conditions could be used: Inlet pressure and Outlet pressure and Inlet pressure and Outlet velocity. The first combination fixes the head value as the designed and floats the mass flow rate; the second combination fixes the mass flow rate and floats the outlet pressure. Both combinations work similarly, and for this research, since the head condition is the most concerned parameter, the first combination is used.

- *Wall boundary Conditions*

The wall of the stator, the inlet channel, and the runner-blades are considered as the wall boundary. All stationary walls are treated as non-slip, isothermal stationary walls, and the rotating runner-blade are treated as no-slip, isothermal rotating wall.

- *Interface*

The frozen-rotor interface method can be used for the steady RANS models. In this method, the interface connecting the stator (stationary) and runner (rotating) domains is prescribed as the frozen rotor with a mixing plan approach [66]. Moreover, appropriate transformation equations in the rotating frame of reference are applied, and the solution has no dependence on the relative positioning of the rotor and the casing [67]. The disadvantage of this model is the interaction between stator and runner is completely ignored due to the averaging of the circumferential non-uniformities of the upstream flow. However, for steady-state simulation, the frozen-rotor model is a good choice for simulating the average performance and was primarily used in this research.

4.3. Summary

By using the numerical methods described above, the main goal of the numerical simulation for this thesis is to verify the proposed design methodology with different geometrical settings and configurations. During the simulations, the overall performance, general flow behavior around the blade, and operating range are three main focuses.

The overall performance is defined by using the overall hydraulic efficiency as

$$\eta_t = \frac{T\omega}{\dot{m}gH} \tag{4-19}$$

where T is the torque on the runner-blade, ω is the rotational speed in rad, $\dot{m}$ is the mass flow rate, g is the standard gravity constant, and H is the available head.

The operating range is defined by using unit flow rate and unit

$$Q_{11} = \frac{Q}{D_{tip}^2\sqrt{H}};\ N_{11} = \frac{\Omega D_{tip}}{\sqrt{H}} \tag{4-20}$$

where Q is the volumetric flow rate, D_{tip} is the turbine tip diameter, Ω is the rotational speed in RPM. **Table 4.2** summaries the basic operating range and numerical simulation settings for the next section's results.

***Table 4.2**. Design and numerical simulation conditions*

Design Conditions Range		Numerical Simulation Conditions	
Design Head (H)	2.5m	Inlet/ Outlet Boundary Condition	Pressure Inlet/Outlet
Unit Flow Rate (Q_{11})	0.103~0.52 $m^{1/2}/s$	Turbulence Model	$k-\omega\ SST$
Overall Diameter (D_{tip})	3.5m	Simulation Type	Steady State
Design Unit Rotation Speed (N_{11})	88.5	Mesh Size	~33 Million

CHAPTER V: NUMERICAL RESULTS AND DISCUSSIONS

This chapter presents detailed numerical simulation results for the design methodology discussed above. The results cover all fundamental geometrical considerations, including general hub size consideration, stator-blade consideration, runner-blade consideration, and off-design considerations.

5.1. General hub size consideration

As shown in **Fig.3.6**, the hub size has a massive impact on the turbine blade design, which can have a significant influence on the overall hydraulic performance. Moreover, for the SMH generation module, the hub should have enough space for generator and control components. So, it is essential to thoroughly investigate the hub size and its impact on overall hydraulic performance.

Five different hub-to-tip ratios (D_{hub}/D_{tip}) were chosen and thoroughly investigated, and **Fig. 5.1** shows the results. The results show that for low, flow-rate conditions (when $Q_{11} < 0.2$), the largest hub diameter (D_{hub}/D_{tip}=0.8) model has the best performance, and the performance decrease with decreasing hub diameter and the maximum performance difference between different hub sizes is around 3.2%. When the flow rate increases, the smallest hub model (D_{hub}/D_{tip}=0.685) has the best overall hydraulic performance, and the maximum performance difference for different hub sizes is around 10.1%. Also, the results indicate that the smaller hub diameter has a more stable performance than larger hub diameter, and the hub size has a larger impact on overall hydraulic performance at a high, flow-rate condition (Red Arrow in **Fig.5.1**).

According to **Eqn (2-16)**, the runner-blade power is determined by the magnitude of the runner-blade, circumferential-velocity difference. Therefore, **Figure 5.2** shows the circumferential velocity difference (C_{u2}-C_{u3}) distribution plots from hub to tip at two selected Q_{11} conditions for all five different hub-size configurations.

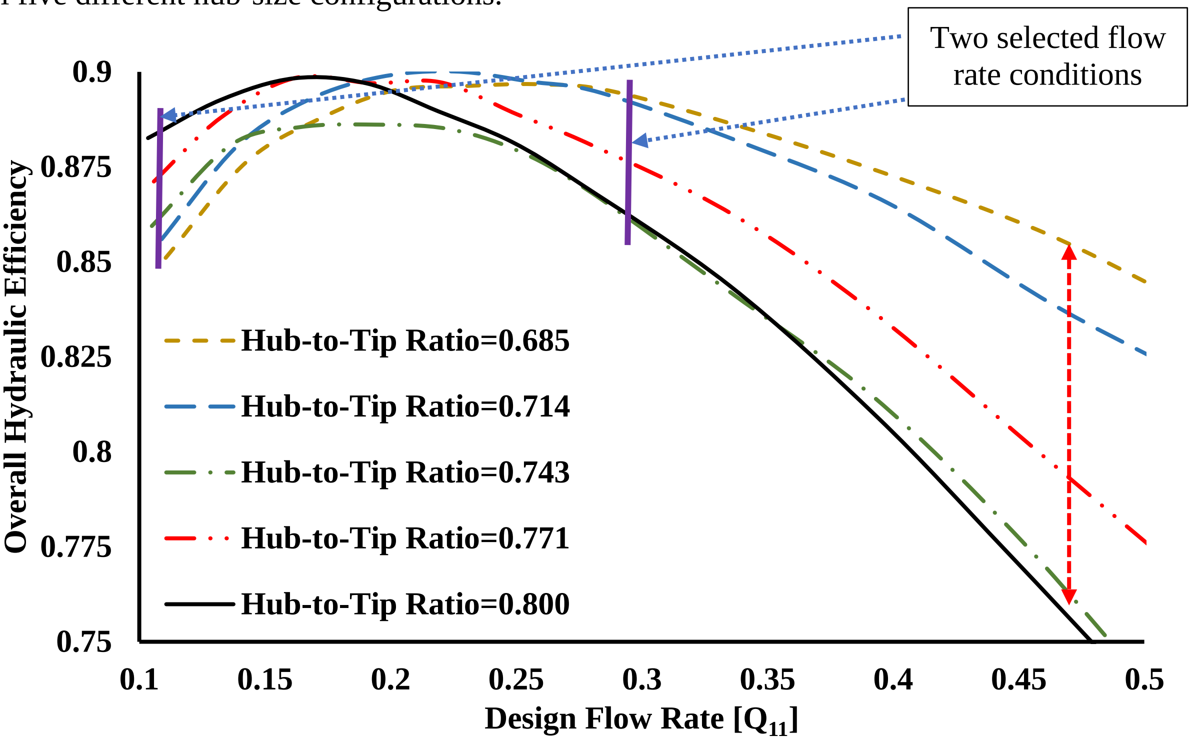

Figure. 5.1. *The relation between overall hydraulic efficiency and design flow rate (Q_{11}) for five selected Hub-to-Tip ratio configurations*

At lower flow-rate condition, **Fig.5.2 (a)**, on the close to hub region (less than 25% Span Location), a smaller hub configuration has a significantly larger circumferential velocity difference (Red Arrow). However, this circumferential-velocity difference drops steeply and remains at a very low value (Black Arrow) on the close to tip region (between 60% and 100% Span Location). In general, at low flow-rate conditions, the smaller hub configuration tends to have worse performance on the close to tip region, which leads to poor overall performance.

At a larger flow rate condition, **Fig.5.2(b)**, the smaller hub configuration has a larger circumferential-velocity difference across all span locations (Blue Arrow). This massive difference causes the smaller hub configuration to have a significantly better overall performance at a larger flow rate condition.

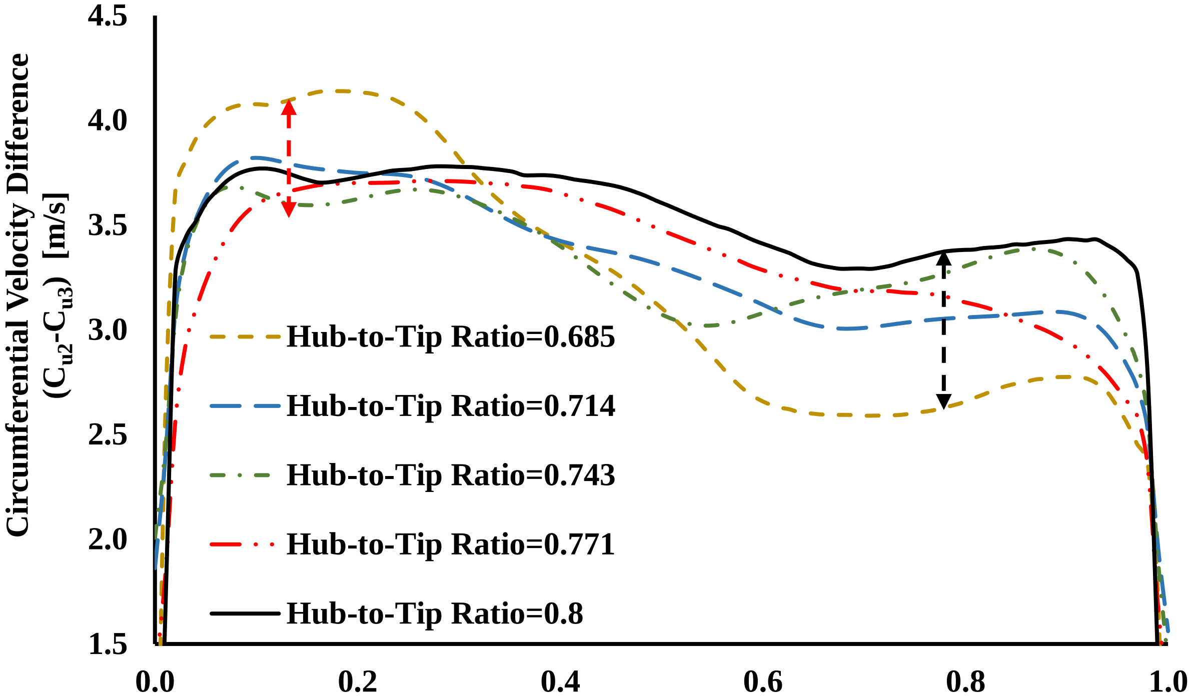

(a). Normalized Span Location ('0' is Hub, '1' is Tip)

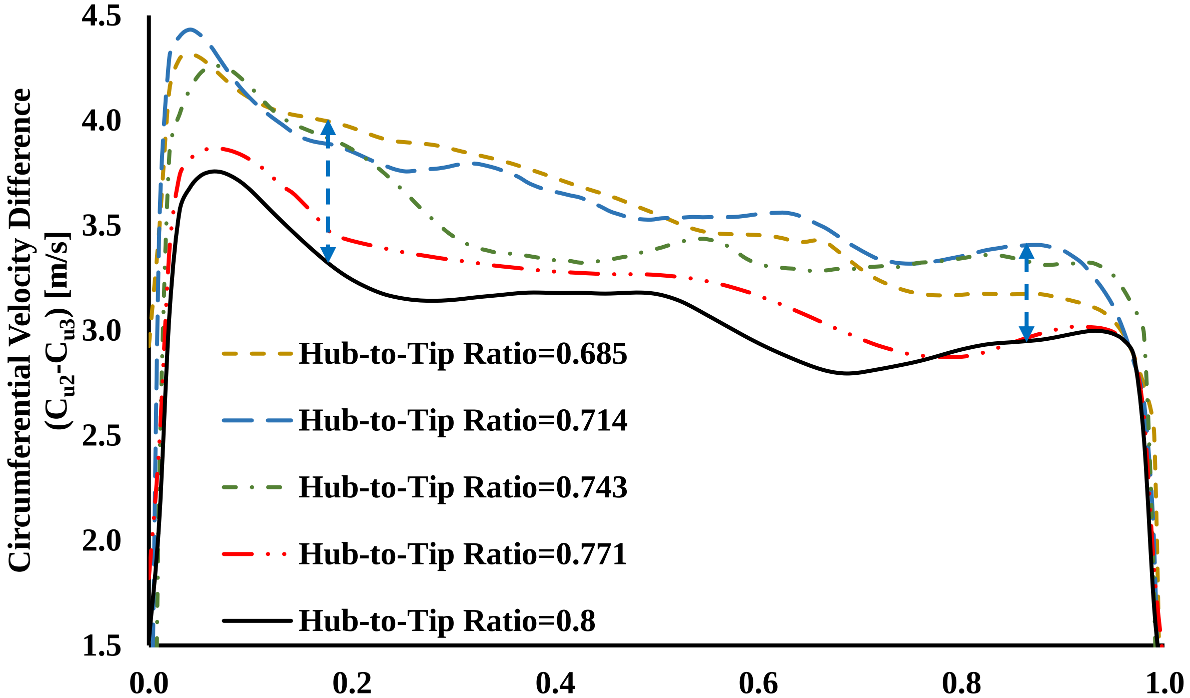

(b). Normalized Span Location ('0' is Hub, '1' is Tip)

Figure.5.2. *The circumferential velocity difference (C_{u2}-C_{u3}) distribution plots from hub to tip at two Q_{11} conditions for all five different hub-size configurations, (a). Low Flow Rate Condition, Q_{11}=0.103. (b). High Flow Rate Condition, Q_{11}=0.31*

In general, choosing the right hub size involves balancing the design flow rate and the required hub volume. At a high flow rate, the smaller hub can provide an excellent overall hydraulic performance but with limited hub volume that can have high over-heating possibilities for the generator, which can further affect the overall electrical performance. Balancing the hub size and performance is the key for the initial sizing of the turbine unite. (Some extra results and plots are in the ***Appendix.C***)

5.2. Stator-blade consideration

5.2.1. Stator-blade stagger-angle setting constant consideration

As shown in **Fig.3.8 (b)** and **Eqn (3-21)**, the Stator-Blade, Stagger-Angle-Setting-Constant (C_{ssa}) is a critical parameter for designing the stator-blade profile. **Figure 5.3** shows how this parameter affects the overall performance at four flow rate conditions.

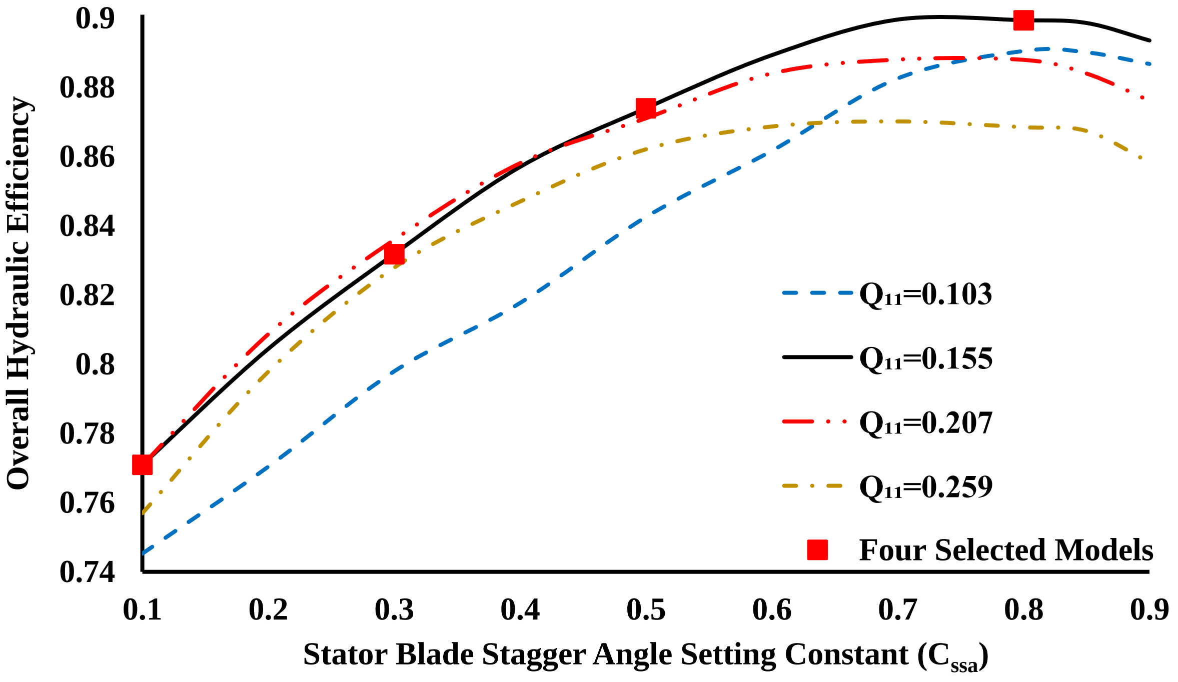

Figure. 5.3. *The relation between overall hydraulic efficiency and stator-blade stagger-angle setting constant* C_{ssa} *for four flow rate conditions*

The results show that at small, flow-rate condition, the overall hydraulic efficiency increases with the increase of C_{ssa} and reaches the maximum efficiency when C_{ssa} is around 0.7~0.8, then decreases with the increase of C_{ssa}. For large, flow-rate conditions, the overall hydraulic efficiency increases with the increase of C_{ssa} and reaches the maximum efficiency when C_{ssa} is around 0.5~0.7, then remains relatively constant, then decreases when C_{ssa} is larger than 0.8. For all flow rate conditions, the initial increase of efficiency with the increase of C_{ssa} is universal, and the maximum efficiency occurs when C_{ssa} is around 0.5~0.8. Four models under one flow-rate condition (Red Square in **Fig.5.3**) were selected for further investigations. Since the primary function of the stator is to redirect the inflow to the runner-blade with the desired angle, for the four selected models, two angles were studied: β_2 and α_2.

- β_2-Considerations

The β_2 is the runner-blade, inlet-relative-flow angle (see in **Fig.2.2**), and under the ideal condition, the $\beta_{2\,flow}$ should be the same as the $\beta_{2\,blade}$, and a large difference between $\beta_{2\,blade}$ and $\beta_{2\,flow}$ means increasing the runner-blade incidence loss, which can affect the overall performance. **Figure 5.4** shows the comparison between the $\beta_{2\,blade}$ and $\beta_{2\,flow}$ for the four selected models. The results show that, near the hub region, because of the boundary flow and low runner circumferential velocity (velocity U in **Fig. 2.2**), the $\beta_{2\,flow}$ is larger than the $\beta_{2\,blade}$ for all four selected models, and the maximum angle-difference is around 12°. And, near the tip region, because of the boundary flow and high runner circumferential velocity, the $\beta_{2\,flow}$ is all larger than the $\beta_{2\,blade}$ for all four selected models and the maximum difference is around 9°. However, results are different in the center of the span region.

- The smaller C_{ssa} models (C_{ssa}=0.1,0.3) trends to have a larger $\beta_{2\,flow}$ than the $\beta_{2\,blade}$, the maximum angle difference is ~+3°.

- The medium C_{ssa} models (C_{ssa}=0.5) trends to have a very similar $\beta_{2\,flow}$ than the $\beta_{2\,blade}$, the maximum angle difference is only ~+0.4°.
- The larger C_{ssa} models (C_{ssa}=0.8) trends to have a smaller $\beta_{2\,flow}$ than the $\beta_{2\,blade}$, the maximum angle difference is ~-4°.

As shown above, the difference between the $\beta_{2\,flow}$ and the $\beta_{2\,blade}$ can undoubtedly affect the overall performance, but the results in **Fig.5.4** cannot fully explain the trend shown in **Fig.5.3**. Therefore, other angles α_2 were studied.

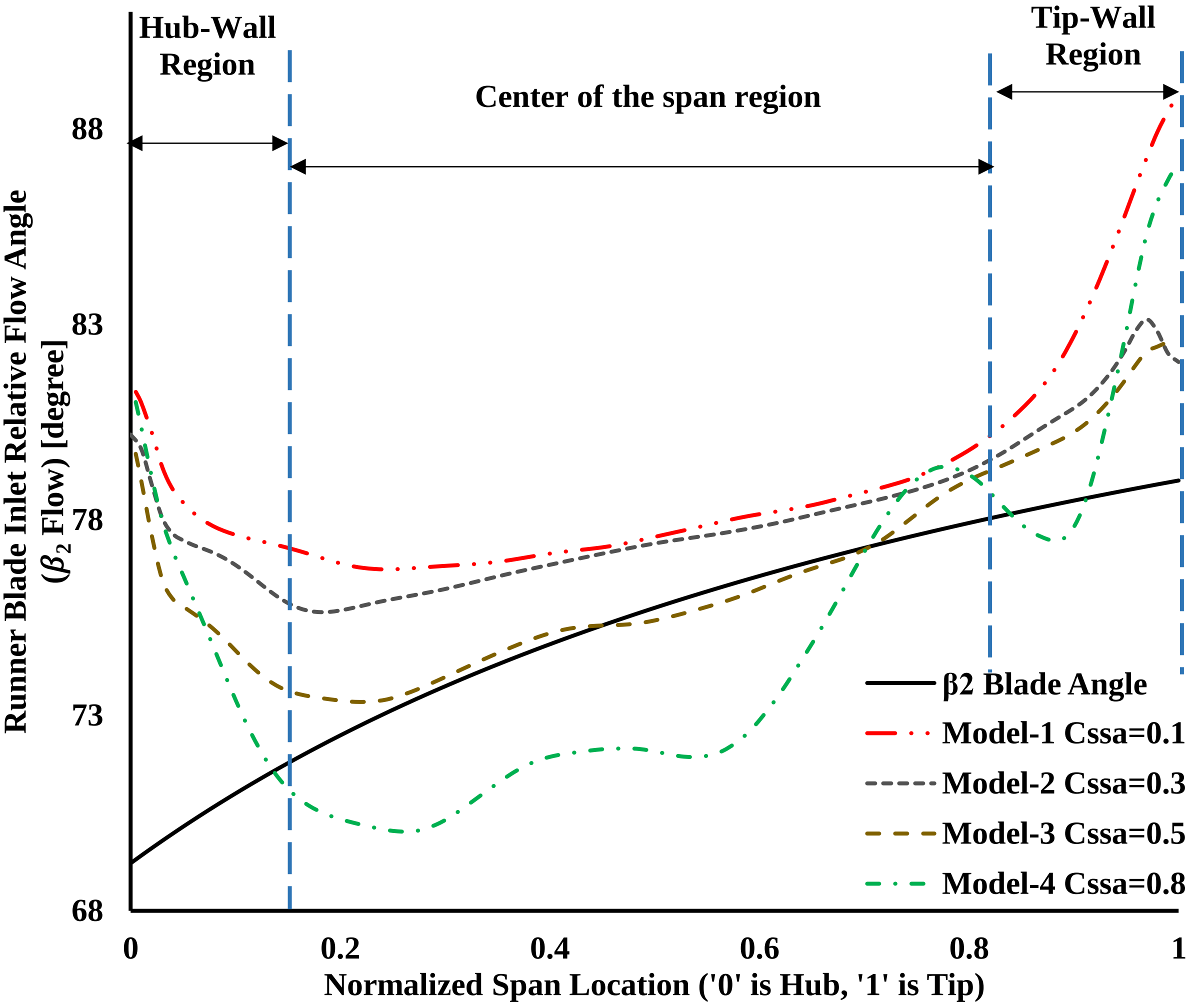

Figure. 5.4. *The runner-blade inlet $\beta_{2\,flow}$ angle distribution plots for four selected models in comparison with the designed $\beta_{2\,blade}$ value*

- α_2-Considerations

The α_2 is the runner-blade-inlet absolute flow angle (see in **Fig.2.2**), and this angle determines the magnitude of the runner-blade, inlet circumferential-velocity (C_{u2}). Larger α_2 means larger C_{u2}, which results in more substantial potential work done on the runner-blade (according to the **Eqn [2-16]**). **Figure 5.5** shows the α_2 distribution plot across all span location for the four selected models with the comparison with the 1-D designed $\alpha_2$values. The smaller C_{ssa} (C_{ssa}=0.1) model shows significant lower α_2 values in the majority center span region (exclude the hub and tip boundary region), the difference is around -60°. For larger C_{ssa}, the (C_{ssa}=0.8) model also shows lower α_2 values in the majority span center region, but the difference is only around -10°. This huge difference in the α_2 values explain why Model-4 (C_{ssa}=0.8) has significantly better performance than the Model-1 (C_{ssa}=0.1).

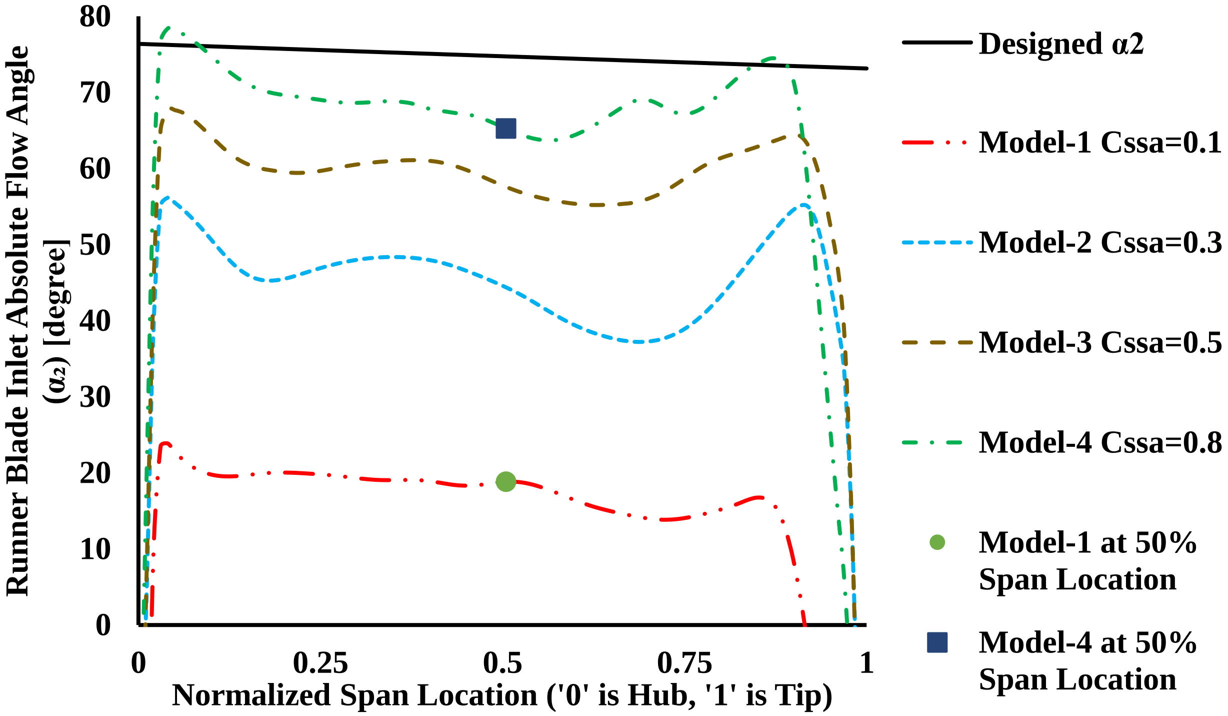

Figure. 5.5. *The runner-blade inlet absolute flow angle (α_2) distribution plots for four selected models in comparison with the designed α_2 value*

For better visualization, **Figure 5.6** shows the stream-line pattern for the Model-1(C_{ssa}=0.1) and Model-4 (C_{ssa}=0.8) at 50% span location. When C_{ssa} is small, as shown in **Fig.5.6-(a)**, the stator-blade camber-line has a flat profile in the font region, and the diversion of the flow only happens near the trailing edge. This profile results in poor flow redirection and leads to very small α_2 values. When C_{ssa} is large, as shown in **Fig.5.6-(b)**, the stator-blade camber-line has a flat profile in the rear region, and the diversion of the flow occurs near the leading edge. This profile results in good flow redirection and leads to the larger α_2 values.

In general, the C_{ssa} value has a larger impact on α_2 values than β_2 value which has a profound influence on stator outlet flow behaviors and can further affect the overall performance. Based on the overall results, initially, the suggesting range for $C_{ssa}$is between 0.7 to 0.8. Some additional results and plots are shown in **Appendix.D**.

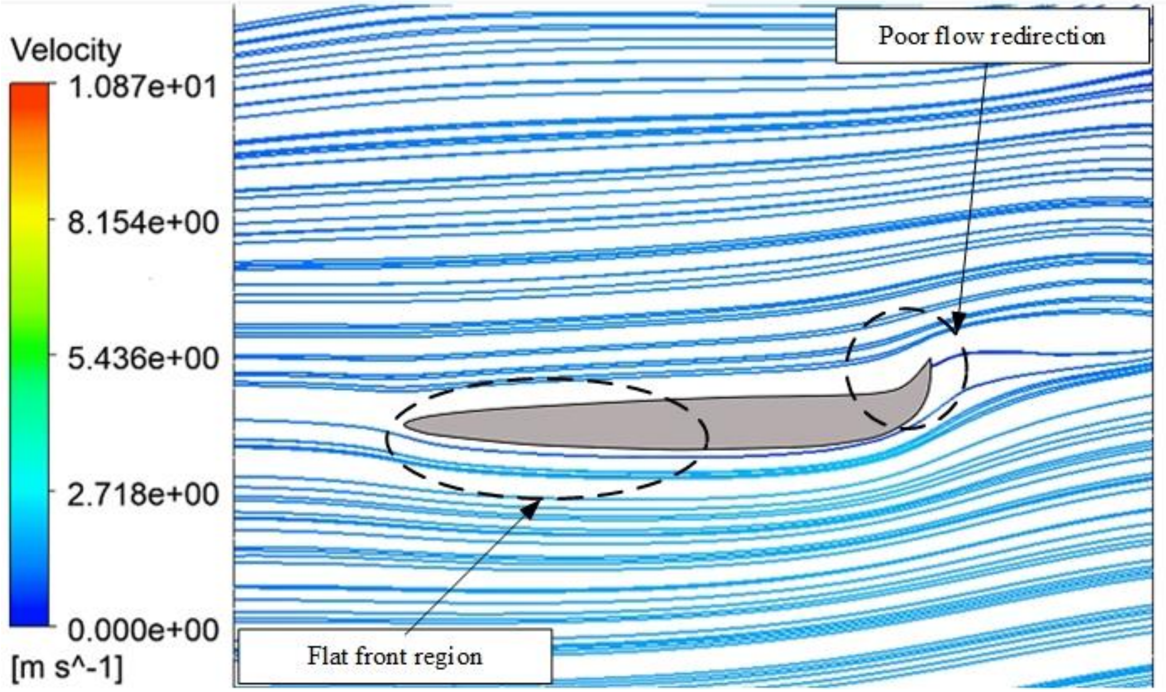

*(a). Model-1 at 50% span location (Green dot in **Fig. 5.5**)*

Figure. 5.6. *The stream-line pattern for the (a) Model-1and (b) Model-4, at 50% span location*

***Figure.* 5.6** *(Cont'd)*

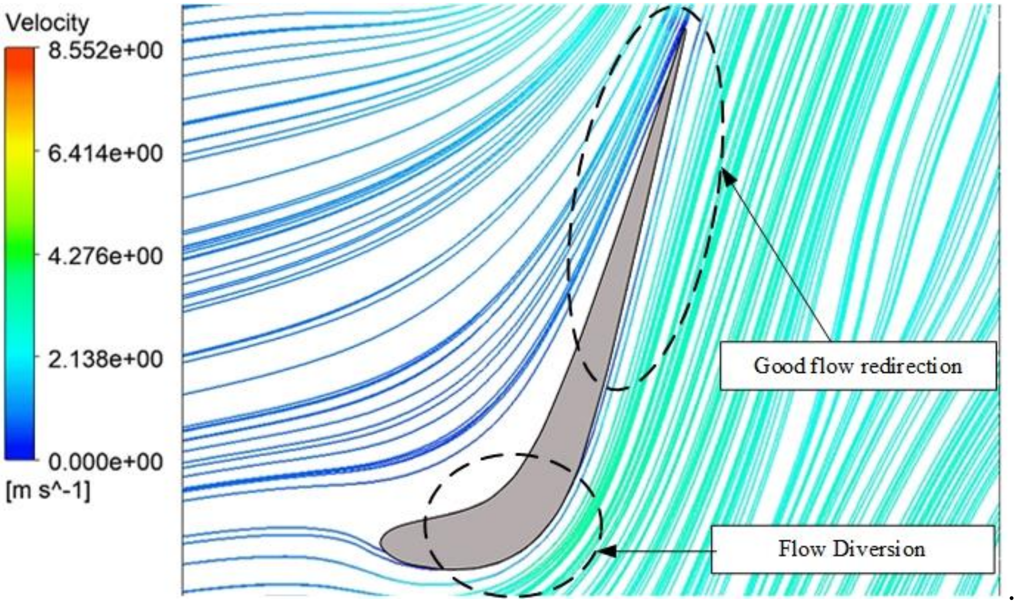

(b). Model-4 at 50% span location (Blue square in ***Fig.* 5.5***)*

5.2.2. Stator-blade inlet angle considerations

As shown in **Fig.3.10**, the stator-blade inlet-angle is another critical parameter for determining the stator-blade shape. **Figure 5.7** shows the inflow angle ($\beta_{1\,flow}$) distribution for the stator at three different general-inclined angle configurations and the results indicate that the general-inclined angle has minimal effect on the $\beta_{1\,flow}$. The inflow angle remains very close to 90° at all span locations (Except at the shroud and hub boundary layer regions) for all different general inclined angle configurations. According to the velocity triangle shown in **Fig. 2.2**, the stator-blade inlet angle ($\beta_{1\,blade}$) should be set equal to the $\beta_{1\,flow}$; however, different $\beta_{1\,blade}$ can have an impact on overall hydraulic performance. **Figure 5.8** shows how different $\beta_{1\,blade}$ affect the overall hydraulic performance and normalized power (the power is normalized with $\beta_{1blade} = 90°$ results) for three different general-inclined angle configurations under the same flow rate condition ($Q_{11} = 0.259$). The results show that decreasing the $\beta_{1\,blade}$ has a positive effect on the overall hydraulic performance, the maximum efficiency difference is 7%.

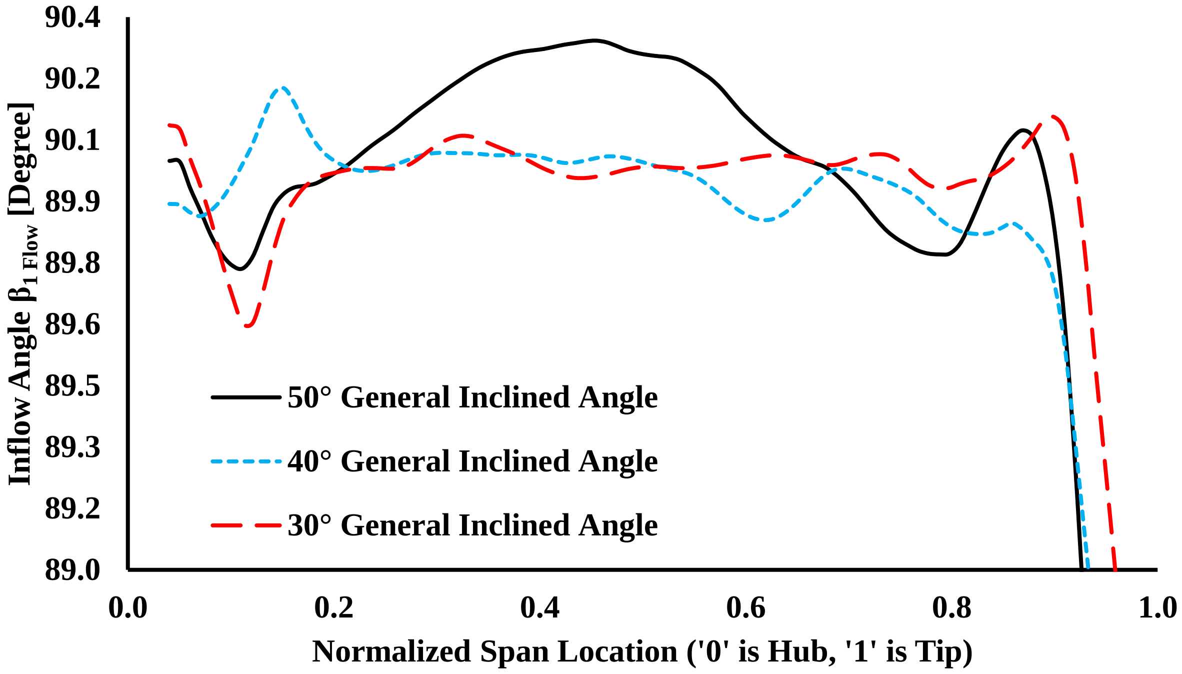

Figure. 5.7. *The Inflow angle (β_{1flow}) distribution across all span location for three general-inclined angle configurations*

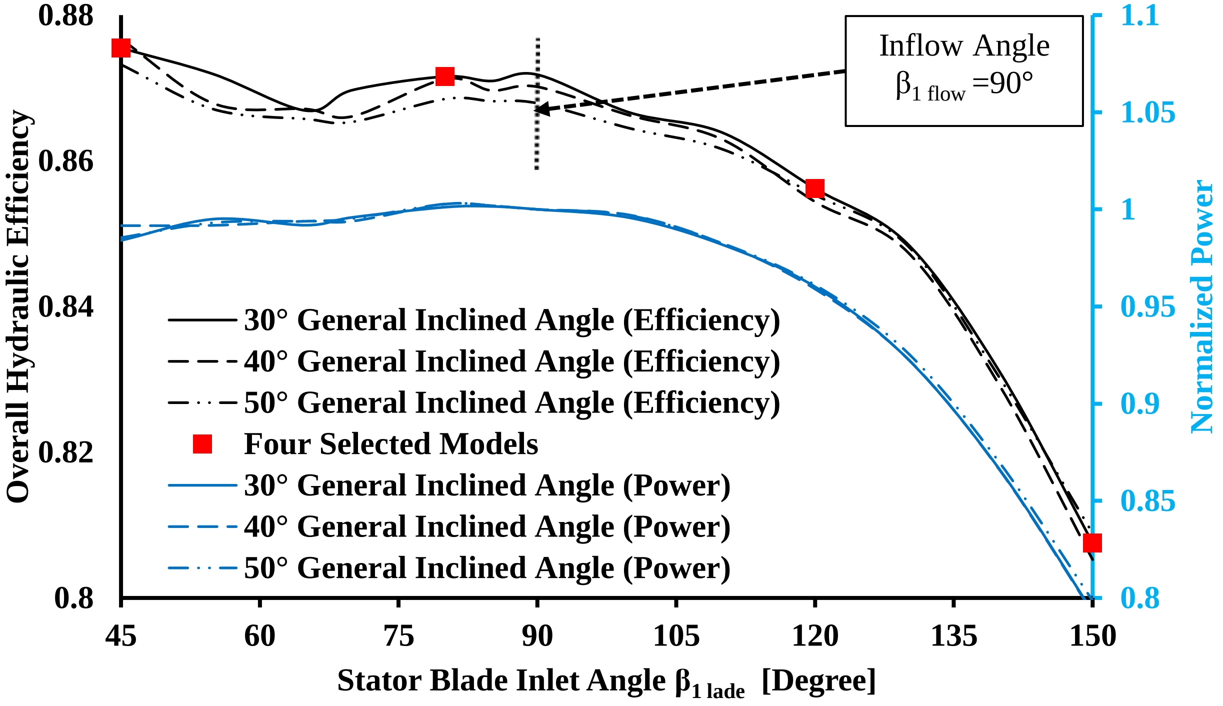

Figure. 5.8. *The Relation between the overall hydraulic efficiency, Power Generation, and the Stator-blade inlet angle ($\beta_{1\ blade}$) for three general-inclined angle configurations under the same design flow rate condition (Q_{11}=0.259)*

Furthermore, the power generation remains relatively constant when $\beta_{1\,blade} < 105°$; however, when $\beta_{1\,blade} > 105°$, the power generation decreases significantly with the increase of the $\beta_{1\,blade}$ because of the efficiency drop. For further investigations, four models (Red Markers in **Fig.5.8**) were chosen. As mentioned above, the primary function of the stator is to redirect the inflow to the runner-blade with the desired angle; therefore, for the four selected models, two angles were studied: β_2 and α_2.

- β_2*-Considerations:*

Figure 5.9 shows the comparison between the $\beta_{2\,blade}$ and $\beta_{2\,flow}$ for the four selected models. The results show that, near the hub region, because of the boundary flow and low runner circumferential velocity (velocity U), the $\beta_{2\,flow}$ is larger than the $\beta_{2\,blade}$ for all four selected models, and the maximum difference is around 20°. Near the tip region, because of the boundary flow and large runner circumferential velocity, the $\beta_{2\,flow}$ is larger than the $\beta_{2\,blade}$ for all four selected models, and the maximum difference is around 8°.

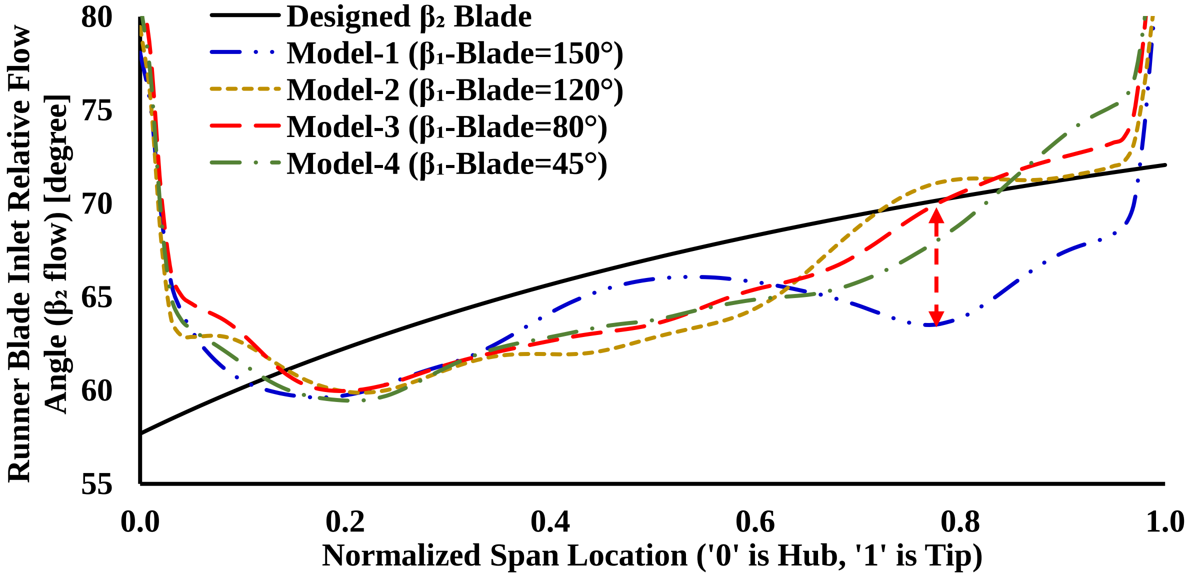

Figure. 5.9. *The runner-blade inlet relative flow angle* $\beta_{2\,flow}$ *distribution plots for four selected models in comparison with the designed* $\beta_{2\,blade}$ *value*

In the majority center of the span region, the $\beta_{2\,flow}$ is relatively close to the $\beta_{2\,blade}$ for Model-2, Model-3, and Model-4; and the maximum difference is only 4°. For Model-1, compared to the other three models, the $\beta_{2\,flow}$ is much smaller than the $\beta_{2\,blade}$ especially in the 80%-90% span region (Red Arrow in **Fig. 5.9**); the maximum difference is 7°.

As mentioned above, the β_2 angle results cannot fully explain the overall trends; so, the α_2 angle results were also studied.

- α_2*-Considerations:*

Figure 5.10 shows the α_2 distribution plot across all span location for the four selected models with the comparison with the designed α_2 value. For model-1 ($\beta_{1\,blade}$=150°), the α_2 is significantly lower than the other three models in the 0% to 50% span location, the maximum difference is 27°compared to the designed α_2 value. This vast difference (Blue Arrow in **Fig. 5.10**) is the main reason that model-1 has significantly lower efficiency. Model-2, 3, and 4 all have a very similar α_2 distribution pattern, in the majority span region (between 10% to 75%), the Model-4 has higher α_2 values than the other two models (Red Arrow in **Fig. 5.10**), which explains why the model-4 has the best overall efficiency.

For better visualization, **Figure 5.11** shows the stream-line pattern for the Model-1 ($\beta_{1\,blade}$=150°) and Model-4 ($\beta_{1\,blade}$=45°) at the 13% span location. Model-1 (**Fig.5.11-a**) has a counter-clockwise vortex pattern on the stator-blade suction side that is close to the trailing edge, which distorts the downstream flow; in comparison, Model-4 (**Fig.5.11-b**) has a clockwise vortex pattern on the stator-blade, pressure side that is close to the leading edge, which improves the downstream flow. Those different vortex patterns have a significant impact on the α_2 values, which can further influence the turbine works and efficiency. Some additional results and plots are shown in **Appendix.E.**

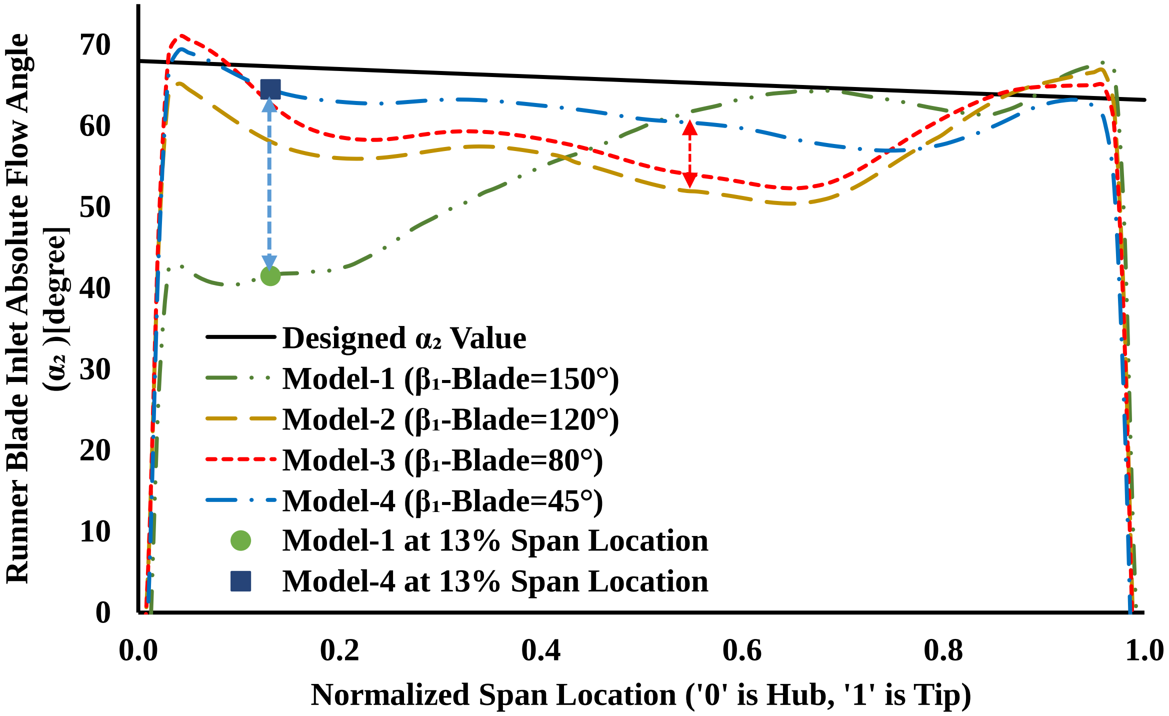

Figure. 5.10. *The runner-blade inlet absolute flow angle (α_2) distribution plots for four selected models in comparison with the designed α_2 value*

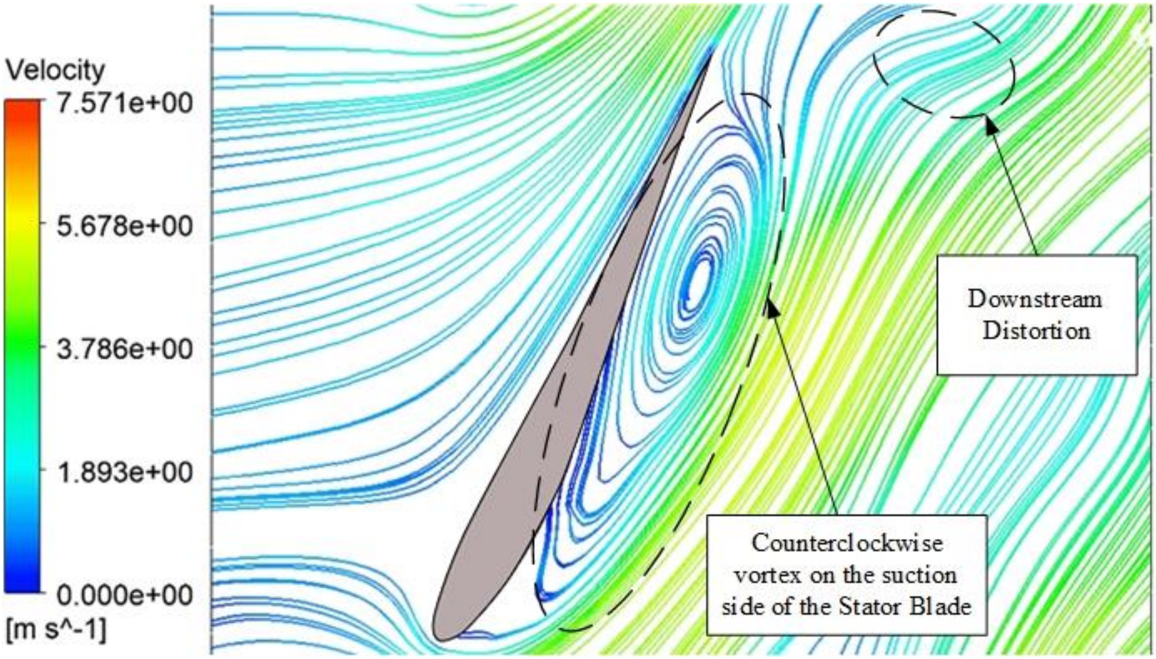

*(a). Model-1 at 13% span location (Green dot in **Fig. 5.10**)*

Figure. 5.11. *The stream-line pattern for the (a) Model-1and (b) Model-4, at 13% span location*

Figure. 5.11 *(Cont'd)*

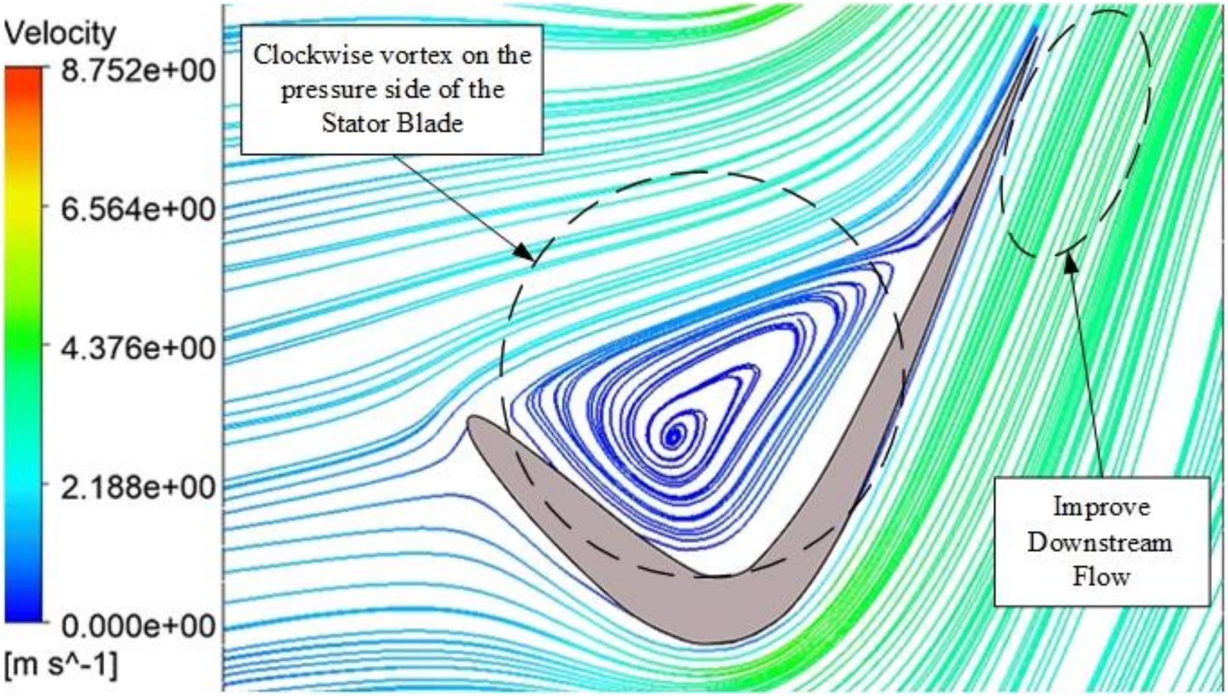

(b). Model-4 at 13% span location (Blue dot in ***Fig. 5.10****)*

5.2.3. **Stator-blade configuration considerations**

The stator-blade number, solidity, and relative thickness are three critical geometrical parameters for configuring the stator-blade, and each parameter has a huge role in guiding inflow to the runner, protecting inflow fish and reducing the overall complexity of the system. Each parameter and how it impacts the system overall performance is covered in this section.

5.2.3.1. ***Stator-blade number consideration***

As shown in **Fig.3.11**., the stator-blade number is essential for SMH technology; less stator can have larger spacing between blade, therefore reducing the fish impact, improving the fish survival rate, and reducing the overall complexity of the system. However, the high stator count can act as a trash rack, which prevents large floating objects from entering the runner-blade section, therefore reducing the runner-blade damage. Because of those reasons, the configuration of the stator should be thoroughly studied. **Figure.5.12** shows the normalized shaft-power output (The power results were normalized with 40-stator model's results) and overall hydraulic performance of the turbine with the variation in the number of stator-blades at four different flow conditions.

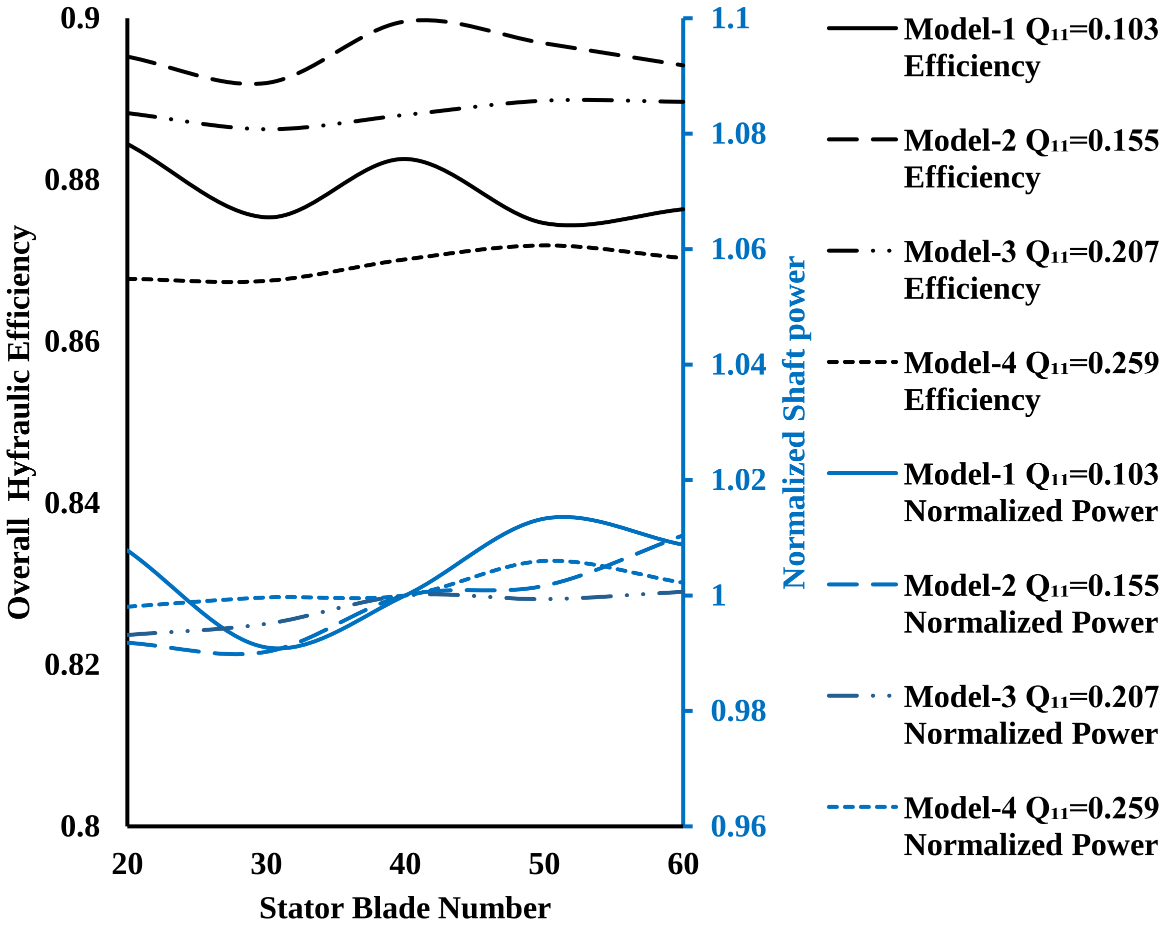

Figure. 5.12. *The relation between stator-blade number, overall hydraulic efficiency, and normalized shaft power for four designed flow conditions*

The results show that among all selected four flow rate conditions, the maximum performance difference is only 0.8%, the maximum shaft power difference is only 2.33%. This less effect means the stator number has a minimal effect on overall hydraulic performance, and a different number of stator-blades can be chosen for various river conditions. For this paper, the 40 stator-blade was chosen as the reference configuration.

5.2.3.2. *Stator-blade solidity consideration*

As shown in **Eqn (3-32,33)** and **Fig. 3.15**, the stator-blade solidity (σ_s) can dramatically change the stator profile and alter the overall performance. Unlike the runner-blade solidity that has an optimum value for initial reference (**Fig. 3.13**), to the author's knowledge, there is very little information regarding the stator-blade solidity. So, it is critical to investigate how stator-blade solidity affects overall performance. For a given stator number, the stator-blade solidity can determine the blade's chord length. Longer chord length can have better flow guidance but with additional friction losses. Also, since the blades' relative thickness is related to the blade chord length, shorter chord length can cause a thin blade profile, which can decrease the blade blockage and flow guidance, alter the blade velocity triangle, and eventually reduce the overall performance. For four flow-rate conditions, **Fig 5.13** shows the overall hydraulic performance of the turbine and the normalized shaft power output (The power results were normalized with $\sigma_s = 1$ model's results) with the variation in the stator-blade solidity.

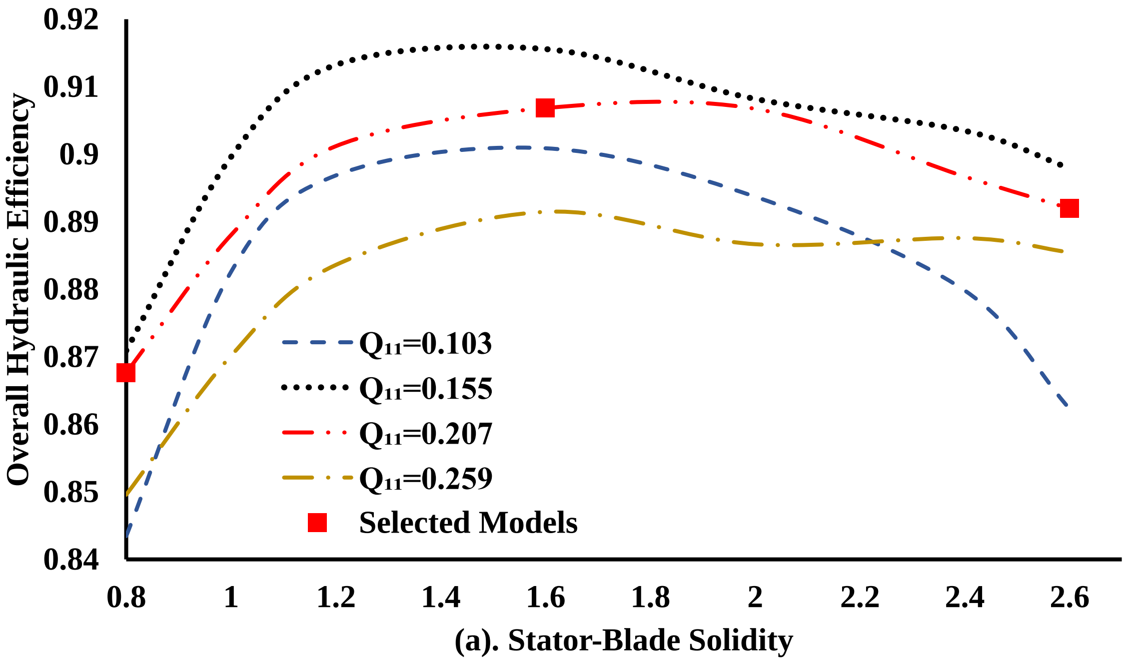

Figure. 5.13. *The relation between stator-blade solidity with (a) overall hydraulic efficiency and (b) normalized shaft power for four designed flow rate conditions*

***Figure. 5.13** (Cont'd)*

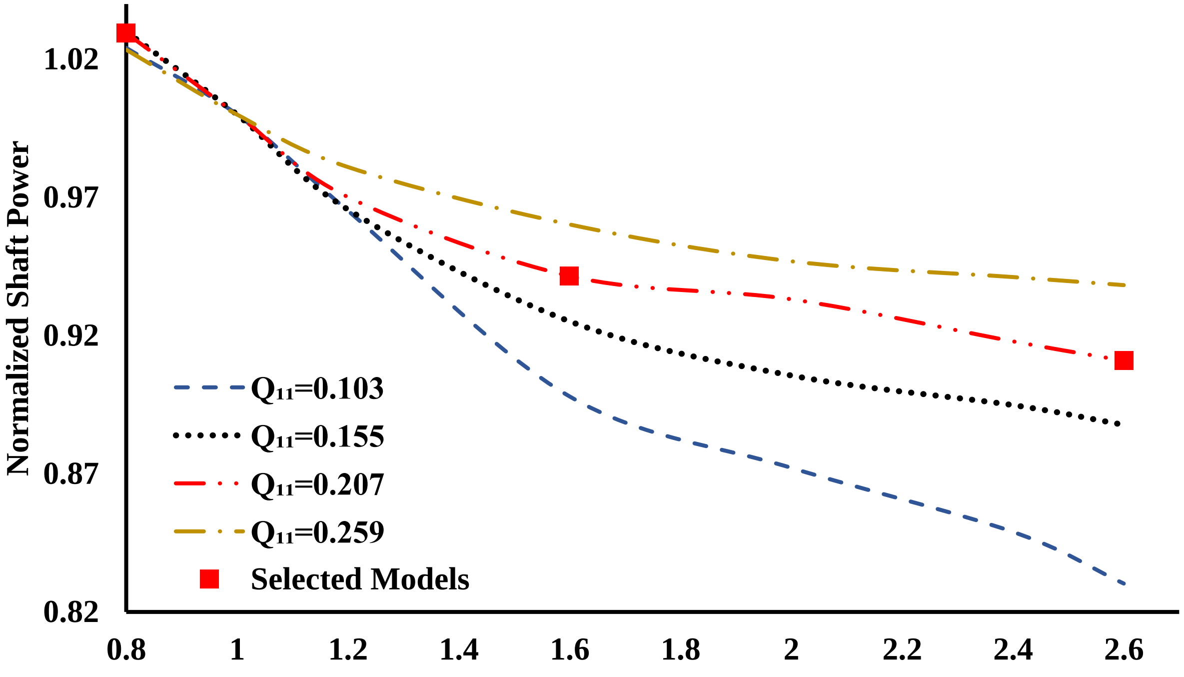

(b). Stator-Blade Solidity

The results show that, for all flow rate conditions, the increase of the stator-blade solidity can first improve the overall hydraulic efficiency, then after reaching an optimum value, the overall hydraulic efficiency drops, and the maximum efficiency difference is around 5.5%. The optimum stator solidity-value is between 1.2 and 1.8 depends on different flow rate conditions. Moreover, the most significant difference happens in shaft power. With the increase of the stator-blade solidity, the shaft power drops dramatically, and the maximum difference is around 20%. Based on **Eqn (2-24)**, the turbine-work (W_T) is related to three factors: the total head difference (ΔH_{total}), mass flow rate ($\dot{m}$), and overall hydraulic efficiency (η_h). As shown in **Fig.5.13-(a)**, the maximum efficiency difference is only 5.5%; and the total head difference is fixed. Therefore, the major reason that causes the turbine-work to drop significantly is the decrease in the mass flow rate. All example models in **Fig.5.13** are designed for four flow conditions ($Q_{11} = 0.103$, $Q_{11} = 0.155$, $Q_{11} = 0.207$, $Q_{11} = 0.259$), and all those flow conditions are the target, designed flow rate conditions. As discussed in *section 4.2.3*, during the numerical simulation, only the head difference is fixed, and the flow rate must float. With the correct design and appropriate geometry setting, the final flow rate results should be close to the designed value. However, irregular geometry, in this case, the stator-blade solidity, can cause a huge flow rate difference and leads to the efficiency and turbine work difference shown in **Fig.5.13**.

For better understanding, three models (Model-1:$\sigma_s = 0.8$; Model-2 :$\sigma_s = 1.6$; Model-3 :$\sigma_s = 2.6$) with one design flow rate condition ($Q_{11} = 0.207$) are selected for further investigations (Red Markers in **Fig.5.13**).

- *β_2 Consideration*

As discussed before, the first step is to evaluate how the β_2 (runner-blade inlet relative flow angle) change with different stator solidity at various span locations. **Figure 5.14** shows the comparison between the $\beta_{2\,blade}$ and $\beta_{2\,flow}$ for the three selected models. The results show that, near the hub region, because of the boundary flow and low runner circumferential velocity (velocity U in **Fig. 2.2**), the $\beta_{2\,flow}$ is larger than the $\beta_{2\,blade}$ for all three selected models, and the maximum difference is around 16°. Additionally, there are two features worth noticing:

- In the center span region, model-1's β_2 values are close to the designed values with the maximum difference only around 2.5° (Back Arrow in **Fig.5.14**).
- In the center span region, compared to the model-1, the difference between model-2,3's β_2 values and the designed values are larger, with the maximum difference around 7° (Red Arrow in **Fig.5.14**).

As mentioned above, the difference between $\beta_{2\,flow}$ and $\beta_{2\,blade}$can undoubtedly affect the overall performance by increasing the runner-blade incidence loss, but the results in **Fig.5.14** cannot fully explain the trend shown in **Fig.5.13**. Therefore, another angle α_2 was studied.

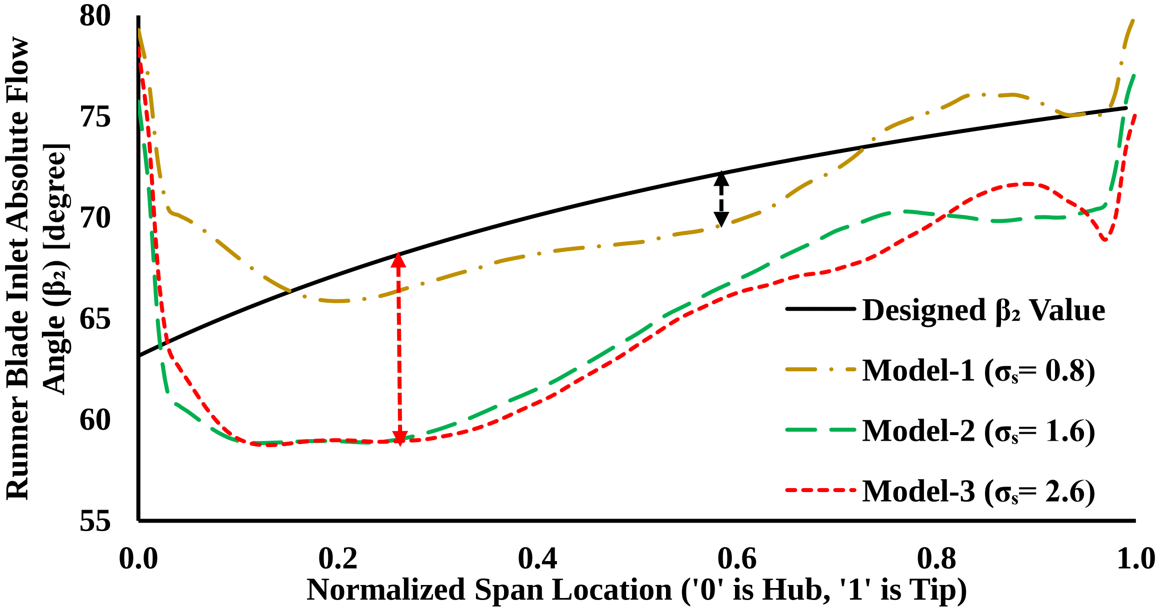

Figure. 5.14. *The runner-blade inlet $\beta_{2\,flow}$ angle distribution plots for three selected models in comparison with the designed $\beta_{2\,blade}$ value*

- *α_2 Consideration*

Figure.5.15 shows the α_2 distribution plot across all span location for the three selected models with the comparison with the designed α_2 value. For model-1 (σ_s =0.8), the α_2 is significantly lower than the other two models in the center of the span region, the maximum difference is around 20°compared to the designed α_2 value. This vast difference (Red Arrow in **Fig.5.15**) is the main reason that model-1 has significantly lower efficiency. For the other two models, the maximum difference in the center span region is only around 5°.

For better visualization, **Figure.5.16** shows the stream-line pattern for the Model-1(σ_s = 0.8) and Model-2 (σ_s=1.6) at 60% span location. Model-1 **(Fig.5.16-a)** which has small stator-blade solidity and shorter blade chord length has relatively poor flow guidance, and this leads to the vast α_2 value difference and low overall efficiency. Model-2 (**Fig.5.16-b)** which has a longer and thicker blade profile has good flow guidance, and this leads to the small α_2 value difference and high overall efficiency.

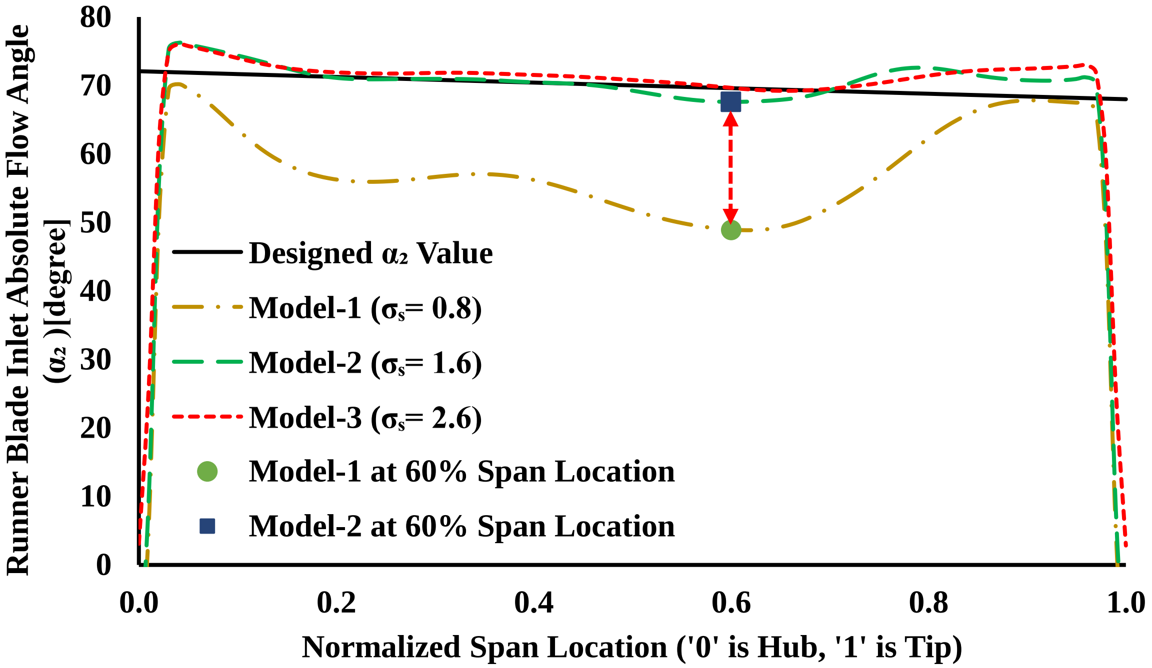

Figure. 5.15. *The runner-blade inlet absolute flow angle (α_2) distribution plots for three selected models in comparison with the designed α_2 value*

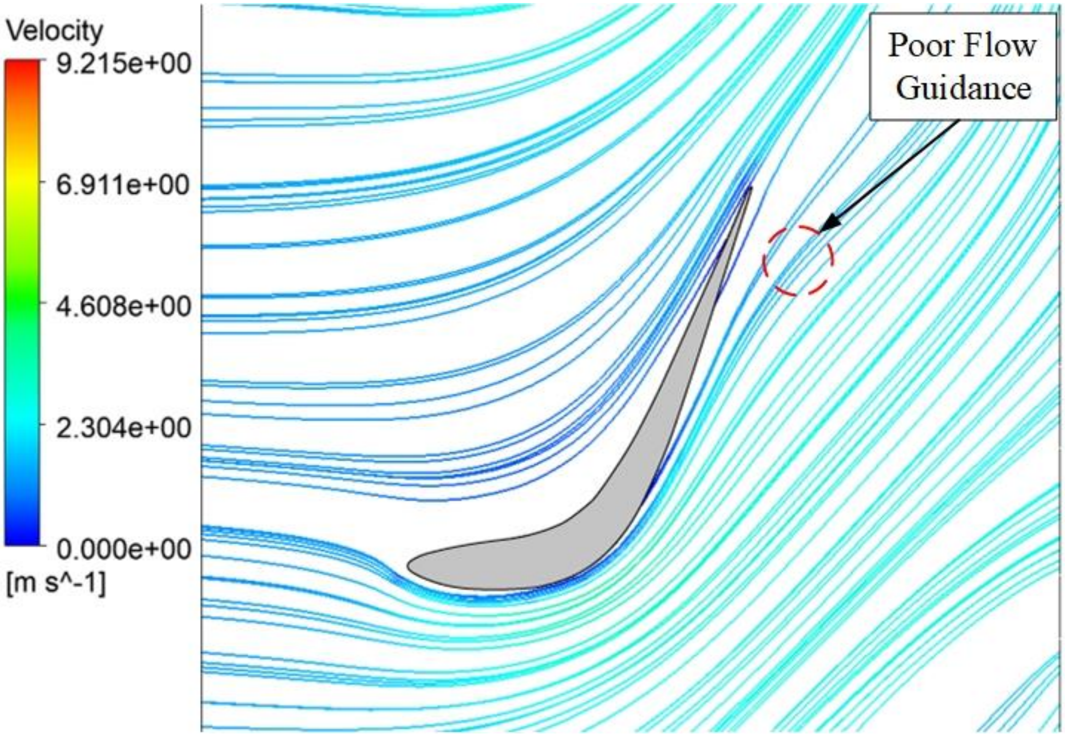

(a). Model-1 ($\sigma_s = 0.8$) at 60% span location (Green dot in ***Fig. 5.15****)*

Figure. 5.16. *The stream-line pattern for the (a) Model-1 and (b) Model-2, at 60% span location*

***Figure. 5.16** (Cont'd)*

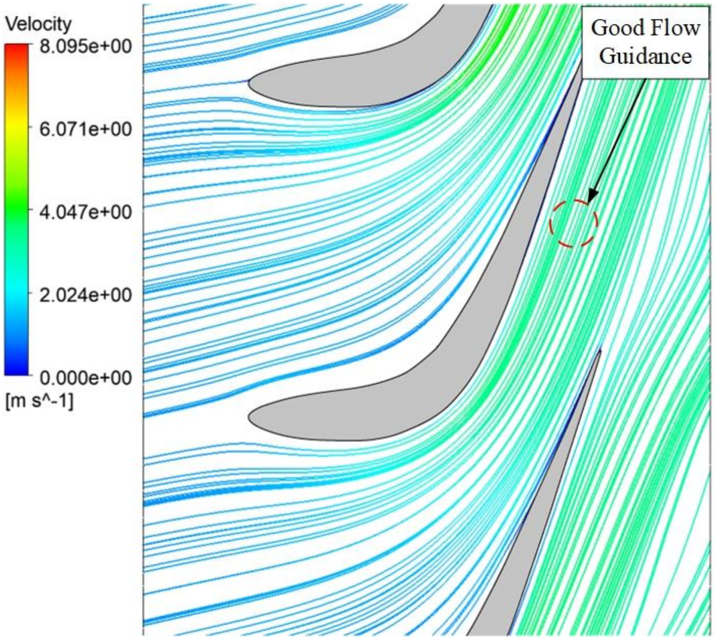

*(b). Model-2 ($\sigma_s = 1.6$) at 60% span location (Blue dot in **Fig. 5.15**)*

- *Velocity Triangle Consideration*

Another key feature in **Fig.5.13-(b)** is the significant power increase with the decrease of the stator-blade solidity. In order to explain this, different velocity components at the stator exit must be studied. Therefore, different velocity components at stator exit (Station 2 in **Fig.2.2**) for *model-1, model-2,* and *model-3* are shown in **Fig.5.17**. **Figure.5.17**-(a) shows the magnitude of the overall velocity (Velocity C_2 in **Fig.2.2**), **Figure.5.17**-(b) shows the magnitude of the circumferential velocity (Velocity C_{u2} in **Fig.2.2**), and **Figure.5.17**-(c) shows the magnitude of the axial velocity (Velocity C_{x2} in **Fig.2.2**). The results show that model-1's C_2 and C_{u2} velocities are significantly lower than model-2, 3's values, and the maximum difference is around $1m/s$. However, model-1's C_{x2} velocity is noticeably higher than model-2, 3's values and the maximum difference is around $0.5m/s$. This axial velocity difference is the main reason for the shaft power difference. As shown in **Eqn 2-2**, the system mass flow rate depends on the axial velocity, and large axial velocity means a large mass flow rate. As mentioned at the beginning of this section, the mass flow rate is one of the three factors that influence the turbine power, and a larger mass flow rate can lead to an increase in turbine shaft power.

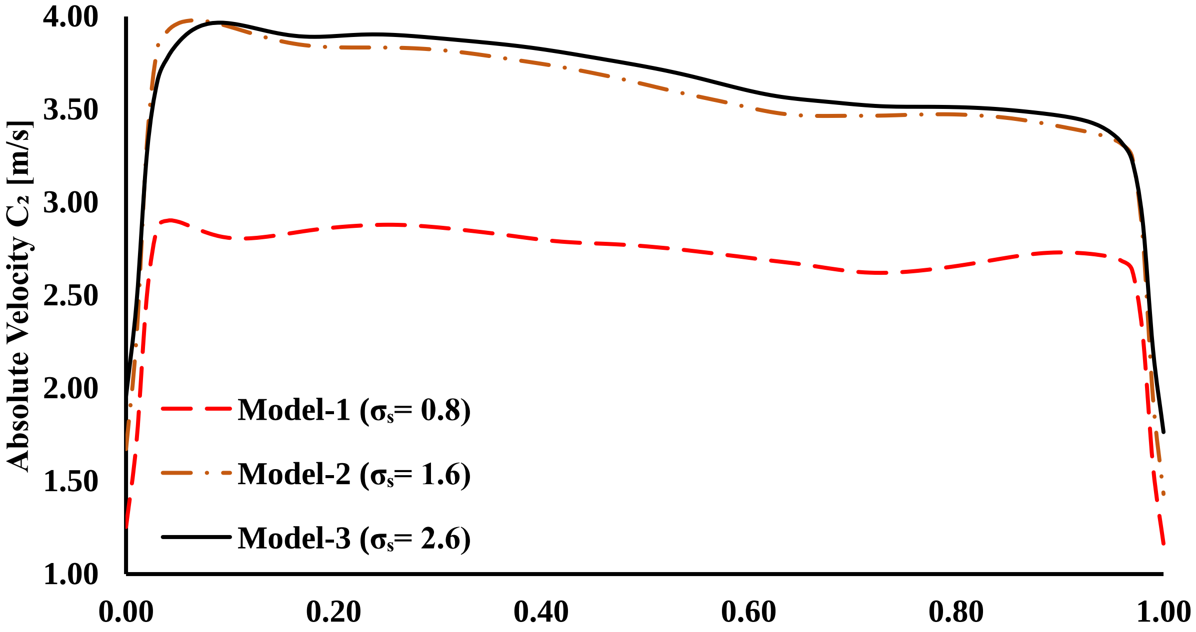

(a). Normalized Span Location ('0' is Hub, '1' is Tip)

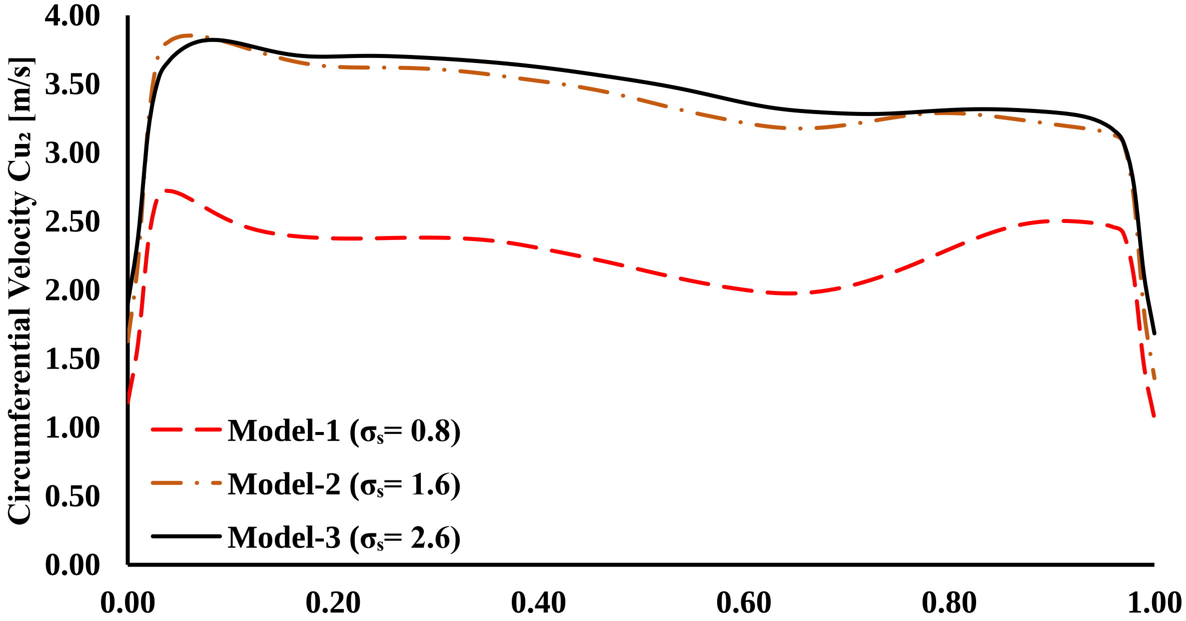

(b). Normalized Span Location ('0' is Hub, '1' is Tip)

Figure. 5.17. *Three different velocity distribution at the stator exit (runner-blade inlet) for all three selected models: (a) Absolute velocity (C_2), (b) Circumferential velocity Cu_2, (c) Axial velocity C_{x2}*

Figure. 5.17 *(Cont'd)*

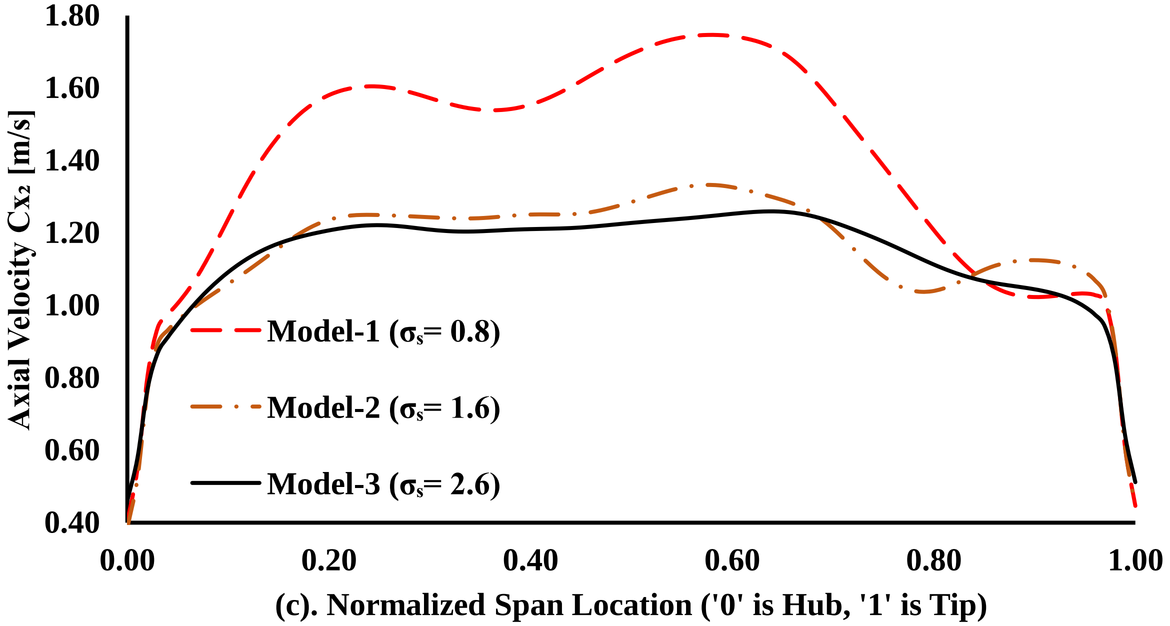

(c). Normalized Span Location ('0' is Hub, '1' is Tip)

The main function of the stator geometry is to guide the inlet velocity to a designed direction with the desired magnitude; therefore, the nature of the stator is similar to a nuzzle. For a better understanding, the static pressure distribution plots at the 60% span location for all three selected models are shown in **Fig.5.18**. The model-1's stator has a shorter and thinner blade, and those geometrical features led to a poor velocity redirection. This poor velocity redirection has two significant consequences, inadequate velocity acceleration, and less velocity redirection angle. For a given head (which means fixed inlet pressure at stator inlet), based on the Bernoulli Equation, the inadequate velocity acceleration (which means low absolute velocity C_2 shown in **Fig.5.17-a**) results in high static pressure at the stator outlet, which shown in **Fig.5.18.** The less velocity redirection angle causes a small α_2 values showed in **Fig.5.15**. Those two consequences reshape the velocity triangle at the stator outlet and inevitably affect the overall performance and power, and **Fig.5.19** shows a comparison between the model-1's, model-3's, and designed stator outlet velocity triangle at 60% span location. Additional results and plots are shown in **Appendix.F**.

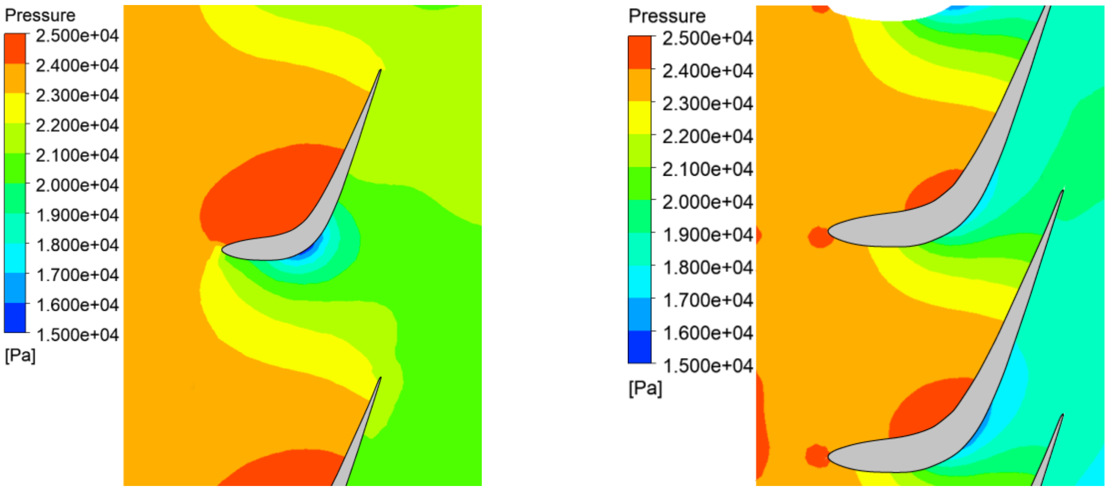

(a). Model-1($\sigma_s = 0.8$) *(b). Model-2* ($\sigma_s = 1.6$)

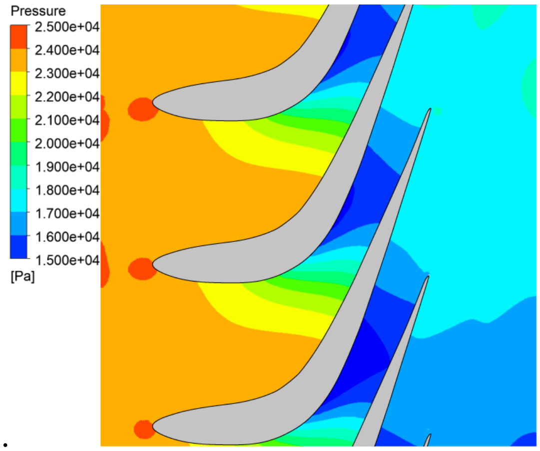

(c). Model-3 ($\sigma_s = 2.6$)

Figure. 5.18. *Static pressure distribution at 60% span location for all three selected models, (a) Model-1,* $\sigma_s=0.8$ *(b) Model-2,* $\sigma_s=1.6$*, (c) Model-3,* $\sigma_s=2.6$

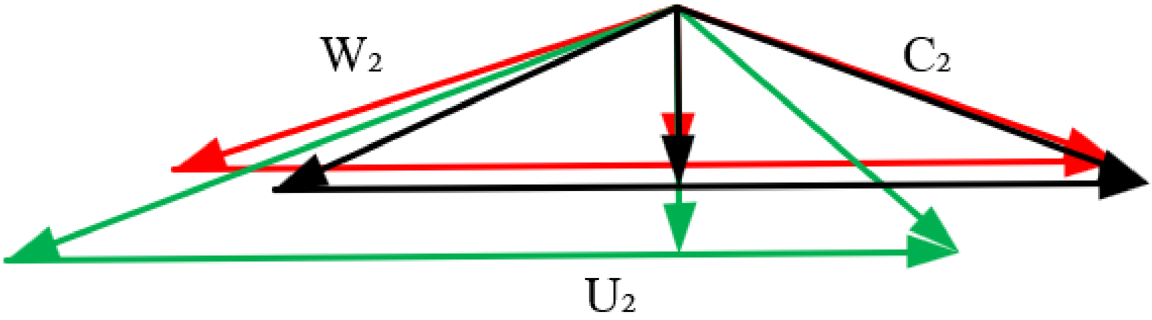

Figure. 5.19. *Velocity Triangle for Model-1,* $\sigma_s=0.8$ *(Green Arrow), Model-3,* $\sigma_s=2.6$ *(Black Arrow), and Designed value (Red Arrow) at 60% span location*

5.2.3.3. *Stator-blade thickness consideration*

As shown in **Fig.3.18**, the stator-blade relative thickness is another parameter that influences the overall stator-blade geometry. **Figure.5.20** shows how relative blade thickness (between 0.05 and 0.15) affects the overall performance and normalized shaft power (The power results were normalized with $S_T = 0.1$ model's results) for four flow rate conditions.

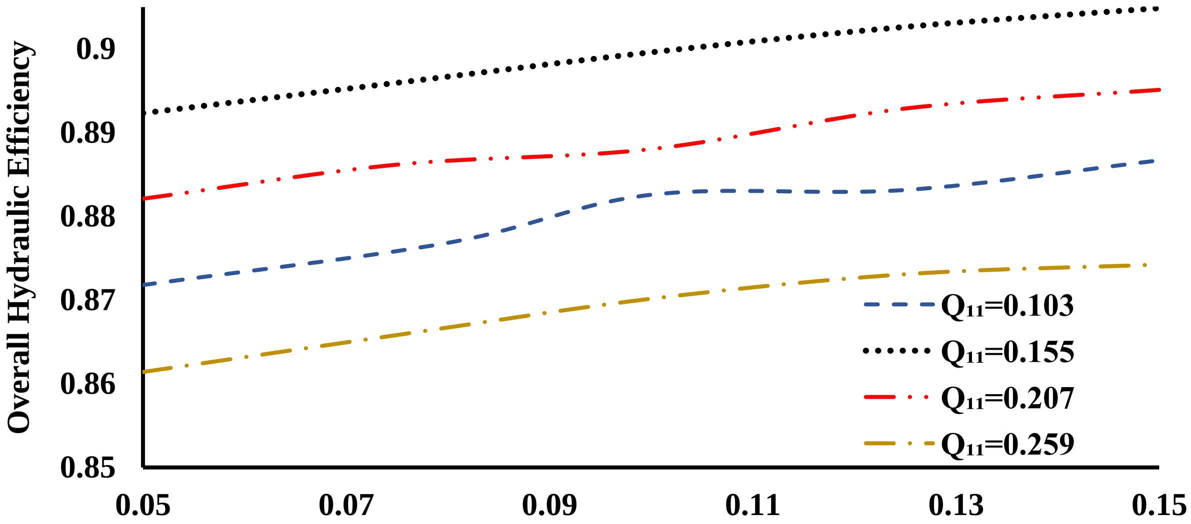

(a). Stator Blade Relative Thickness (S_T)

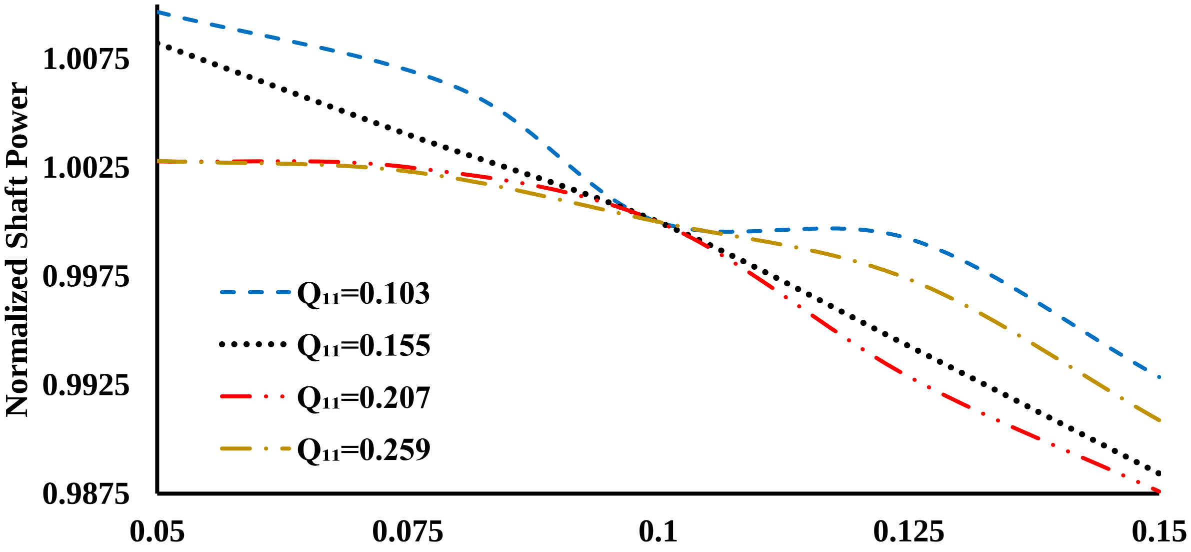

(b). Stator Blade Relative Thickness (S_T)

Figure. 5.20. *The relation between stator-blade relative thickness with (a) overall hydraulic efficiency and (b) normalized shaft power for four designed flow rate conditions*

The results show that the increase of the stator-blade relative thickness can slightly improve the overall performance and decrease the shaft power, the maximum efficiency increase is around 1%, and the maximum shaft power decrease is around 1.5%. Unlike the stator-blade solidity, the stator-blade relative thickness has a limited effect on overall performance; therefore, different thickness values can be applied to different flow and environmental conditions.

Additionally, the small stator-blade relative thickness can improve the overall performance when the stator-blade solidity is too large. **Figure.5.21** shows the relation between overall performance, normalized power and stator-blade solidity under three stator-blade relative thickness values for one selected flow rate condition ($Q_{11} = 0.207$). The results show that when $S_T = 0.1\ and\ 0.15$, there is a significant efficiency drop when σ_S is larger than two. This drop is caused by the increase of the blade thickness and chord length, which increases the stator blockage and friction loss. However, with smaller stator-blade relative thickness, the overall efficiency can be improved and maintain relatively constant when σ_S is larger (Red Arrow in **Fig.5.21**). For better understanding, two models were selected for further investigation (Red Squares in **Fig.5.21**).

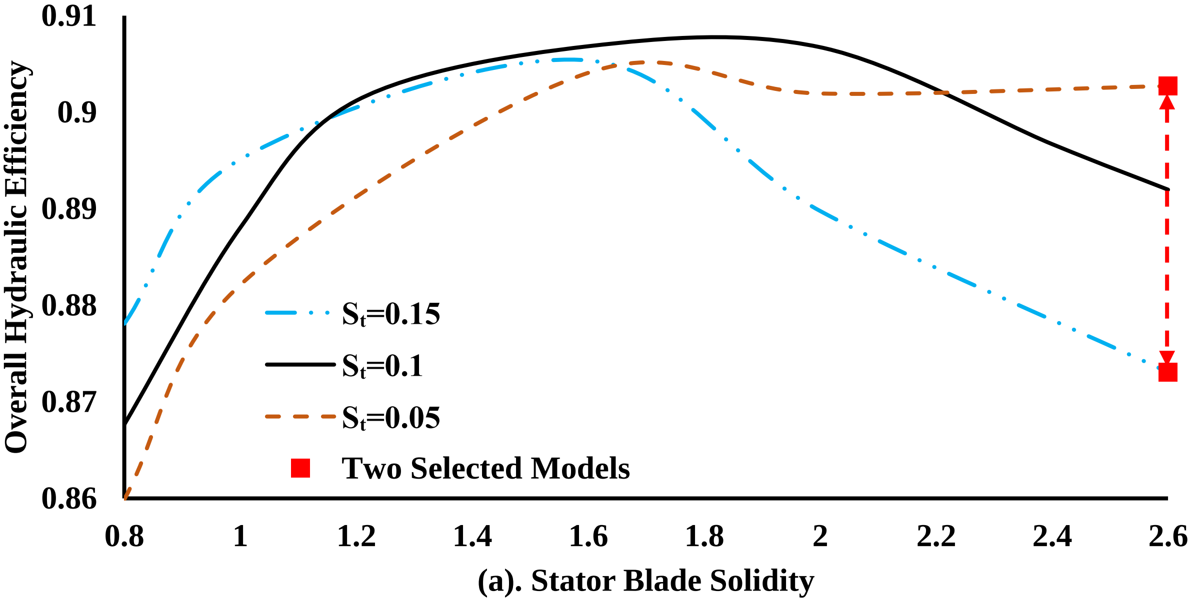

Figure. 5.21. *The relation between (a). Overall performance (b). Normalized Power, and stator-blade solidity under three stator-blade relative thickness values for one flow rate condition (Q_{11}=0.207)*

Figure. 5.21 *(Cont'd)*

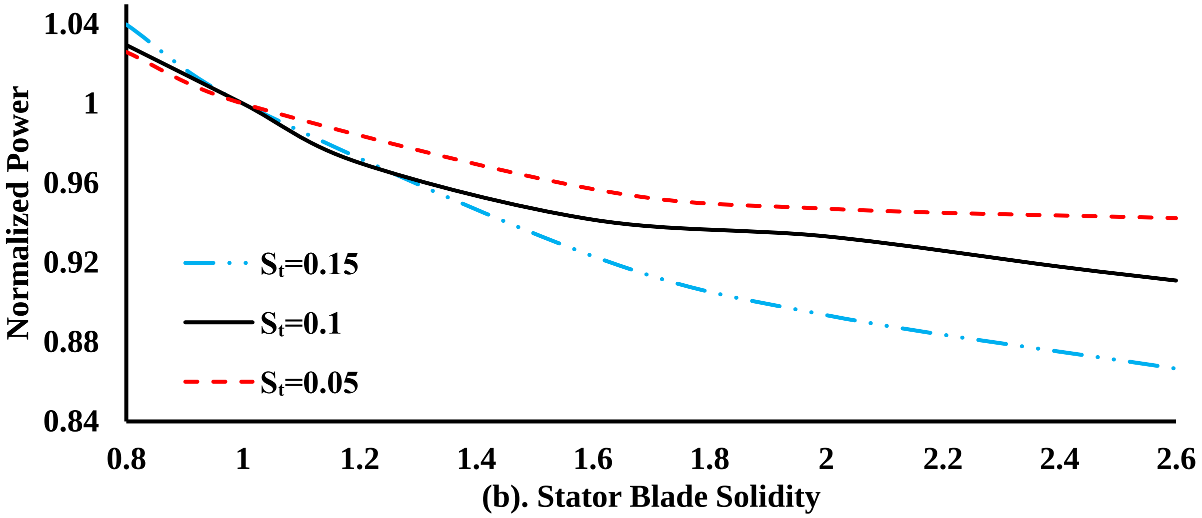

(b). Stator Blade Solidity

Figure 5.22, 5.23 show the α_2 and β_2 values for the two selected models. Unlike in **Fig.5.14** and **Fig.5.15**, the two selected models' α_2 and β_2 values are relatively close to each other, with the maximum difference around 5°. Undoubtedly, this small difference can affect the overall performance; however, it cannot result in a nearly 3% efficiency difference between the two selected models solely. Therefore, it is important to examine the stator closely.

Stator geometry can affect the overall performance in two ways, first is changing the velocity and velocity triangle, which can influence the runner-blade performance; second is increasing local stator loss to impact the overall performance. There are two main sources of loss for the stator, and one is the blade profile loss (surface friction), anther one is the blade blockage loss. By using the design method covered in ***section 3.2***, changing blade thickness has very little effect on the stator surface area, which means under the same solidity, the stator-blade profile loss is similar for the two selected models. Therefore, the main source for the 3% efficiency difference is from the stator blockage. For the two selected models, **Fig.5.24** shows the total pressure drop across all span locations at the stator exit (Station-2 in **Fig.2.2**); and the pressure drop value is normalized by the inlet total pressure.

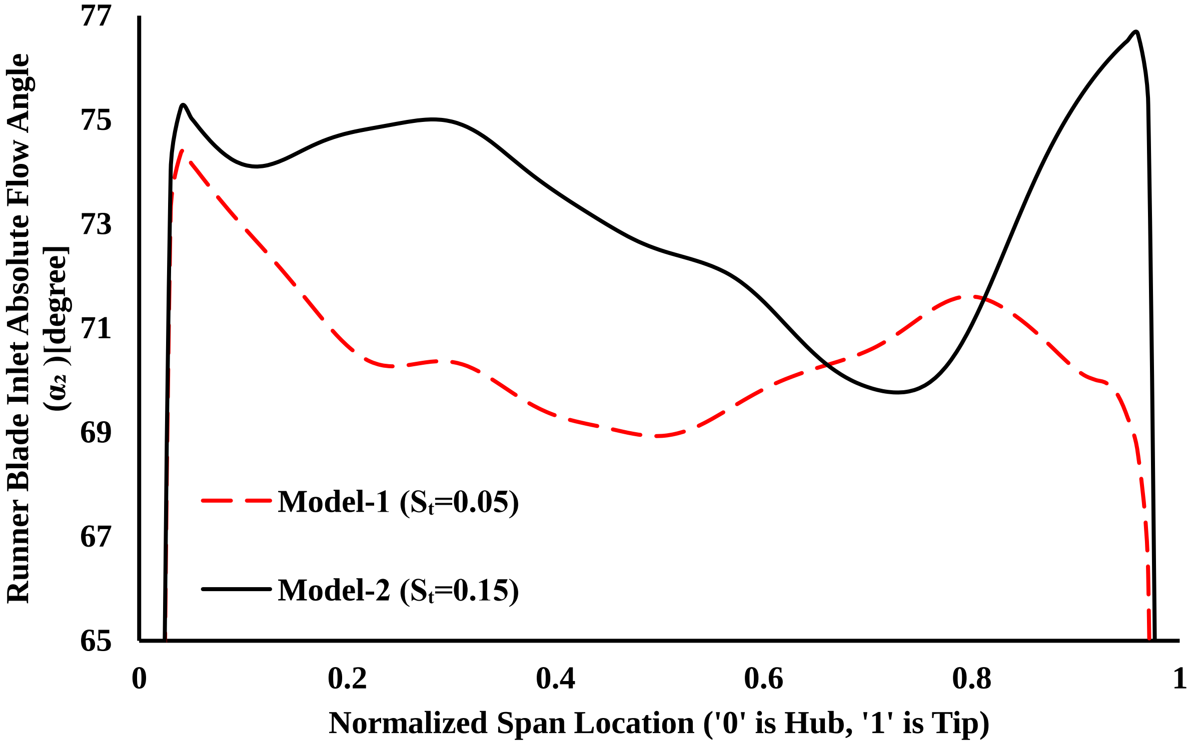

Figure. 5.22.*The runner-blade inlet absolute flow angle (α_2) distribution plots for the two selected models in comparison with the designed α_2 value*

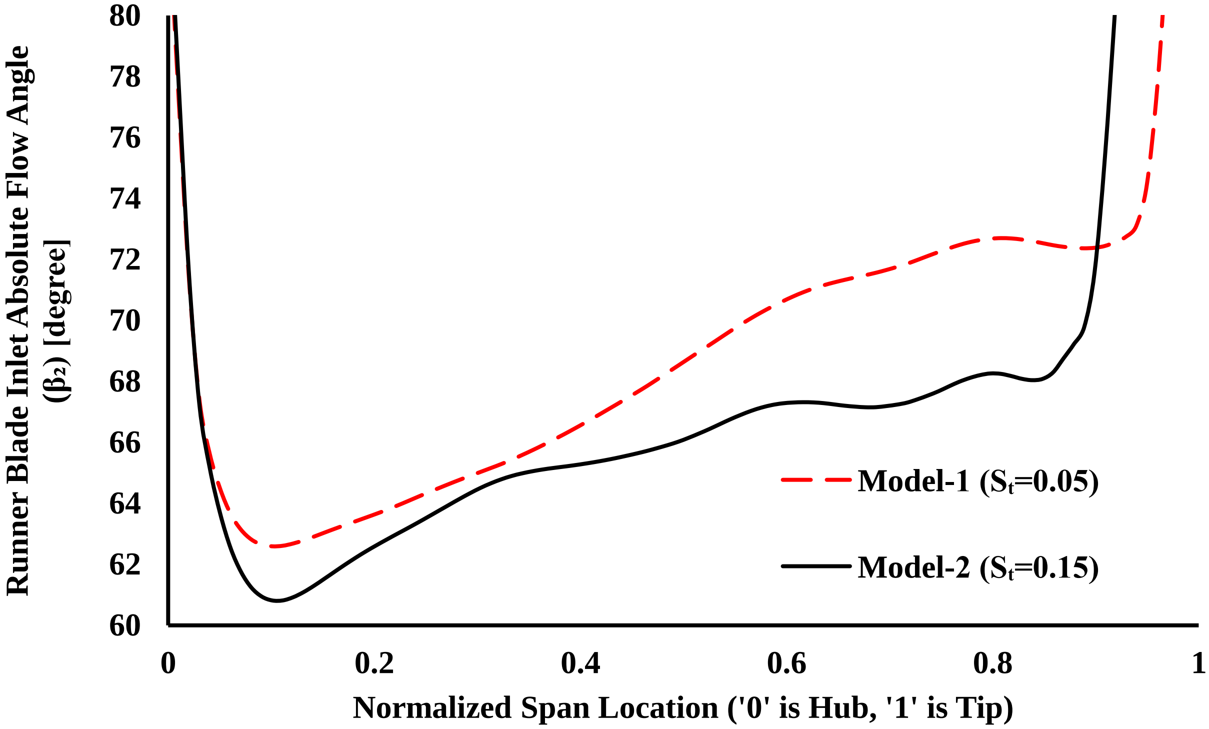

Figure. 5.23. *The runner-blade inlet $\beta_{2\,flow}$ angle distribution plots for the two selected models in comparison with the designed $\beta_{2\,blade}$ value*

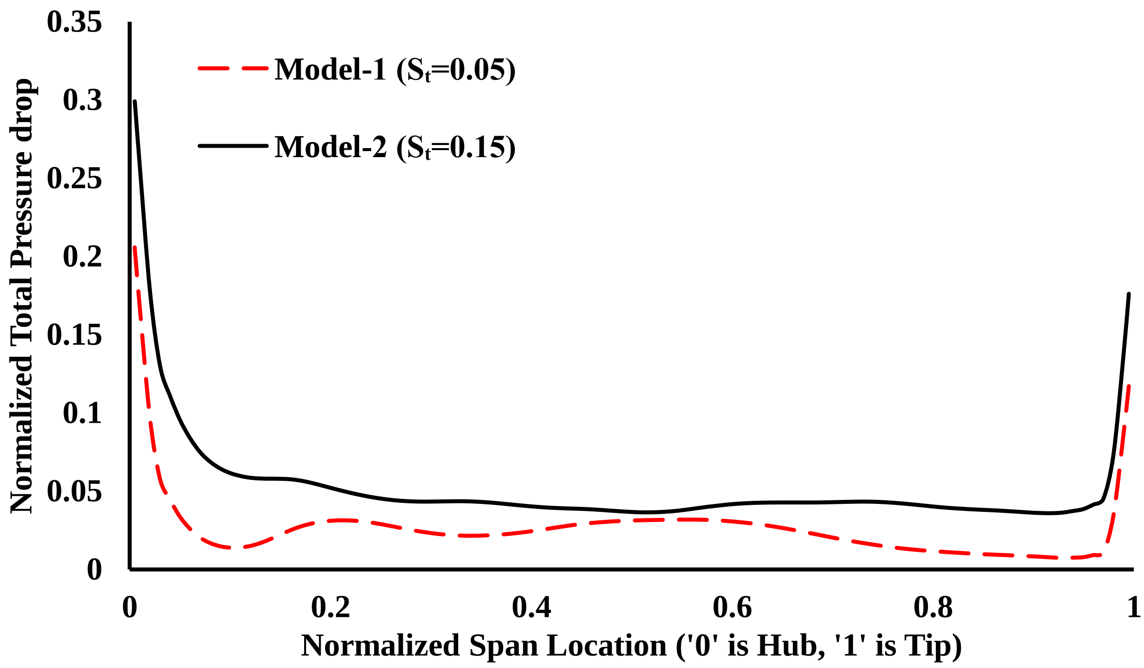

Figure. 5.24. *The normalized total pressure drop across all span locations for the two selected models at the stator exit*

The results show that except near the tip and hub region where the boundary layers are, the Model-2 has a larger total pressure drop across all span locations than Model-1, and the overall averaged stator total pressure drop ratios (normalized by the inlet total pressure) are 5.34% and 2.74% for Model-2 and Model-1 respectively. The difference in total pressure drop ratio between the two selected models is around 2.6%, which is the main source for the 3% overall efficiency difference mentioned above. Some additional results and plots are shown in **Appendix.G**.

5.3. Runner-blade consideration

5.3.1. Runner-blade stagger-angle setting constant consideration

Just like the stator-blade stagger-angle setting constant, the runner-blade stagger-angle setting constant (C_{rsa}) also is a critical geometrical parameter for the runner-blade profile. As shown in **Fig.3.8(a)**, this parameter can alter the blade shape dramatically, and **Fig.5.25** shows how this parameter affects the overall performance under four different flow rate conditions. For all flow rate conditions, the efficiency first increases with the increase of C_{rsa}, then reach the maximum efficiency when C_{rsa} is between 0.3 and 0.5, then the efficiency decreases significantly with the increase of the C_{rsa}. Four models were selected (Red Squares in **Fig.5.25**) for further investigation.

As described in ***section 5.1***, the magnitude of the circumferential velocity difference (C_{u2}-C_{u3}) represents how effective a runner-blade is converting the hydraulic power to mechanical power. So, **Fig.5.26** shows the circumferential velocity difference distribution plots for all four selected models. Model-2 has a higher (C_{u2}-C_{u3}) value than the other three models across most of the span location, which is reasonable for its highest efficiency. Model-1 has a very similar trend as Model-2, but with a small decrease in value near the tip region (Red Arrow in **Fig.5.26**), which causes a small efficiency drop compared to the Model-2. Model-3 and Model-4 have significantly lower (C_{u2}-C_{u3}) values, especially in the 40% to 80% span location (Blue Arrow), which causes them to have lower efficiency.

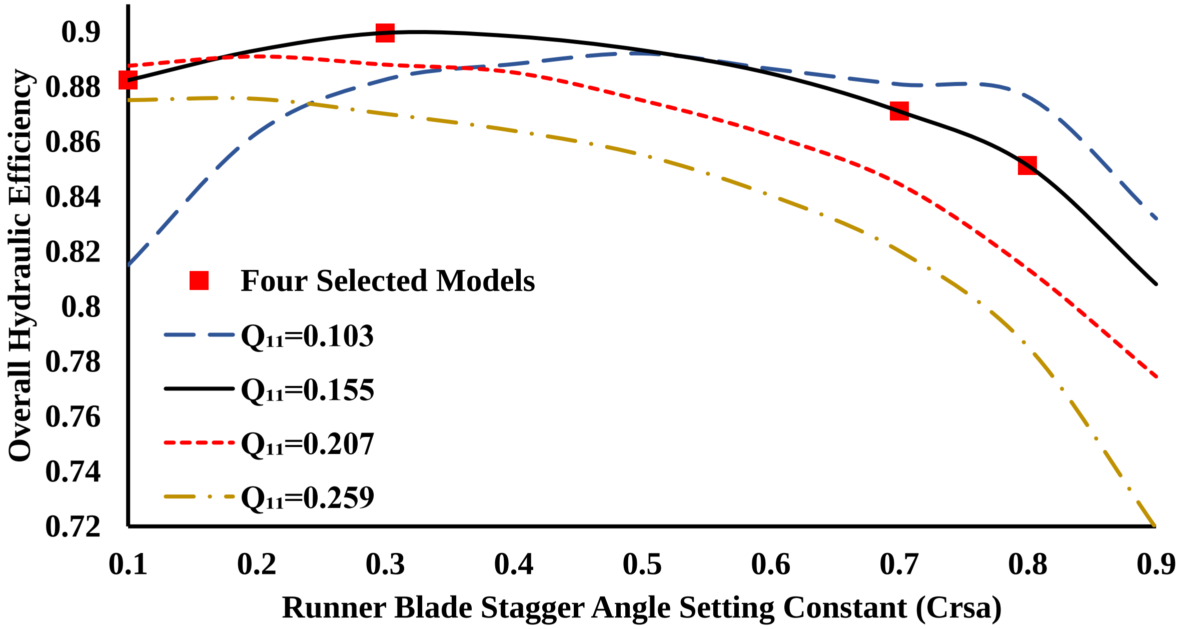

Figure 5.25. *The Relation between overall hydraulic efficiency and runner-blade stagger-angle setting constant* C_{rsa} *for four flow rate conditions.*

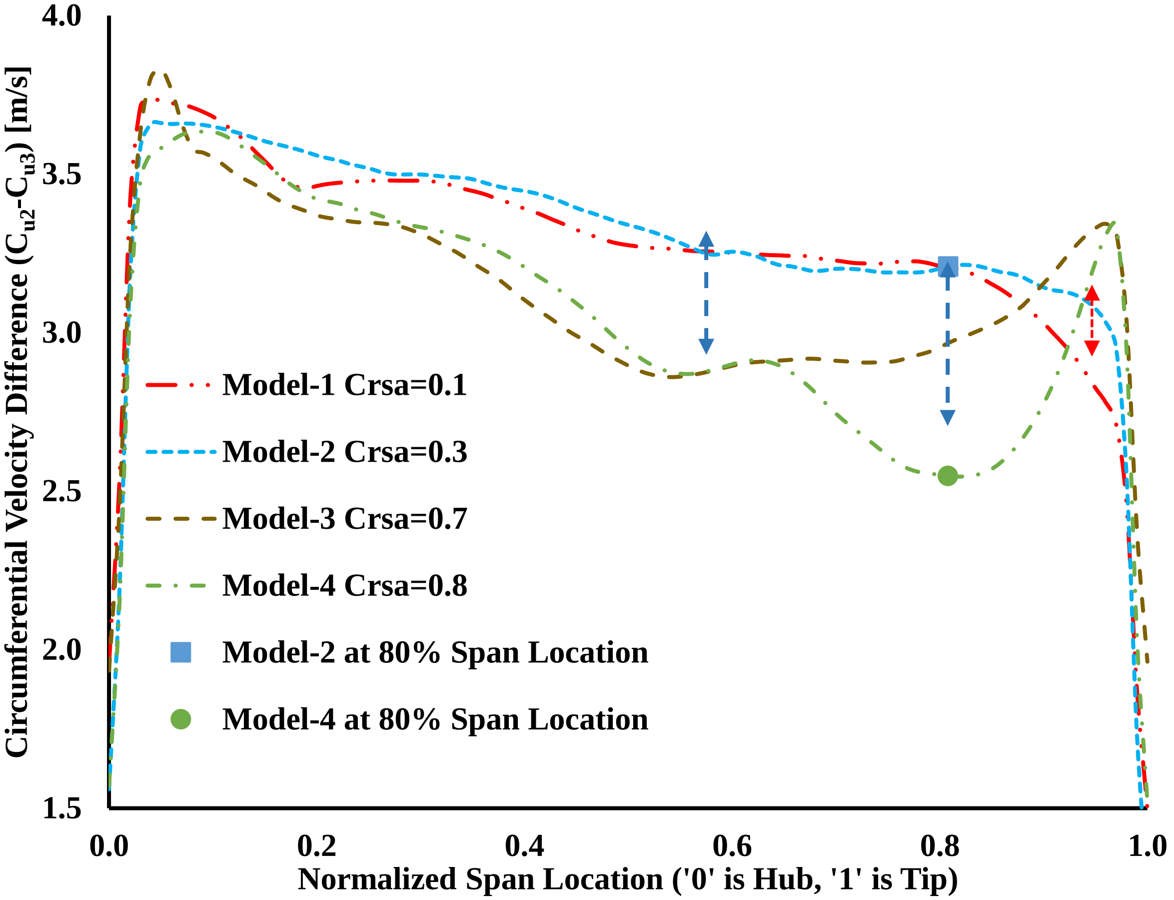

Figure. 5.26. *The circumferential velocity difference (C_{u2}-C_{u3}) distribution plots from hub to tip for four selected models.*

For better visualization, **Fig.5.27** shows the stream-line pattern for the Model-2 (C_{rsa}=0.3) and Model-4 (C_{rsa}=0.8) at 80% span location. The Model-2 (**Fig.5.27-a**) shows a great flow attachment, which gives it a better performance, and the Model-4 (**Fig. 5.27-b)** shows some flow distortion near the leading edge on the pressure side of the blade, which causes the drawback of the efficiency. In comparison with C_{ssa} that has a 12% maximum efficiency difference, the C_{rsa} with a 9% maximum efficiency difference has less impact on the performance. However, this impact is still significant enough and needs to be carefully considered. Base on the overall results, initially, the suggesting range for C_{rsa} is between 0.2 to 0.3. Some additional results and plots are shown in **Appendix.H**.

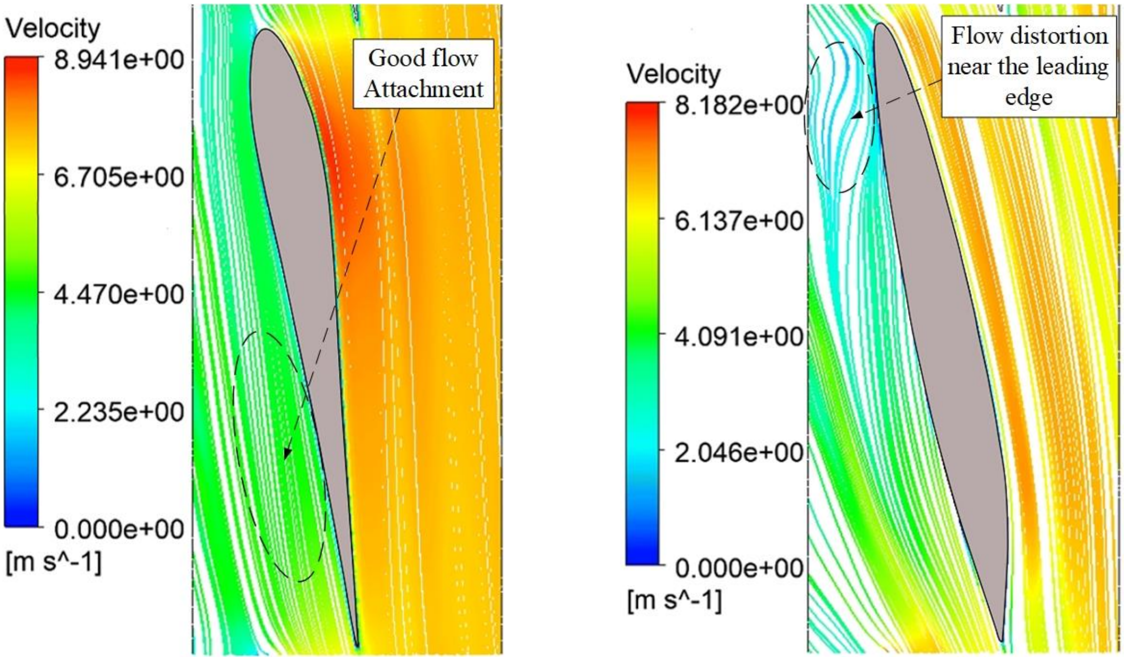

(a). Model-2 at 80% span location (Blue square in ***Fig.5.26****)*

(b). Model-4 at 80% span location (Green dot in ***Fig.5.26****)*

Figure. 5.27. *The runner blade stream-line pattern for the (a) Model-2, and (b) Model-4, at 80% span location*

5.3.2. **Runner-blade configuration considerations**

Like the stator-blade configuration, the runner-blade number, solidity, and relative thickness are three critical geometrical parameters for configuring the runner-blade, and each parameter has a huge role in converting the hydraulic energy to mechanical energy effectively, which is the key of any hydraulic turbine system. Each parameter and how it impacts the overall performance are covered in this section.

5.3.2.1. ***Runner-blade number consideration***

As shown in **Fig.3.12**, the runner-blade number is another critical parameter for SMH technology. As the proposed generation module has an adjustable blade mechanism for various flow conditions, less blade means a small and straightforward adjustable mechanism; this can help reduce the cost and the complexity of the generation modules. **Figure.5.28** shows the normalized shaft power output (The power results were normalized with 8-blade model's results) and overall hydraulic performance of the turbine with the variation in the number of runner-blades at four different flow conditions.

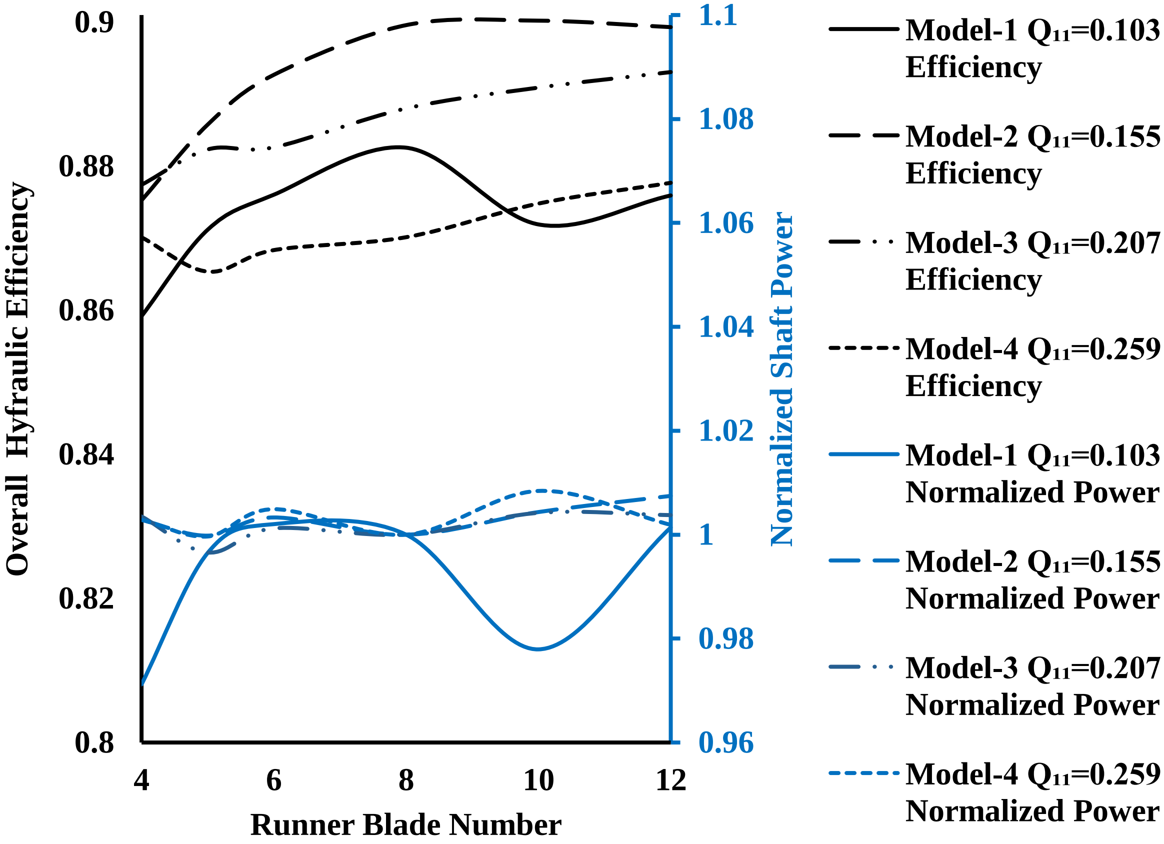

Figure.5.28. *The relation between runner-blade number, overall hydraulic efficiency, and normalized shaft power at four flow conditions*

The results show that, with the increase of runner-blade numbers, the overall hydraulic efficiency can be improved, and the shaft power remains relatively constant. Generally, with more runner-blades, the conversion between hydraulic power and shaft power is more effective, but at the same time, more runner-blades mean reducing turbine spacing between blades which can have a negative effect on larger fish survival rate and increase blocking loss. The runner-blade number configuration needs to balance the overall performance, costs, complexity, and fish damage and for this thesis, eight runner-blade was chosen as the reference configuration.

5.3.2.2. ***Runner-blade solidity consideration***

Compared to the stator-blade solidity, the runner-blade solidity can have a more significant effect on the overall performance, design, and cost. As shown in **Fig.3.14**, the runner-blade solidity can dramatically change the flow passage shape, therefore alter the overall flow behavior. Thus, **Fig.5.29** shows how the runner-blade solidity influences the overall hydraulic performance and the shaft powers under four flow rate conditions (The power results were normalized with $\sigma_r = 1$ model's results).

The results in **Fig.5.29-(a)** show that with an increase of the blade solidity, the overall efficiency first increases and reaches an optimum point, then decreases with the increase of the blade solidity; the maximum efficiency difference is around 10%, and the optimum runner-blade solidity is between 0.9 and 1.2. Additionally, because of the runner-blade configuration, the runner-blade solidity has more impact on performance at low mass flow rate conditions than the larger flow rate. **Figure.5.30** shows comparisons of different runner-blades geometry between small flow rate and larger flow rate conditions. At lower flow rate condition, the runner-blade angles (β_2, and β_3 in **Fig. 2.2**) are very close; this results in a very small stagger-angle and narrower runner-blade spacing near the trailing edge region (Red circle in **Fig.5.30-a**).

Larger blade solidity at lower flow rate can cause narrow flow passage, which increases the blockage loss, therefore causes a huge performance drop (Blue arrow in **Fig.5.29-a**). Moreover, at low flow rate conditions, larger runner-blade solidity can make the blade intersecting with each other and should be avoided. The results in **Fig.5.29-(b)** show that, at low flow rate condition, when runner-blade solidity is larger than 0.8, with the increase of the runner-blade solidity, the shaft power drop significantly, the maximum power difference is around 85%; additionally, the power increase when runner-blade solidity is between 0.7 and 0.8 (Red arrow in **Fig.5.29-b**). At higher flow rate condition, the power remains relatively constant when runner-blade solidity is between 0.7 and 0.8, and drop with a further increase of the solidity with the maximum efficiency around 20%. For better understanding, four models under one flow conditions were chosen for further investigation (Red squares in **Fig.5.29**).

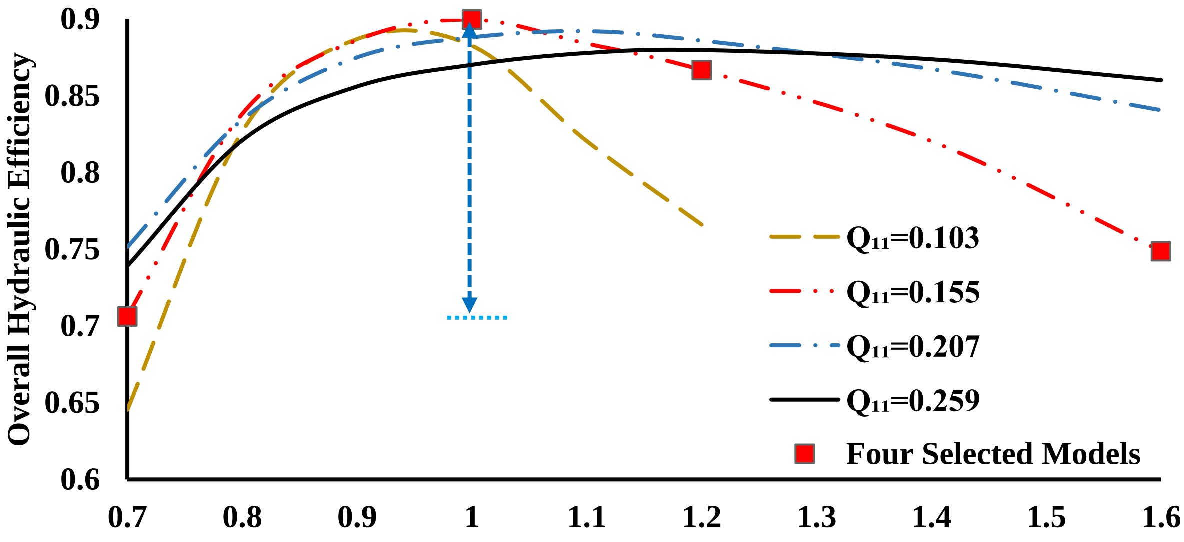

(a). Runner Blade Solidity

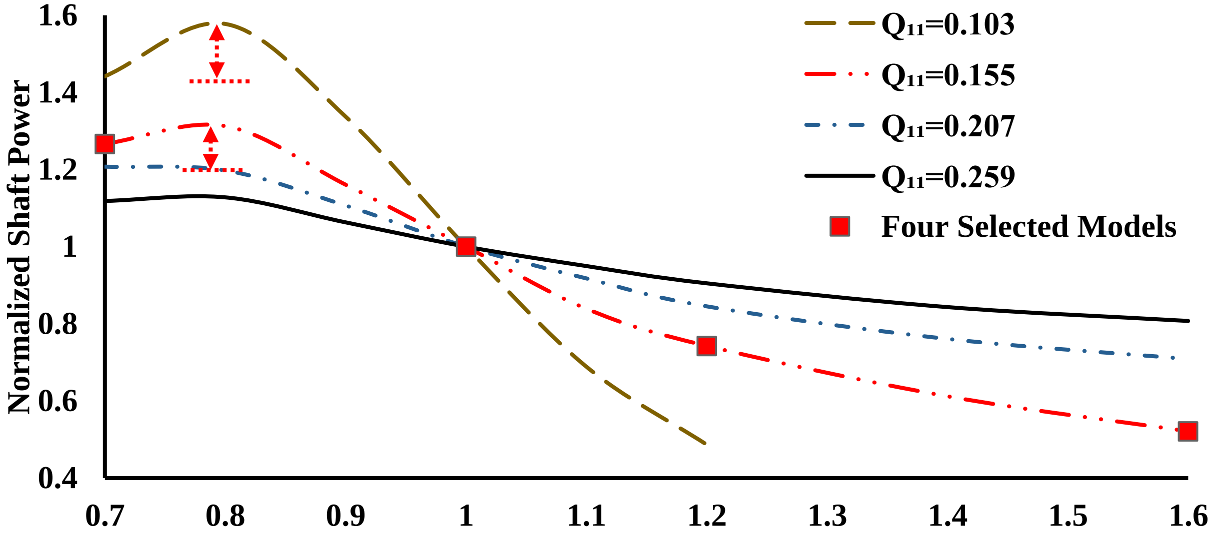

(b). Runner Blade Solidity

Figure. 5.29. *The relation between runner-blade solidity, (a) overall hydraulic efficiency, and (b) normalized shaft power for four flow conditions*

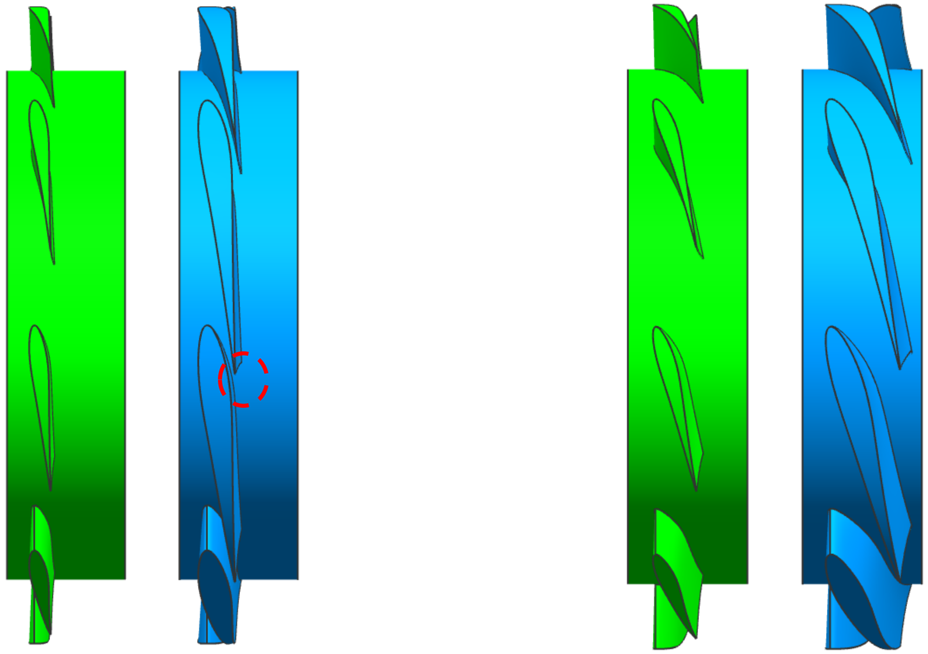

(a). Two runner-blade geometries at low flow rate condition ($Q_{11} = 0.103$) with two blade solidity; Left: $\sigma_R = 0.7$, Right: $\sigma_R = 1.2$.

(b). Two runner-blade geometry at high flow rate condition ($Q_{11} = 0.259$) with two blade solidity; Left: $\sigma_R = 0.7$, Right: $\sigma_R = 1.2$.

Figure. 5.30. *Two runner-blade geometries at two flow rate conditions with two blade solidity values*

Figure 5.31 shows the relative flow angle at runner inlet and outlet for all four selected models (β_2, β_3 in **Fig.2.2**). The results show, expect Model-1's values, and all other three models have very similar $\beta_2,$ and β_3 distribution-trend and the maximum angle difference is around 10° for β_1 and 5° for β_2 compared to the designed value (Except for some points near the tip region).

However, for model-1, the $\beta_2,$ and β_3 values are significantly lower than the designed value, and the maximum difference is around 35° for β_1 and 20° for β_2. **Figure 5.32** shows an example of the streamline pattern comparison of Model-1 and Model-2 at the 50% span location. Model-2's streamline pattern shows good flow attachment near the runner-blade leading and trailing edge; on the contrary, the Model-1's streamline pattern shows flow distortion near the runner-blade leading edge and insufficient flow turning near the trailing edge. Because of the lower blade solidity value, Model-1 has a considerably shorter blade, and this causes a mismatch of the inlet stagnation point and the runner leading-edge, hence cause the flow distortion. Moreover, the shorter blade configuration also causes the misalignment between velocity direction and the blade direction at the runner-blade trailing edge which means poor flow turning performance.

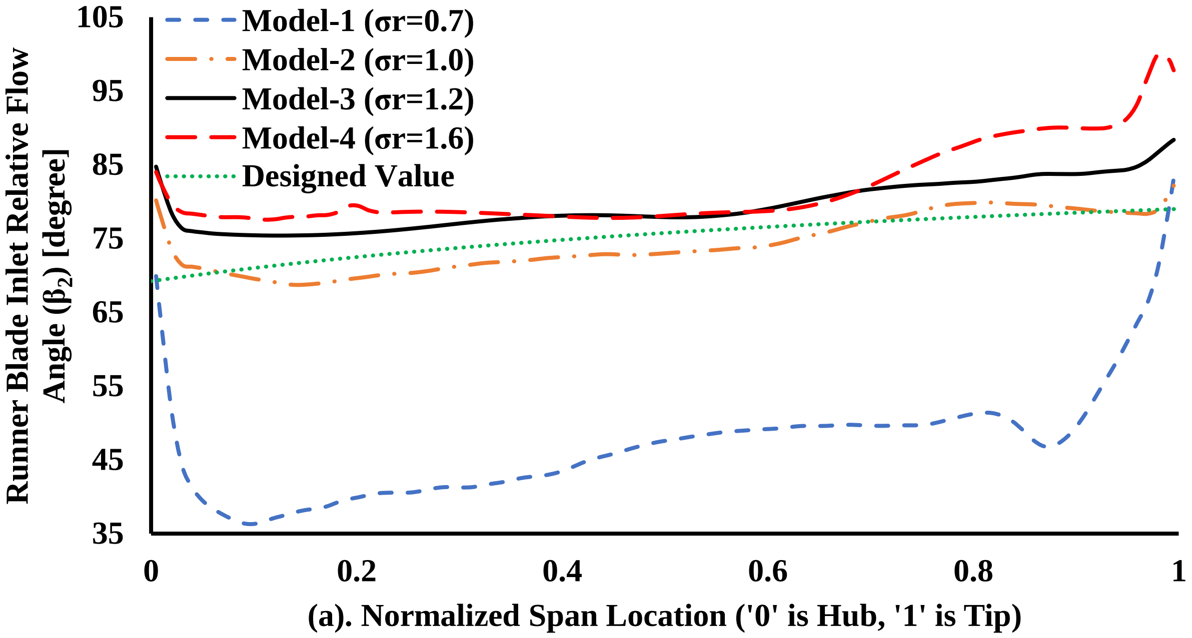

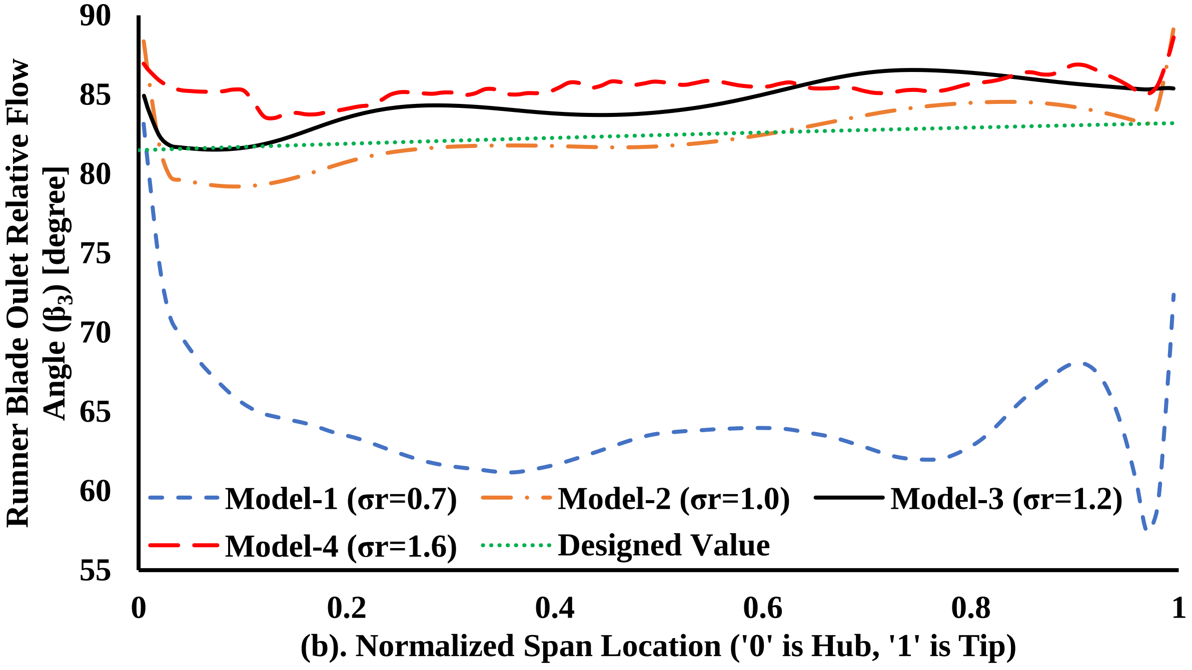

Figure. 5.31. *The relative flow angle at (a). runner inlet (β_2) and (b). runner outlet (β_3) for all four selected models with the comparison of the designed value*

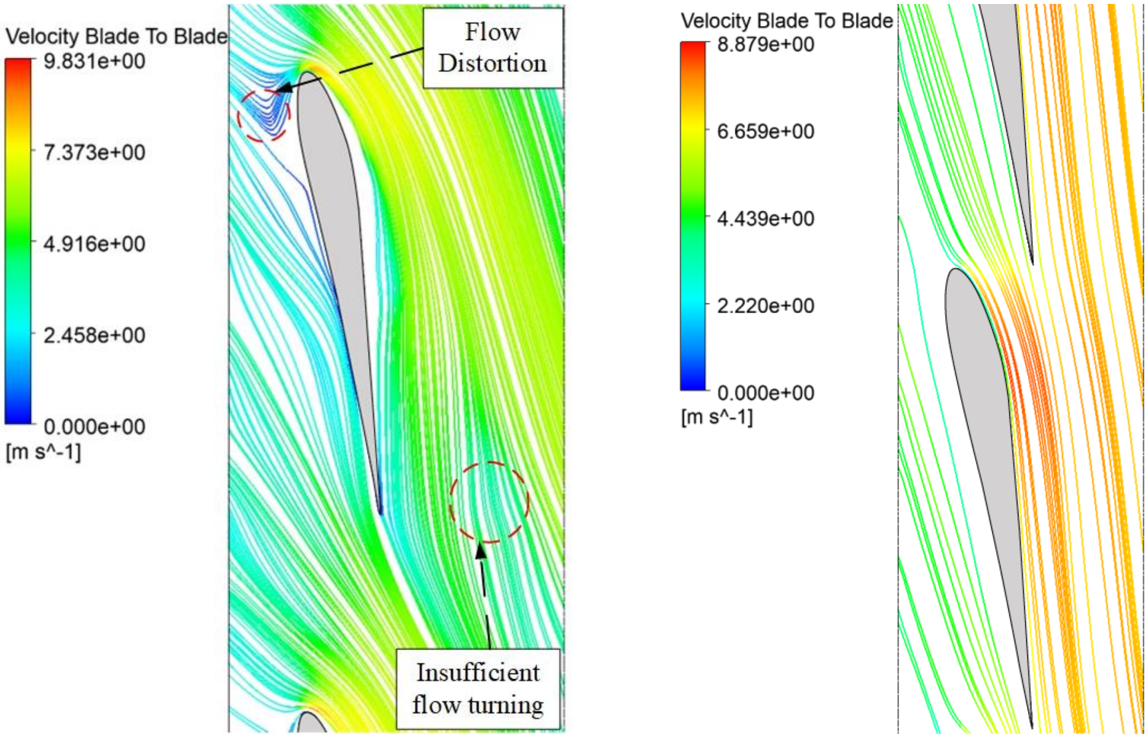

(a). Model-1 ($\sigma_r = 0.7$) at 50% span location *(b). Model-2 ($\sigma_r = 1$) at 50% span location*

Figure. 5.32. *The streamline pattern comparison of (a) Model-1 and (b) Model-2 at the 50% span location*

Figure 5.33 shows the runner-blade circumferential velocity difference ($C_{u2} - C_{u3}$) distribution for all four models. Because of the above-mentioned reasons, the Model-1 has the lowest values across the majority of the span location (Red Arrow in **Fig.5.33**); hence it has the worst performance among all four models. And Model-2 has the largest values across the majority of the span location; hence it has the best performance.

Model-4, which has the largest blade solidity, has the second-worst performance among all four selected models. When the blade is too long, one blade's pressure side can interfere with the adjacent blade's suction side; this interference changes the pressure distribution of the blade. **Figure 5.34** shows the comparison between Model-2 and Model-4's pressure distribution contour at the 50% span location. The red circle indicates the pressure interference, and this pressure interference can be shown more directly in a blade loading plot, as in **Figure 5.35**.

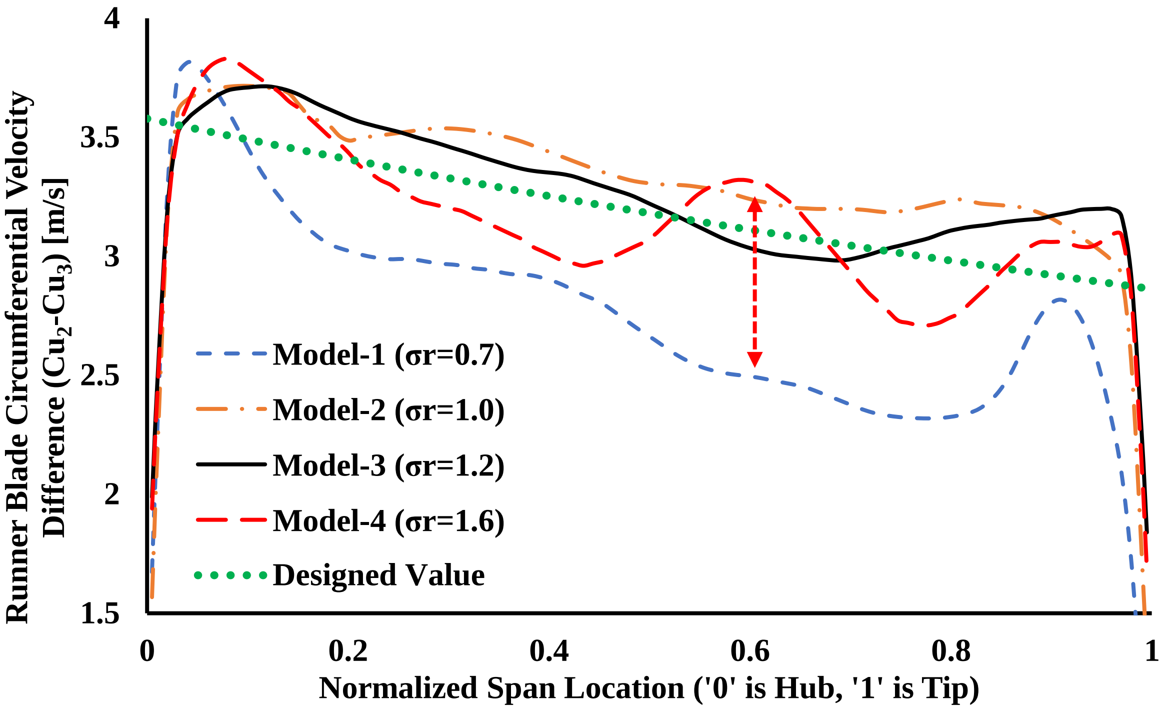

Figure. 5.33. *The runner-blade circumferential velocity difference (C_{u2}-C_{u3}) distribution for all four models*

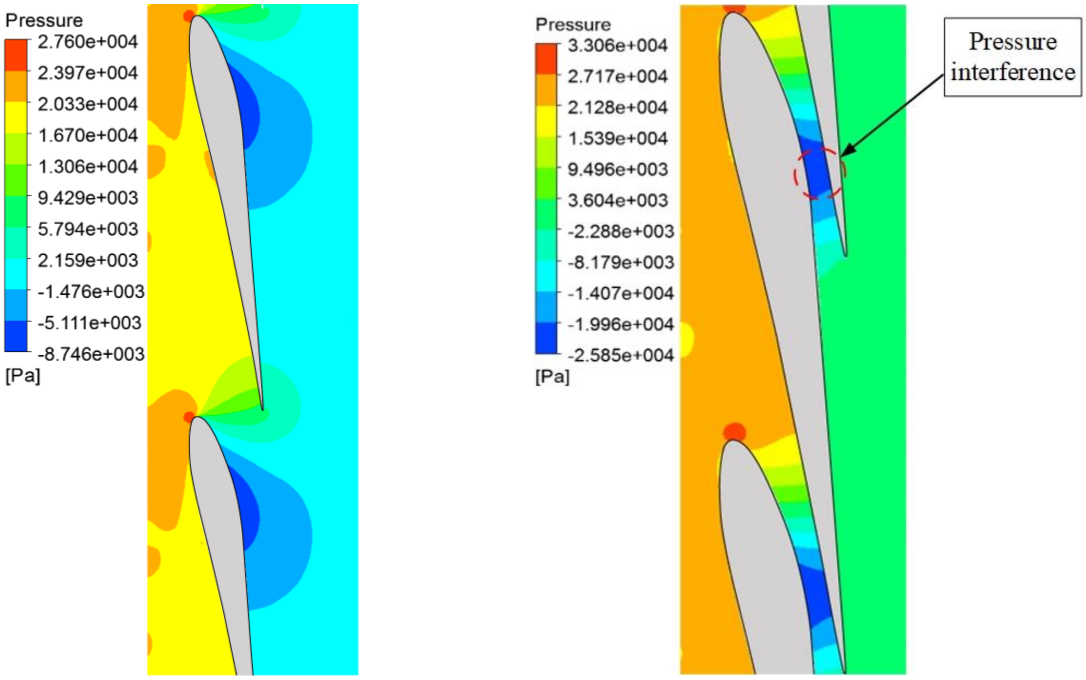

(a). Model-2 pressure distribution

(b). Model-4 pressure distribution

Figure. 5.34. *The comparison between (a). Model-2's and (b). Model-4's pressure distribution contour at the 50% span location*

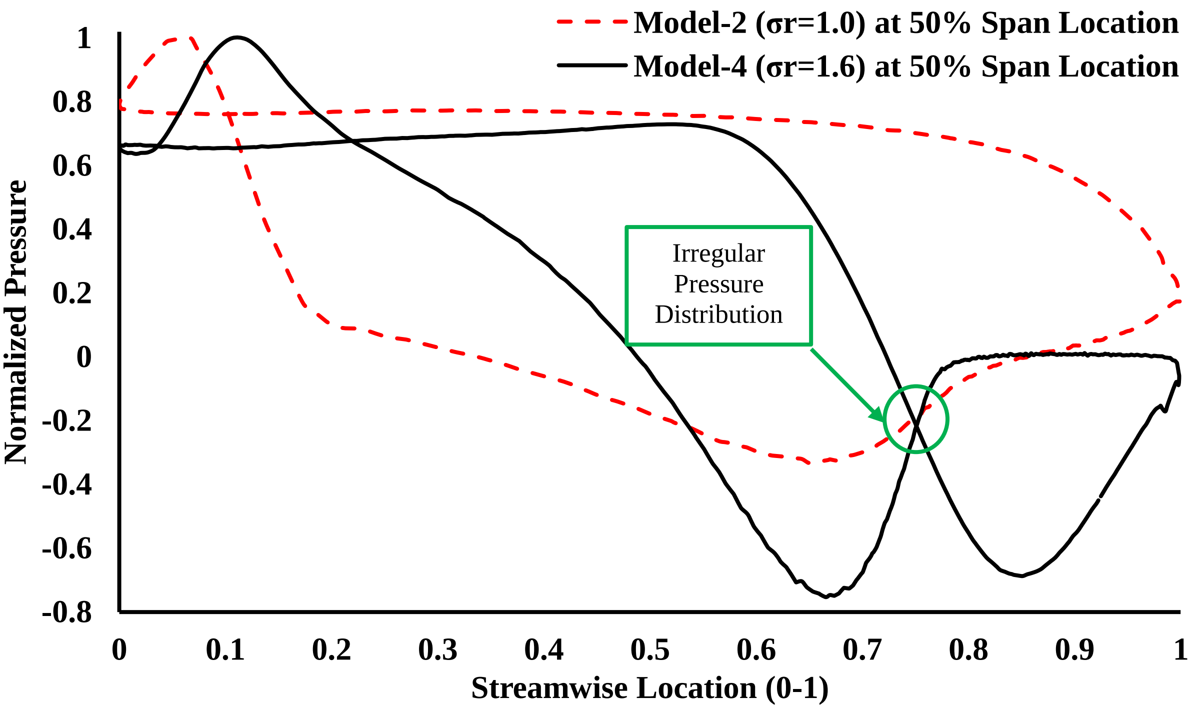

***Figure. 5.35**. Normalized-pressure distribution along the streamwise direction of the runner-blade for Model-2 and Model-4 at 50% span location*

For Model-2, the normalized pressure distribution plot shows a smooth pressure distribution across the pressure and the suction side of the blade; however, for Model-4, the normalized pressure distribution plot shows an irregular distribution trend, especially near the location when streamwise=0.75 (Green Circle in **Fig.5.35**). This irregular distribution leads to a velocity disturbance for Model-4, especially in the radial direction. As discussed in *section 3.2.3*, one of the assumptions for the free vortex is zero radial velocity (C_r) across all span location. **Figure 5.36** shows the radial velocity distribution at runner-blade inlet and outlet for Model-2 and Model-4. The results show that the Model-4's irregular pressure distribution causes a significantly larger radial velocity at the runner inlet and outlet than the Model-1's. This vast velocity difference leads to a strong flow misalignment, thus results in worse performance for the Model-4.

Generally, under the same head condition, the runner-blade solidity can significantly influence the overall velocity triangle for the runner-blade, which affects the overall performance and power production. **Figure 5.37** shows the runner-blade inlet and outlet velocity triangle for the four selected models and the designed values at 50% span location. Some additional results and plots are shown in **Appendix.I**.

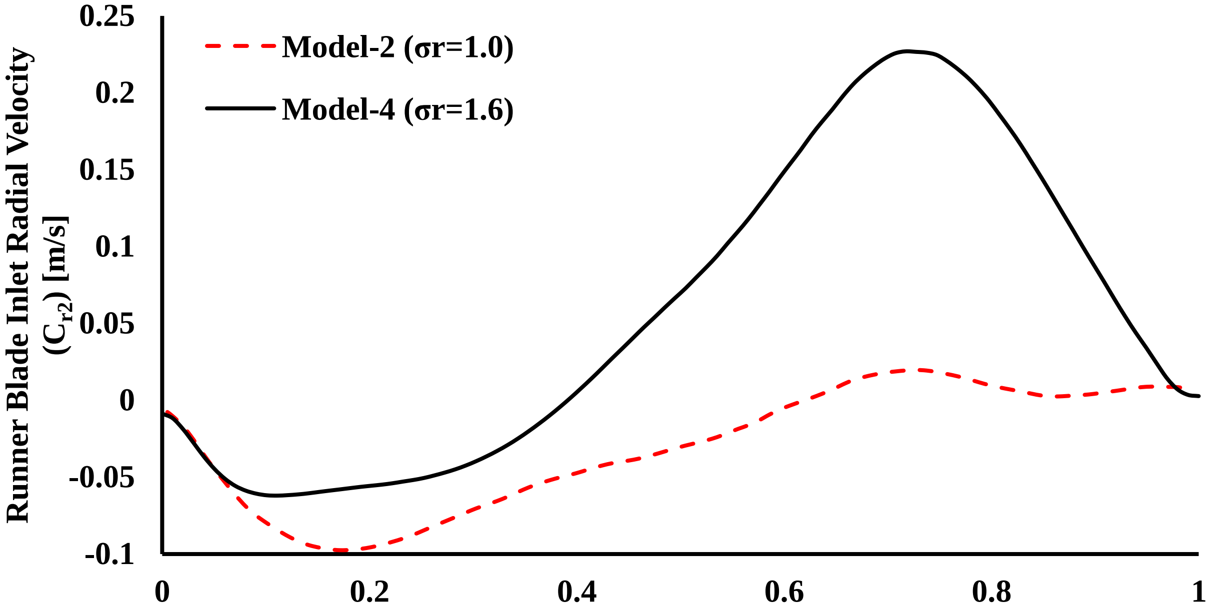

(a). Normalized Span Location ('0' is Hub, '1' is Tip)

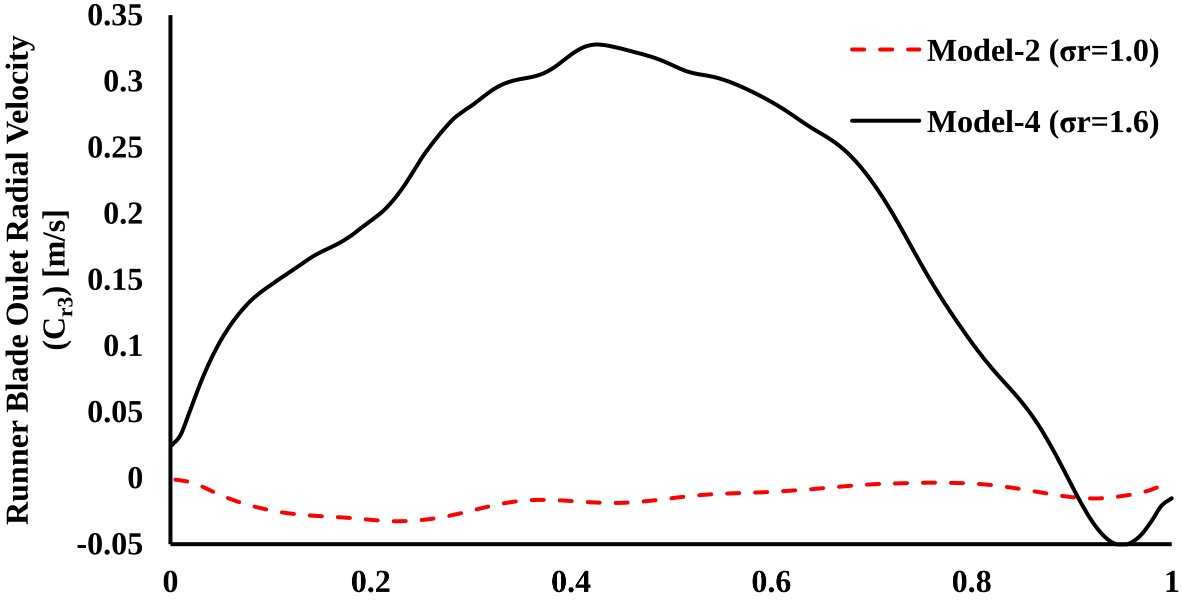

(b). Normalized Span Location ('0' is Hub, '1' is Tip)

Figure. 5.36. *The radial velocity (C_r) distribution at runner-blade (a). Inlet, and (b). Outlet for Model-2 and Model-4*

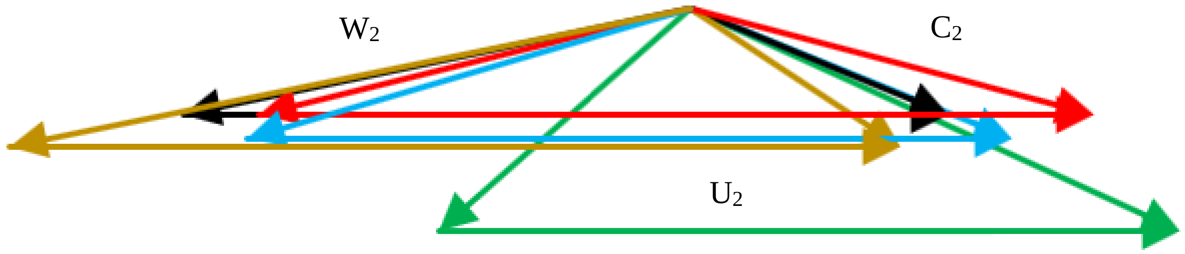

(a) . Runner-blade Inlet Velocity Triangle.

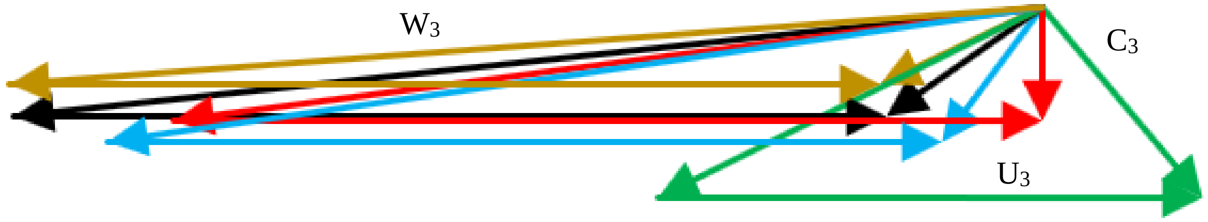

(b) . Runner-blade Outlet Velocity Triangle.

Figure. 5.37. *The runner-blade (a). Inlet, and (b). Outlet velocity triangle for the four selected models and the designed values at 50% span location. [Green Arrow: Model-1; Blue Arrow: Model-2; Black Arrow: Model-3; Gold Arrow: Model-4; Red Arrow: Designed Value]*

5.3.2.3. ***Runner-blade thickness consideration***

As shown in **Fig 3.17**, the runner-blade thickness can hugely impact the geometry of the runner-blade, and this impact is not only important for performance consideration, but also further deformation, stress analysis, and material selection. This section only studies how it influences the overall performance.

For four flow rate conditions, **Fig. 5.38** shows the overall hydraulic performance of the turbine and the normalized shaft power output (The power results were normalized with $R_T = 0.1$ model's results) with the variation in the runner-blade thickness. For all four flow rate conditions, initially, the overall efficiency increases with the increase of the thickness, then reaches an optimum value before decreasing with the increase of the thickness. However, the relative thickness is more influential at a lower flow rate condition. When $Q_{11} = 0.103$, the maximum efficiency difference is around 9%, with a 10% relative thickness increase; on the contrary, when $Q_{11} = 0.259$, the maximum efficiency difference is only around 0.6%, with a 10% relative thickness increase. The logic behind this phenomes are: the overall trend for the average β_2 (runner-blade inlet angle, in **Fig.2.2**) decreases with the increase of the flow rate based on the proposed design method, and according to the **Eqn 3-35**, a higher β_2 means lower $cos\beta_2$ value and a higher Γ_{RM} (runner-blade maximum-blockage ratio), this will increase the blockage loss by changing the overall flow behavior for lower flow rate conditions, hence cause the vast efficiency influence shown in **Fig.5.38**, and **Fig. 5.39** shows how mean Γ_{RM} change with the runner-blade relative thickness for the four flow rate conditions.

Moreover, for all four flow rate conditions, the power decrease with the increase of the runner-blade thickness. At the lowest flow rate condition ($Q_{11} = 0.103$), the maximum difference is around 47% with a 10% relative thickness increase; at the highest flow rate condition ($Q_{11} = 0.103$), the maximum difference is around 13%, with a 10% relative thickness increase. **Figure. 5.40** shows the overall hydraulic performance of the turbine and the normalized shaft power output with the variation in the mean runner-blade maximum-blockage Γ_{RM}.

For a better understanding, three models were selected (Red squares in **Fig.5.38**) for the lowest flow rate condition. **Figure.5.41** shows the runner-blade inlet absolute flow angle (α_2), and the runner-blade inlet relative flow angle (β_2). The results show that, with the increase in the runner-blade relative thickness, there is a significant α_2 decrease, especially in the close to tip region (Red Arrow in **Fig.5.41-a**). As discussed before, lower α_2 value can dramatically impact the overall performance. **Figure.5.42** shows the axial velocity (C_{x2}), and radial velocity (C_{r2}) distribution for the three selected models at the runner-blade inlet. The results indicate that the C_{x2} drops significantly near the tip for larger thickness models; also, the C_{r2} increases significantly toward the tip region for the larger thickness model.

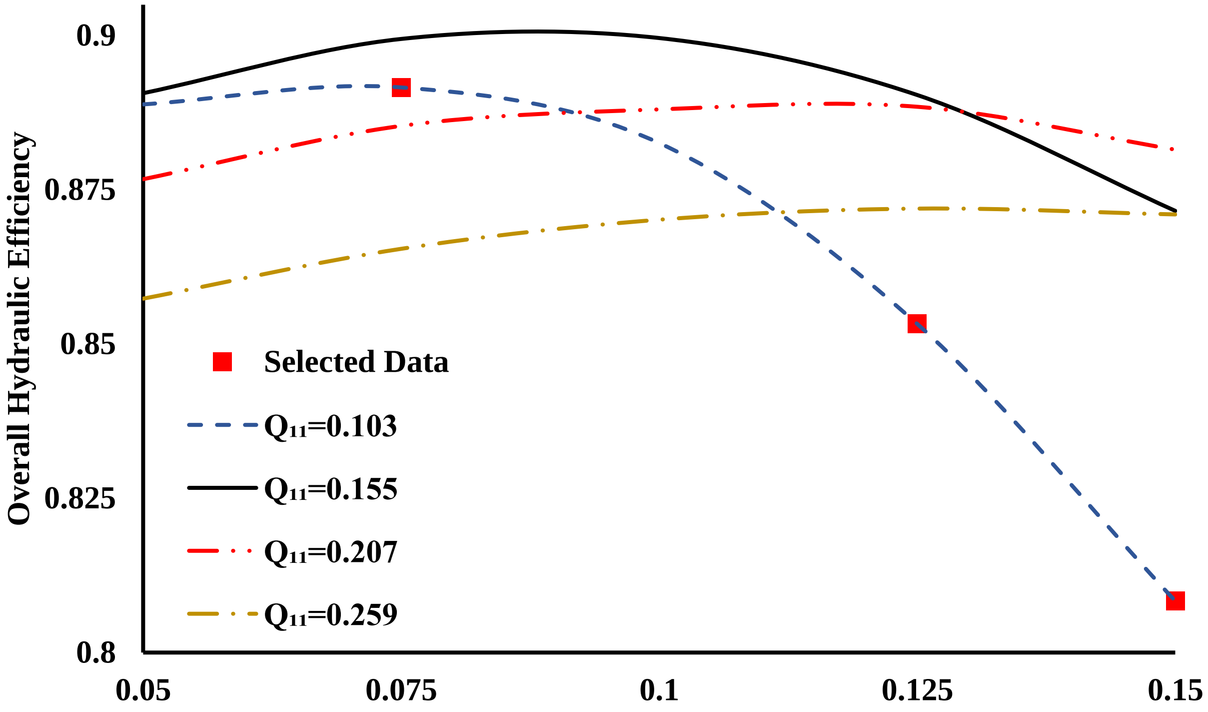

(a). Ruuner Blade Relative Thickness (R_t)

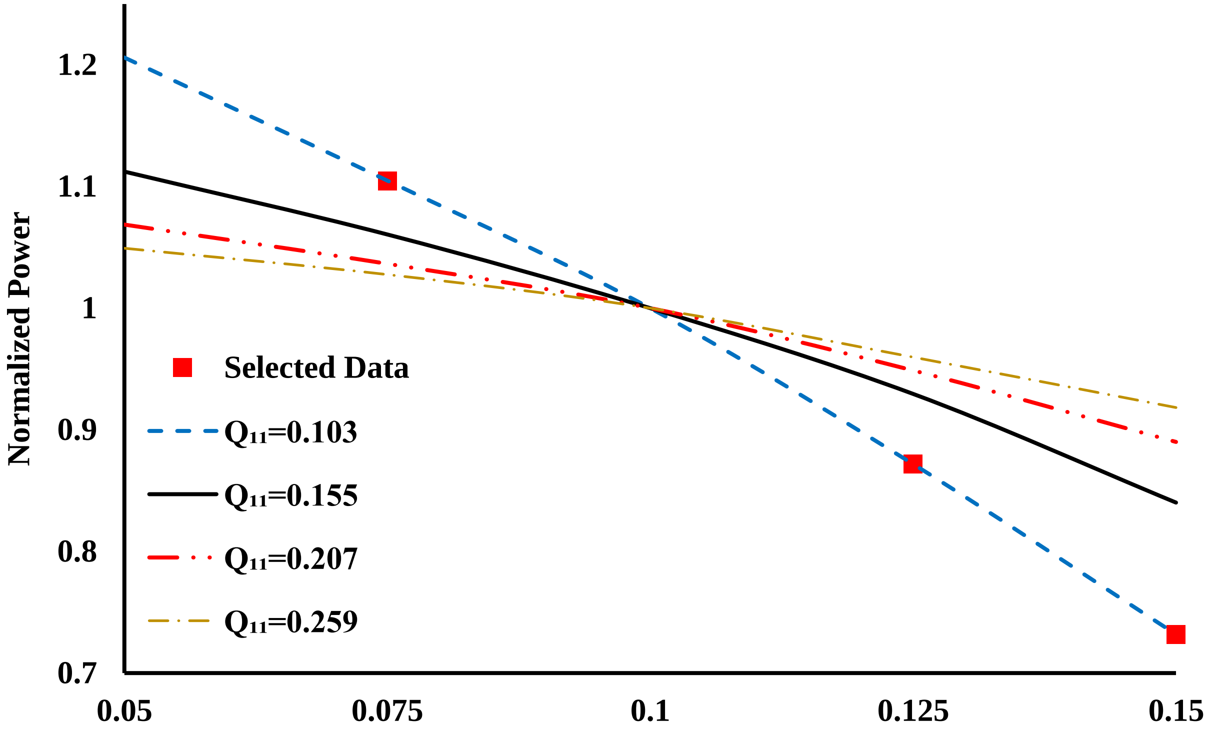

(b). Ruuner Blade Relative Thickness (R_t)

Figure. 5.38. *The relation between runner-blade relative thickness with (a). Overall hydraulic efficiency and (b). Normalized shaft power for four designed flow rate conditions*

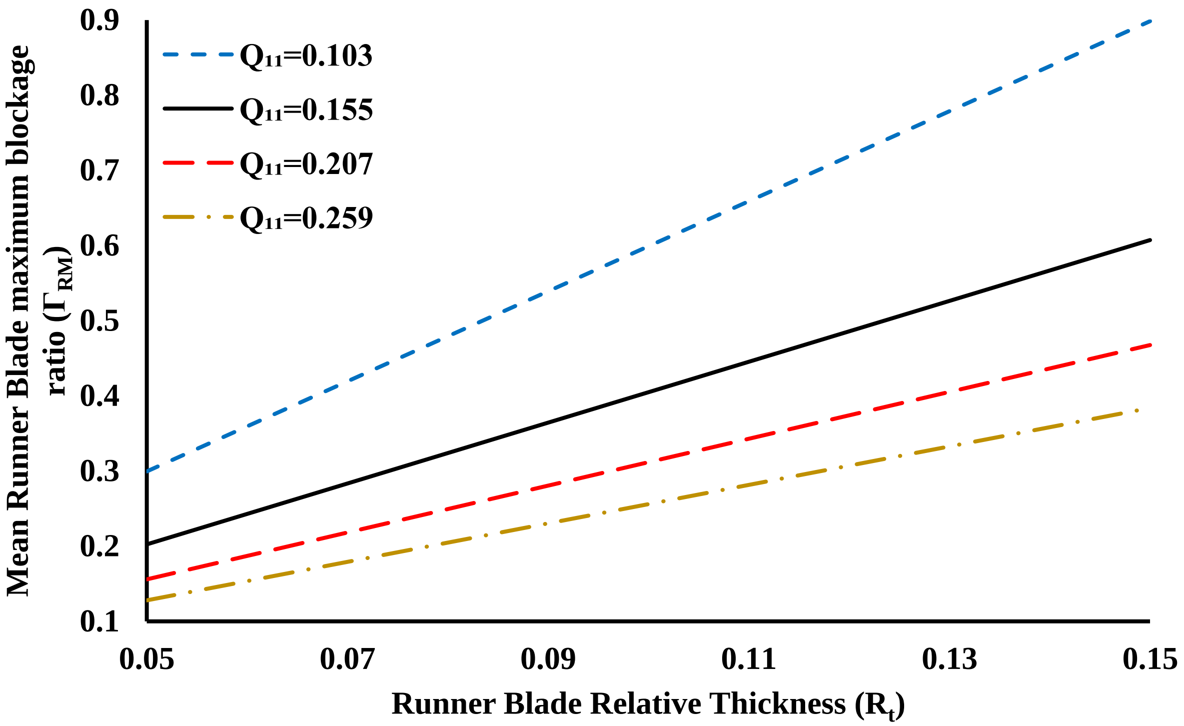

Figure. 5.39. *The relation between runner-blade relative thickness and runner-blade maximum-blockage ratio for four flow conditions*

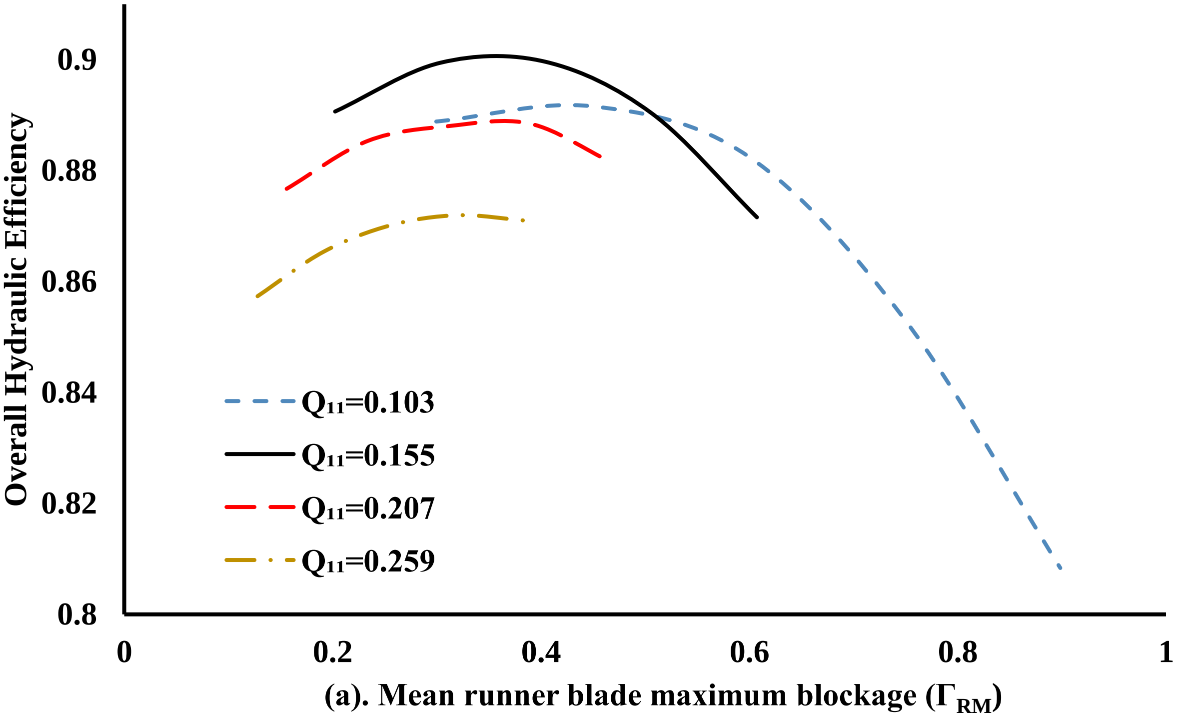

Figure. 5.40. *The relation between mean runner-blade maximum-blockage ratio with (a). Overall hydraulic efficiency and (b). Normalized shaft power for four designed flow rate conditions.*

Figure.5.40 (Cont'd)

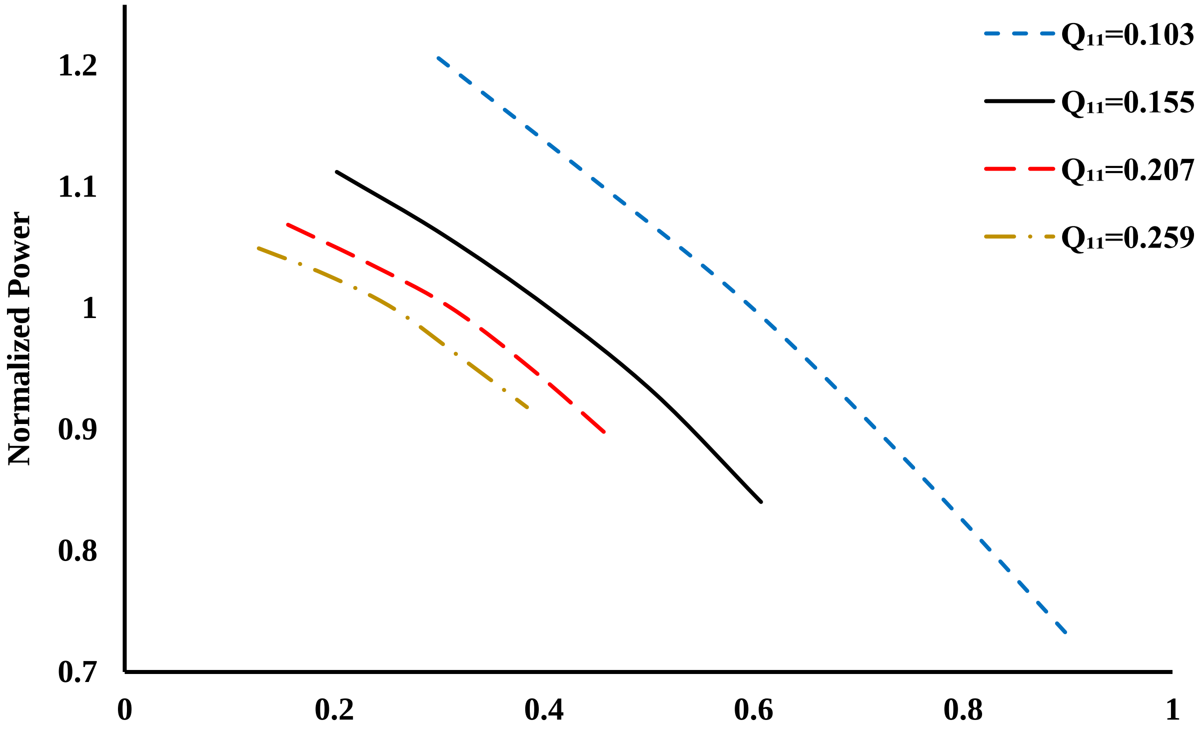

(b). Mean runner blade maximum blockage (Γ_{RM})

Although the **Fig.5.39 and Fig.5.40** shows the mean runner-blade maximum-blockage for all three models, and this mean value use the mean span values; however, since near tip the local β_2 value is larger, which causes a larger local blockage near the tip region. This effect is more noticeable at lower flow rate condition, and **Fig.5.43** shows the overall Γ_{RM} distribution from tip to hub for the four flow rate conditions at 10% relative thickness settings. At a lower flow rate condition, near the tip, the blockage ratio becomes noticeably larger. This large blockage can reduce the axial velocity, and increase the radial velocity which causes a lower α_2 value, and overall performance.

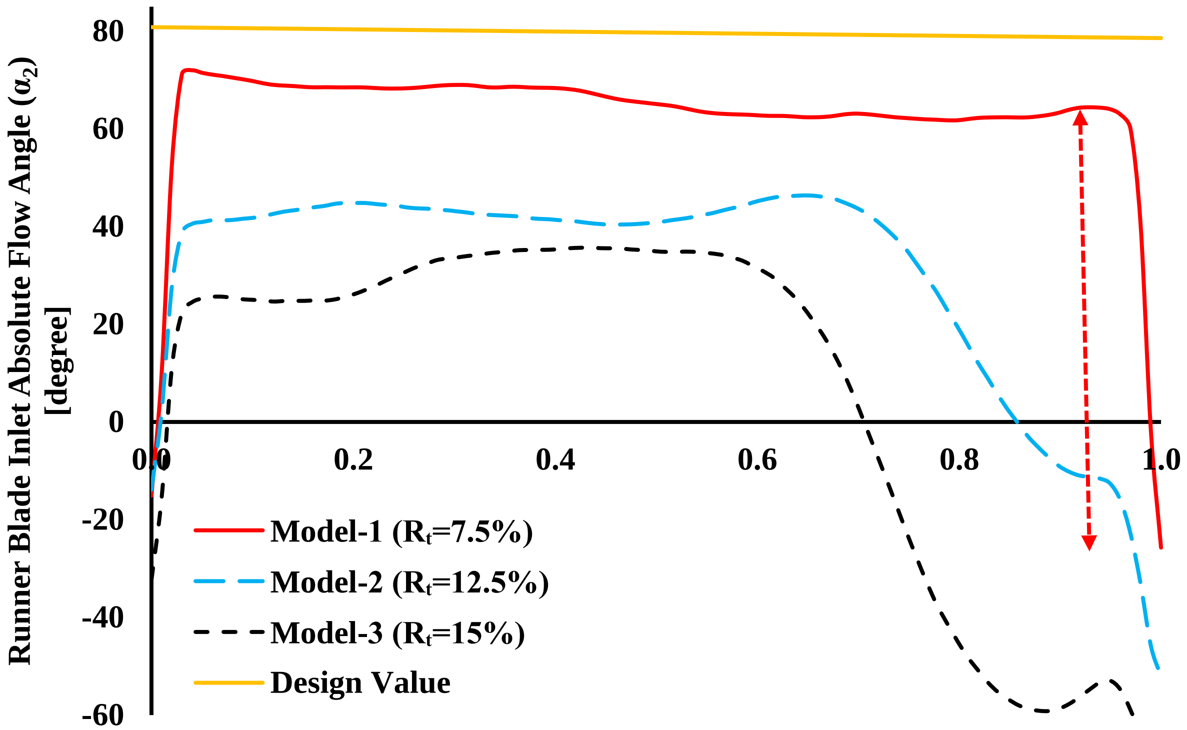

(a). Normalized Span Location ('0' is Hub, '1' is Tip)

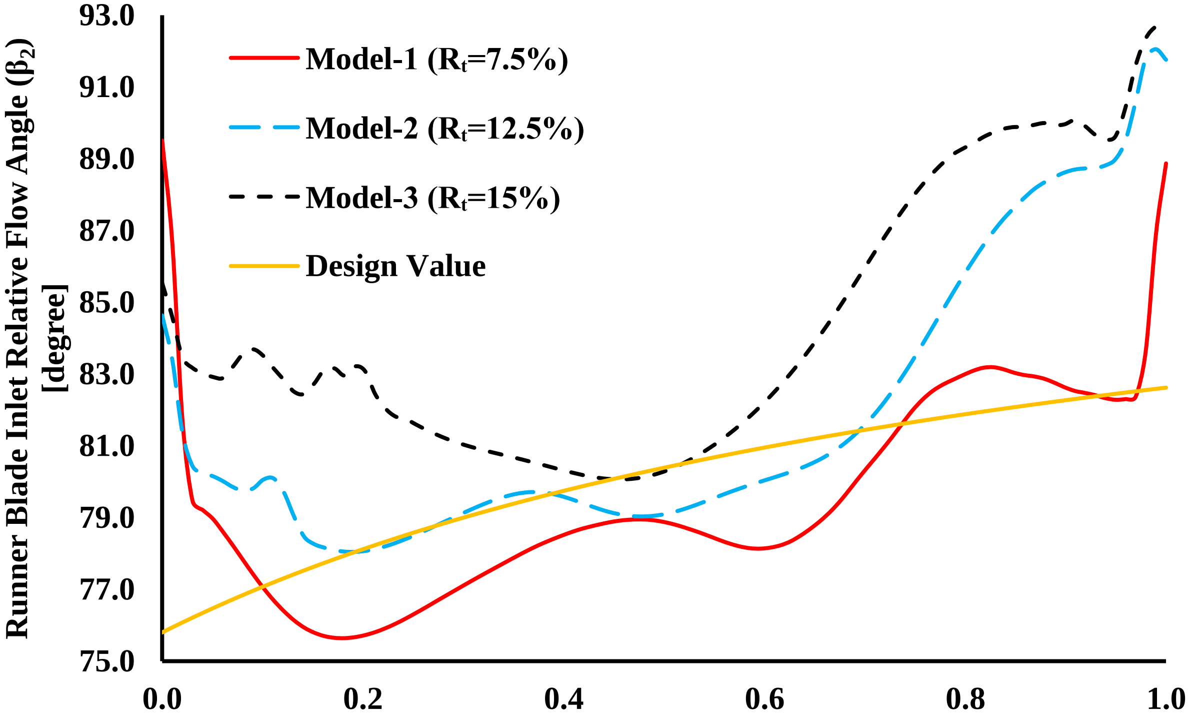

(b). Normalized Span Location ('0' is Hub, '1' is Tip)

Figure. 5.41. *(a). Runner-blade inlet absolute flow angle (α_2) and (b). runner-blade inlet relative flow angle (β_2) distribution across all span locations for the three selected models.*

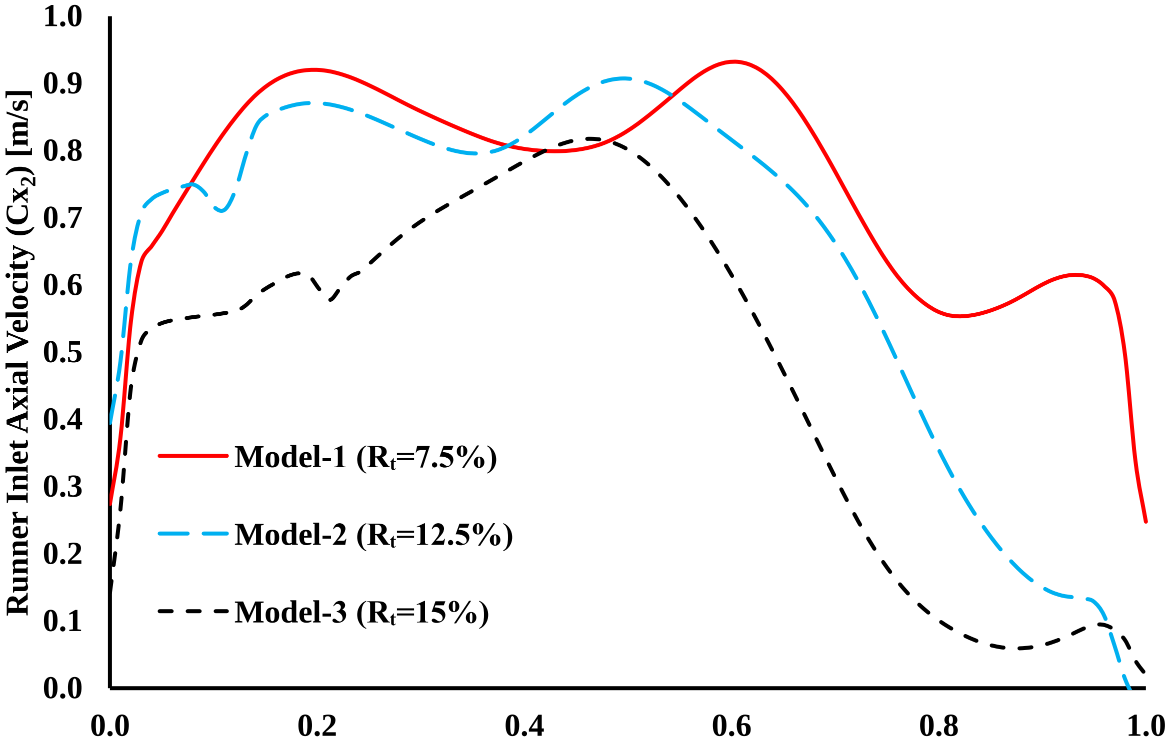

(a). Normalized Span Location ('0' is Hub, '1' is Tip)

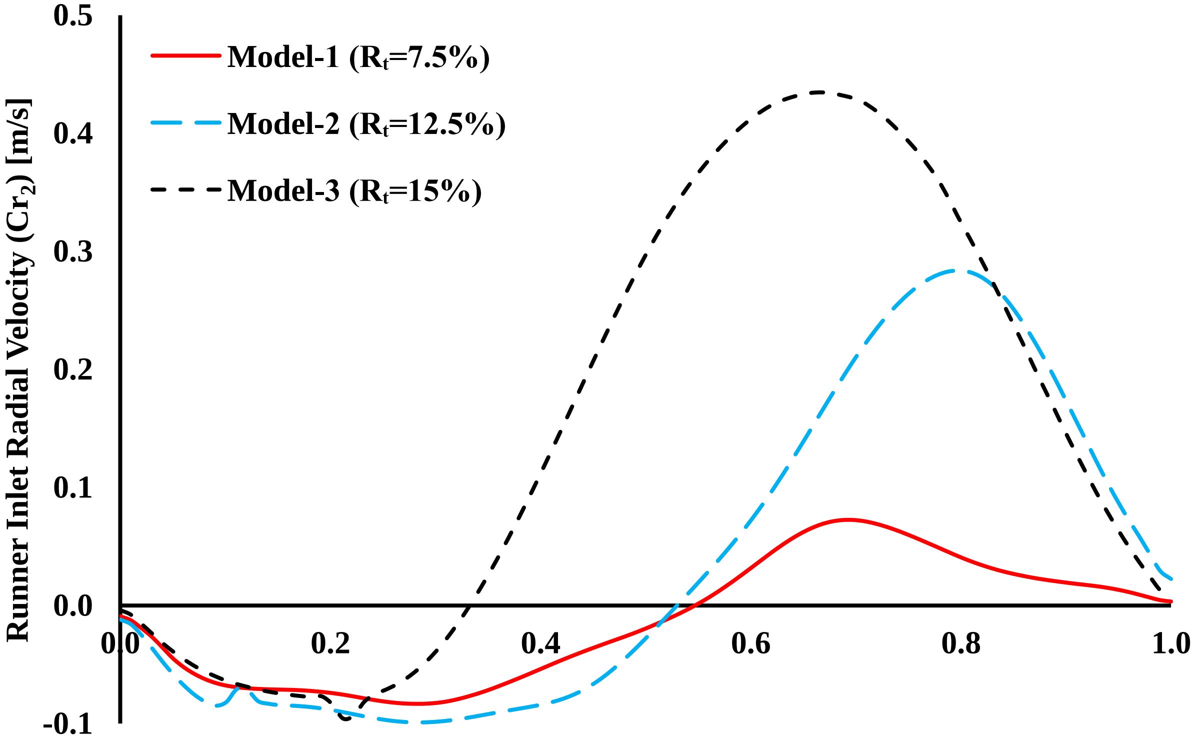

(b). Normalized Span Location ('0' is Hub, '1' is Tip)

Figure. 5.42. *(a). The runner-blade inlet axial velocity (C_{x2}), and (b).The runner-blade inlet radial velocity (C_{r2}) distribution across all span locations for the three selected models*

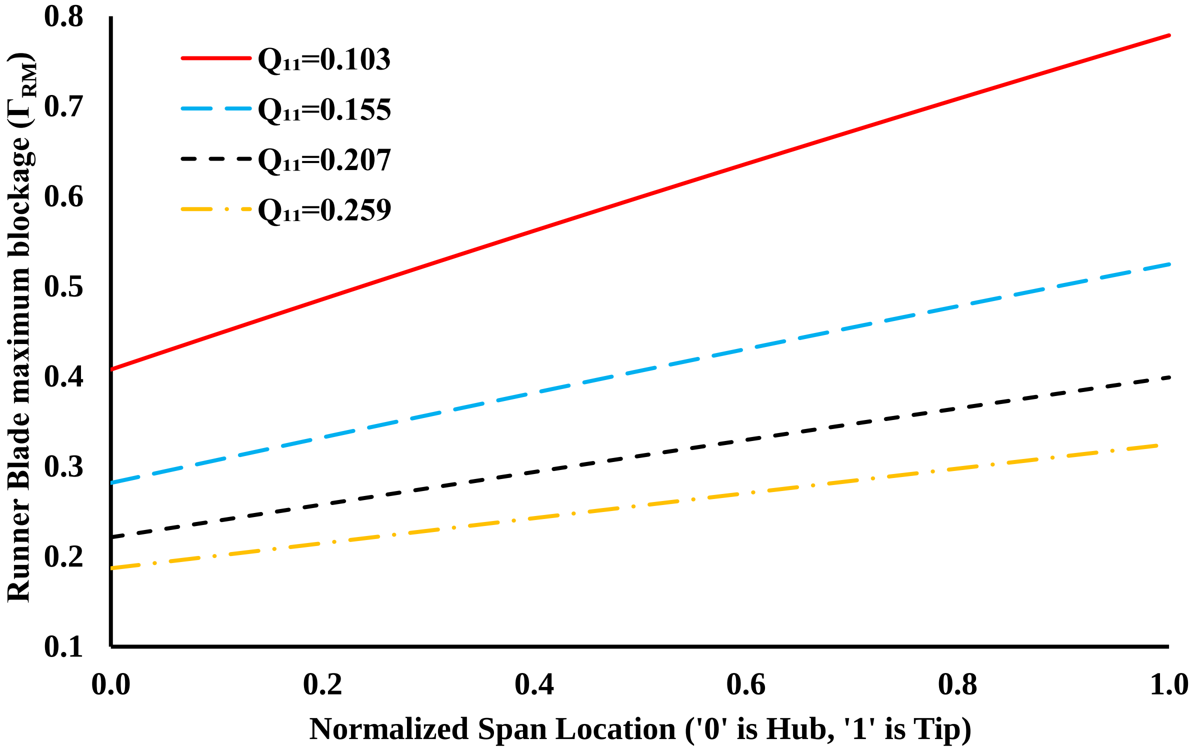

Figure. 5.43. *The Γ_{RM} distribution from tip to hub for the four flow rate conditions at 10% relative thickness settings*

Additionally, the small runner-blade thickness can improve the overall performance and power generation for the larger solidity condition. **Figure.5.44** shows the relation between overall performance, normalized power (The power results were normalized with $R_T = 0.1$ and $\sigma_r = 1$ model's results), and the runner-blade solidity with three different runner-blade thickness values under one selected flow rate condition ($Q_{11} = 0.207$), and **Fig.5.45** shows the same results but in terms of the mean runner blockage ratio.

The results show that, at lower solidity value, larger blade thickness has a better overall performance and power generation, the optimum solidity value for all three thickness conditions is around 1~1.1. However, with the increase of the runner-blade solidity, the lower thickness models show a significant performance and power generation advantage (Red Arrow in **Fig.5.44-a**); the maximum efficiency and power difference is around 20% and 50%, respectively. For better understanding, two pair models were selected: lower runner-blade solidity models (Green Dots in **Fig. 5.44**), higher runner-blade solidity models (Red Squares in **Fig. 5.44**). **Figure.5.46** shows the streamline pattern for the selected Models-II (Low solidity) at three different span locations (10%, 50%, and 90%).

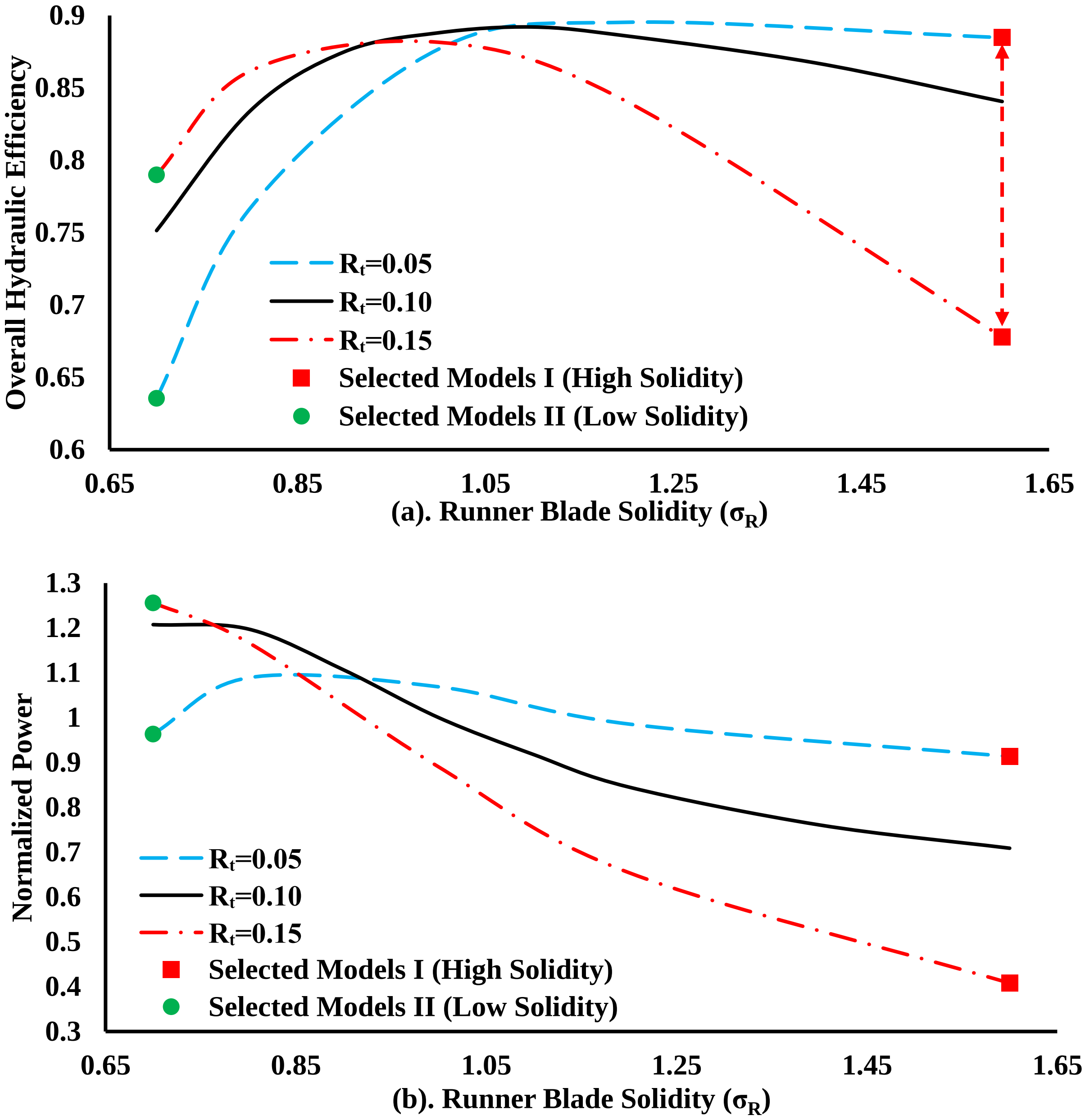

Figure. 5.44. *The relation between runner-blade solidity with (a). Overall hydraulic efficiency and (b). Normalized shaft power for three runner-blade thickness conditions at one flow rate condition (Q_{11}=0.207)*

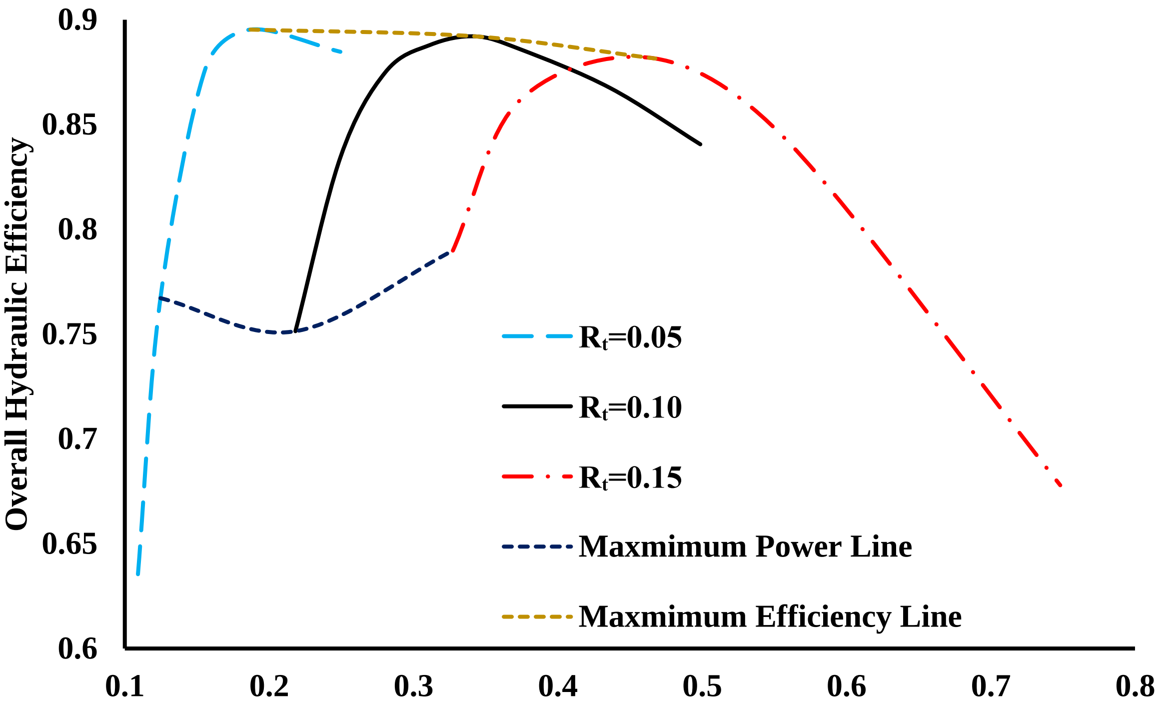

(a). Mean runner blade maximum blockage (Γ_{RM})

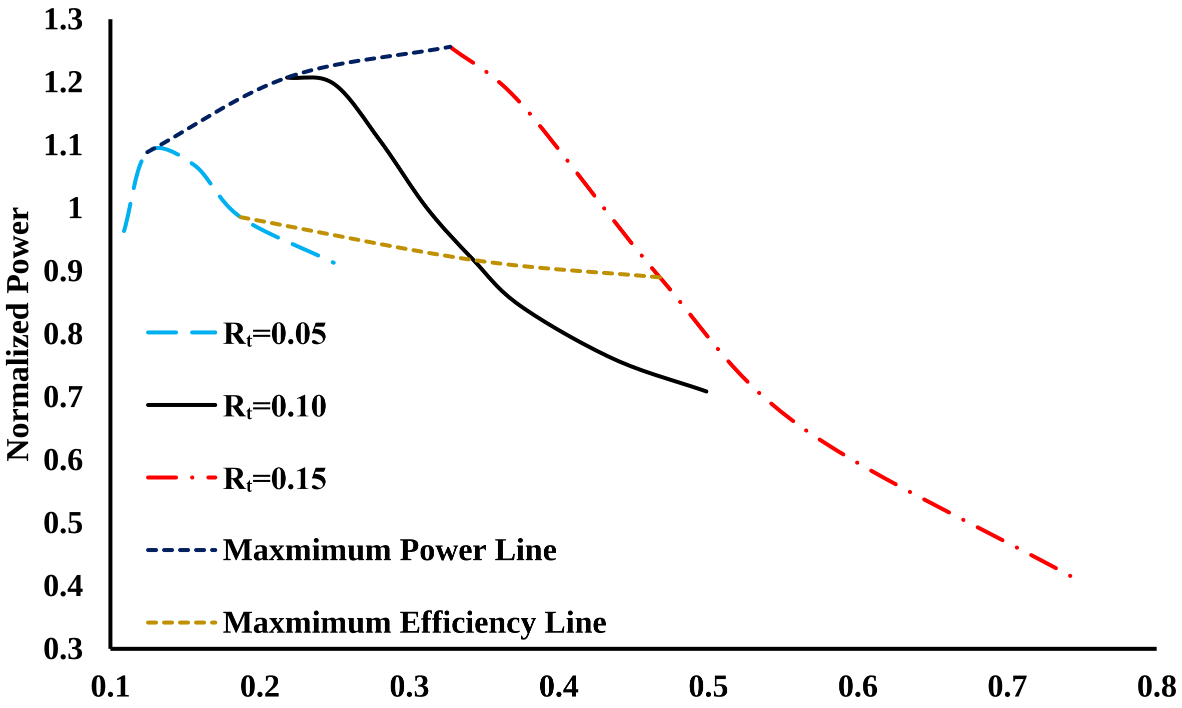

(b). Mean runner blade maximum blockage (Γ_{RM})

Figure. 5.45. *The relation between the mean runner-blade blockage ratio (Γ_{RM}) with (a). Overall hydraulic efficiency and (b). Normalized shaft power for three runner-blade thickness conditions at one flow rate condition (Q_{11}=0.207)*

All those plots show that, although both low and high runner-blade thickness models have flow distortion near the leading edge for all selected span locations (Red circle in **Fig.5.46**), the low runner-blade thickness models have a sever flow separation on the suction side of the blade, especially approaching to the tip region (Black circle in **Fig.5.46**), which do not present in large thickness models. This sever separation is the main reason, at lower solidity condition, the smaller thickness models have a significantly lower performance.

Figure.5.47 shows the pressure distribution for the Selected Models-I (High solidity) at three different span locations (10%, 50%, and 90%). The plots show that a larger blade solidity model but with smaller thickness has an overall better pressure distribution pattern in both suction side and pressure side of the blade; on the contrary, the one with larger thickness has severe pressure interference between adjacent blades which is similar with **Fig.5.34**.

Figure.5.48 shows the normalized pressure distribution plot for selected Models-I at the 50% span location. The plot shows both models have a pressure interference (Red Circles in **Fig.5.47,** green circles in **Fig.5.48**); for the smaller thickness model, this interference happens around 87% streamwise location and only decrease the pressure on the pressure side surface by a small amount (Blue arrow in **Fig.5.48**). However larger blade thickness model shows a more profound influence, because of the larger blockage ratio, there is a steep drop of pressure on the suction side of the blade, then the presence of the adjacent blade's pressure side causes an interference near 75% streamwise location which induces a significant pressure dropping on the pressure side surface and lead to a significant pressure rise on the suction side surface (Red arrow in **Fig.5.48**). This severe pressure interference (or alternation) is the main reason for the lower performance and power of the larger thickness model at larger solidity conditions. Some additional results and plots are shown in **Appendix.J**.

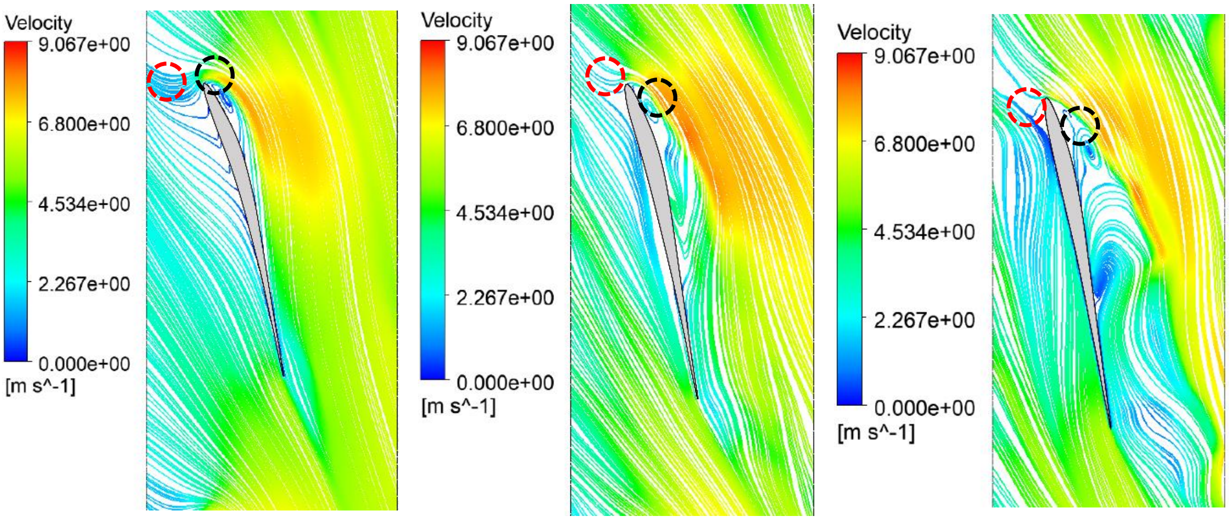

(a). Streamline pattern at 10% span location, $\sigma_r = 0.7, R_T = 0.05.$

(b). Streamline pattern at 50% span location, $\sigma_r = 0.7, R_T = 0.05.$

(c). Streamline pattern at 90% span location, $\sigma_r = 0.7, R_T = 0.05.$

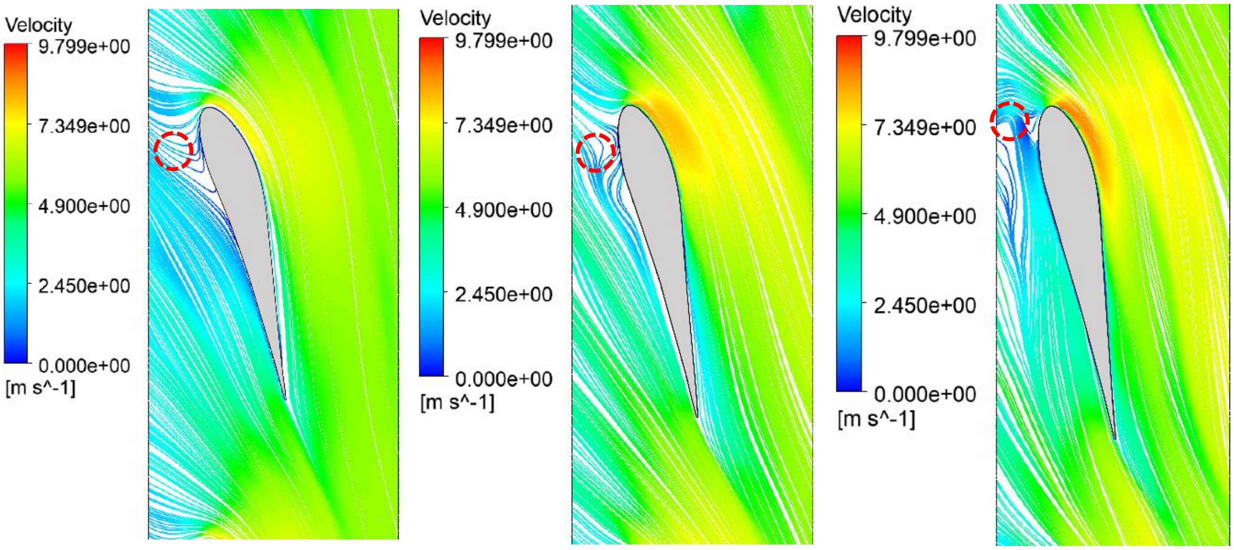

(d). Streamline pattern at 10% span location, $\sigma_r = 0.7, R_T = 0.15.$

(e). Streamline pattern at 50% span location, $\sigma_r = 0.7, R_T = 0.15.$

(f). Streamline pattern at 90% span location, $\sigma_r = 0.7, R_T = 0.15.$

Figure. 5.46. *Streamline pattern for the Selected Models-II (Low solidity) at three different span locations, (a)-(c): Small runner-blade thickness,* $R_{T=}0.05$*; (d)-(e): Large runner-blade thickness,* $R_T=0.15$

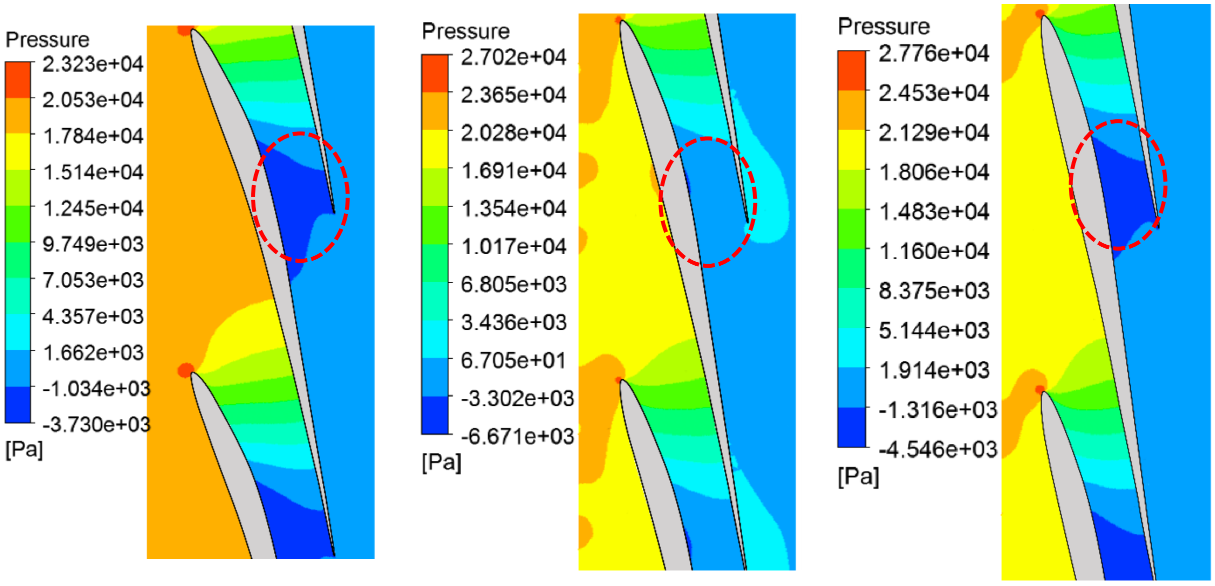

(a). Pressure Distribution at 10% span location, $\sigma_r = 1.6, R_T = 0.05.$

(b). Pressure Distribution at 50% span location, $\sigma_r = 1.6, R_T = 0.05.$

(c). Pressure Distribution at 90% span location, $\sigma_r = 1.6, R_T = 0.05.$

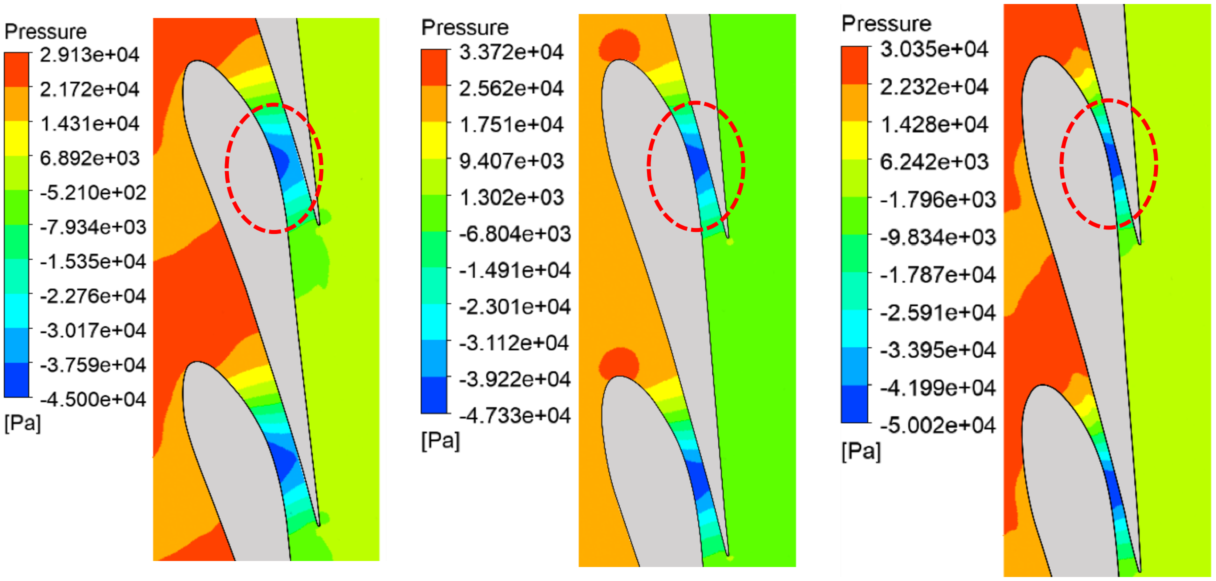

(a). Pressure Distribution at 10% span location, $\sigma_r = 1.6, R_T = 0.15.$

(b). Pressure Distribution at 50% span location, $\sigma_r = 1.6, R_T = 0.15.$

(c). Pressure Distribution at 90% span location, $\sigma_r = 1.6, R_T = 0.15.$

Figure. 5.47. *Pressure Distribution Pattern for the Selected Models I (High solidity) at three different span locations, (a)-(c): Small runner-blade thickness,* R_T*=0.05 ; (d)-(e): Large runner-blade thickness,* R_T*=0.15*

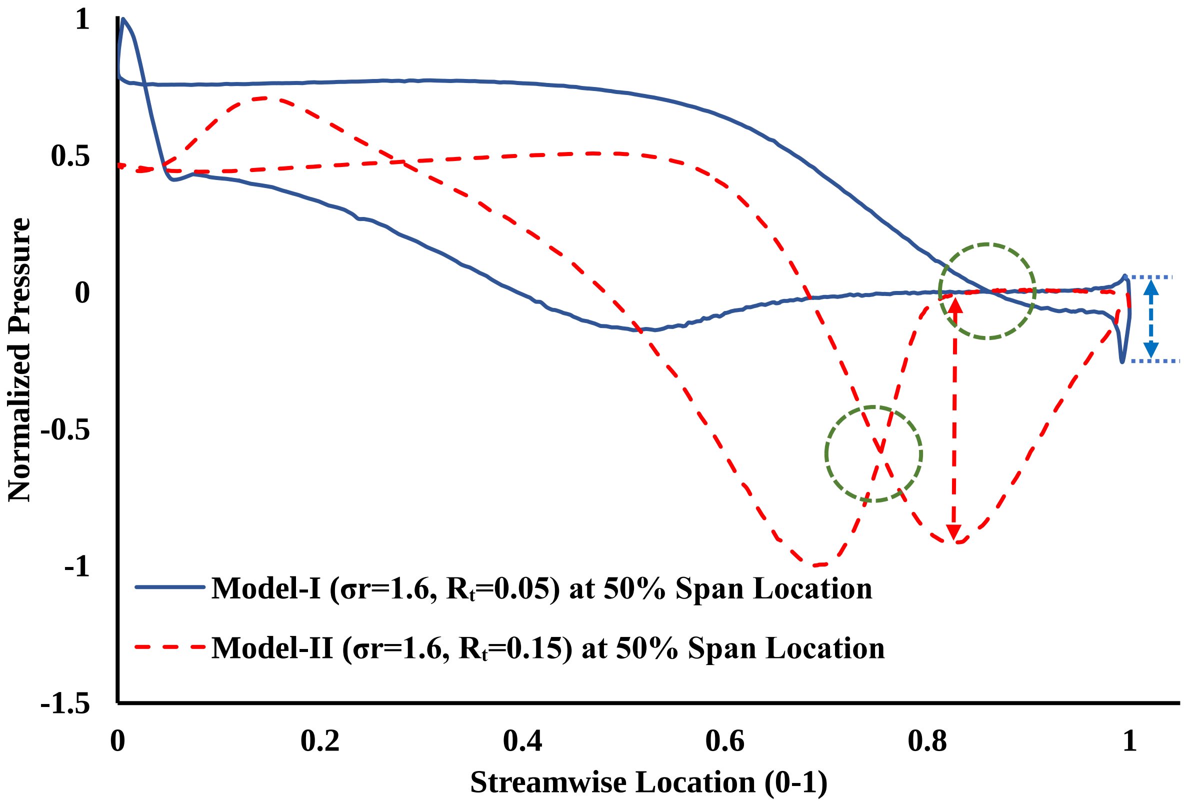

Figure. 5.48. *Normalized Pressure distribution along the streamwise direction of the runner-blade for the selected Models I (High solidity) at 50% span location*

5.4. Off-design consideration

As mentioned in *section 1.3.1*, an essential characteristic of the new stream-reach site is its high variability in flow and head. This high variability means any turbine system proposed for the SMH resource has to equip with different regulation methods. Conventionally, there are three major regulation methods for a Kaplan turbine system: variable stator pitch, variable runner pitch, variable rotational speed. The variable stator pitch method is normally equipped by some large Kaplan turbine system, which has less stator number (**see in Fig.1.10**). Since the proposed system has more stator number, the stator regulation method can significantly increase the complexity of the system and is not utilized in the proposed system. Variable runner pitch and variable rotational speed are the two major methods for the proposed system.

This section focuses on how different runner-blade geometrical configurations affect the overall off-design performance under the variable runner-blade pitch and variable rotation speed condition. One design point was chosen as the base condition, and three different geometrical parameters were studied: Runner-blade thickness, Runner-blade solidity, and Runner-blade number. ***Table. 5.1*** shows the base design-condition and all four models' geometrical configurations. For all four models, three rotational speeds were numerical tested, Ω=30Rpm, Ω =40Rpm (designed condition), and Ω =50Rpm; together with seven head conditions, H=1.5m, H=2.0m, H=2.5m (designed condition), H=3.0m, H=3.5m, H=7.5m, H=10m; and with nine different runner-blade pitch angles between 8° and 32°. All those data were used to construct the performance map, and **Fig.5.49-5.51** shows the Q_{11} and N_{11} based performance map with the blade opening angle line for all four models under three different rotational speed conditions.

Table.5.1. *The design conditions and geometrical configurations for four selected models*

General Design Point Conditions				
Designed Head (H)	2.5m			
Designed unit flow rate (Q_{11})	0.22			
Designed rotational speed (N_{11})	88.543			
Designed runner-blade pitch angle at the hub location (μ_r)	16°			
Designed Power Output (P)	83kw			
Four selected models' runner-blade configuration				
	Model-1	Model-2	Model-3	Model-4
Runner-blade Number	8	8	8	6
Runner-blade Relative Thickness	0.1	0.1	0.075	0.1
Runner-blade Solidity	1	1.1	1	1

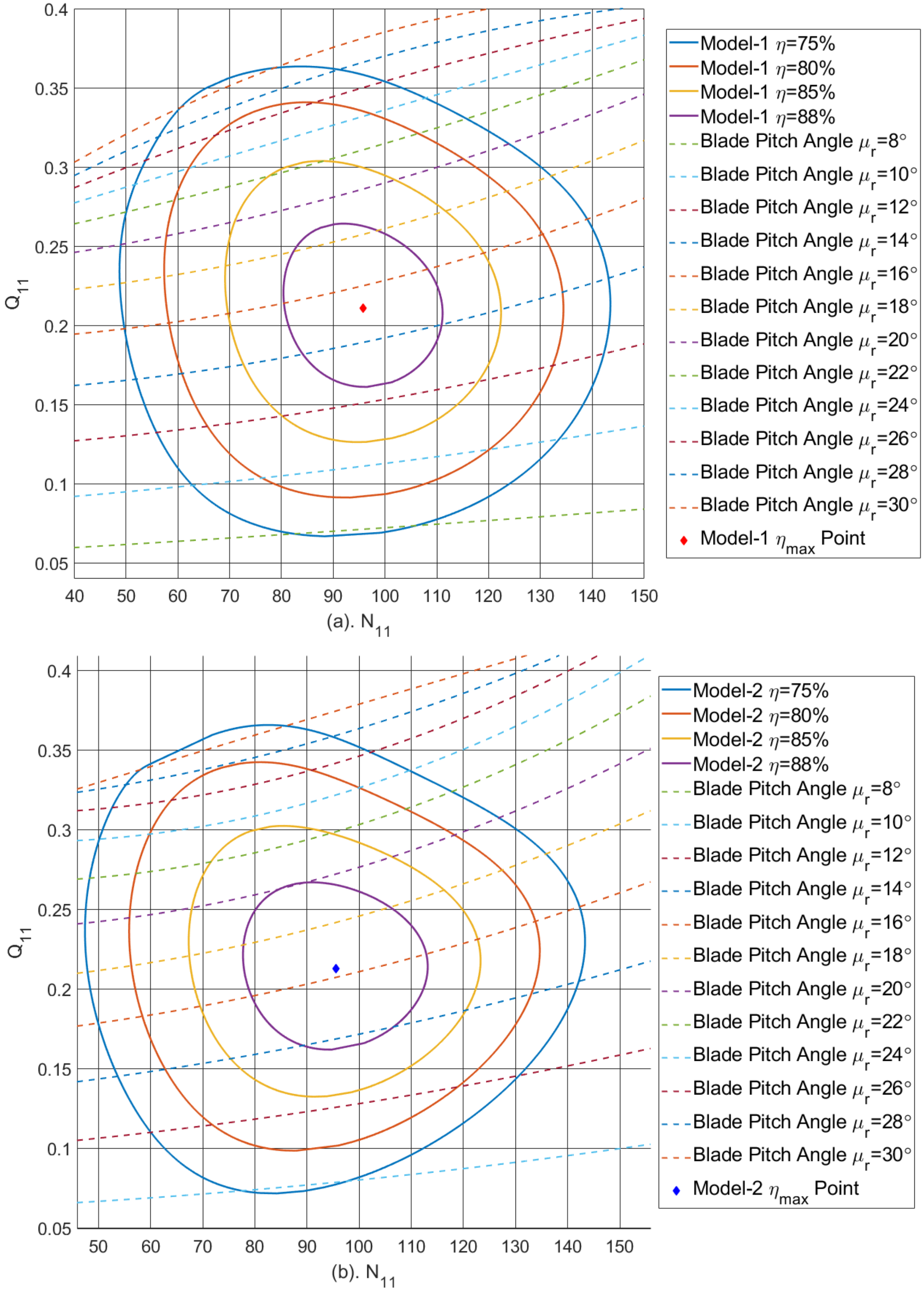

Figure. 5.49. *N_{11} and Q_{11} based performance map at the design rotational speed (Ω=40Rpm) for four selected models, (a). Model-1; (b). Model-2; (c). Model-3; (d). Model-4*

Figure. 5.49 *(Cont'd)*

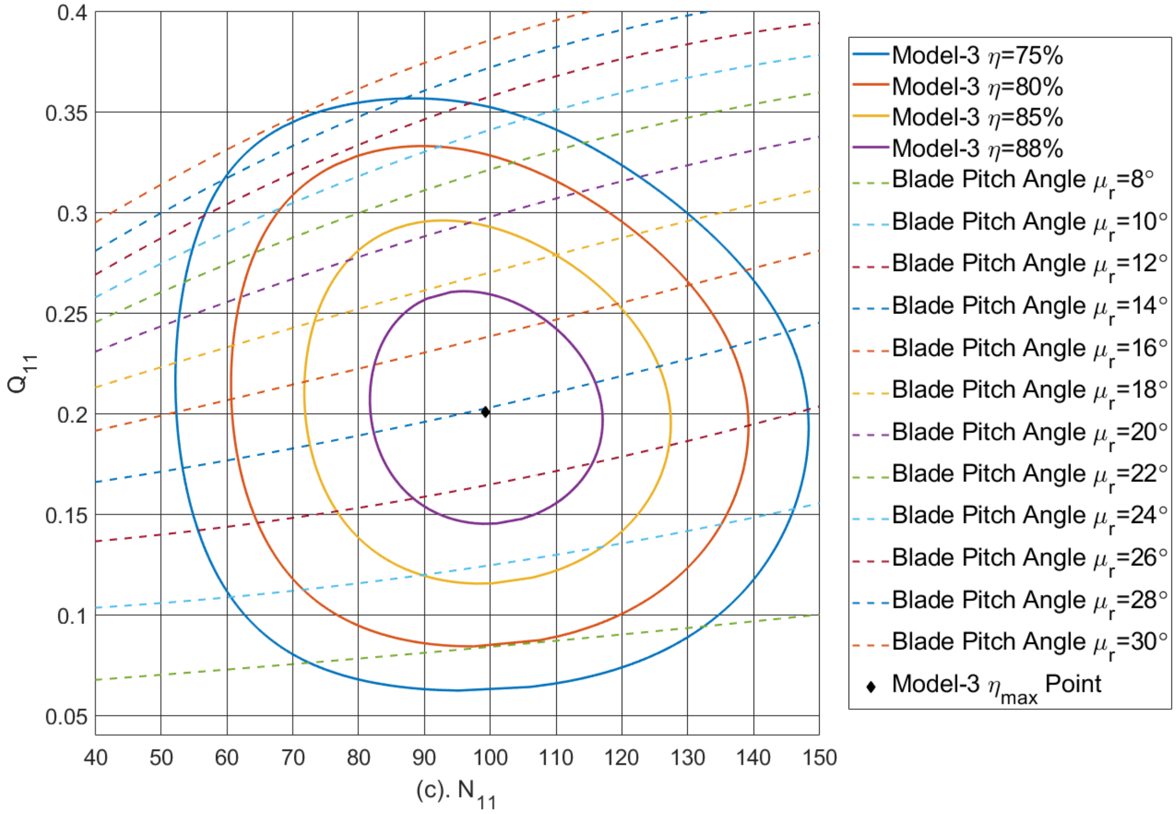

(c). N_{11}

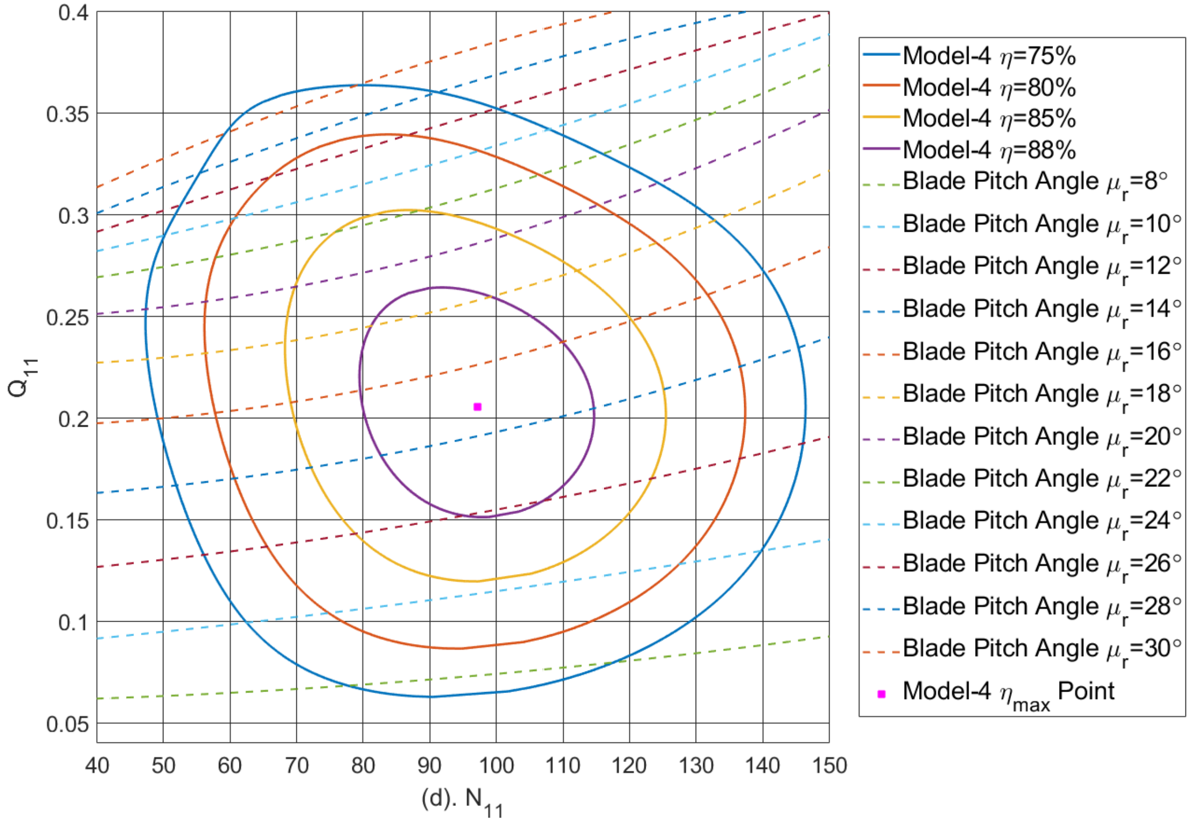

(d). N_{11}

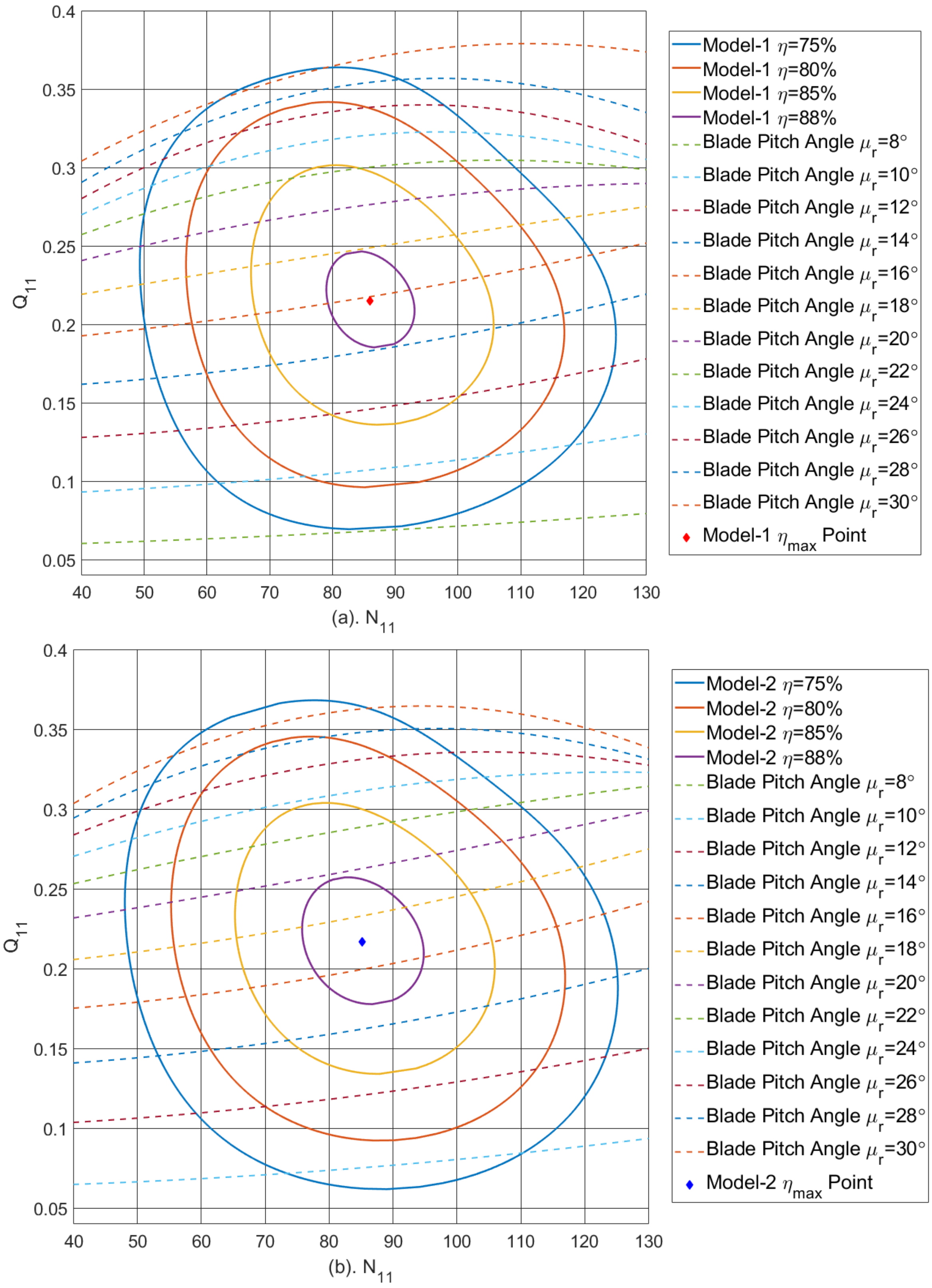

Figure. 5.50. *N_{11} and Q_{11} based performance map at the lower rotational speed (Ω=30Rpm) for four selected models, (a). Model-1; (b). Model-2; (c). Model-3; (d). Model-4.*

Figure. 5.50 *(Cont'd)*

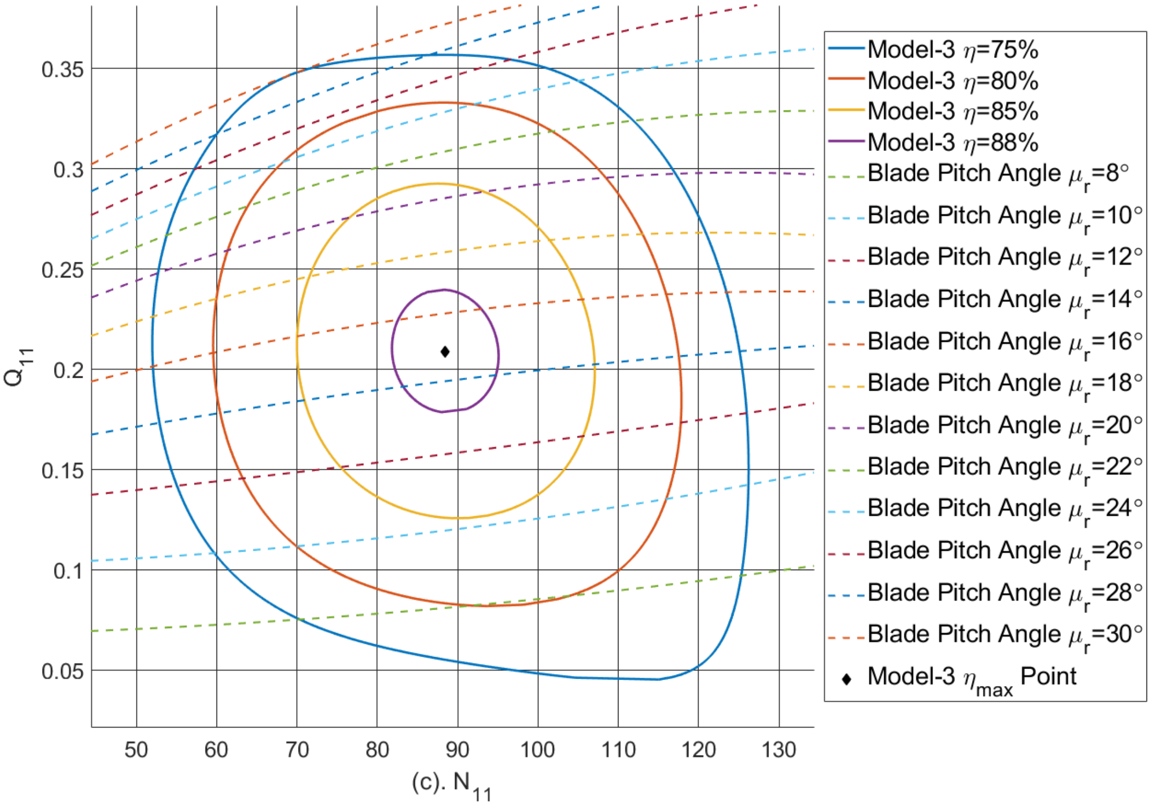

(c). N_{11}

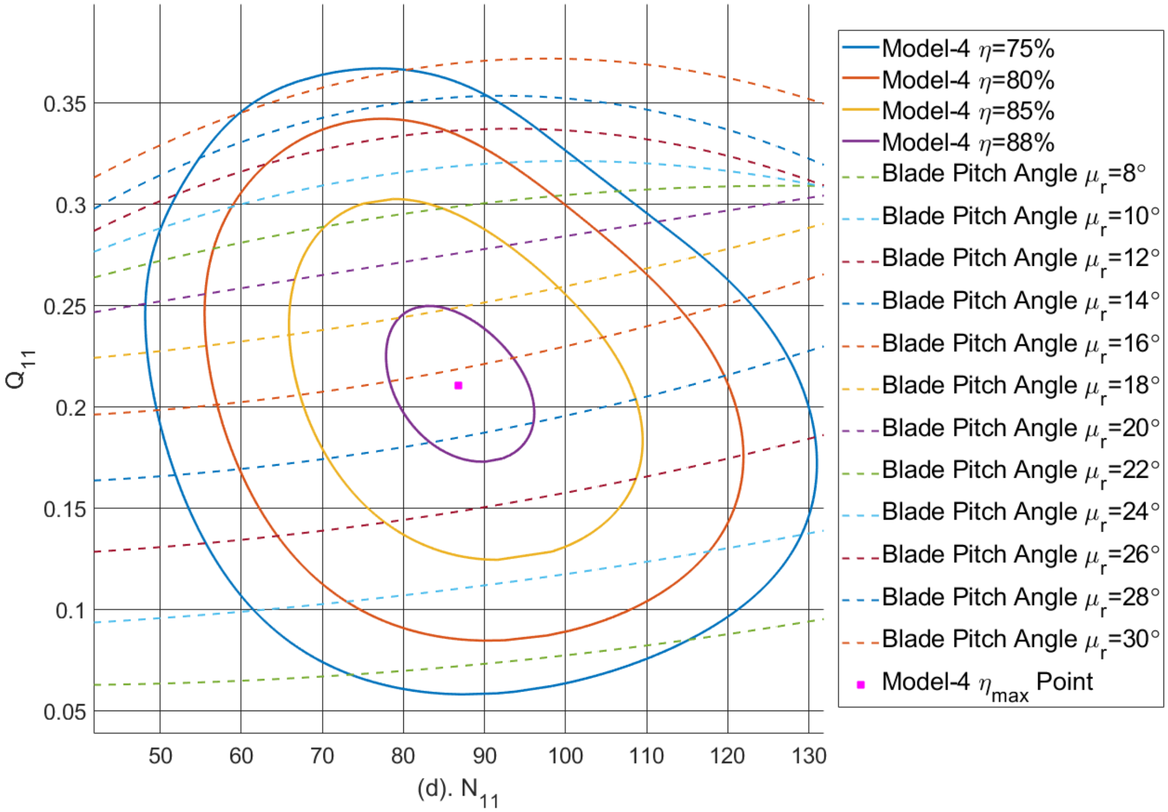

(d). N_{11}

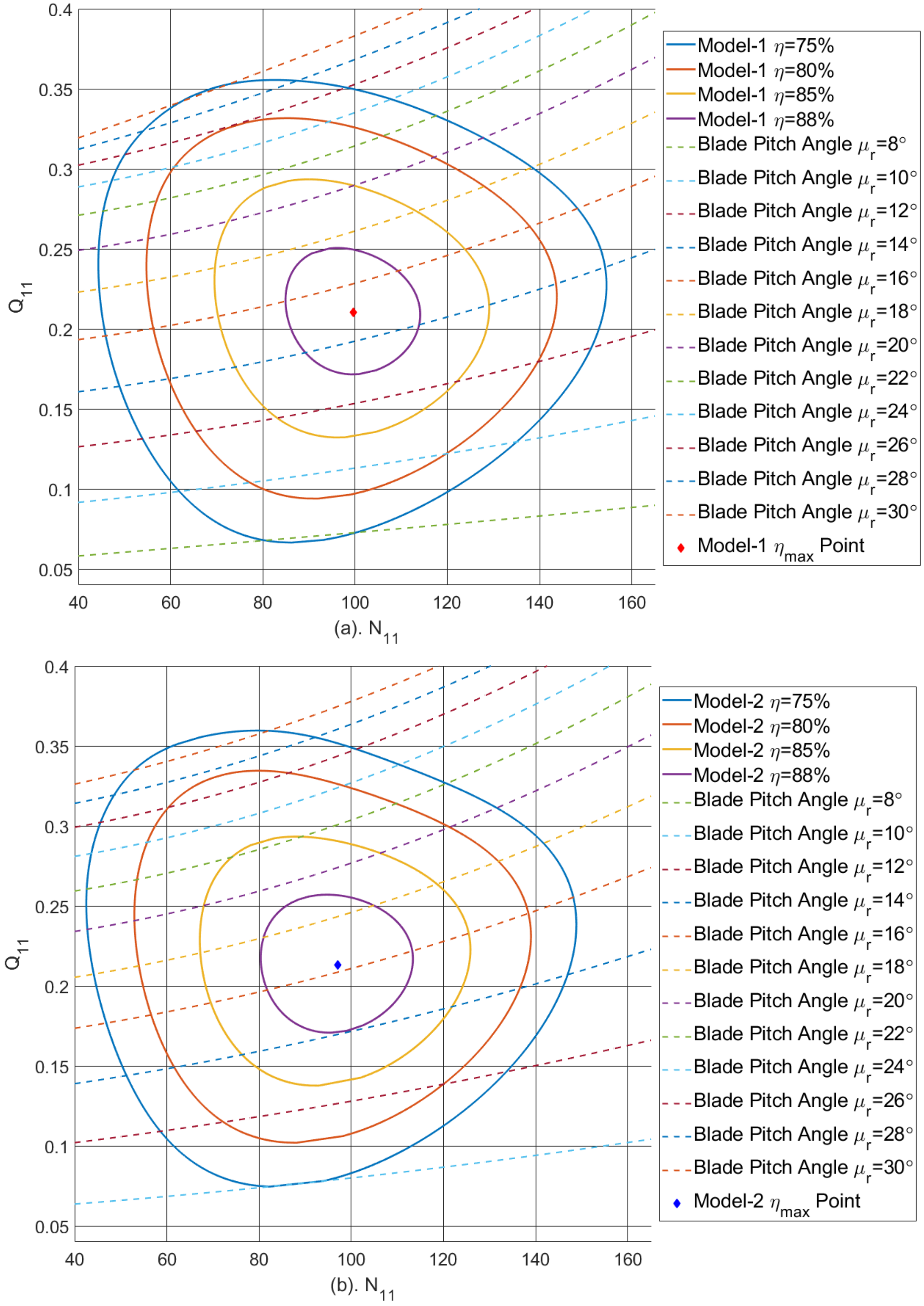

Figure. 5.51. *N_{11} and Q_{11} based performance map at the higher rotational speed (Ω=50Rpm) for four selected models, (a). Model-1; (b). Model-2; (c). Model-3; (d). Model-4.*

Figure. 5.51 *(Cont'd)*

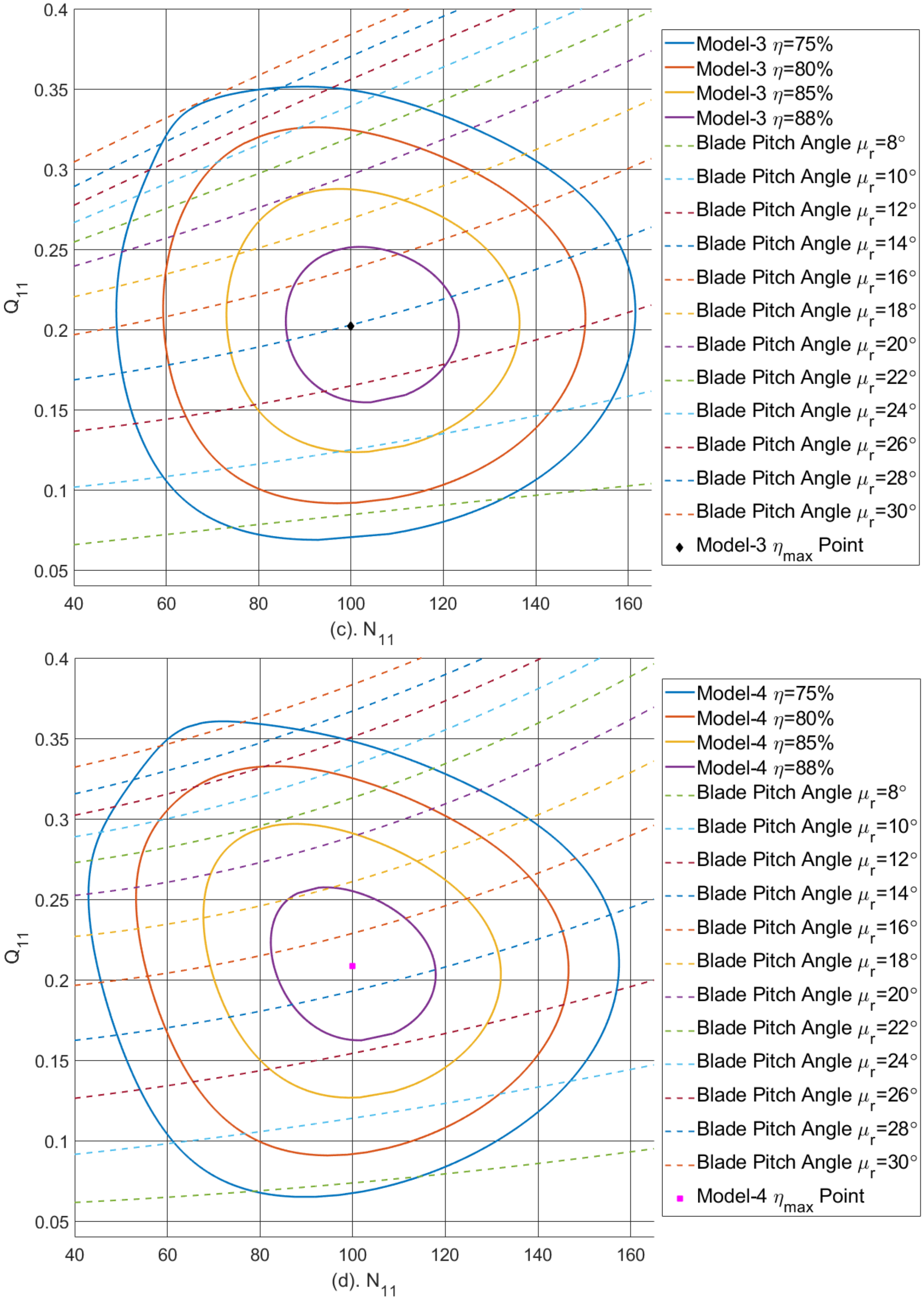

5.4.1. Maximum performance (η_{max}) considerations

- At designed rotational speed ($\Omega = 40$Rpm, ***Fig.5.49***), the results show that all four models have similar η_{max} values and the maximum performance difference between the four models is around 0.54%. However, the locations of the maximum efficiency are slightly different. ***Table.5.2*** summaries the maximum efficiency and its locations for all four selected models.

Table. 5.2. *Maximum efficiency values and its location for all selected models under the design rotational speed (Ω=40Rpm)*

	Model-1	Model-2	Model-3	Model-4
Maximum efficiency	89.48%	89.99%	90.02%	89.83%
N_{11} Location	95.78	95.59	99.28	97.21
Q_{11} Location	0.211	0.212	0.2	0.205
Blade pitch angle Location (μ_r)	15.25	16.4	13.9	14.75

- At lower rotational speed ($\Omega = 30$Rpm, ***Fig.5.50***), the results show that all four models also have similar η_{max} values, the maximum performance difference between the four models is around 0.4%. However, the locations of the maximum efficiency are slightly different. ***Table.5.3*** summaries the maximum efficiency and its locations for all four selected models.

Table. 5.3. *Maximum efficiency values and its location for all selected models under the lower rotational speed (Ω=30Rpm)*

	Model-1	Model-2	Model-3	Model-4
Maximum efficiency	88.45%	88.84%	88.44%	88.62%
N_{11} Location	86.01	85.22	88.45	86.83
Q_{11} Location	0.215	0.217	0.209	0.21
Blade pitch angle Location (μ_r)	15.9	17	14.8	15.5

- At higher rotational speed ($\Omega = 50$Rpm, ***Fig.5.51***), the results show that all four models also have similar η_{max} values, the maximum performance difference between the four models is around 0.56%. However, the locations of the maximum efficiency are slightly different. ***Table.5.4*** summaries the maximum efficiency and its locations for all four selected models.

Table. 5.4. *Maximum efficiency values and its location for all selected models under the higher rotational speed (Ω=50Rpm)*

	Model-1	Model-2	Model-3	Model-4
Maximum efficiency	88.94%	89.40%	89.50%	89.32%
N_{11} Location	99.6	97.07	100	100
Q_{11} Location	0.211	0.213	0.202	0.209
Blade pitch angle Location (μ_r)	15	16.3	14	14.9

All those results show that various runner-blade geometrical settings (runner thickness, solidity, and blade number) has minimal effect on the maximum efficiency values; however, the locations of the maximum efficiency are different. For model-2 which with $\sigma_r = 1.1$ has a longer runner-blade profile; this leads to the more significant blockage at lower μ_r value (according to **Eqn-3-35**). Thus, for model-2, the maximum efficiency occurs at a slightly higher μ_r location with a higher flow rate (compared to the based model, Model-1). In comparison, for model-3 that with smaller thickness, the maximum efficiency occurs at a slightly lower μ_r location with a lower flow rate (compared to the based model, Model-1). Additionally, with a lesser blade count, the model-4 has very similar performance compared to the Model-1. The general trends for all selected models are: at lower head condition, a lower rotational speed can provide a higher performance; at higher head condition, a high rotational speed can provide higher performance. And with $\mp 25\%$ Ω difference, the maximum efficiency difference is around 1%. All those data show variable rotational speed has a very limited impact on the maximum efficiency and the overall performance.

5.4.2. **Off-design operating range considerations**

The previous section focuses on the maximum efficiency for all four selected models, but for off-design consideration, the operating range is the critical concern regarding the system's overall performance. The above figures show the Q_{11} and N_{11} based performance map; here are the head and power-based performance maps (**Fig.5.52-5.54**) for the four selected models.

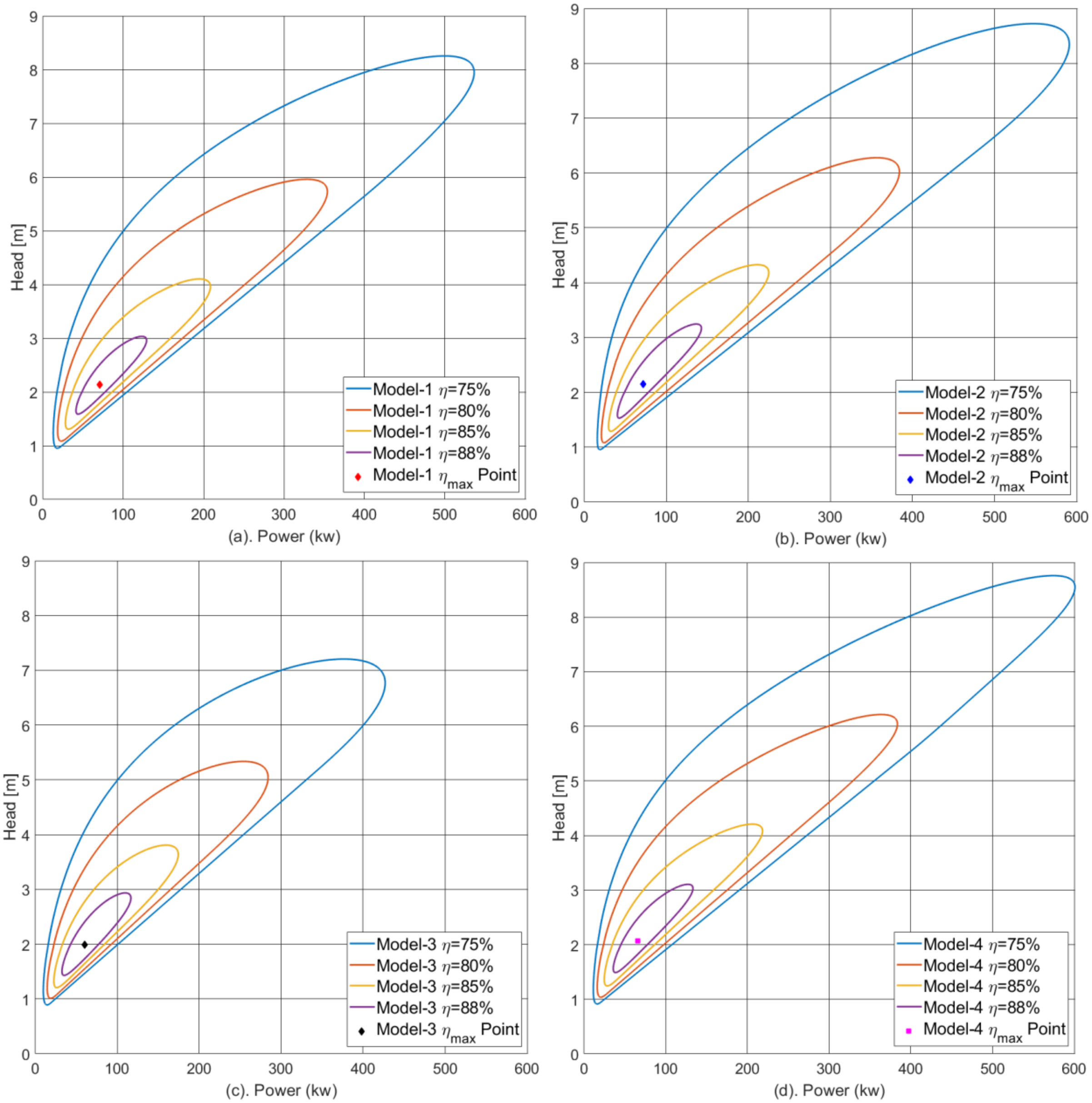

Figure. 5.52. *Power and head based performance map at the design rotational speed (Ω=40Rpm) for four selected models, (a). Model-1; (b). Model-2; (c). Model-3; (d). Model-4*

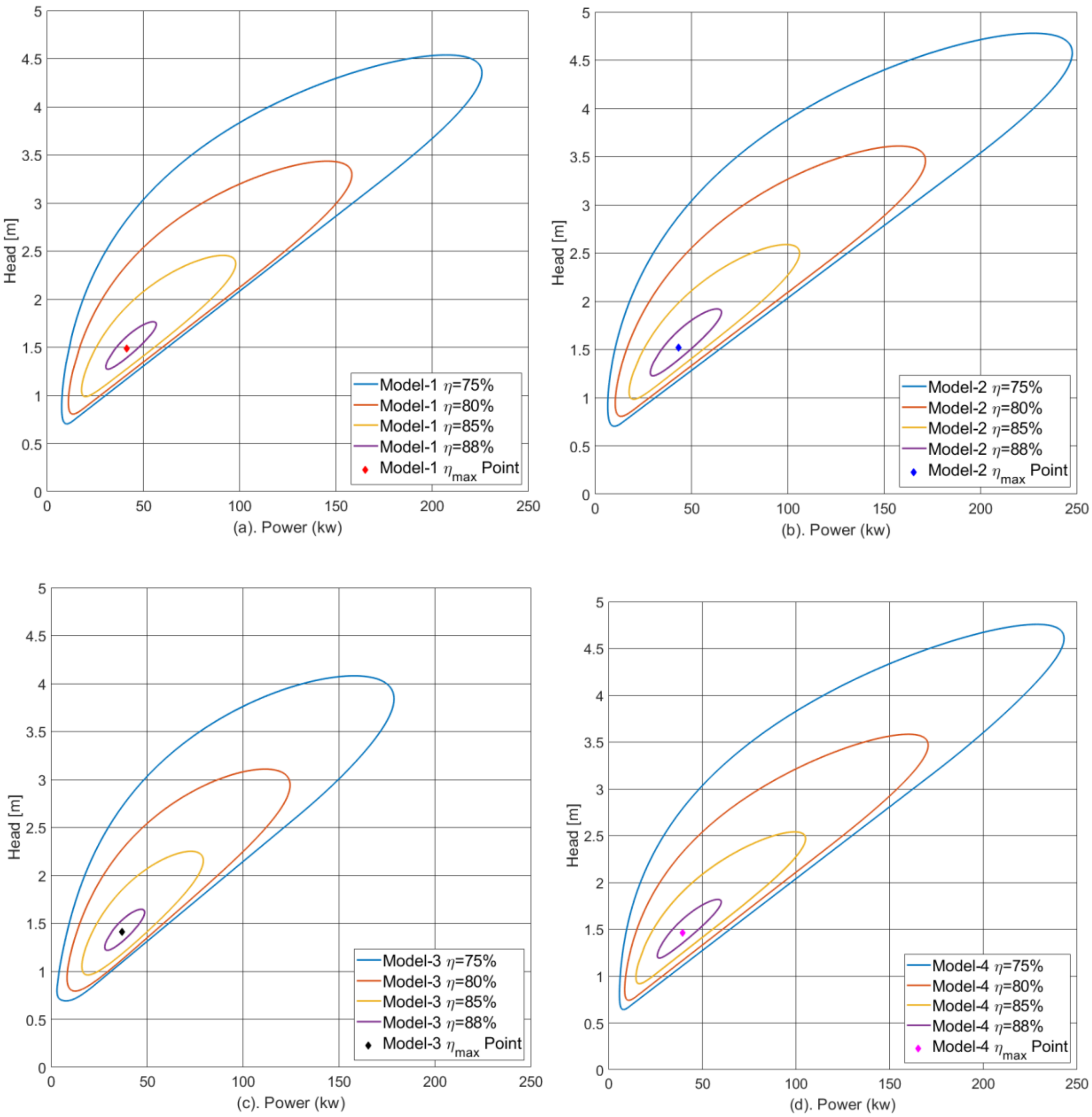

Figure. 5.53. *Power and head based performance map at the lower rotational speed (Ω=30Rpm) for four selected models, (a). Model-1; (b). Model-2; (c). Model-3; (d). Model-4*

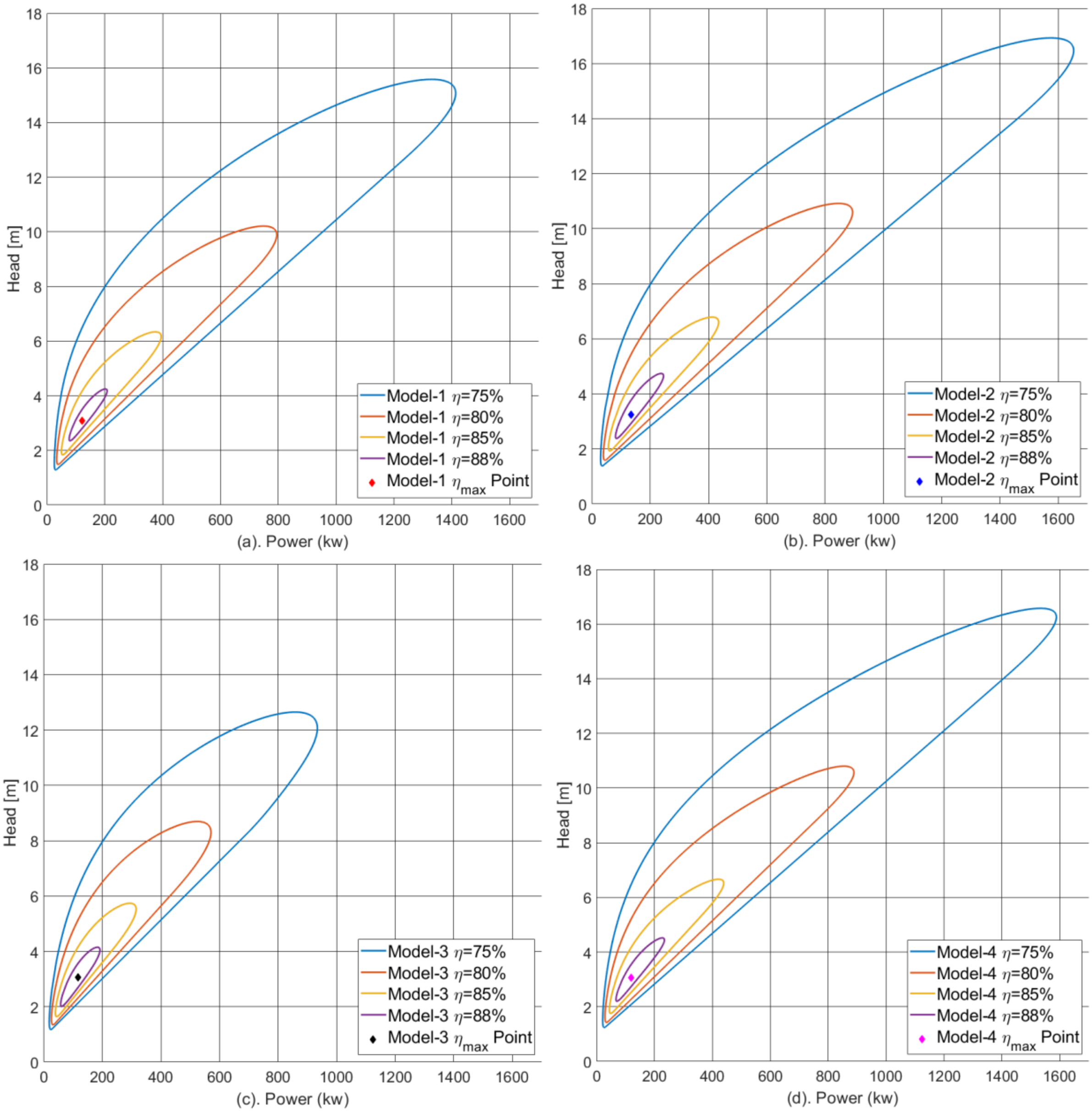

Figure. 5.54. *Power and head based performance map at the higher rotational speed (Ω=50Rpm) for four selected models, (a). Model-1; (b). Model-2; (c). Model-3; (d). Model-4*

- *Design rotational speed*

At the designed rotational speed ($\Omega = 40$Rpm, **Fig.5.52**), **Table.5.5** summaries the head and power operating range with the corresponding performance, and for better visualization, **Fig.5.56,57** shows the simplifying operating range (Head and Power) for all four models.

Table. 5.5. *Operating range and the corresponding performance for all selected models under the design rotational speed (Ω=40Rpm)*

	Model-1	Model-2	Model-3	Model-4
Maximum efficiency	89.48%	89.99%	90.02%	89.83%
η_{max} point's location $\frac{Power}{Head}$	$\frac{71kw}{2.14m}$	$\frac{72kw}{2.15m}$	$\frac{61kw}{1.99m}$	$\frac{66kw}{2.07m}$
>88% Performance Range $\frac{Power}{Head}$	$\frac{43\sim128kw}{1.6\sim3m}$	$\frac{42\sim141kw}{1.53\sim3.2m}$	$\frac{35\sim115kw}{1.43\sim2.9m}$	$\frac{37\sim131kw}{1.5\sim3.1m}$
>85% Performance Range $\frac{Power}{Head}$	$\frac{30\sim206kw}{1.3\sim4.1m}$	$\frac{31\sim221kw}{1.3\sim4.3m}$	$\frac{25\sim170kw}{1.2\sim3.8m}$	$\frac{27\sim216kw}{1.3\sim4.2m}$
>80%Performance Range $\frac{Power}{Head}$	$\frac{22\sim351kw}{1.1\sim5.9m}$	$\frac{23\sim379kw}{1\sim6.2m}$	$\frac{18\sim282kw}{1\sim5.3m}$	$\frac{19\sim378kw}{1\sim6.2m}$
>75% Performance Range $\frac{Power}{Head}$	$\frac{16\sim532kw}{0.96\sim8.1m}$	$\frac{17\sim584kw}{0.96\sim8.6m}$	$\frac{13\sim417kw}{0.9\sim7m}$	$\frac{14\sim596kw}{0.92\sim8.7m}$

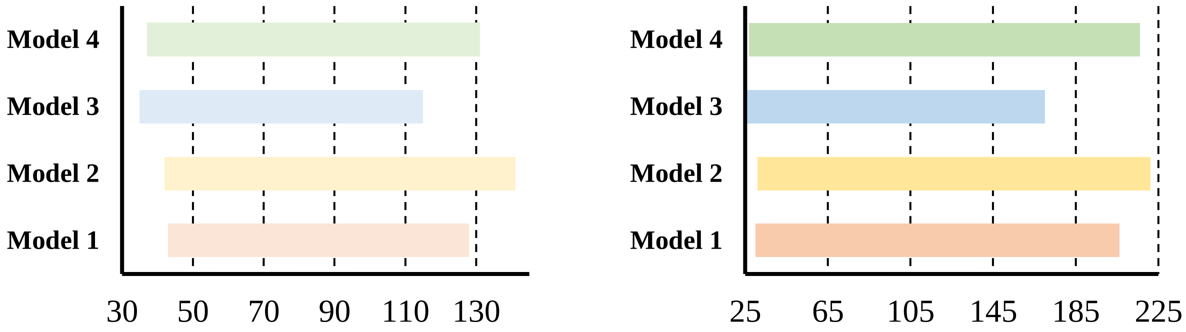

(a). Power Range 88% Efficiency [kw]

(b). Power Range 85% Efficiency [kw]

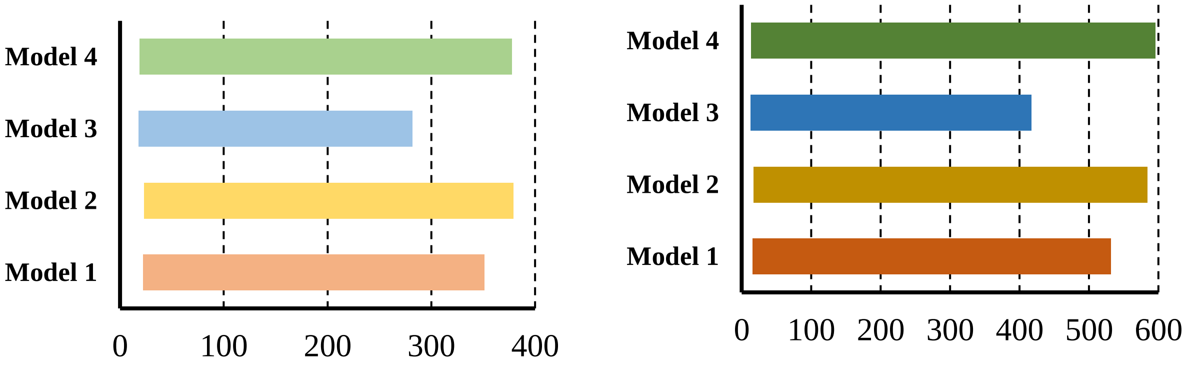

(c). Power Range 80% Efficiency [kw]

(d). Power Range 75% Efficiency [kw]

Figure. 5.55. *Simplified power operating range for all four models under the design rotational speed*

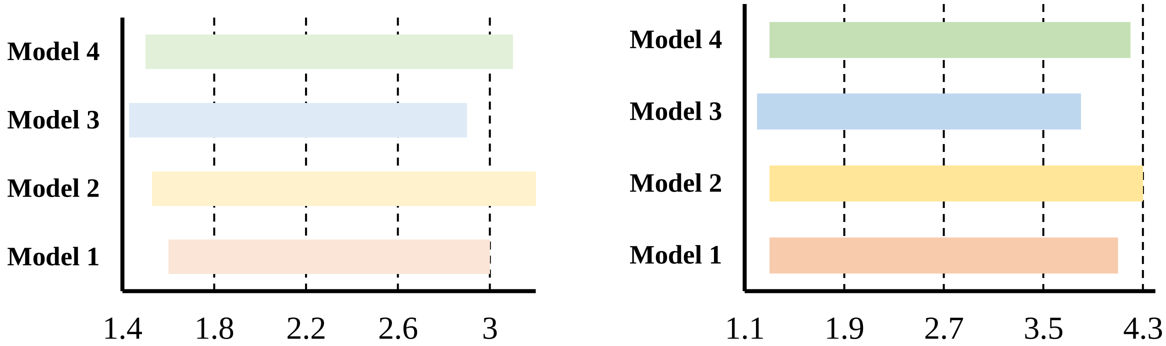

(a). Head Range 88% Efficiency [m] *(b). Head Range 85% Efficiency [m]*

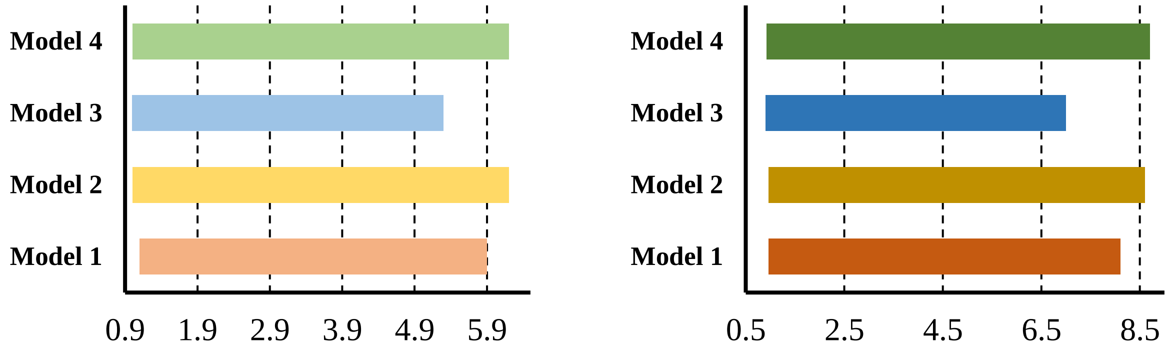

(c). Head Range 80% Efficiency [m] *(d). Head Range 75% Efficiency [m]*

Figure. 5.56. *Simplified head operating range for all four models under the design rotational speed*

- *Lower rotational speed*

At the lower rotational speed ($\Omega = 30$Rpm, ***Fig.5.53***), **Table.5.6** summaries the head and power operating range with the corresponding performance, and for better visualization, **Fig.5.57,58** shows the simplifying operating range (Head and Power) for all four models.

Table. 5.6. *Operating range and the corresponding performance for all selected models under the lower rotational speed (Ω=30Rpm)*

	Model-1	Model-2	Model-3	Model-4
Maximum efficiency	88.45%	88.84%	88.44%	88.62%
η_{max} point's location $\frac{Power}{Head}$	$\frac{42kw}{1.5m}$	$\frac{43.2kw}{1.5m}$	$\frac{37kw}{1.4m}$	$\frac{40kw}{1.5m}$
>88% Performance Range $\frac{Power}{Head}$	$\frac{31\sim56kw}{1.3\sim1.8m}$	$\frac{29\sim65kw}{1.2\sim1.9m}$	$\frac{29\sim48kw}{1.2\sim1.6m}$	$\frac{27\sim59kw}{1.2\sim1.8m}$

***Table.* 5.6** *(Cont'd)*

>85% Performance Range $\frac{Power}{Head}$	$\frac{20\sim96kw}{1\sim2.4m}$	$\frac{20\sim104kw}{1\sim2.6m}$	$\frac{18\sim76kw}{1\sim2.2m}$	$\frac{16\sim104kw}{0.92\sim2.5m}$
>80%Performance Range $\frac{Power}{Head}$	$\frac{13\sim155kw}{0.8\sim3.4m}$	$\frac{12\sim168kw}{0.8\sim3.6m}$	$\frac{11\sim120kw}{0.8\sim3m}$	$\frac{9.5\sim168kw}{0.8\sim3.5m}$
>75% Performance Range $\frac{Power}{Head}$	$\frac{9\sim222kw}{0.7\sim4.5m}$	$\frac{9.7\sim244kw}{0.7\sim4.7m}$	$\frac{5\sim172kw}{0.7\sim4m}$	$\frac{7.5\sim240kw}{0.6\sim4.7m}$

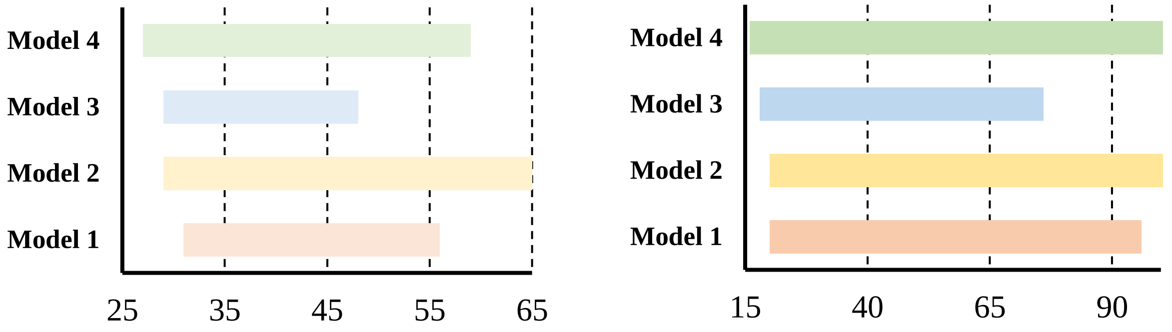

(a). Power Range 88% Efficiency [kw] *(b). Power Range 85% Efficiency [kw]*

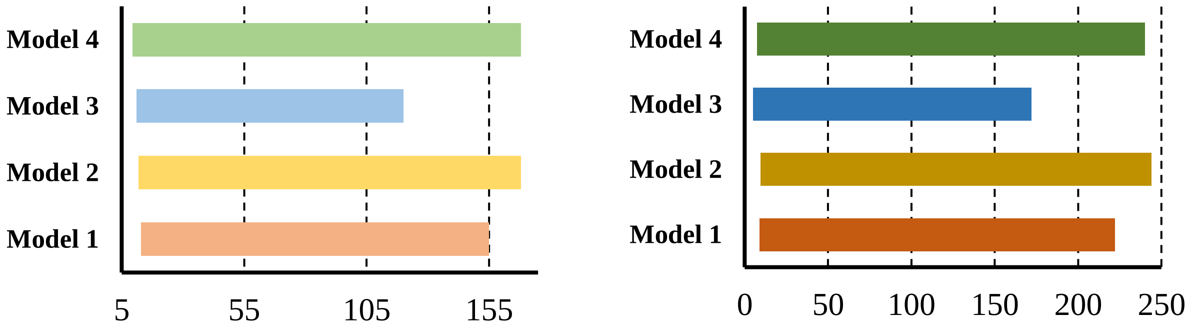

(c). Power Range 80% Efficiency [kw] *(d). Power Range 75% Efficiency [kw]*

***Figure.* 5.57.** *Simplified power operating range for all four models under the lower rotational speed*

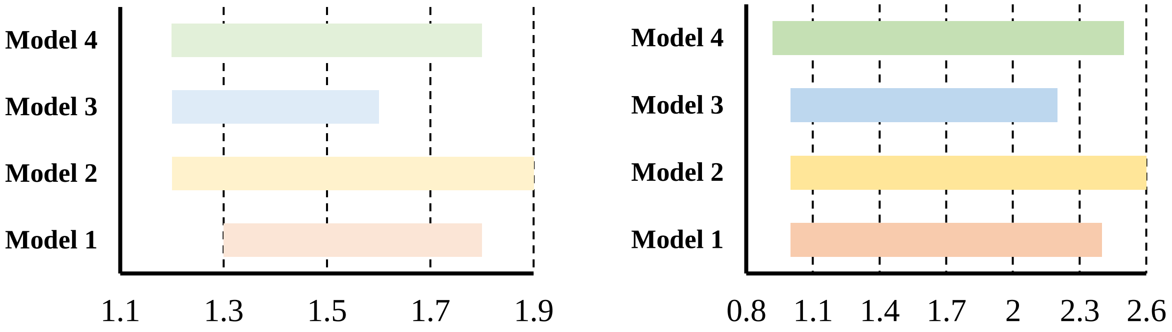

(a). Head Range 88% Efficiency [m] *(b). Head Range 85% Efficiency [m]*

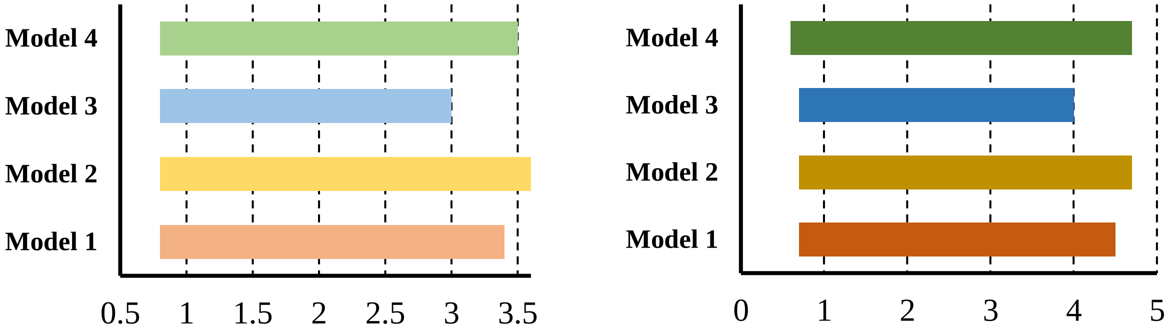

(c). Head Range 80% Efficiency [m] *(d). Head Range 75% Efficiency [m]*

Figure.* 5.58. Simplified head operating range for all four models under the lower rotational speed*

- *Higher rotational speed*

At the higher rotational speed ($\Omega = 50$Rpm, **Fig.5.54**), **Table.5.7** summaries the head and power operating range with the corresponding performance, and for better visualization, **Fig.5.59,60** shows the simplifying operating range (Head and Power) for all four models.

Table. 5.7. *Operating range and the corresponding performance for all selected models under the higher rotational speed (Ω=50Rpm)*

	Model-1	Model-2	Model-3	Model-4
Maximum efficiency	88.94%	89.40%	89.50%	89.32%
η_{max} point's location $\frac{Power}{Head}$	$\frac{122kw}{3m}$	$\frac{134kw}{3.3m}$	$\frac{116kw}{3m}$	$\frac{120kw}{3.1m}$
>88% Performance Range $\frac{Power}{Head}$	$\frac{78\sim207kw}{2.4\sim4.2m}$	$\frac{83\sim242kw}{2.4\sim4.7m}$	$\frac{60\sim189kw}{2\sim4.1m}$	$\frac{67\sim233kw}{2.2\sim4.5m}$

Table. 5.7 *(Cont'd)*

>85% Performance Range	$\frac{Power}{Head}$	$\frac{51\sim391kw}{1.9\sim6.3m}$	$\frac{60\sim429kw}{1.9\sim6.7m}$	$\frac{43\sim310kw}{1.6\sim5.7m}$	$\frac{46\sim438kw}{1.8\sim6.6m}$
>80%Performance Range	$\frac{Power}{Head}$	$\frac{36\sim790kw}{1.5\sim10m}$	$\frac{42\sim892kw}{1.6\sim10.7m}$	$\frac{30\sim563kw}{1.35\sim8.5m}$	$\frac{33\sim887kw}{1.4\sim10.7m}$
>75% Performance Range	$\frac{Power}{Head}$	$\frac{29\sim1410kw}{1.3\sim15m}$	$\frac{32\sim1646kw}{1.4\sim16.7m}$	$\frac{22\sim926kw}{1.2\sim12.4m}$	$\frac{25\sim1585kw}{1.2\sim16.4m}$

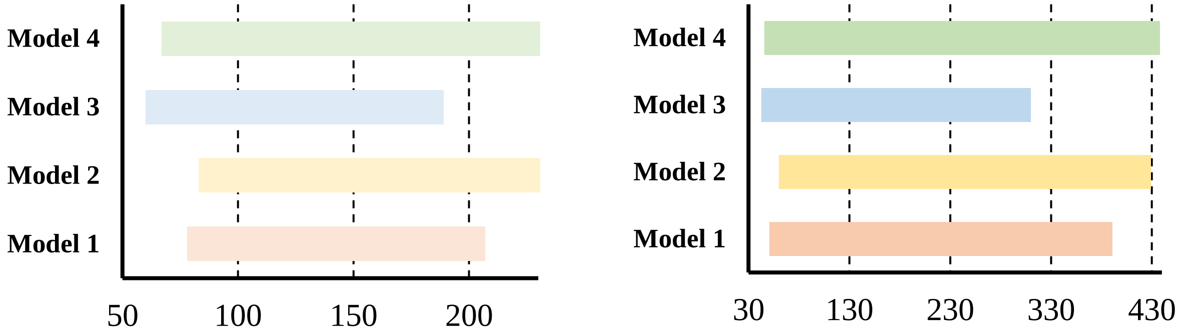

(a). Power Range 88% Efficiency [kw] *(b). Power Range 85% Efficiency [kw]*

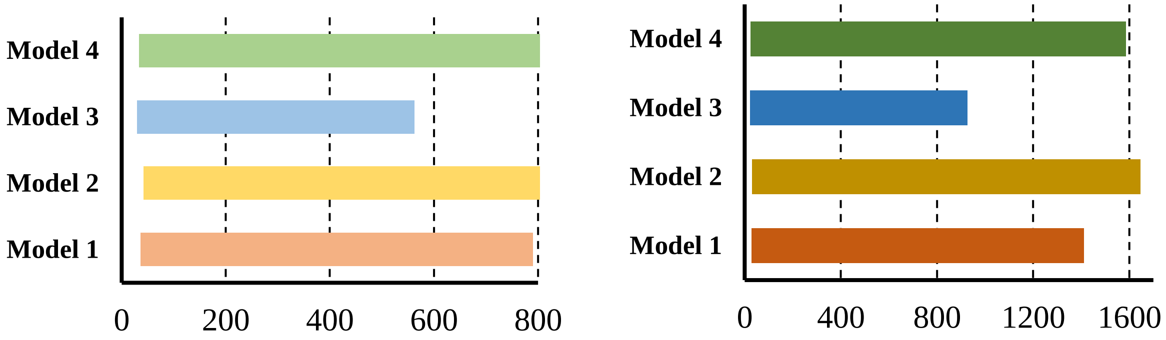

(c). Power Range 80% Efficiency [kw] *(d). Power Range 75% Efficiency [kw]*

Figure. 5.59. Simplified power operating range for all four models under the higher rotational speed

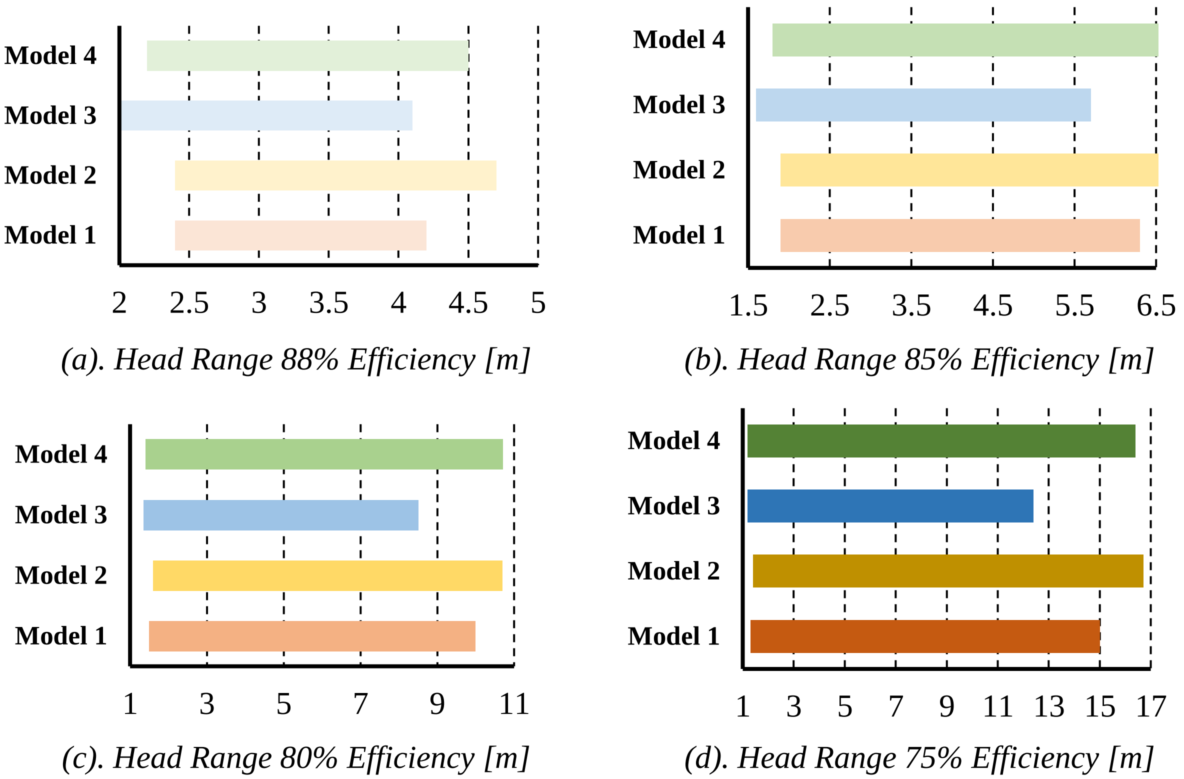

Figure. 5.60. *Simplified head operating range for all four models under the higher rotational speed*

The above results show, by using the proposed design methodology, all selected models have significant large operating ranges; however, each model has its unique features. Under all rotational speed conditions, due to the larger blade solidity, the model-2 has the overall best operating range. The larger blade solidity gives the model-2 a longer blade, which enables a better flow redirection, especially at larger blade opening angle, flow rate, and head conditions, therefore in **Fig.5.55 (a)-(c),** the model-2 has the largest upper bound among all four models. However, when the flow rate is exceedingly high, longer blades can cause high blade profile loss, and this explains in **Fig.5.55 (d)**, model-2 has a slightly lower upper bound than the model-4.

On the other hand, the model-3, which has a thinner blade profile, has the worst operating range. Due to the thinner blade profile, the model-3 cannot provide enough flow redirection at larger flow conditions; this limits the upper bound of operating range for model-3 which precisely shown in **Fig.5.55 (a)-(d)**. Although model-3 has the best lower bound of operating range, due to the low blockage ratio at the small blade pitch opening angle, this slim advantage is neglectable compared to the huge drawback at the upper bound. Model-4, which has the second-best operating range, compared to the model-1 has lesser blade count which cause less blade loss at higher flow rate condition; thus the model-4 has a significantly better operating range than the model-1.

This section demonstrates the proposed system had a vast operating range potential. And based on different flow conditions and requirements, different blade settings and configurations can be applied to achieve the desired operating range.

CHAPTER VI: CONCLUSIONS AND FUTURE WORKS

6.1. Summary of the SMH technology

Low-head hydropower has the potential to generate a significant amount of electricity from rivers that traditionally were unsuitable for developing hydraulic power plants and supporting the resiliency of the U.S electricity system. The development of those resources could be possible only if the technologies for low-head hydropower that balance efficiency, economics, and environmental sustainability were developed. The traditional hydropower design method was limited to the new challenges of the Low-head application. Therefore, a ***Standard Modular Hydropower Technology (SMH)*** was proposed by the U.S. Department of Energy (DOE) in 2017. This new concept offers a new paradigm for small hydropower technology development based on the premise that standardization, modularity, and preservation of stream functionality must become essential and fully realized features of next-generation hydropower technologies and project designs [39]. This technology has three primary modules: generation module, passage modules, foundation modules.

This thesis developed a new design methodology for configuring an ***SMH*** generation module, and with the affluent amount of numerical simulation results, this design methodology has high-level flexibility that can be optimized and configurated according to different river conditions.

6.2. Summary of the design methodology

The first step of the design process is to determine the overall size and operating conditions. Due to the unconventional design, the proposed generation module has a completely different approach regarding the overall size, positioning, operating condition, and blade configuration. The proposed generation module is a damless Kaplan turbine system, and it uses its structure to provide the necessary low-head condition. This unconventional concept means the overall turbine size and positioning angle are critical to the system which are extensively studied in the thesis.

Additionally, in order to achieve high-level flexibility for various applications, a new blade design method, five-point Bezier curve method, was created here for configuring the stator and runner-blade profile for different operating conditions. This method allows the blade profile being further optimized for different scenarios. Ten different geometrical parameters were thoroughly studied by numerical simulations, including general hub size, stator-blade stagger-angle setting constant, stator-blade inlet angle, stator-blade number, stator-blade solidity, stator-blade thickness, runner-blade stagger-angle setting constant, runner-blade number, runner-blade solidity, runner-blade thickness.

6.3. Summary of the numerical results

Detailed numerical simulations were conducted for studying how each proposed geometrical parameter affects the overall performance.

- *General hub size*

At low flow rate conditions, the smaller hub configuration tends to have worse performance on the close to tip region, which leads to poor overall performance. At a larger flow rate condition, the smaller hub configuration has a significantly better overall performance at a larger flow rate condition. Moreover, choosing the right hub size is about balancing the design flow rate and the required hub volume. At a high flow rate, the smaller hub can provide an excellent overall hydraulic performance but with limited hub volume that can have high over-heating possibilities for the generator, which can further affect the overall electrical performance. Balancing the hub size and performance is the key to the initial turbine unite sizing.

- *Stator-blade stagger-angle setting constant*

In general, the stator-blade stagger-angle setting constant (C_{ssa}) value has a larger impact on runner-blade inlet absolute flow angle (α_2) values than runner-blade inlet relative flow angle (β_2) values which have a profound influence on stator outlet flow behaviors, and can further affect the overall performance. Based on the overall results, initially, the suggesting range for C_{ssa} is between 0.7 to 0.8.

- *Stator-blade inlet angle*

In general, larger stator-blade inlet angle ($\beta_{1\ blade}$) can cause a counter-clockwise vortex pattern on the stator-blade suction side, where close to the trailing edge which distorts the downstream flow; small stator-blade inlet angle ($\beta_{1\ blade}$) can cause a clockwise vortex pattern on the stator-blade pressure side that close to the leading edge, which improves the downstream flow. The suggested stator inlet angle is between 60° to 90°.

- *Stator-blade number*

The results show that, among all selected four flow rate conditions, the maximum performance difference is only 0.8%, the maximum shaft power difference is only 2.33%. This relatively small effect means the stator number has a minimal effect on overall hydraulic performance, and a different number of stator-blades can be chosen for various river conditions.

- *Stator-blade solidity*

A small solidity stator-blade has a shorter and thinner blade profile, which led to a poor velocity redirection and acceleration with less velocity redirection angle. Those two consequences reshape the velocity triangle at the stator outlet and affect the overall performance and power of the turbine. Based on the results, the optimum stator-blade solidity value is between 1.2-1.8 depends on flow rate conditions.

- *Stator-blade thickness*

The results show that the increase of the stator-blade relative thickness can slightly improve the overall performance and decrease the shaft power, the maximum efficiency increase is around 1%, and the maximum shaft power decrease is around 1.5%. Additionally, by decreasing the stator local blockage loss, the small stator-blade relative thickness can improve the overall performance when the stator-blade solidity is too large.

- *Runner-blade stagger-angle setting constant*

The results show that larger runner-blade stagger-angle setting constant (C_{rsa}) causes some flow distortion near the leading edge on the pressure side of the blade, which lead to lower performance; and small C_{rsa} has an excellent overall flow attachment, which leads to better performance. The maximum efficiency differences between different C_{rsa} models are around 9% and based on the results the optimum value for C_{rsa} is between 0.2 to 0.3.

- *Runner-blade number*

The results show that, with the increase of runner-blade numbers, the overall hydraulic efficiency can be improved, and the shaft power remains relatively constant. Generally, with more runner-blades, the conversion between hydraulic power and shaft power is more effective, but at the same time, more runner-blades mean reducing turbine spacing between blades, which can harm larger fish survival rate and increase blocking loss. The runner-blade number configuration needs to balance the overall performance, costs, complexity, and fish damage.

- *Runner-blade solidity*

The lower blade solidity value means a considerably shorter blade and causes a mismatch of the inlet stagnation point and the runner leading-edge, hence the flow distortion. Moreover, the shorter blade configuration also causes the misalignment between velocity direction and the blade direction at the runner-blade trailing edge, which means poor flow turning performance. The large blade solidity means a longer blade which can cause the blade's pressure side to interfere with the adjacent blade's suction side. This interference changes the pressure distribution of the blade and further affects the overall performance.

Generally, under the same head condition, the runner-blade solidity can significantly influence the overall velocity triangle for the runner-blade, which affects the overall performance and power production. The optimum runner-blade solidity is between 0.9 and 1.2.

- *Runner-blade thickness.*

The runner-blade thickness has more influence at low flow rate condition than high flow rate condition, at $Q_{11} = 0.103$, the maximum efficiency difference is around 9%, with a 10% relative thickness increase. On the contrary, when $Q_{11} = 0.259$, the maximum efficiency difference is only around 0.6%, with a 10% relative thickness increase. Additionally, the power decrease with the increase of the runner-blade thickness. At the lowest flow rate condition ($Q_{11} = 0.103$), the maximum power difference is around 47% with a 10% relative thickness increase; at the highest flow rate condition ($Q_{11} = 0.103$), the maximum difference is around 13%, with a 10% relative thickness increase.

Moreover, the small runner-blade thickness can improve the overall performance and power generation at larger solidity conditions. With the increase of the runner-blade solidity, the lower thickness models show significantly better performance and power generation, the maximum efficiency and power difference is around 20% and 50%, respectively.

- *Off design considerations*

Since the new stream-reach sites have high variability in flow and head, the off-design and the operating range is critical to study. For the proposed system, variable blade pitch opening and variable rotational speed are the two main methods for regulating the off-design conditions. In order to demonstrate the off-design potential for the proposed system, one design condition was chosen, and four models with different runner-blade configurations were studied. With numerous simulation results, the operating ranges for all four models were calculated. The results show that the larger blade solidity model has the best overall operating range; the thinner blade model has the worst overall operating range. However, all four models have a vast operating range, and the maximum operating range is between 23% and 1220% with over 75% efficiency. Those results demonstrate that the proposed system had a vast operating range potential. And based on different flow conditions and requirements, different blade settings and configurations can be applied to achieve the desired operating range.

6.4. Future works suggestions

This thesis focusses on the relation between the selected geometrical configuration parameters and the overall performance. Future works can emphasize structure deformation and blade material selection. Also, the stator and runner-blade interaction during the off-design condition are also needed to study. Environmental studies, such as fish strike simulation, sediment transport simulation, are also in need to complete the overall system design.

Finally, a scaled experimental model is required for validating all numerical and theoretical assumptions and results. To build a lab-scale testing unit, two major similarity laws must be used to ensure the scaling up performance: Kinematic Similitude and Reynolds Similitude.

- Kinematic Similitude: The kinematic similarity between scaled model and full-scale prototype turbine can be achieved by matching the Froude number:

$$Fr = \frac{U_{avg}^2}{gH} = \frac{U_{avg}^2}{gD} \tag{6-1}$$

where, U_{avg}= Average Inflow velocity; H=Designed Head; D=Turbine Diameter.

This number will ensure the free surface flow condition is the same between the prototype turbine and the scaled model.

- Reynolds Similitude: The Reynolds Similitude between scaled model and full-scale prototype turbine can be achieved by matching the normalized flow rate and speed:

$$Q_{11}(\text{normalized flow rate}) = \frac{Q}{D^2\sqrt{H}}; \qquad N_{11}(\text{normalized speed}) = \frac{nD}{\sqrt{H}} \tag{6-2}$$

Those two numbers will ensure the prototype performance testing results can be applied to the scaled model. The challenge for experimental testing the proposed SMH generation module is to balance the size and flow rate. By following the two similarity laws, **Table.6.1** shows a geometrical and operational conditions comparison between a real-size model and a 2/7 scale model. As shown, the experimental challenge is to balance the scale model size and water usage, which is the key to future experimental developments.

***Table 6.1**. Geometrical and operational conditions comparison between a real-size model and a 2/7 scale model*

	Real Size Model	2/7 Scale Model
D_{tip} [m]	5.00	1.43
D_{hub} [m]	3.50	1.00
Head [m]	3.50	1.00
Volumetric Flow Rate [m^3/s]	14.93	0.65
State Inlet Speed [m/s]	1.49	0.80
Power [kW]	450.20	5.61
RPM [Rpm]	40.00	74.83
Fr number	0.065	0.065
N_{11}	106.90	106.90
Q_{11}	0.32	0.32

APPENDICES

APPENDIX A: The DOE’s ten criteria for designing a fish-friendly hydraulic turbine

Table Appendix.1. *The full list of DOE’s ten criteria for designing a fish-friendly hydraulic turbine [50]*

Criteria Description	Value Chosen	Reasoning
Fish-friendly turbine runner	A new runner design	Project’s objective
Hydraulic design parameter	Flow=1,000 ft^3/s ($28.3m^3/s$) Head=75 ft to 100 ft (23-30m)	A representative of most hydroelectric turbines installed in the U.S., including Kaplan and Francis Tube turbines.
Turbine operating efficiency	85% minimum (3-D calculations included scroll case and draft tube)	Efficiency for most turbines’ peaks at 90% to 93%. 85% was chosen, so the new runner can be competitive with existing designs.
Peripheral runner speed	Less than 40 ft/sec (preferably 20 ft/sec)	Reduces strikes injury and minimizes shear stresses and vortices between moving and stationary parts
Minimum pressure	10 Psia (68.8 kPa)	Downstream migrating fish are typically found within the top 34 ft, i.e., at 30 Psia (206 kPa), and mortality occurs when the pressure drop is more than 30% of acclimation pressure.
Rate of change of pressure	Less than 80 psi/sec (550.3 kPa/sec)	Assuming fish injury occurs at a pressure rate of 160 psia/sec in Kaplan turbines.

Table Appendix.1 *(cont’d)*

Shear stress indicator (Rate of Strain, du/dy)	Less than 15 ft/sec/in (180ft/sec/ft or 180 m/sec/m)	Tests of alewives, a fragile fish, at ARL with 15 ft/sec/in did not cause injury
The number and the total length of leading blade edges	Minimize	Fewer blades and shorter leading edges reduce the probability of the strike
Clearance between runner and fixed turbine housing components	2 mm or less	Small clearances reduce the possibility of mechanical injury. 2 mm is less than the 3 mm gap chosen by the USACE for testing in a Kaplan turbine.
Flow passage Sizes	Maximize	Large amounts of water between blades should reduce abrasion injury by keeping fish away from the blades
Flow control and plant configuration (Not tested for during this phase of the AHTS project)	Maximize distance between runner and wicket gates and minimize travel time from intake to runner	Kaplan turbines are more fish-friendly than Francis turbines. A small distance between wicket gates and the runner in Francis turbines may increase the chance for abrasion and grinding injury.

APPENDIX B: Initial design parameters with description and suggested setting values

Table Appendix.2. *Initial design parameters with description and recommend setting values*

	Design Parameters	Symbol	Descriptions	Recommend values
General geometry parameters	General Inclined angle	θ	The angle between the turbine structure and the inlet flow. This would affect turbine structure length and stator geometry.	Between 30°~50°
	Turbine Tip diameter	D_{tip}	The turbine general diameter.	Tip diameter set as equal to turbine minimum structure length
	Turbine Hub diameter	D_{hub}	The turbine hub diameter.	No Recommended value, depending on flow rate and generator design.
General operation parameter	Rotational speed	Ω	The turbine design rotational speed.	Must keep turbine peripheral speed lower than 12.24m/s. (preferably 6.12m/s)
	Initial guess design efficiency	η	The turbine assumed design efficiency for initial velocity calculation.	Kaplan turbine has a general efficiency of 86%~90%.
General Blade Geometry setting	Runner and stator-blade thickness distribution equation	$y(t)$	Determine the thickness distribution along the blade camber line.	NACA 4-series distribution function.

Table Appendix.2 *(cont'd)*

	Design Parameters	Symbol	Descriptions	Recommend values
Runner-blade geometry Parameters	Runner-blade number	N_R	The turbine runner-blade number.	Between 4~12. 8-blade is the reference setting value
	Runner-blade Stagger-angle setting constant	C_{rsa}	Determine the stagger-angle of the runner-blade at each span location.	Recommend C_{rsa} =0.2~0.5
	Runner-blade control point coefficient	C_{r1}; C_{r2}	Control the runner-blade camber line shape	Recommend Value=0.8
	Runner-blade relative maximum thickness	R_T/ R_t	Runner-blade relative maximum thickness.	R_T=0.1~0.18
	Runner-blade Solidity	σ_r	The ratio between runner-blade chord length and spacing.	Recommend Value $\sigma_R \approx 1\sim1.1$
Stator-blade geometry parameters	Stator-blade number	N_S	The turbine stator number	Between 20~60, 40-blade is the reference setting value
	Stator-blade Stagger-angle setting constant	C_{ssa}	Determine the stagger-angle of the stator-blade at each span location	Recommend C_{ssa}=0.7~0.8
	Stator-blade control point coefficient	C_{s1}; C_{s2}	Control the stator-blade camber line shape	Recommend Value=0.8

__Table Appendix.2__ (cont'd)

	Design Parameters	Symbol	Descriptions	Recommend values
Stator-blade geometry parameters	Stator-blade relative maximum thickness	S_T /S_t	Stator-blade relative maximum thickness	S_T=0.1~0.18
	Stator-blade Solidity	σ_S	The ratio between stator-blade chord length and spacing	Recommend Value $\sigma_S = 1.2\sim2$
	Stator-blade inlet angle	$\beta_{1\ blade}$	The stator-blade inlet setting angle	Recommend Value $\beta_{1\ blade} = 45°\sim90°$

APPENDIX C: Additional results and plots for various hub size considerations.

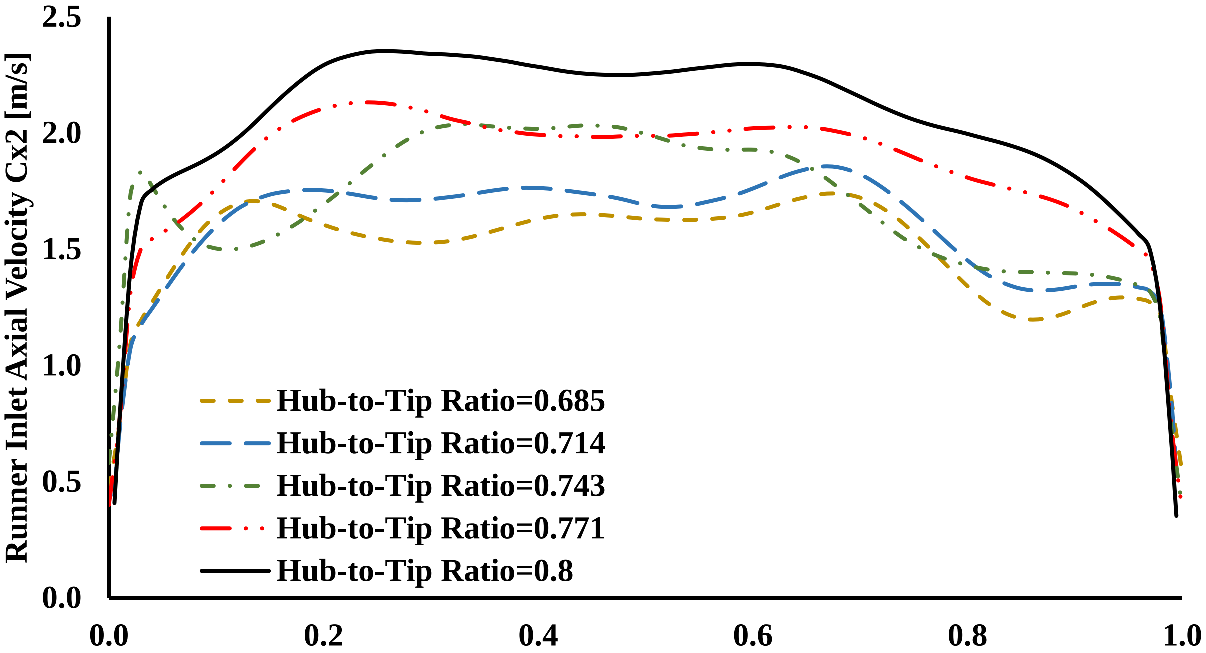

(a). Normalized Span Location ('0' is Hub, '1' is Tip)

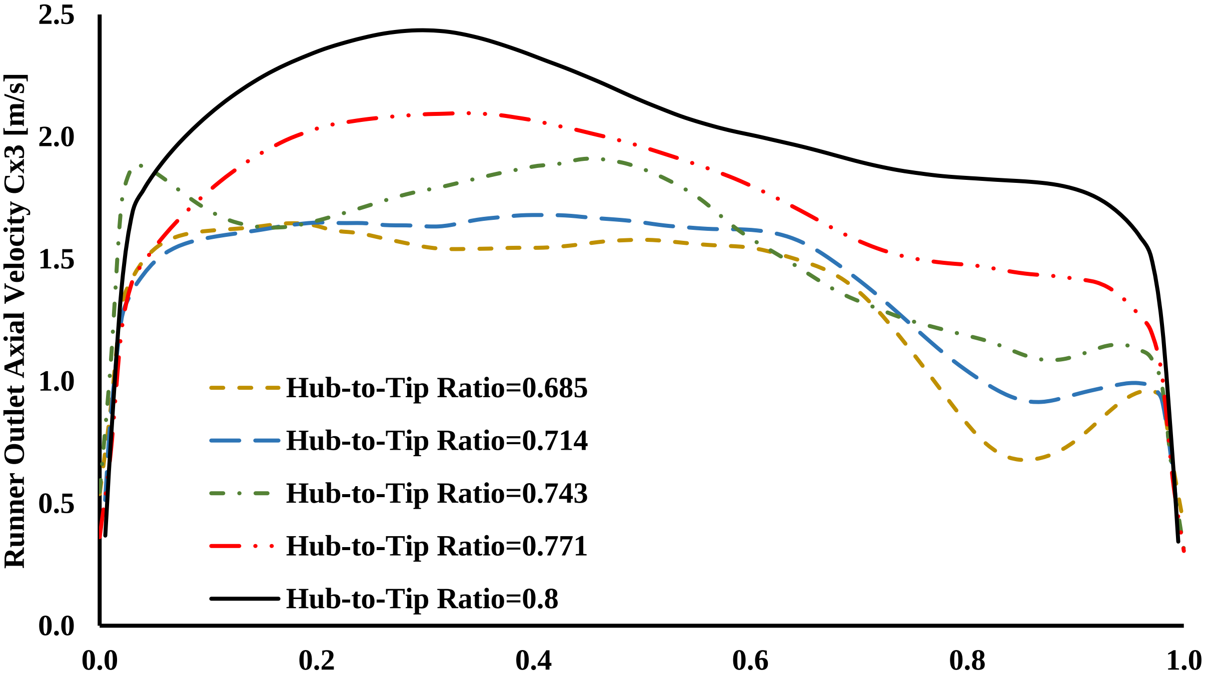

(b). Normalized Span Location ('0' is Hub, '1' is Tip)

Figure. Appendix C.1*. Runner-blade Axial velocity (C_x) distribution at (a). Runner Inlet; (b). Runner Outlet; for the five different hub sizes at high flow rate condition Q_{11}=0.31*

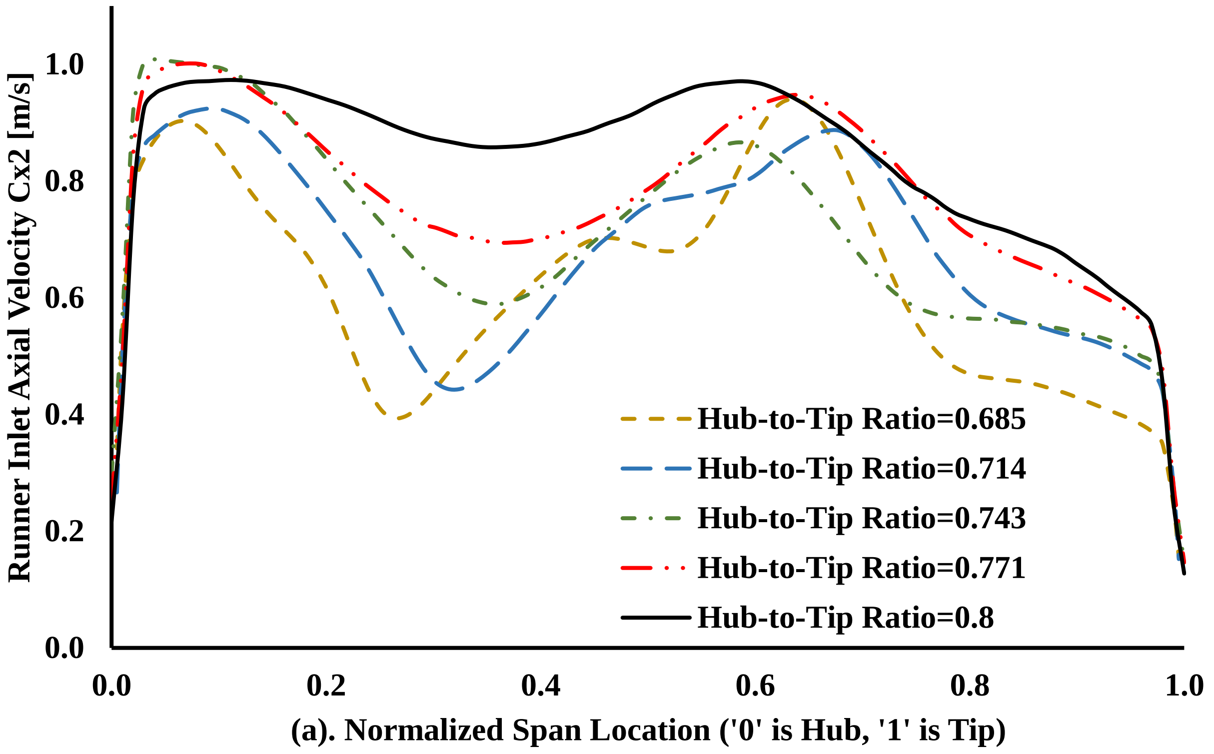

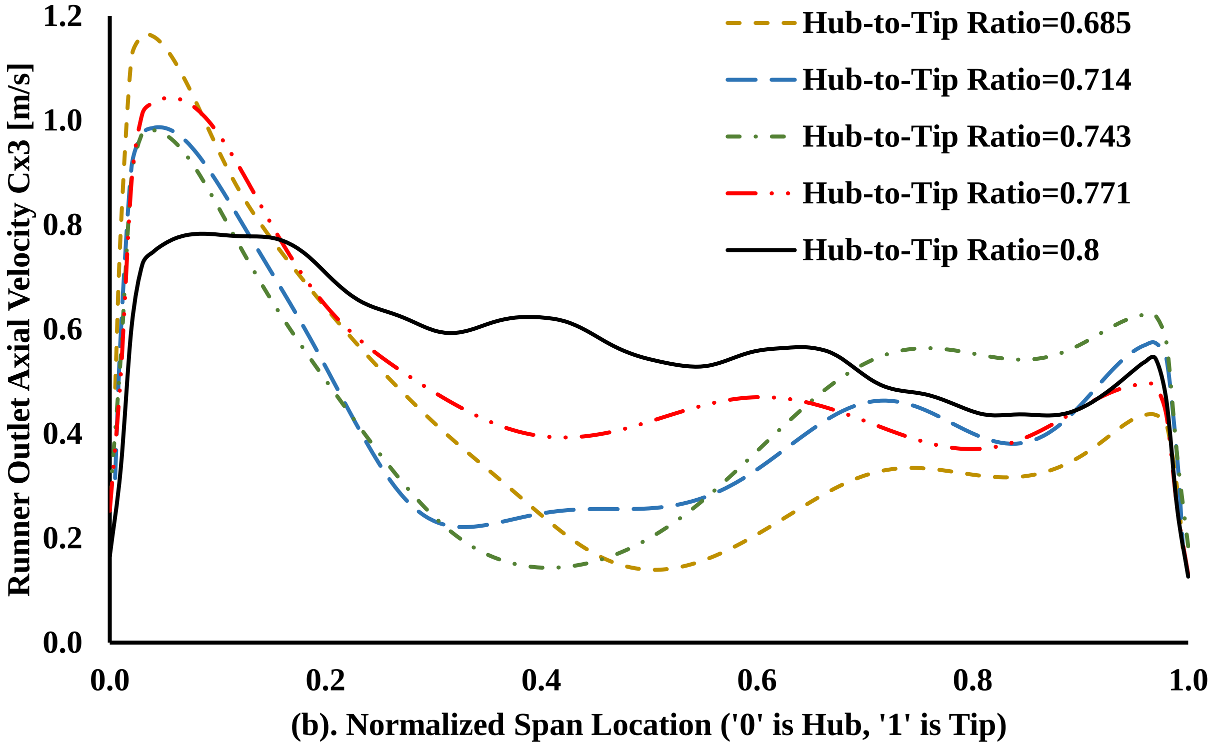

Figure. Appendix C.2. *Runner-blade Axial velocity (C_x) distribution at (a). Runner Inlet; (b). Runner Outlet; for the five different hub sizes at low flow rate condition Q_{11}=0.103*

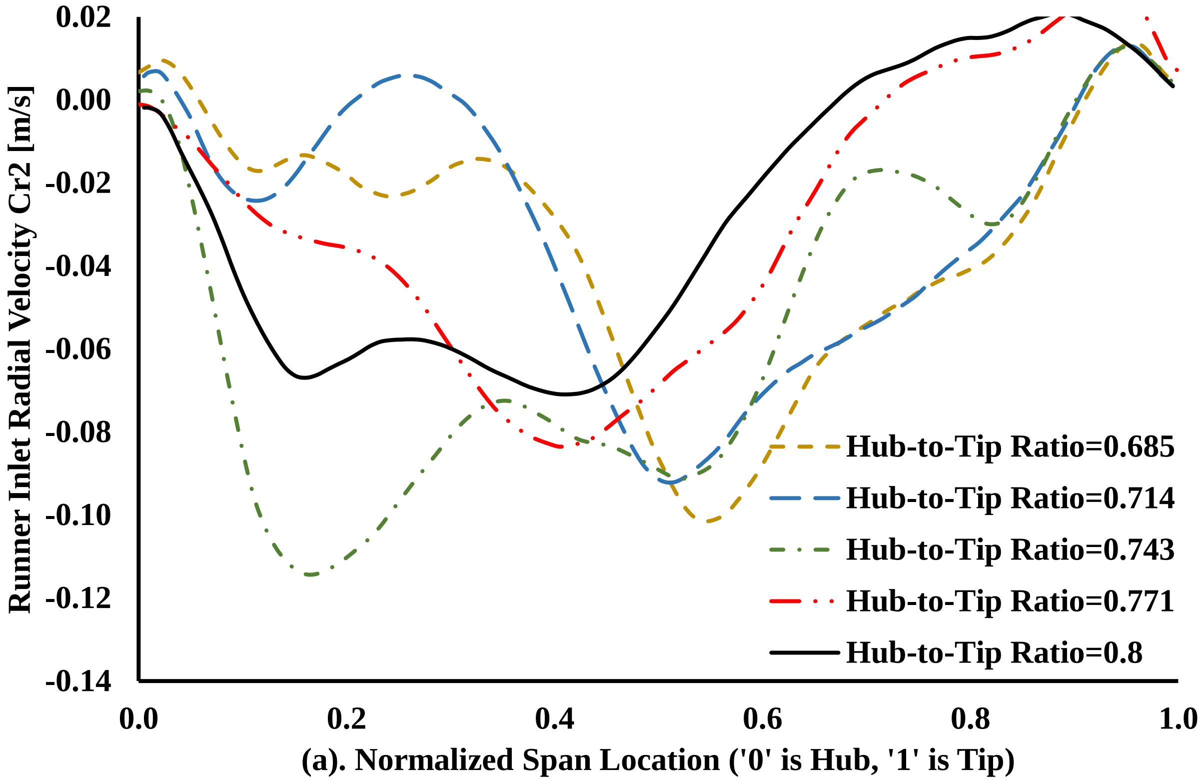

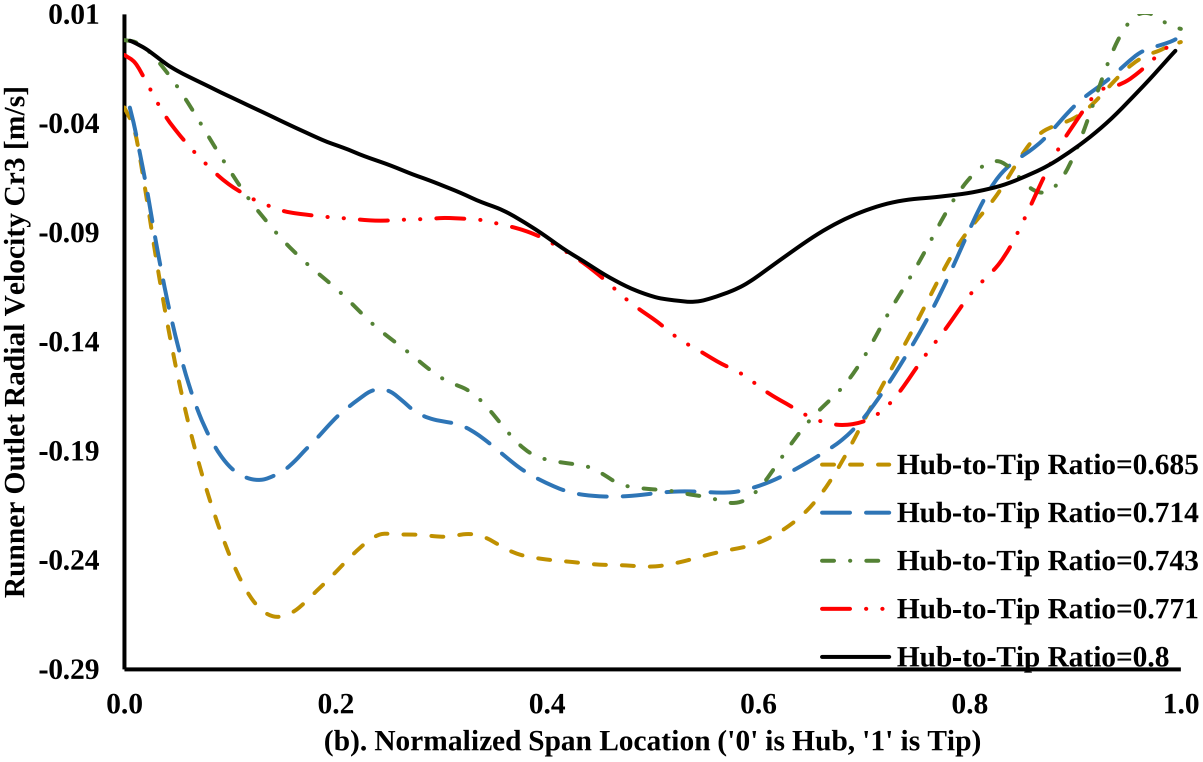

Figure. Appendix C.3*. Runner-blade Radial velocity (C_r) distribution at (a). Runner Inlet; (b). Runner Outlet; for the five different hub sizes at high flow rate condition Q_{11}=0.31*

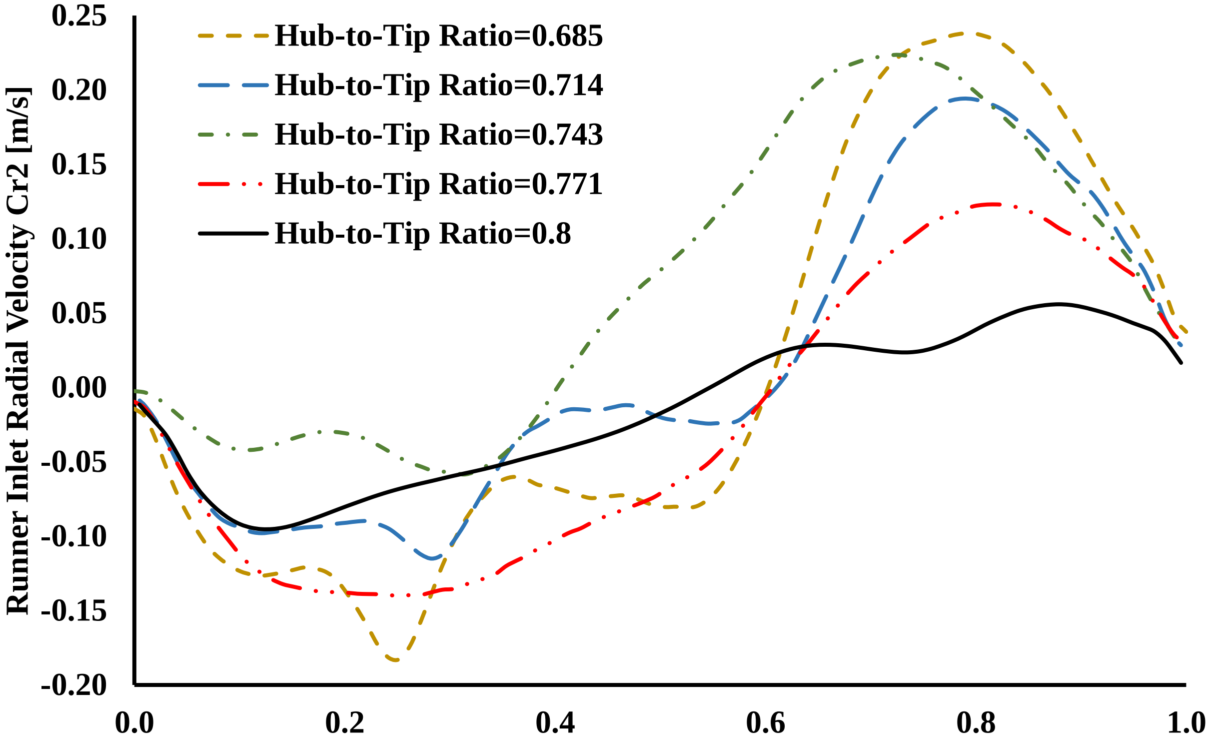

(a). Normalized Span Location ('0' is Hub, '1' is Tip)

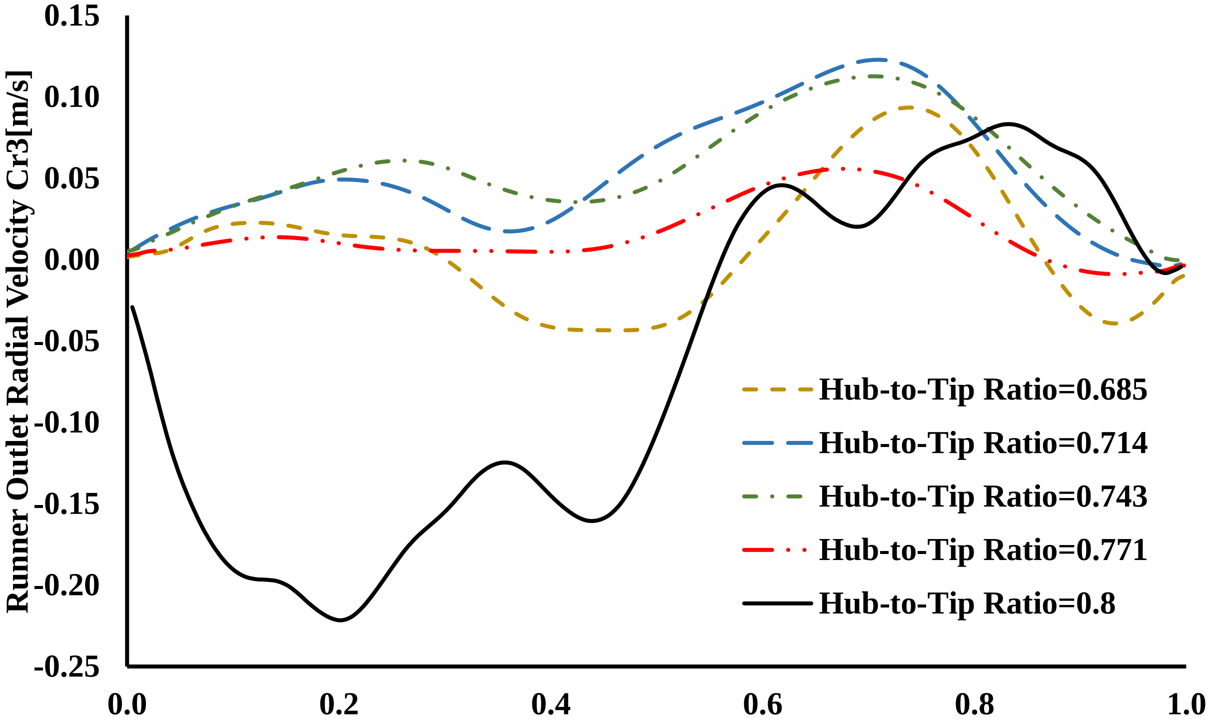

(b). Normalized Span Location ('0' is Hub, '1' is Tip)

Figure. Appendix C.4. *Runner-blade Radial velocity (C_r) distribution at (a). Runner Inlet; (b). Runner Outlet; for the five different hub sizes at low flow rate condition Q_{11}=0.103*

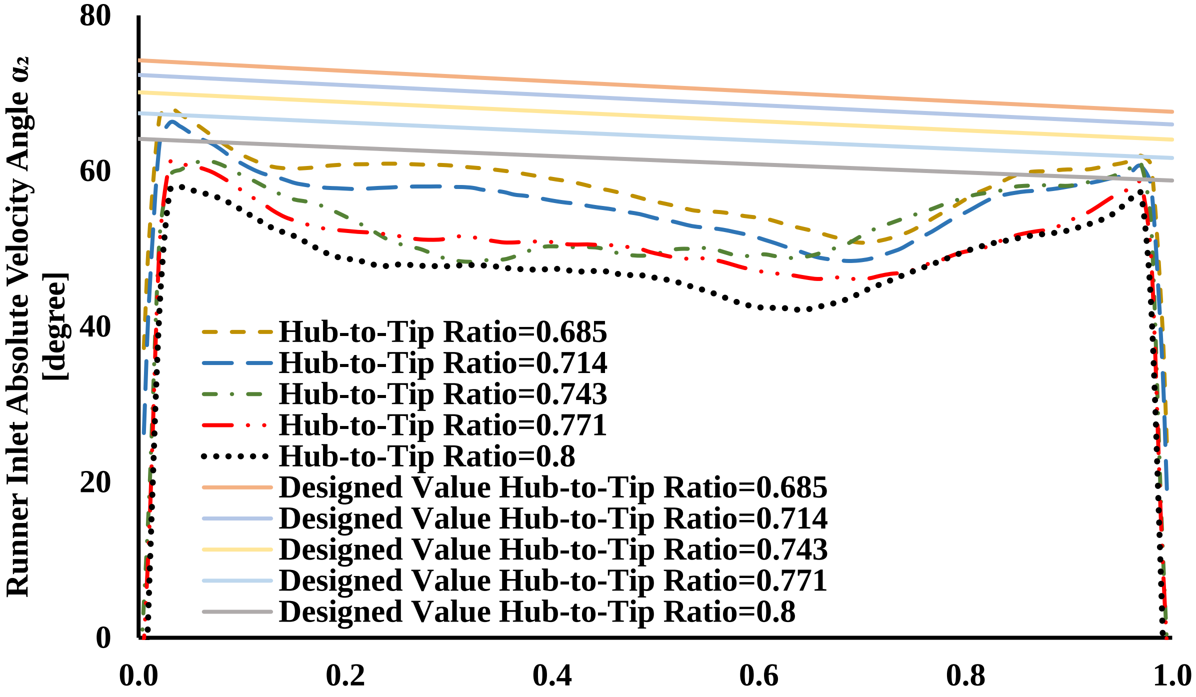

(a). Normalized Span Location ('0' is Hub, '1' is Tip)

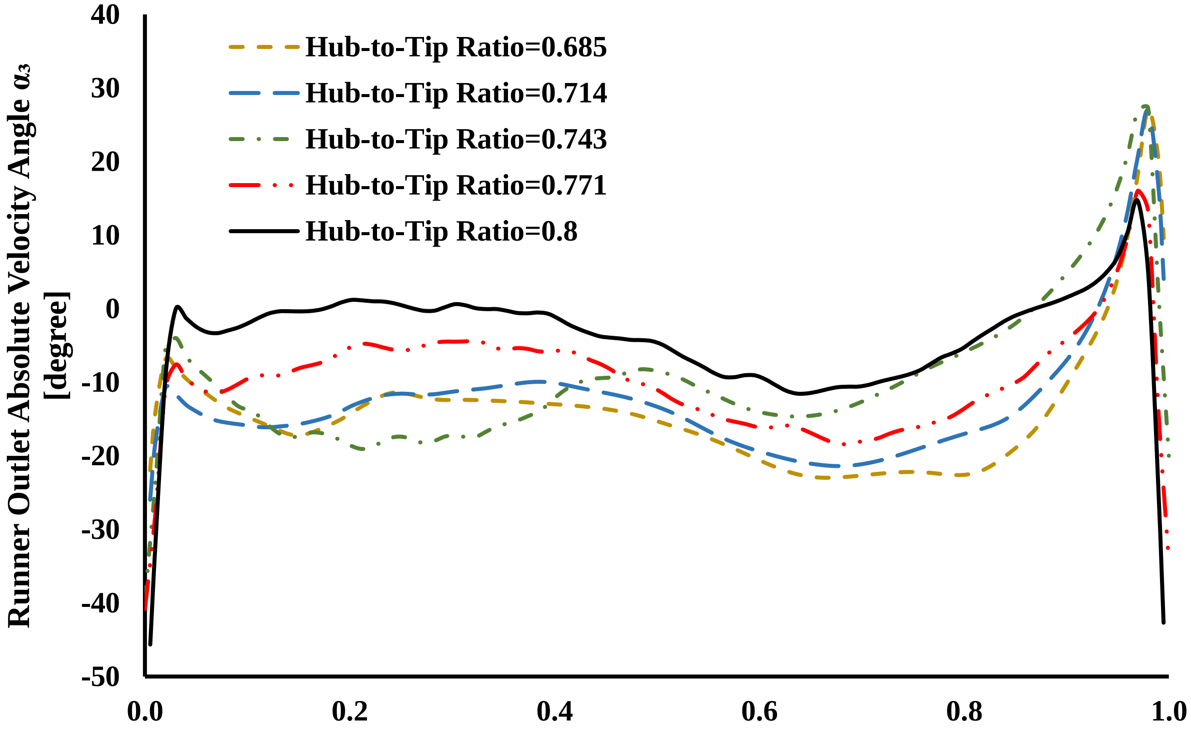

(b). Normalized Span Location ('0' is Hub, '1' is Tip)

Figure. Appendix C.5*. Runner-blade Absolute velocity angle (α) distribution at (a). Runner Inlet; (b). Runner Outlet; for the five different hub sizes at high flow rate condition $Q_{11}=0.31$, with comparison to the designed values [The designed value for α_3 is 0° across all span locations, which is not shown.]*

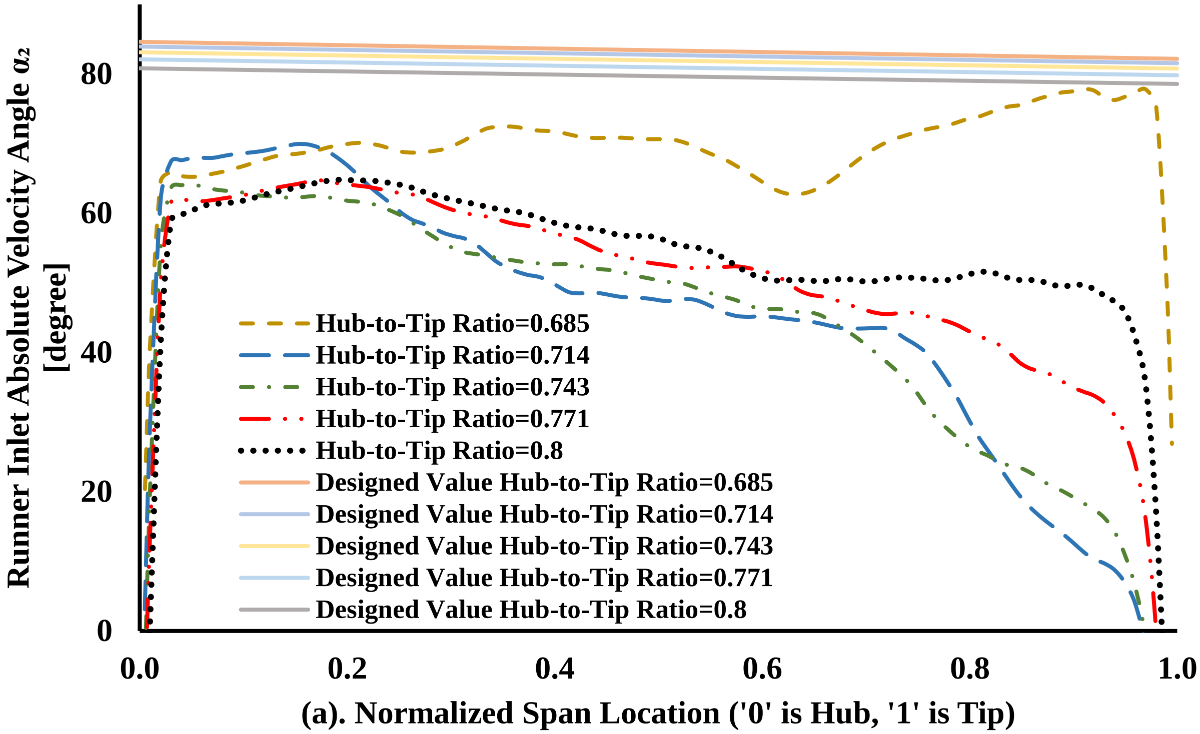

(a). Normalized Span Location ('0' is Hub, '1' is Tip)

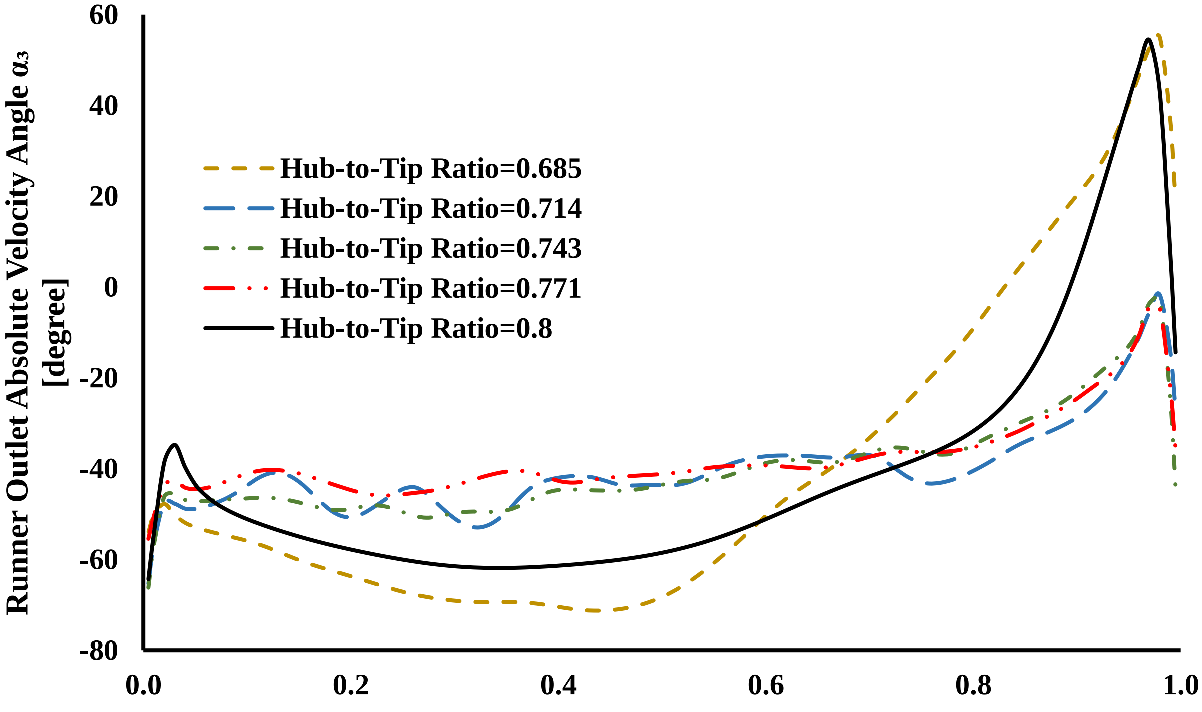

(b). Normalized Span Location ('0' is Hub, '1' is Tip)

Figure. Appendix C.6. *Runner-blade Absolute velocity angle (α) distribution at (a). Runner Inlet; (b). Runner Outlet; for the five different hub sizes at low flow rate condition* Q_{11}*=0.103, with comparison to the designed values [The designed value for* α_3 *is* 0° *across all span locations, which is not shown.]*

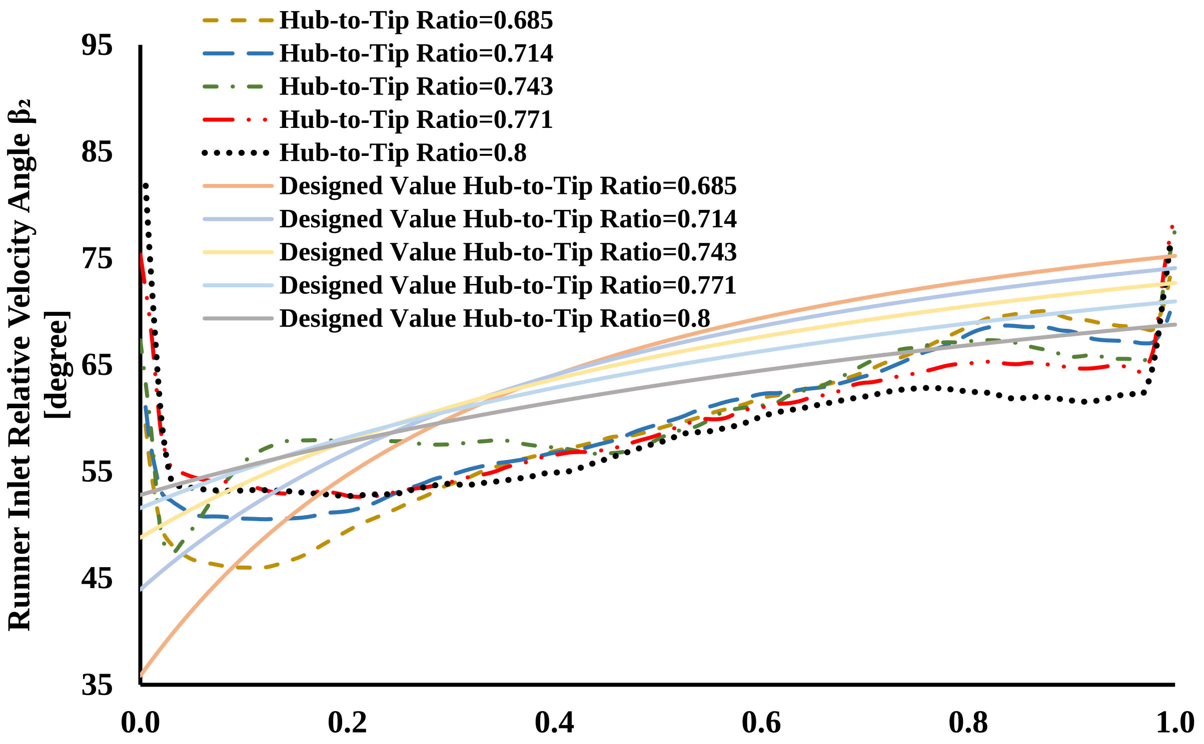

(a). Normalized Span Location ('0' is Hub, '1' is Tip)

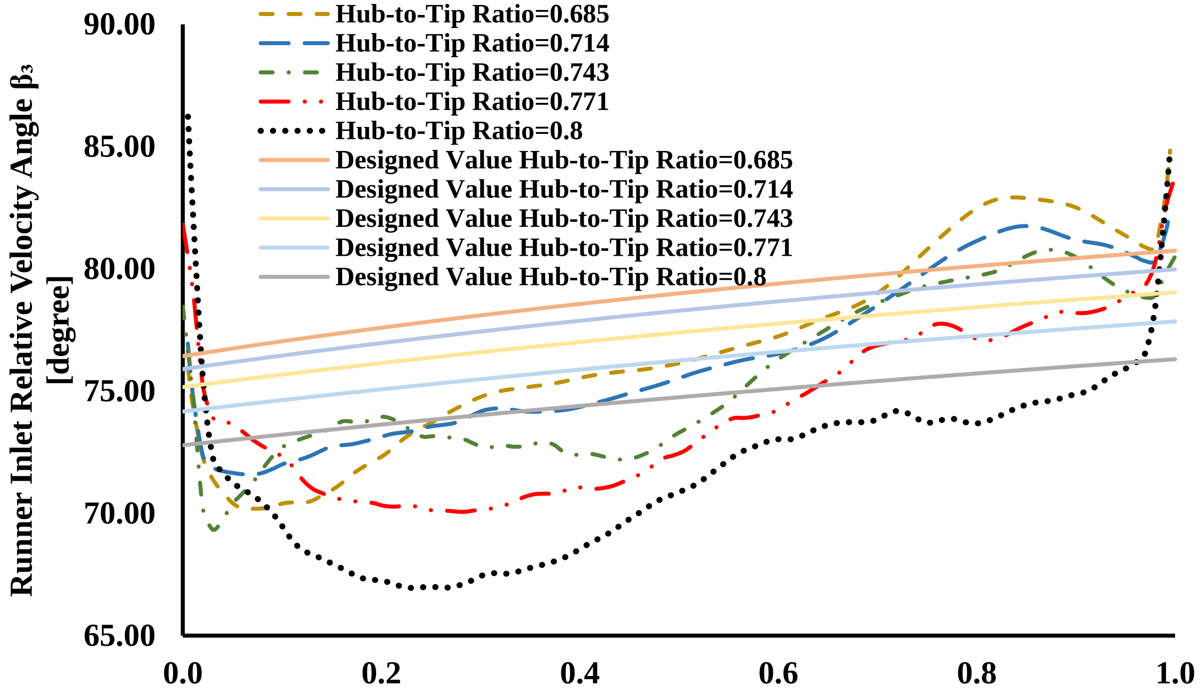

(b). Normalized Span Location ('0' is Hub, '1' is Tip)

Figure. Appendix C.7. *Runner-blade Relative velocity angle (β) distribution at (a). Runner Inlet; (b). Runner Outlet; for the five different hub sizes at high flow rate condition Q_{11}=0.31, with comparison to the designed values*

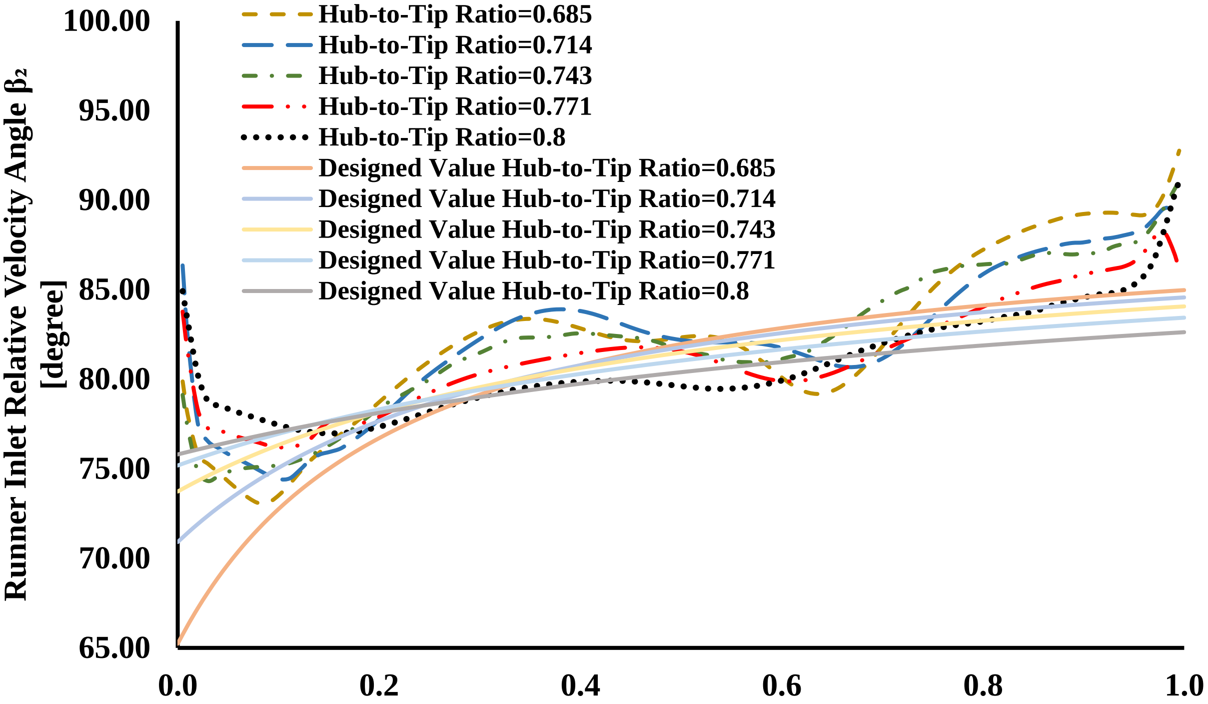

(a). Normalized Span Location ('0' is Hub, '1' is Tip)

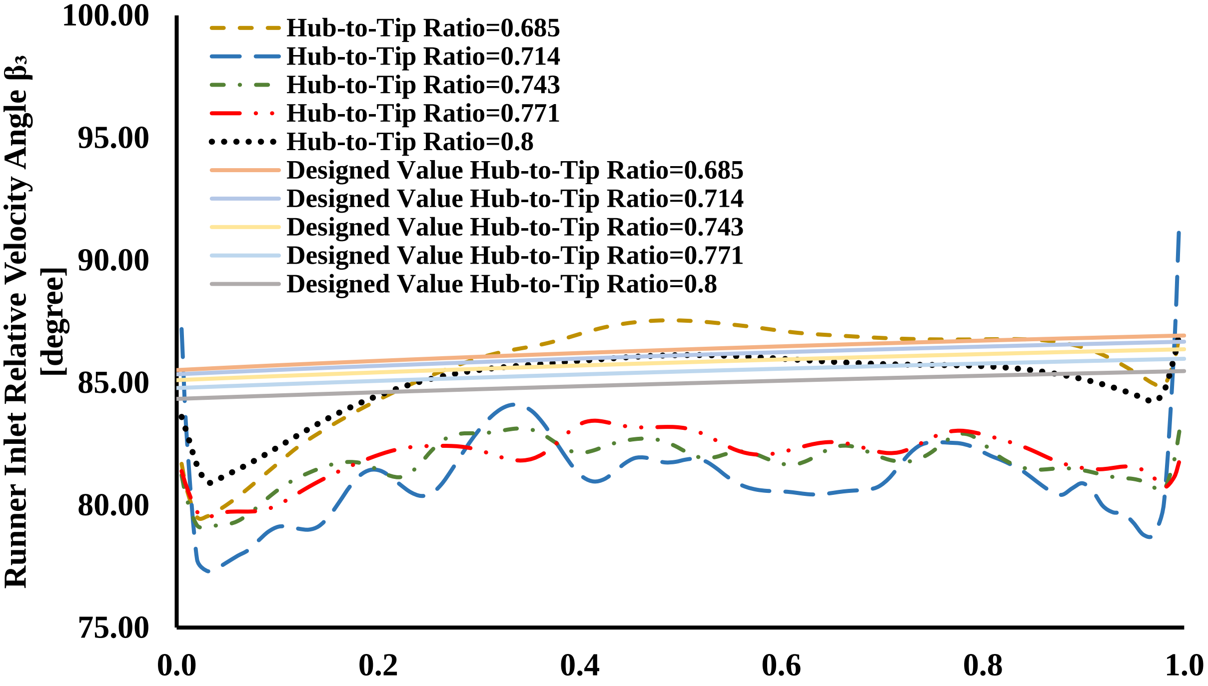

(b). Normalized Span Location ('0' is Hub, '1' is Tip)

Figure. Appendix C.8*. Runner-blade Relative velocity angle (β) distribution at (a). Runner Inlet; (b). Runner Outlet; for the five different hub sizes at low flow rate condition Q_{11}=0.103, with comparison to the designed values*

APPENDIX D: Additional results and plots for stator Cssa constant considerations.

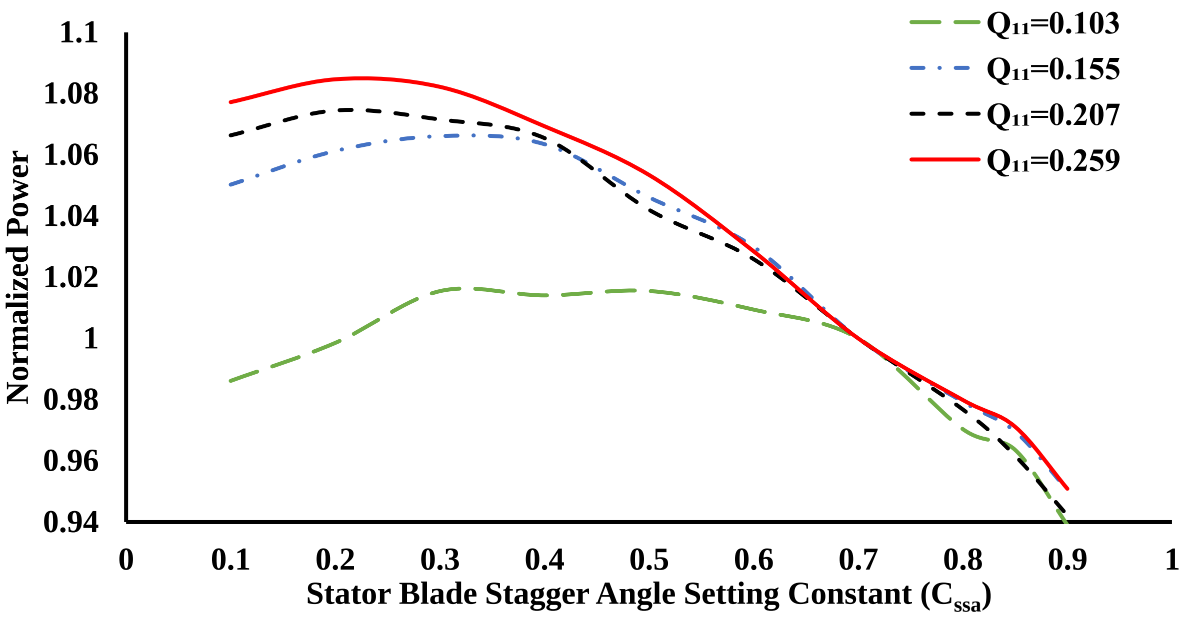

Figure. Appendix D.9. *The relation between normalized power and stator-blade stagger-angle setting constant C_{ssa} for four flow rate conditions. (The power is normalized with C_{ssa}=0.7 models)*

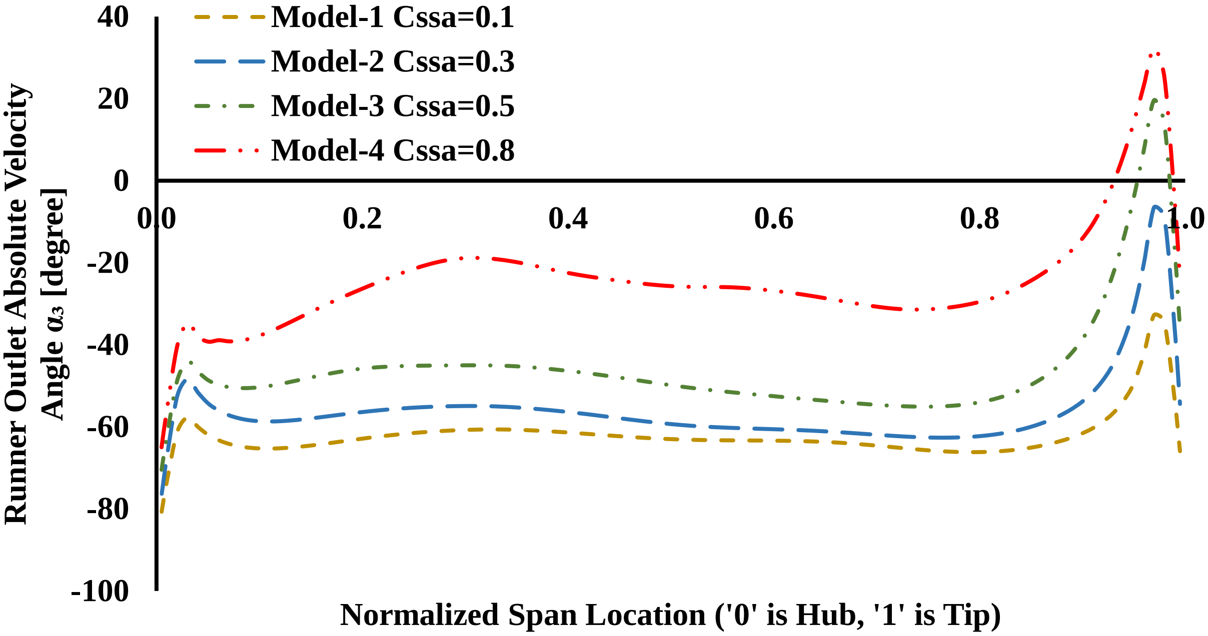

Figure. Appendix D.10. *Runner-blade Outlet absolute velocity angle (α_3) distribution for the four selected models*

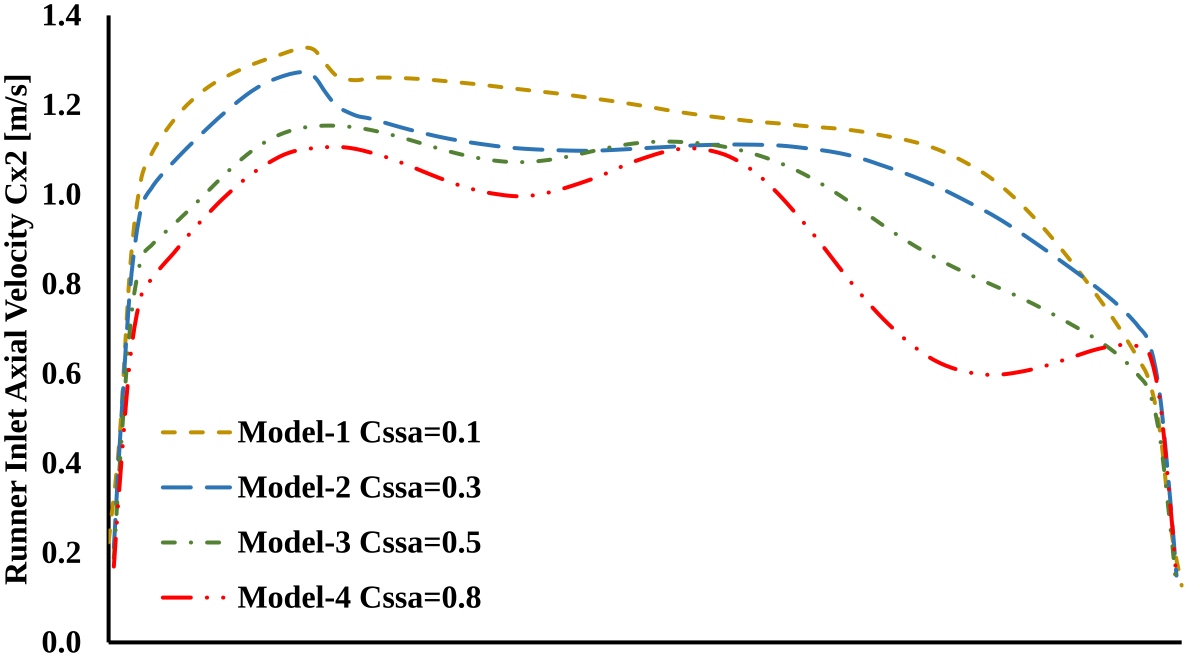

(a). Normalized Span Location ('0' is Hub, '1' is Tip)

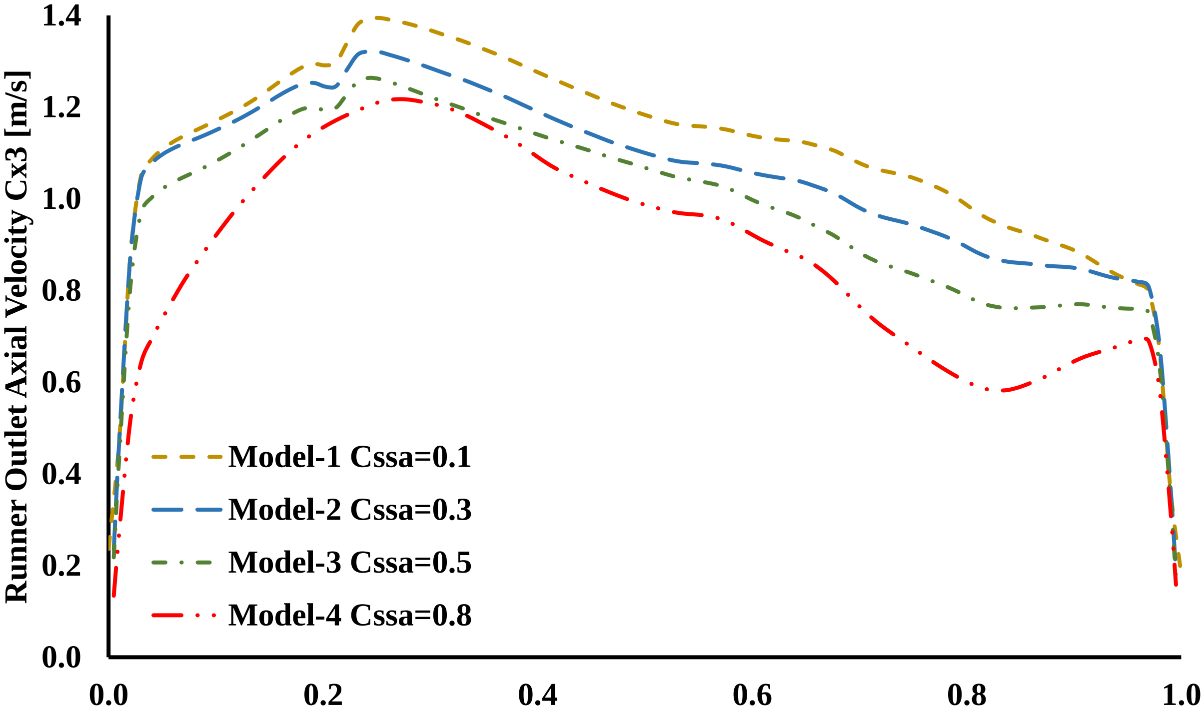

(b). Normalized Span Location ('0' is Hub, '1' is Tip)

Figure. Appendix D.11*. Runner-blade Axial velocity (C_x) distribution at (a). Runner Inlet; (b). Runner Outlet; for the four selected models*

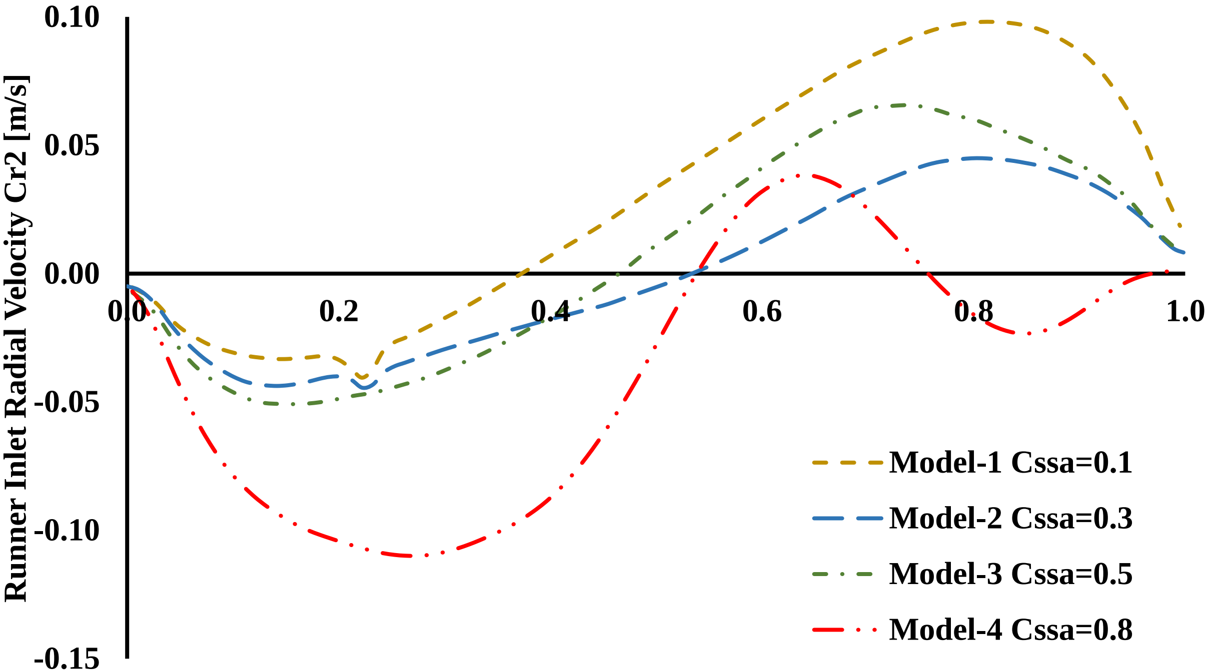

(a). Normalized Span Location ('0' is Hub, '1' is Tip)

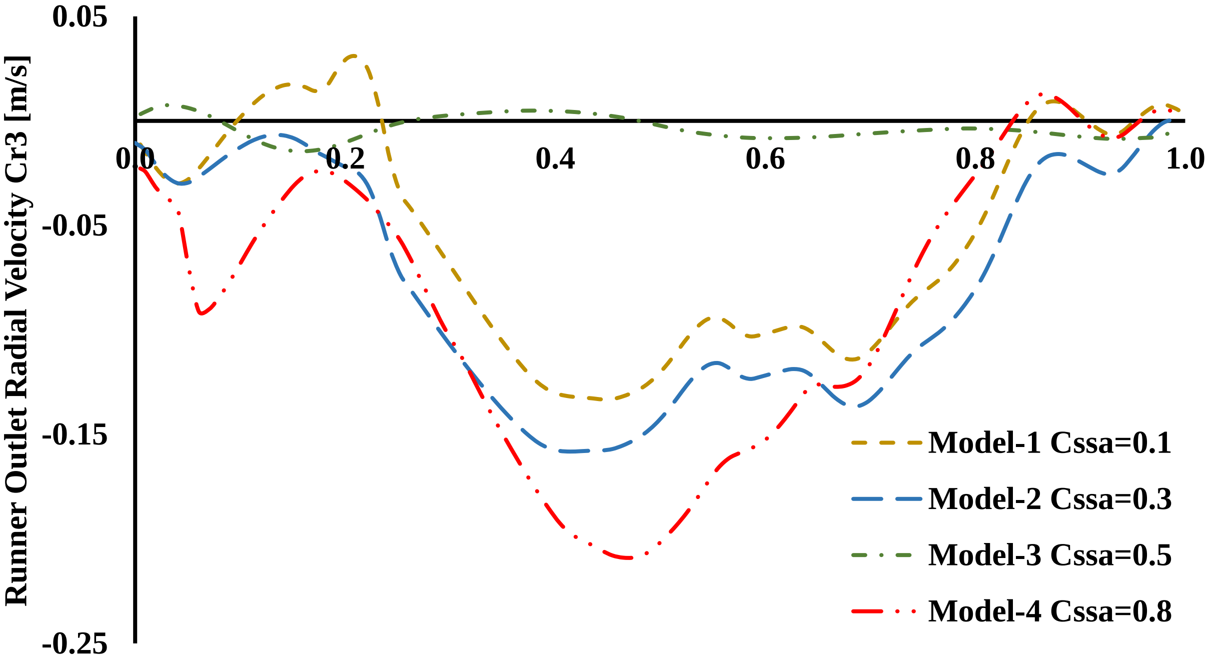

(b). Normalized Span Location ('0' is Hub, '1' is Tip)

Figure. Appendix D.12. *Runner-blade Radial velocity (C_r) distribution at (a). Runner Inlet; (b). Runner Outlet; for the four selected models*

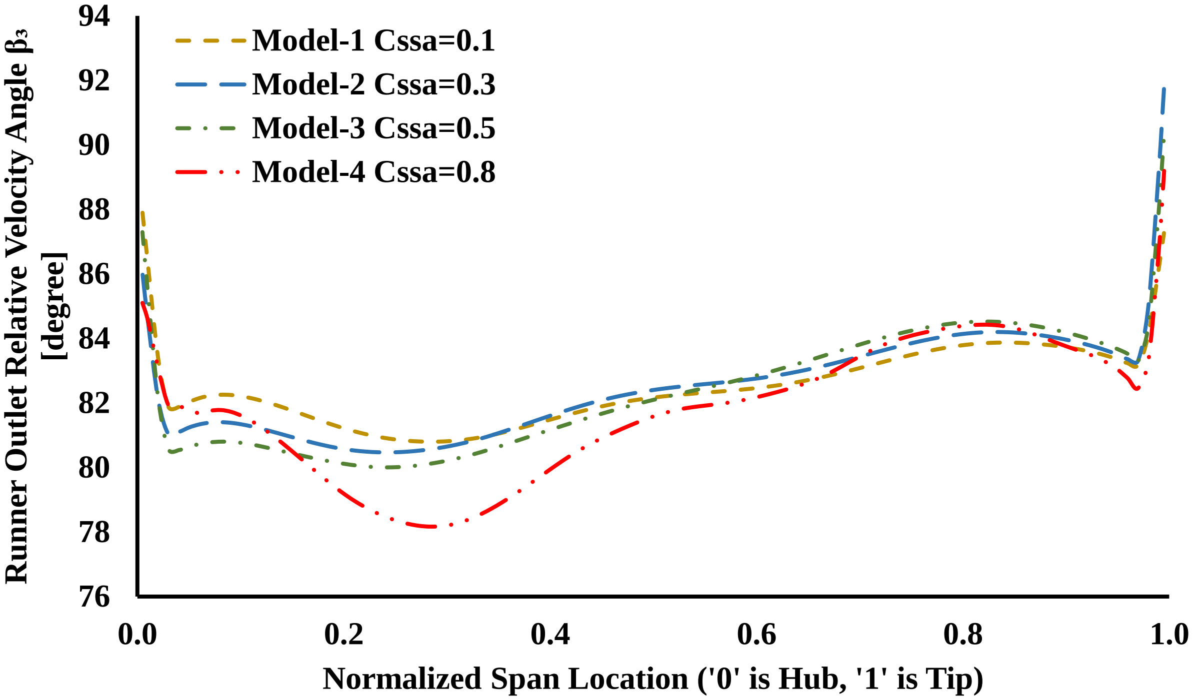

Figure. Appendix D.13. *Runner-blade Outlet relative velocity angle (*β_3*) distribution for the four selected models*

APPENDIX E: Additional results and plots for stator-blade inlet angle considerations.

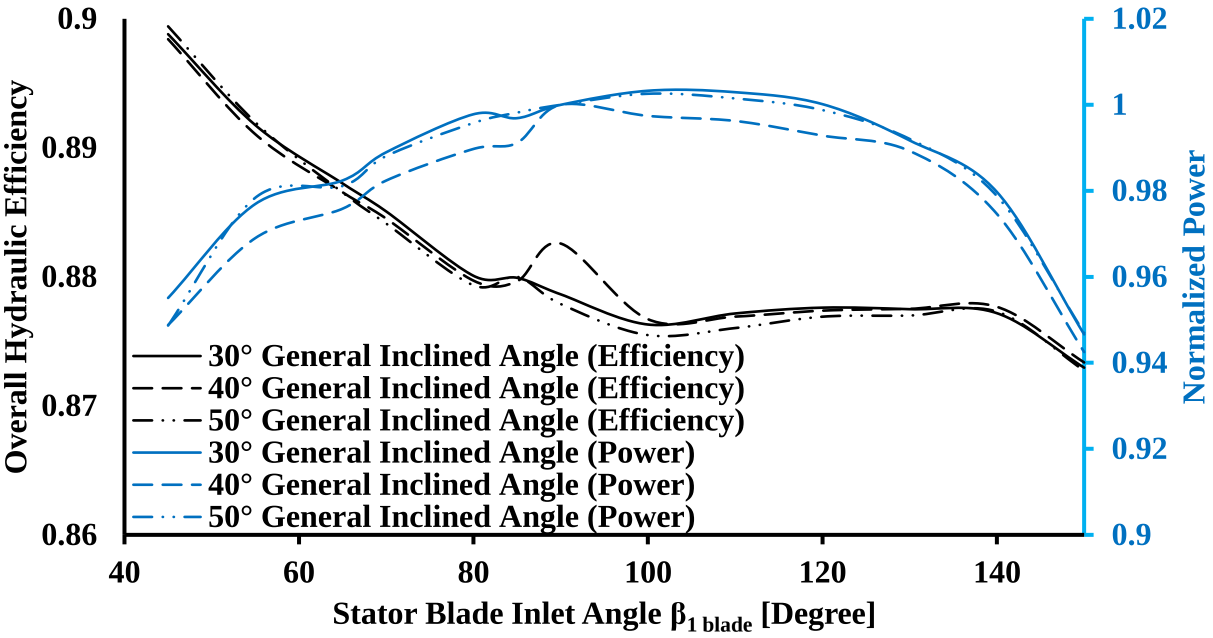

Figure. Appendix E.14. *The Relation between the overall hydraulic efficiency, Power Generation, and the Stator-blade inlet angle ($\beta_{1\ blade}$) for three general-inclined angle configurations under the same design flow rate condition (Q_{11}=0.103)*

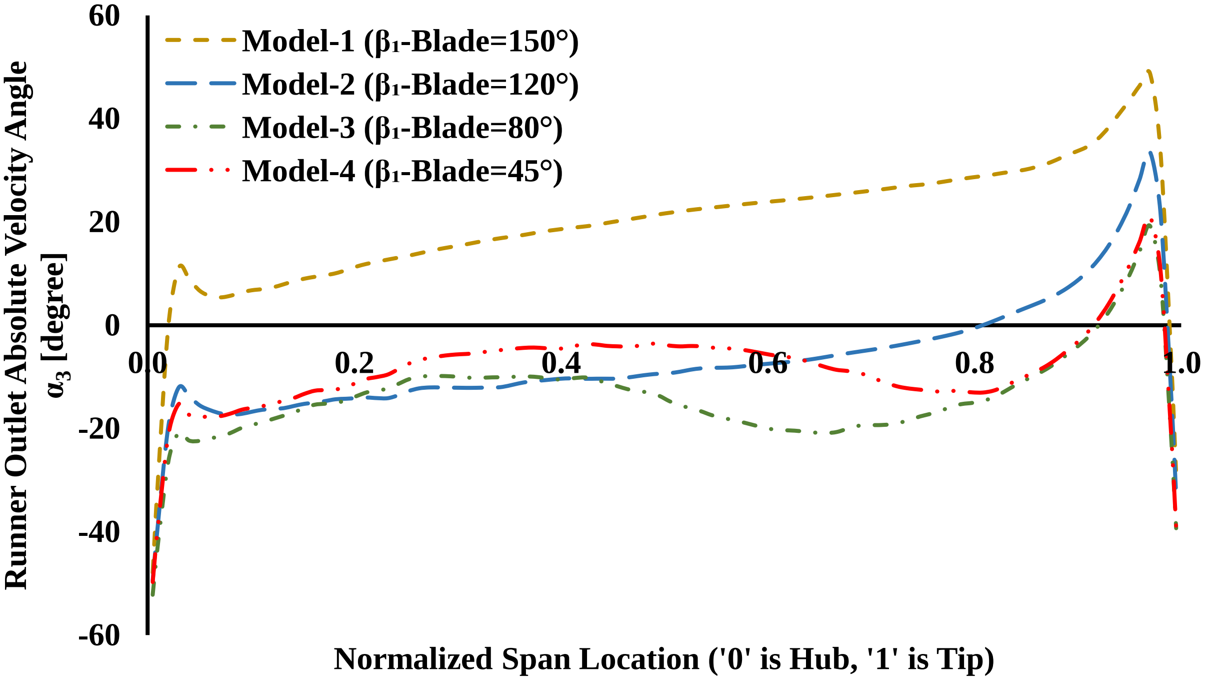

Figure. Appendix E.15. *Runner-blade Outlet absolute velocity angle (α_3) distribution for the four selected models*

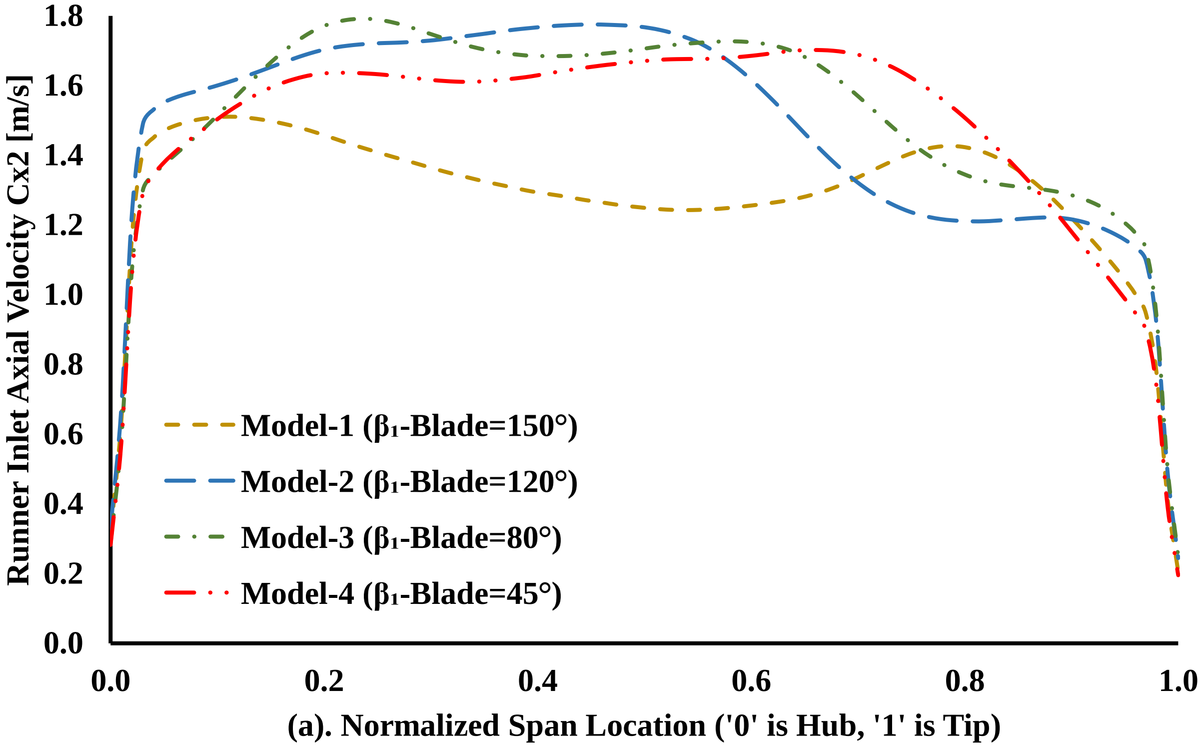

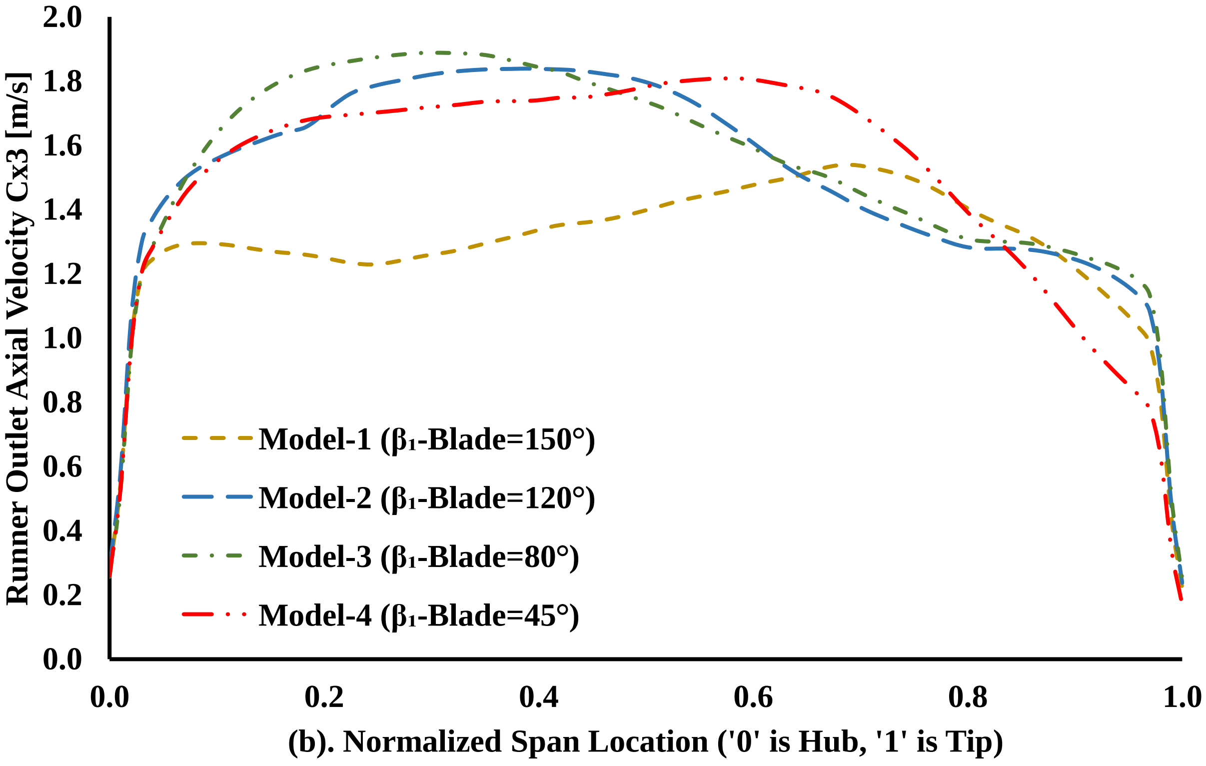

Figure. Appendix E.16. *Runner-blade Axial velocity (C_x) distribution at (a). Runner Inlet; (b). Runner Outlet; for the four selected models*

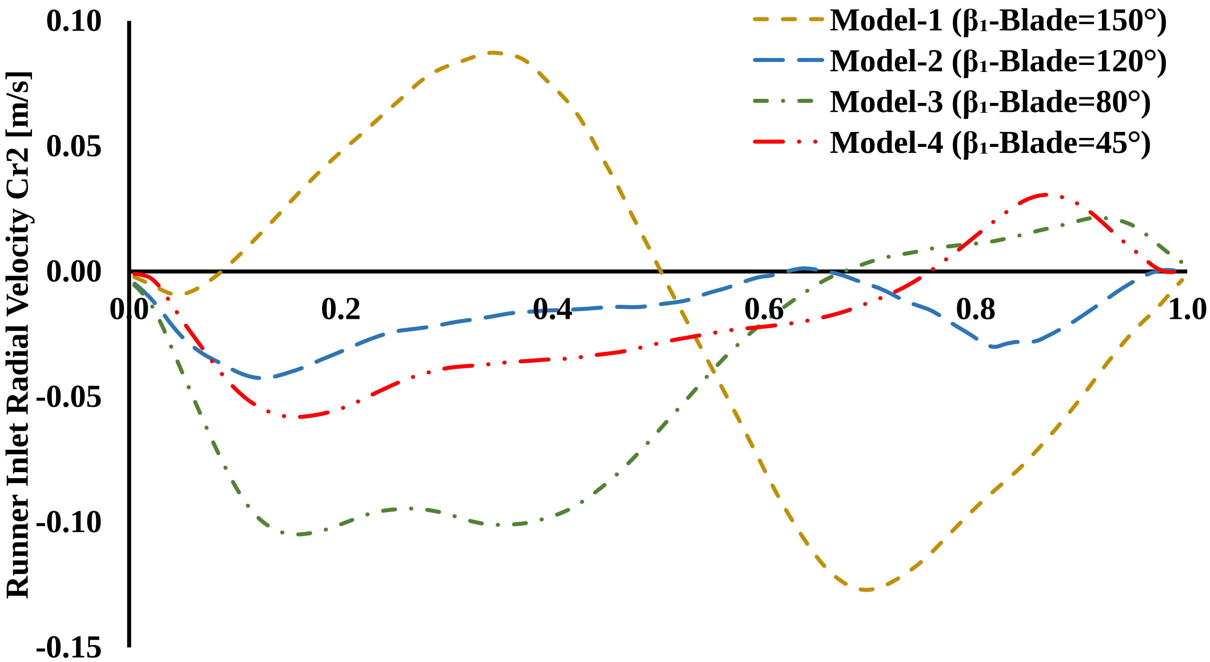

(a). Normalized Span Location ('0' is Hub, '1' is Tip)

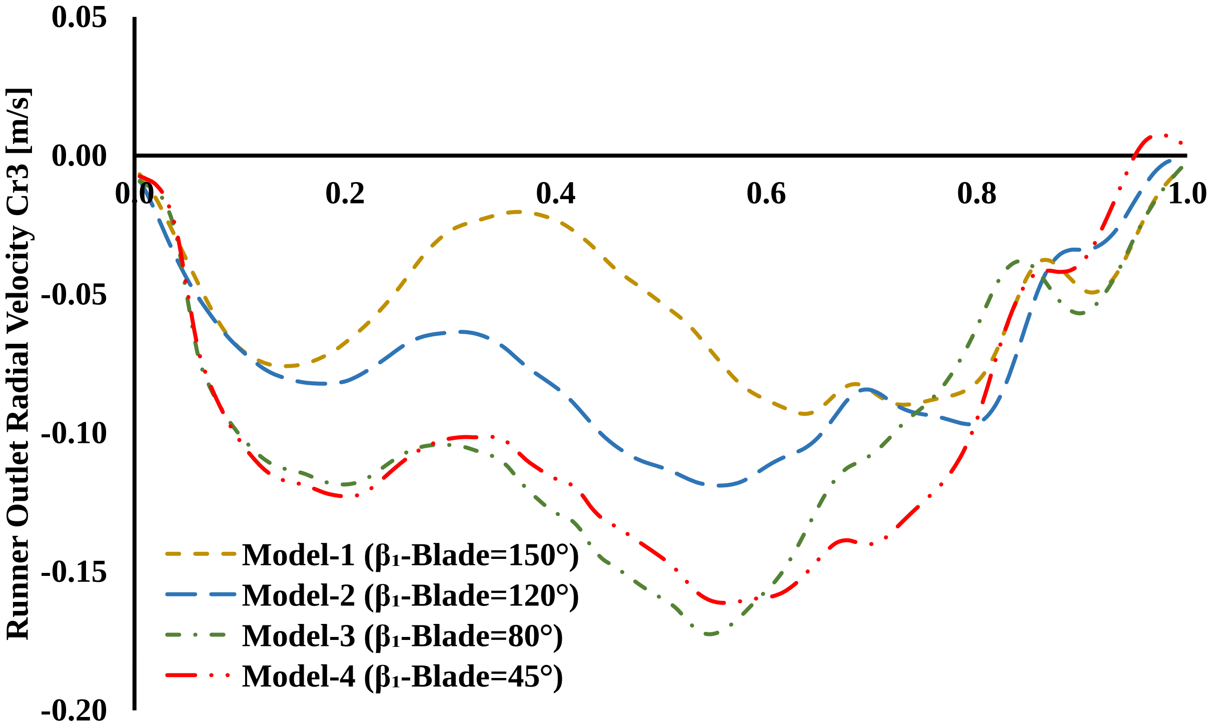

(b). Normalized Span Location ('0' is Hub, '1' is Tip)

***Figure. Appendix E.17**. Runner-blade Radial velocity (C_r) distribution at (a). Runner Inlet; (b). Runner Outlet; for the four selected models*

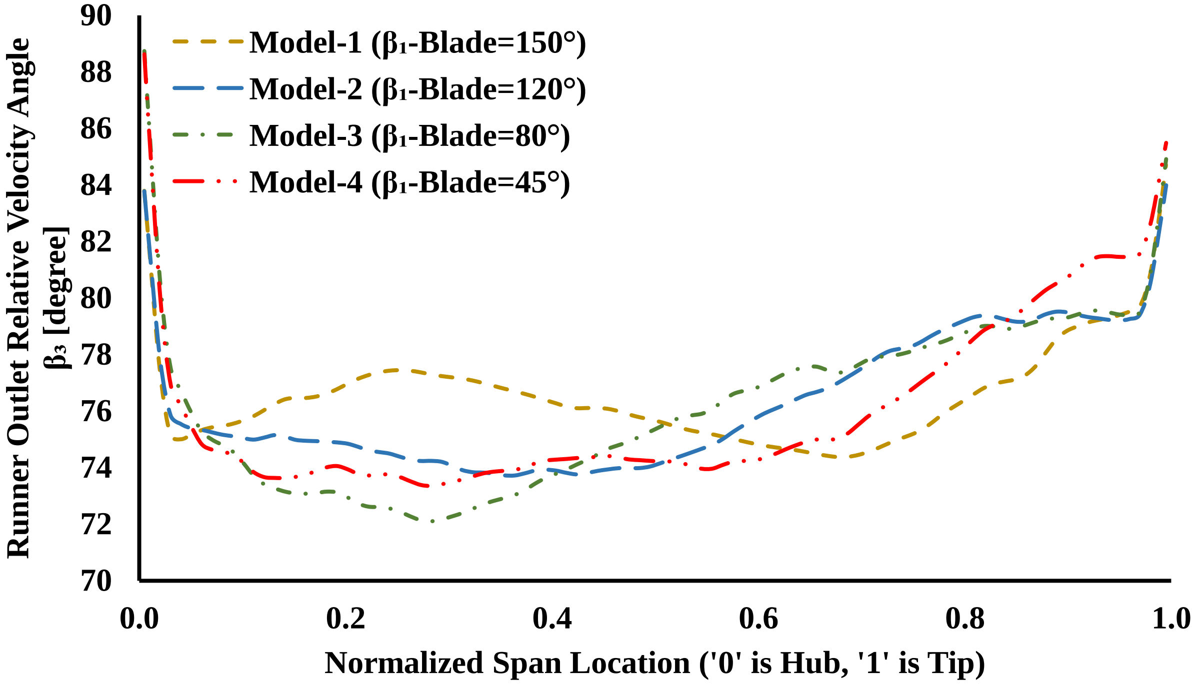

Figure. Appendix E.18*. Runner-blade Outlet relative velocity angle (β₃) distribution for the four selected models*

APPENDIX F: Additional results and plots for stator-blade solidity considerations.

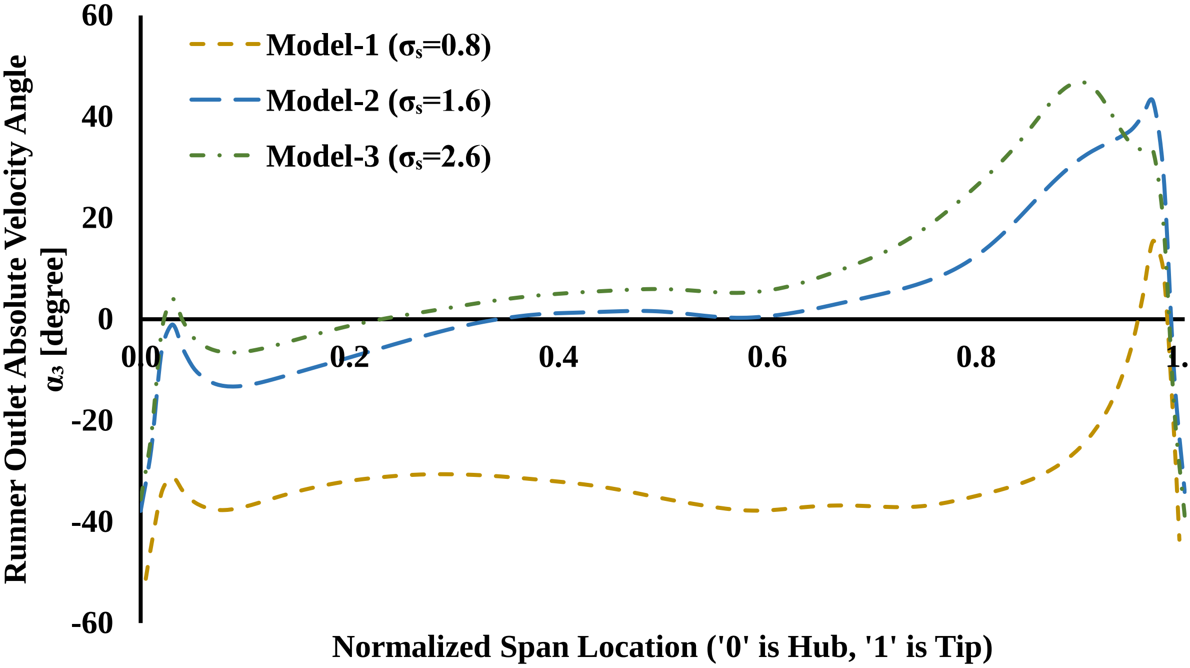

Figure. Appendix F.19. *Runner-blade Outlet absolute velocity angle (α_3) distribution for the three selected models*

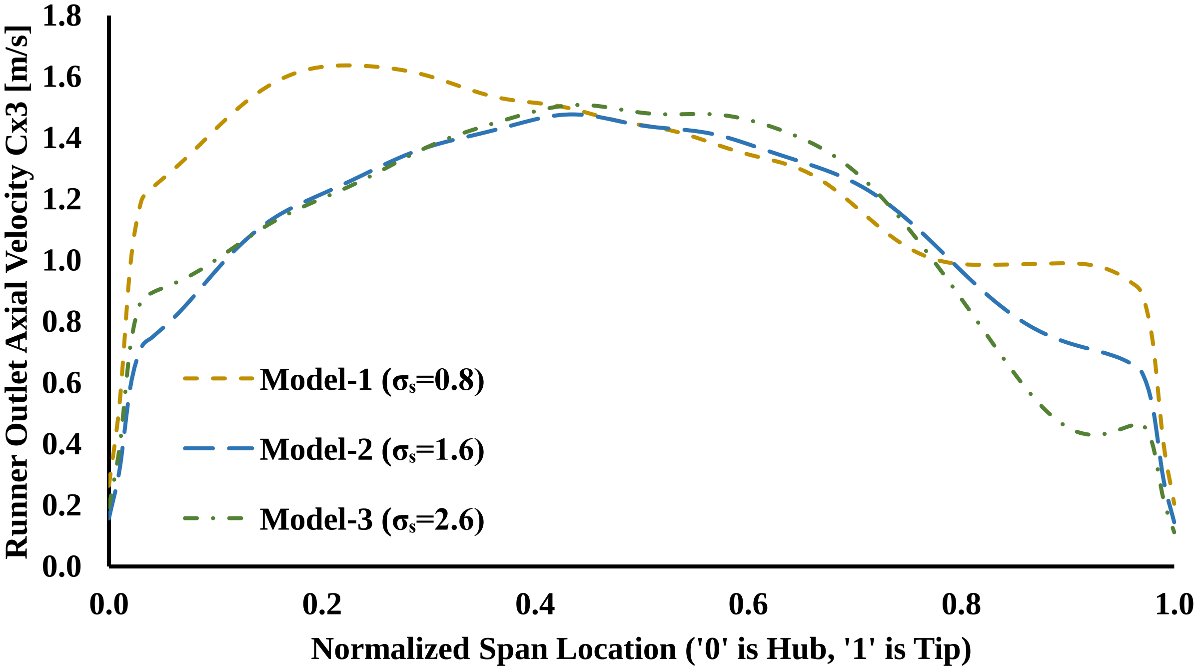

Figure. Appendix F.20. *Runner-blade Axial velocity (C_x) distribution at Runner Outlet, for the three selected models*

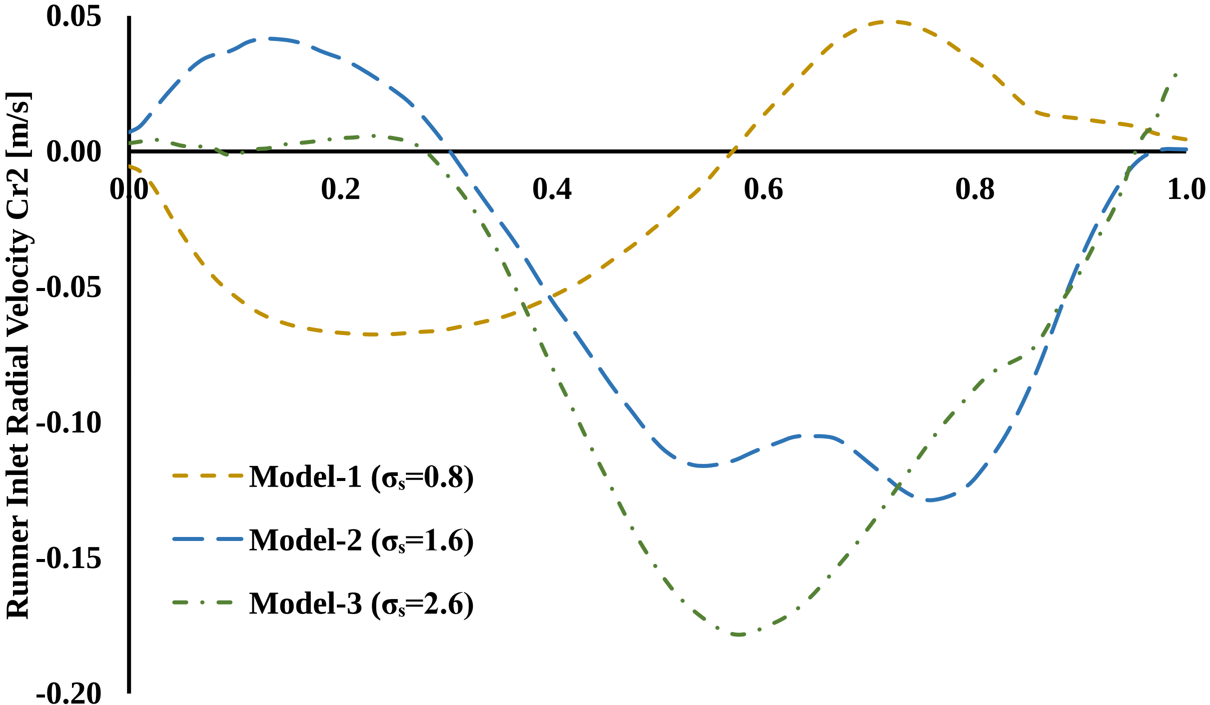

(a). Normalized Span Location ('0' is Hub, '1' is Tip)

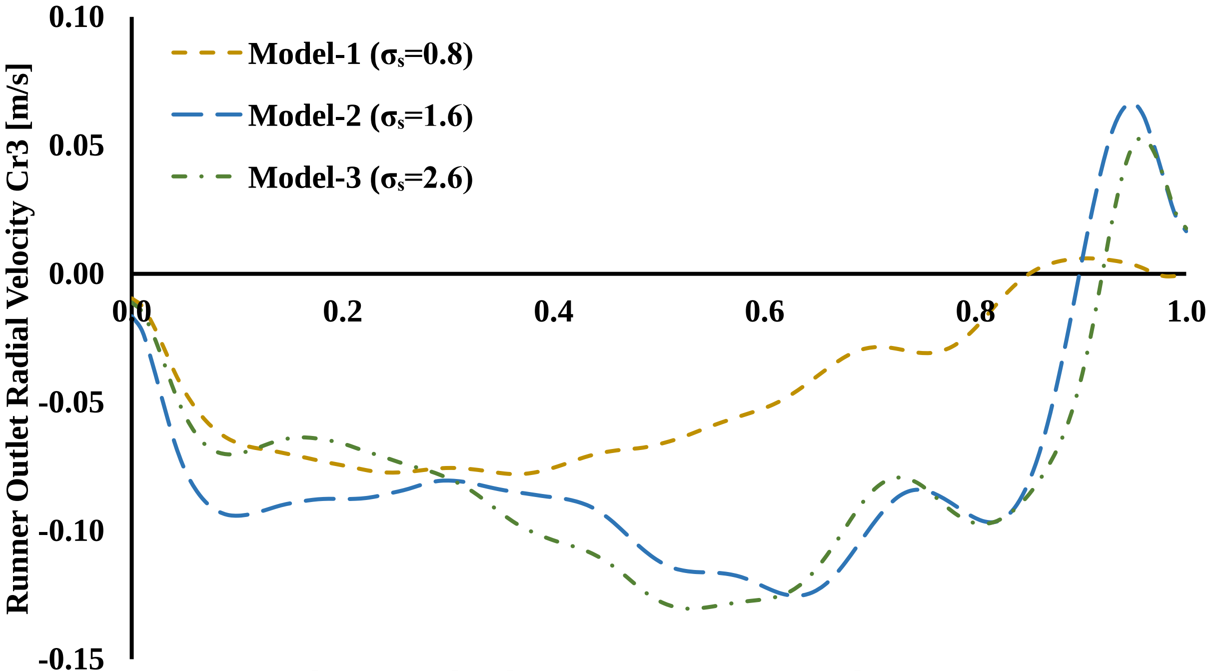

(b). Normalized Span Location ('0' is Hub, '1' is Tip)

Figure. Appendix F.21. *Runner-blade Radial velocity (C_r) distribution at (a). Runner Inlet; (b). Runner Outlet; for the three selected models*

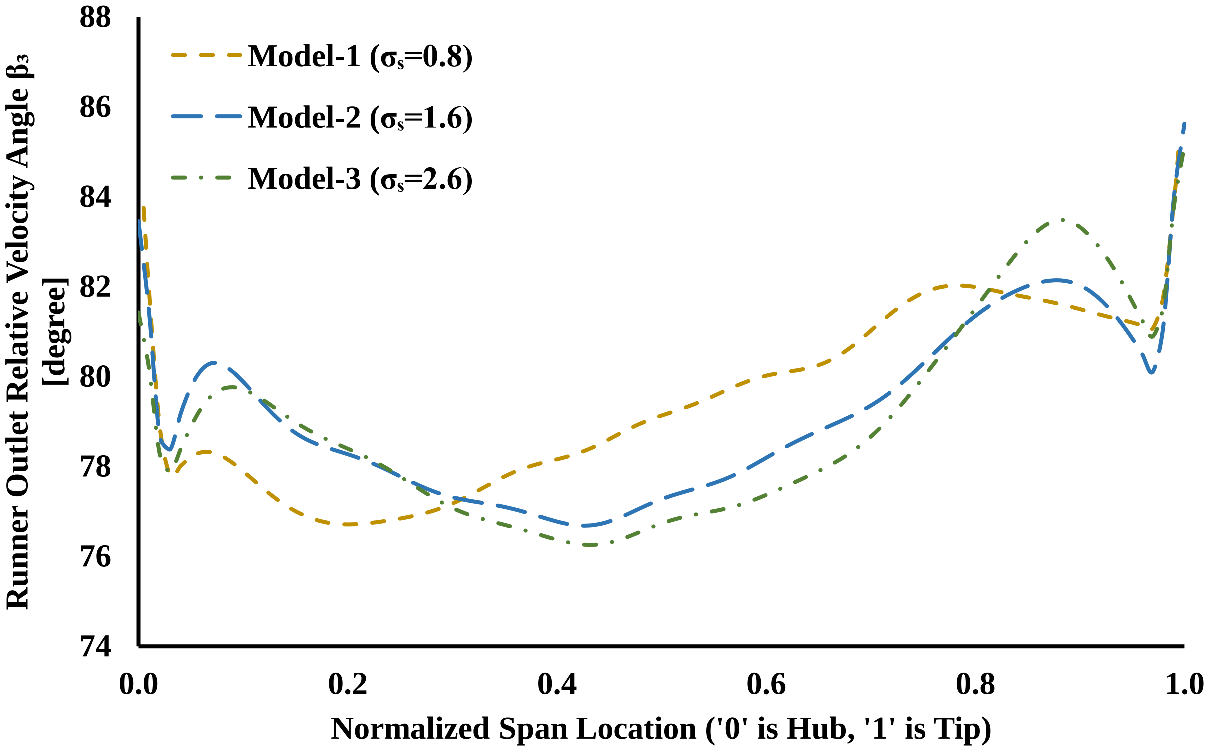

Figure. Appendix F.22. *Runner-blade Outlet relative velocity angle (β_3) distribution for the three selected models*

APPENDIX G: Additional results and plots for stator-blade thickness considerations.

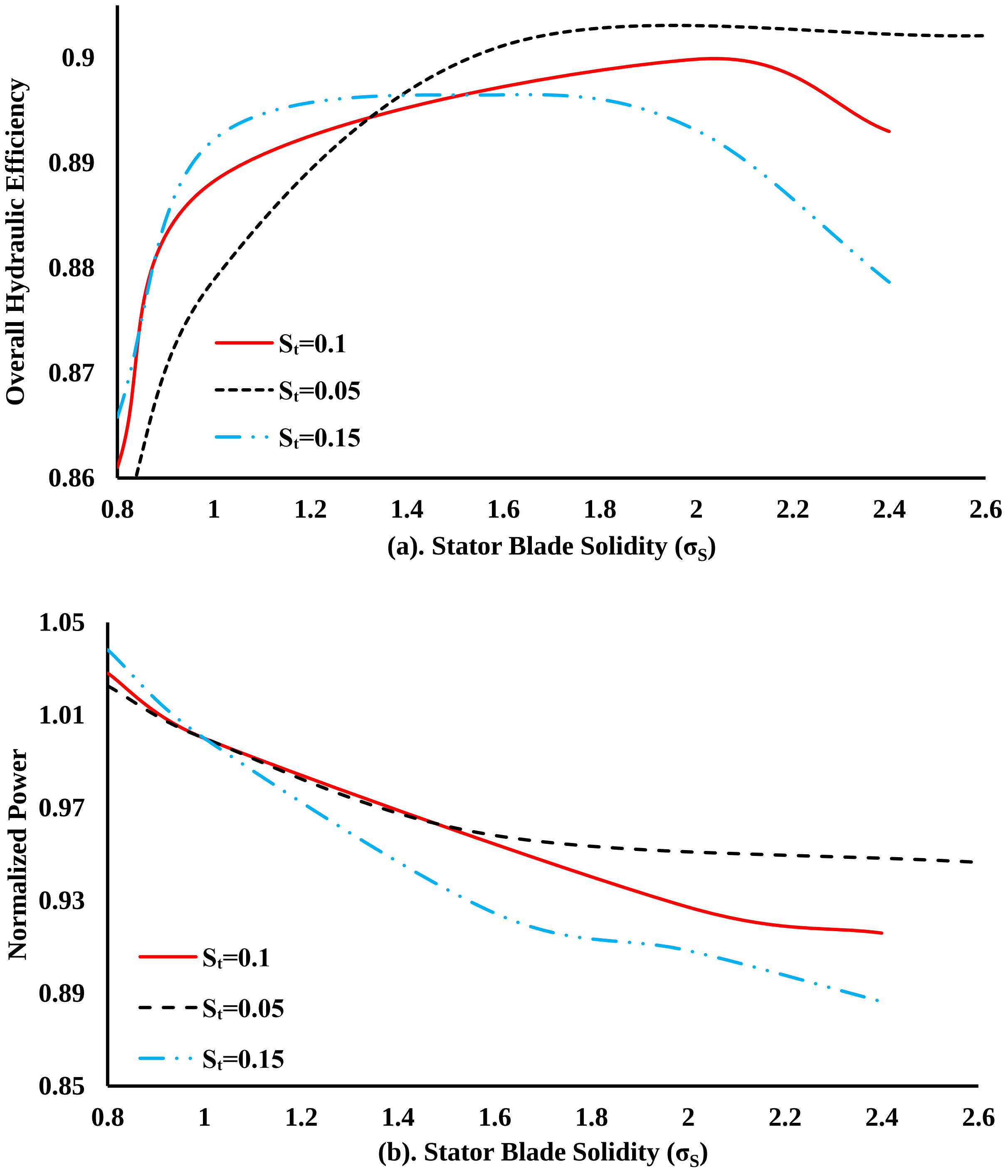

Figure. Appendix G.23*. The relation between (a). overall performance, (b). Normalized Power, and stator-blade solidity under three stator-blade relative thickness values for one flow rate condition (Q_{11}=0.207), and 20 stator configuration*

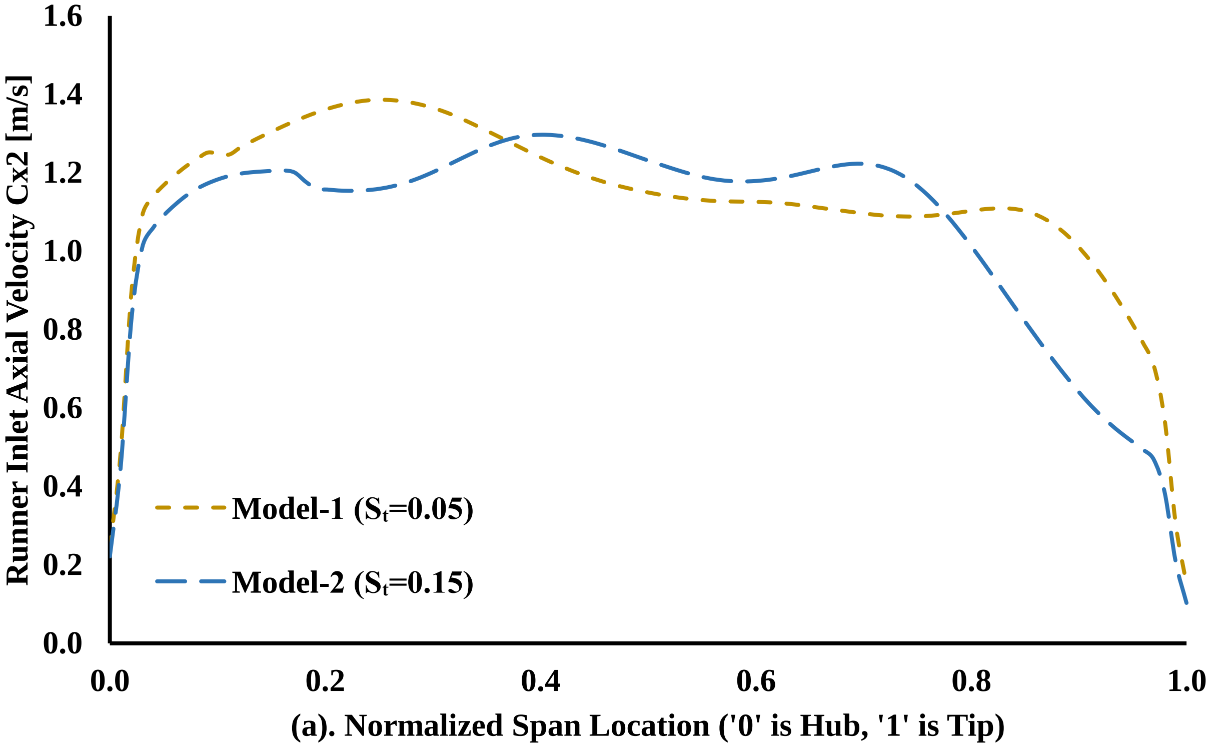

(a). Normalized Span Location ('0' is Hub, '1' is Tip)

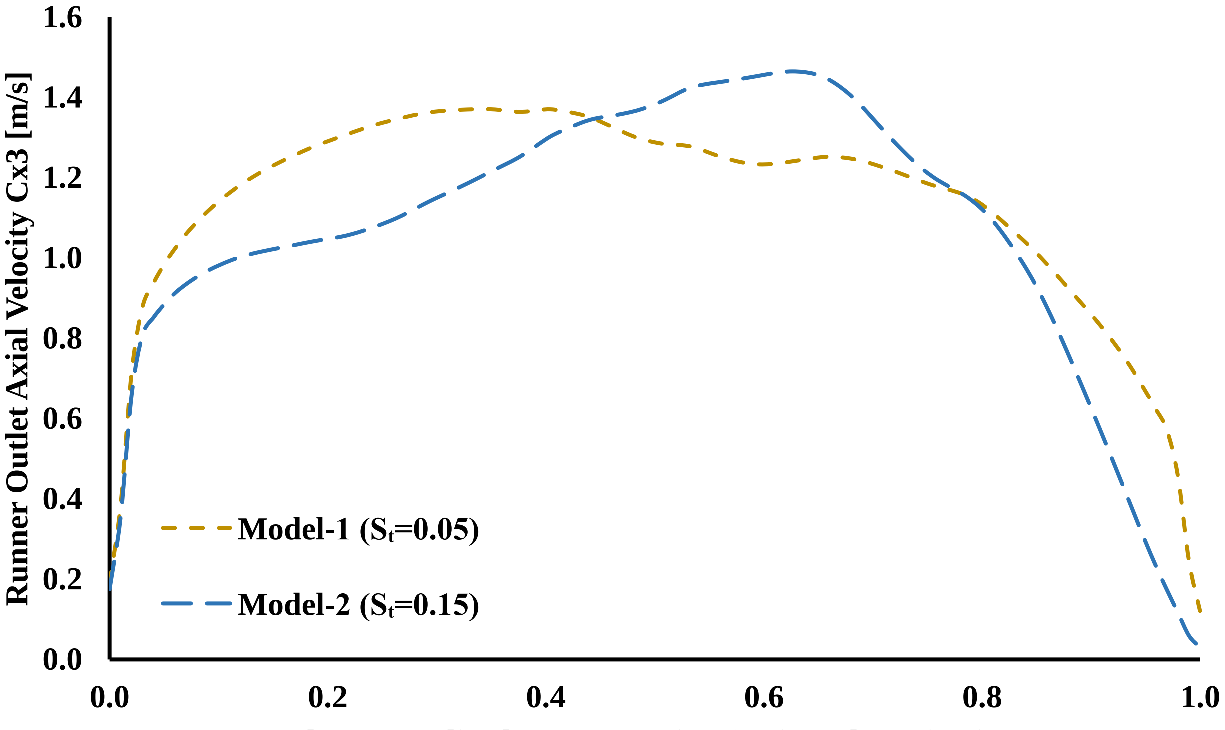

(b). Normalized Span Location ('0' is Hub, '1' is Tip)

Figure. Appendix G.24. *Runner-blade Axial velocity (C_x) distribution at (a). Runner Inlet; (b). Runner Outlet; for the two selected models*

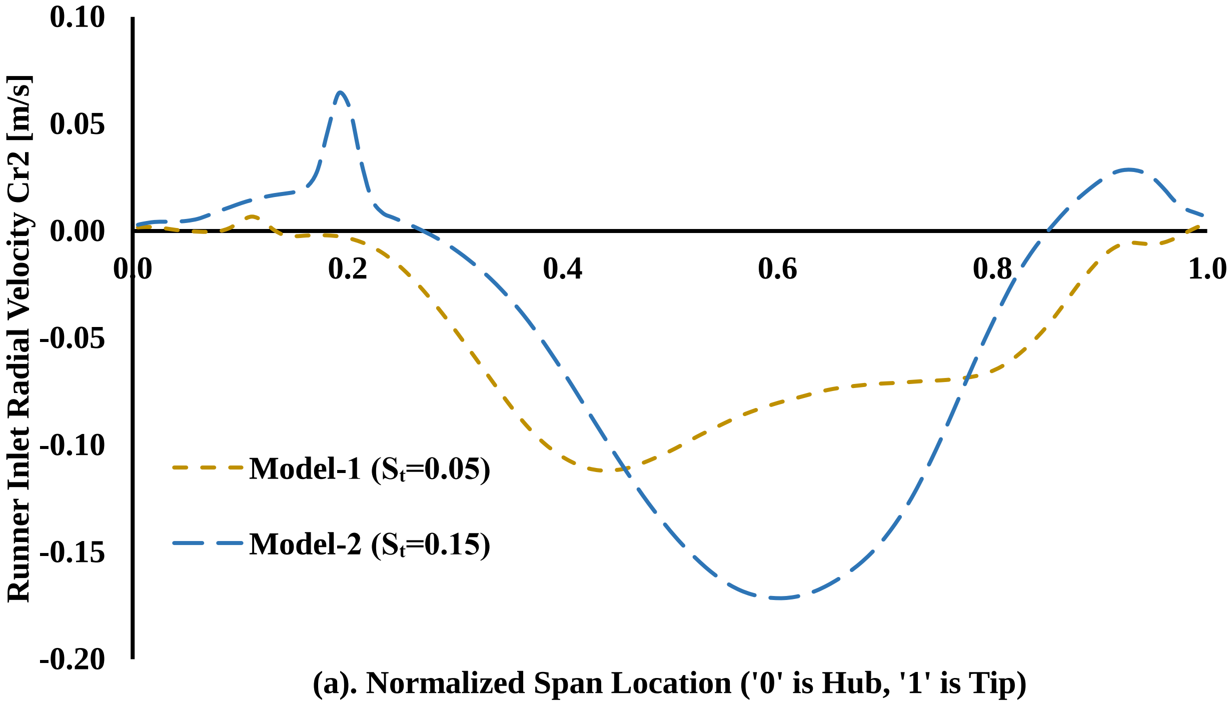

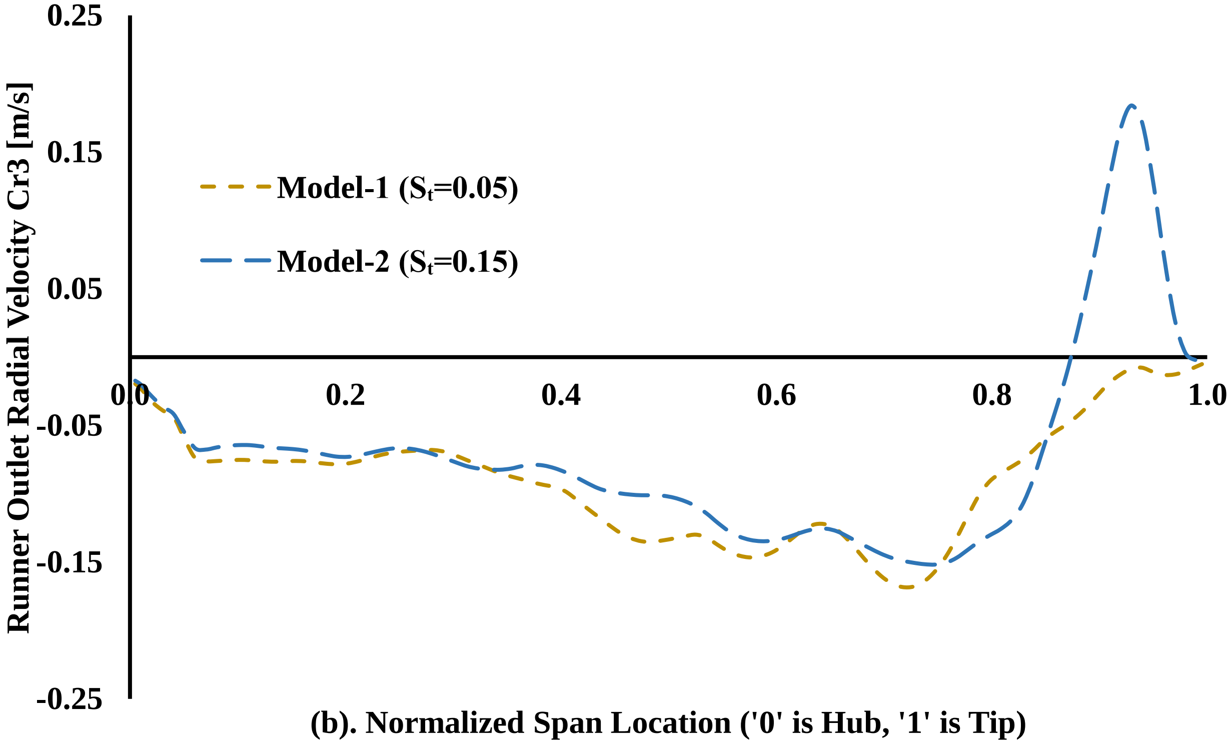

Figure. Appendix G.25. *Runner-blade Radial velocity (C_r) distribution at (a). Runner Inlet; (b). Runner Outlet; for the two selected models*

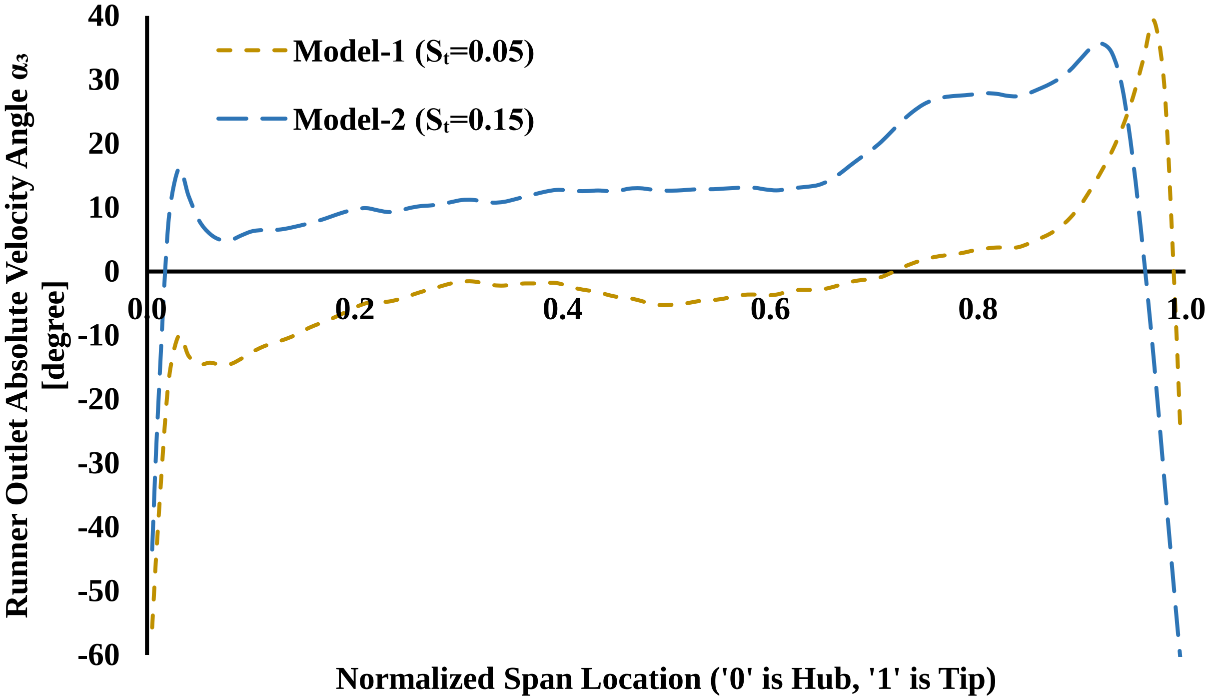

Figure. Appendix G.26*. Runner-blade Outlet absolute velocity angle (α_3) distribution for the two selected models.*

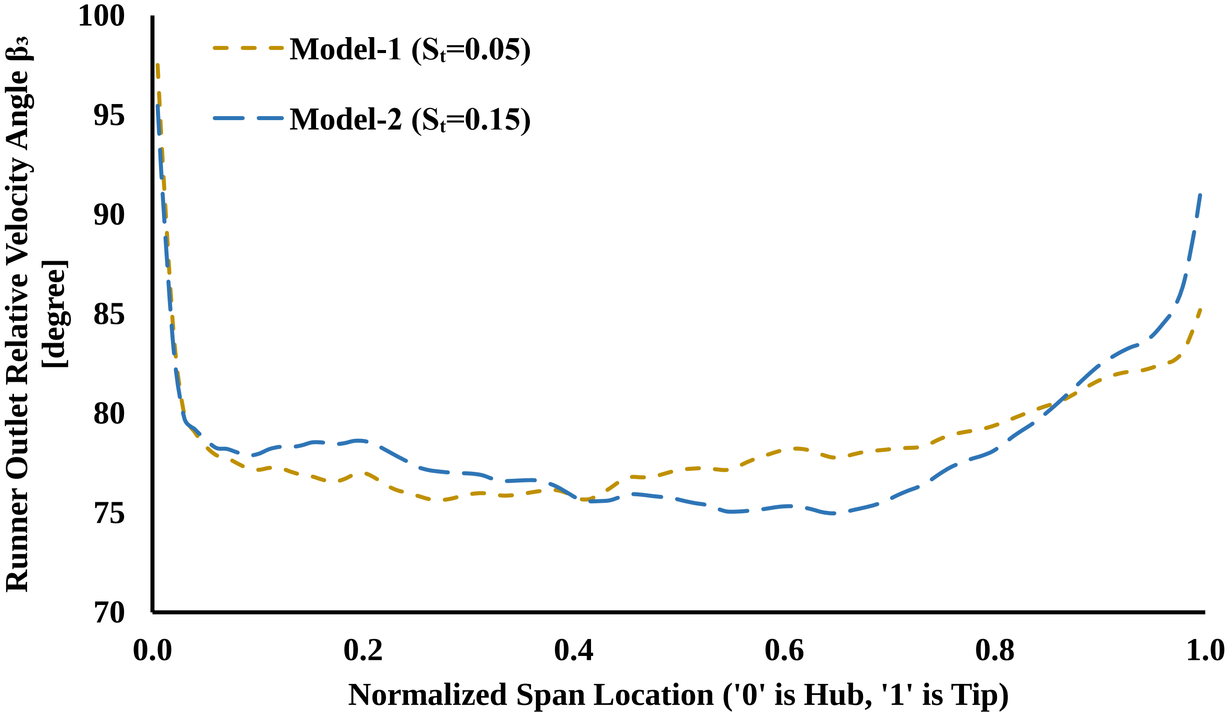

Figure. Appendix G.27*. Runner-blade Outlet relative velocity angle (β_3) distribution for the two selected models*

APPENDIX H: Additional results and plots for runner-blade Crsa constant considerations.

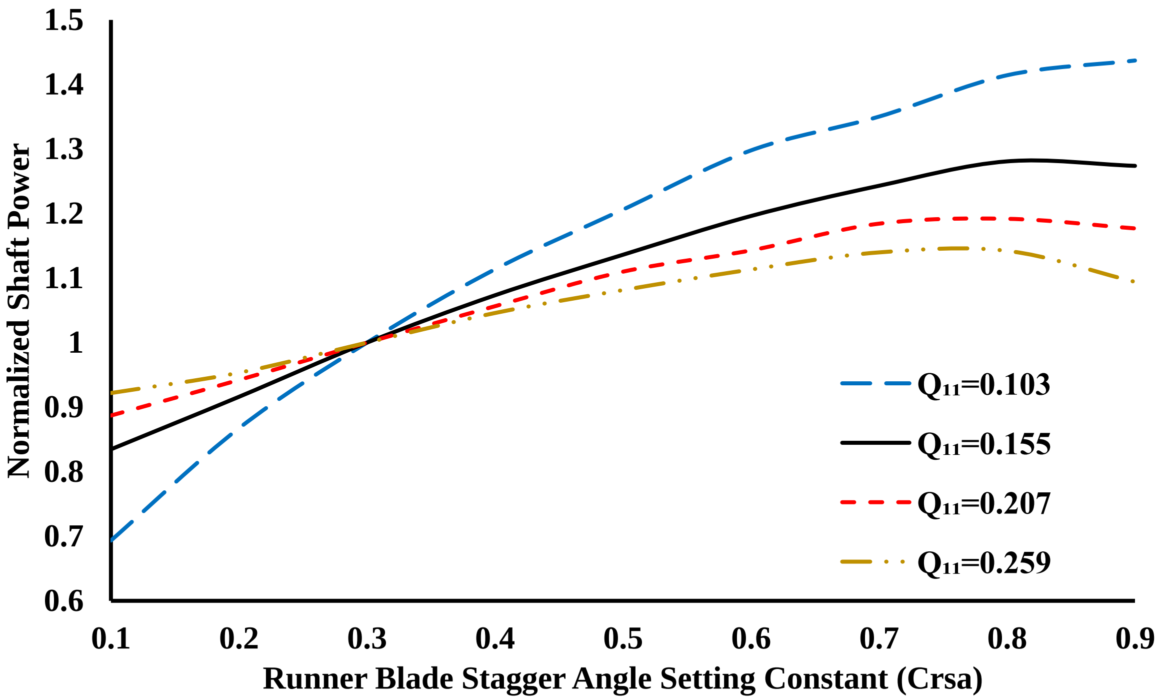

Figure. Appendix H.28. *The relation between normalized power and runner-blade stagger-angle setting constant* C_{rsa} *for four flow rate conditions. (The power is normalized with* C_{rsa}*=0.3 models)*

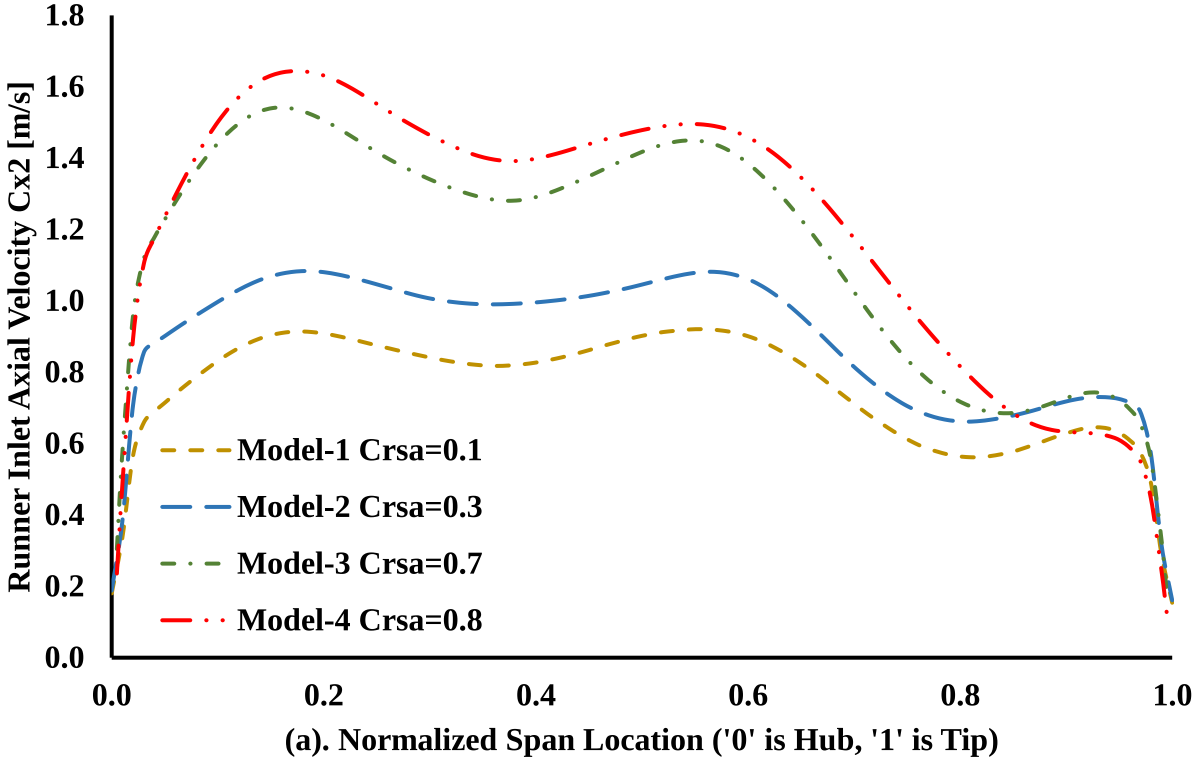

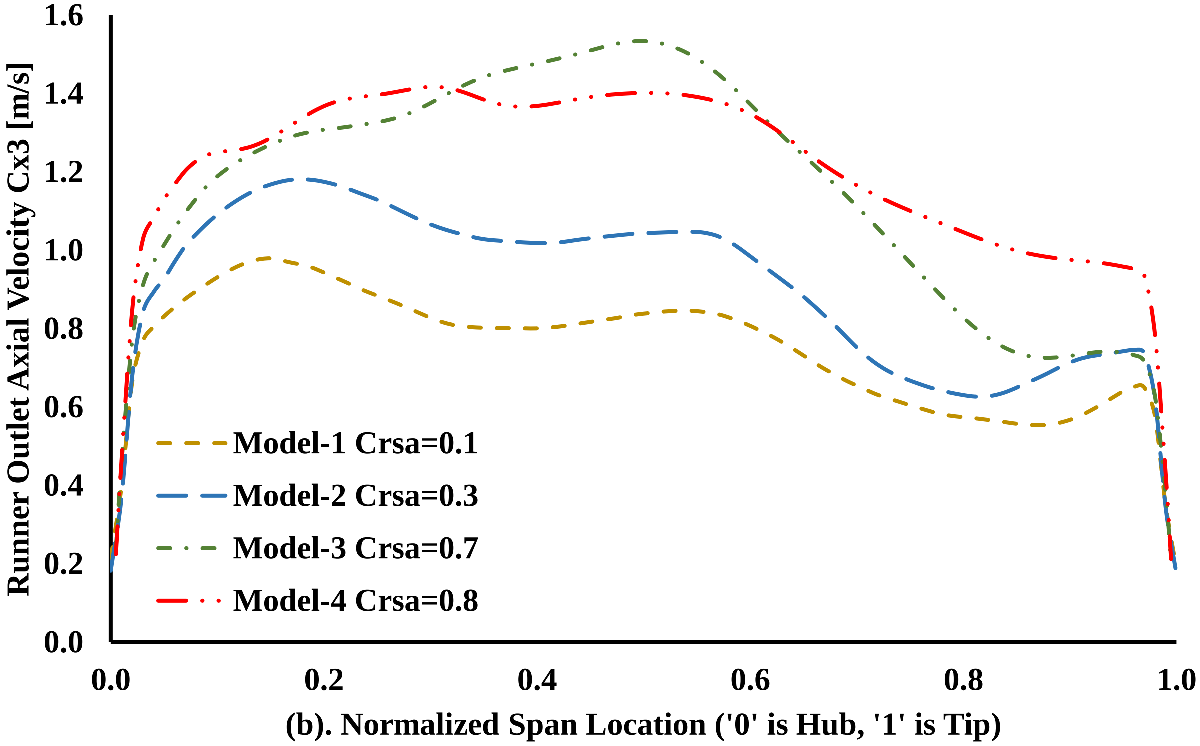

Figure. Appendix H.29. *Runner-blade Axial velocity (C_x) distribution at (a). Runner Inlet; (b). Runner Outlet; for the four selected models*

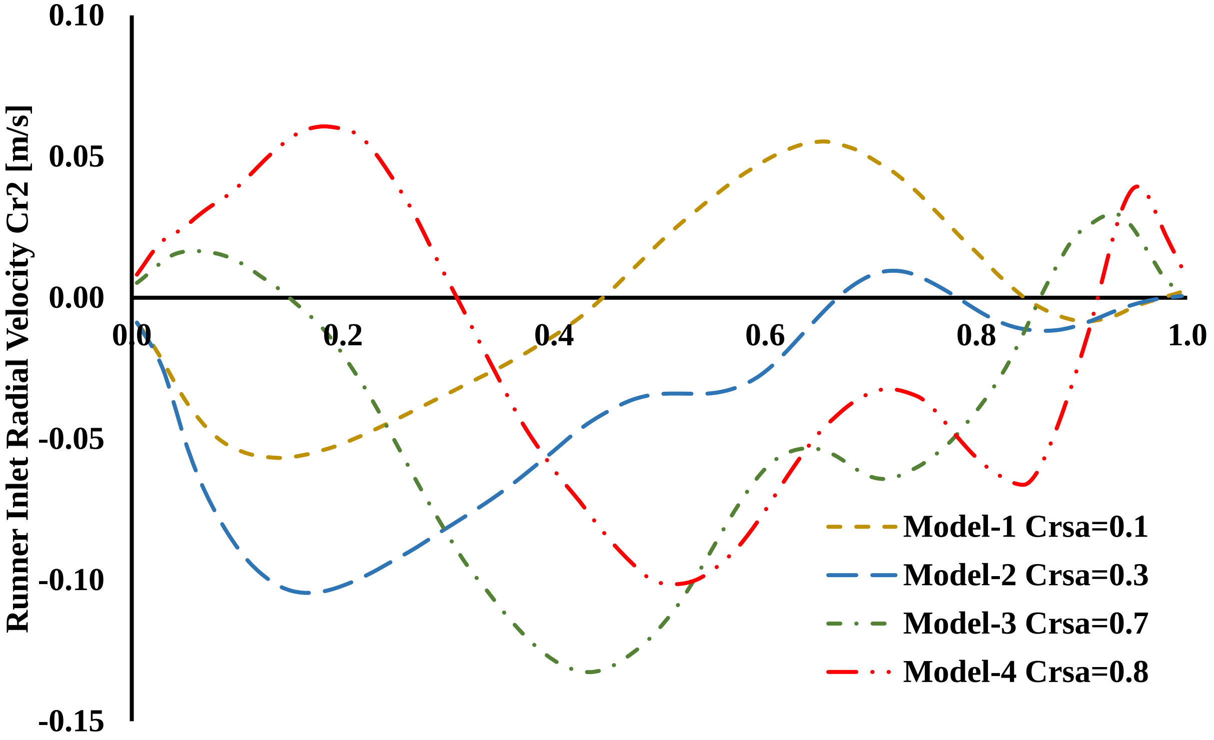

(a). Normalized Span Location ('0' is Hub, '1' is Tip)

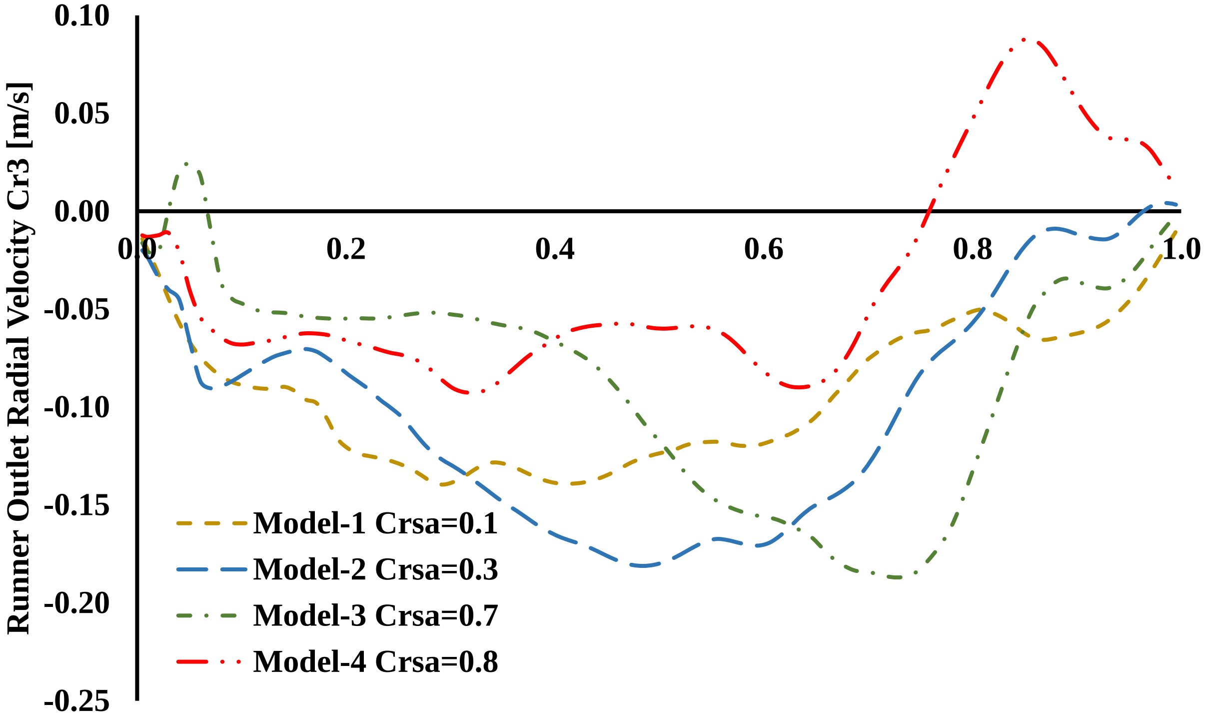

(b). Normalized Span Location ('0' is Hub, '1' is Tip)

***Figure. Appendix H.30**. Runner-blade Radial velocity (C_r) distribution at (a). Runner Inlet; (b). Runner Outlet; for the four selected models*

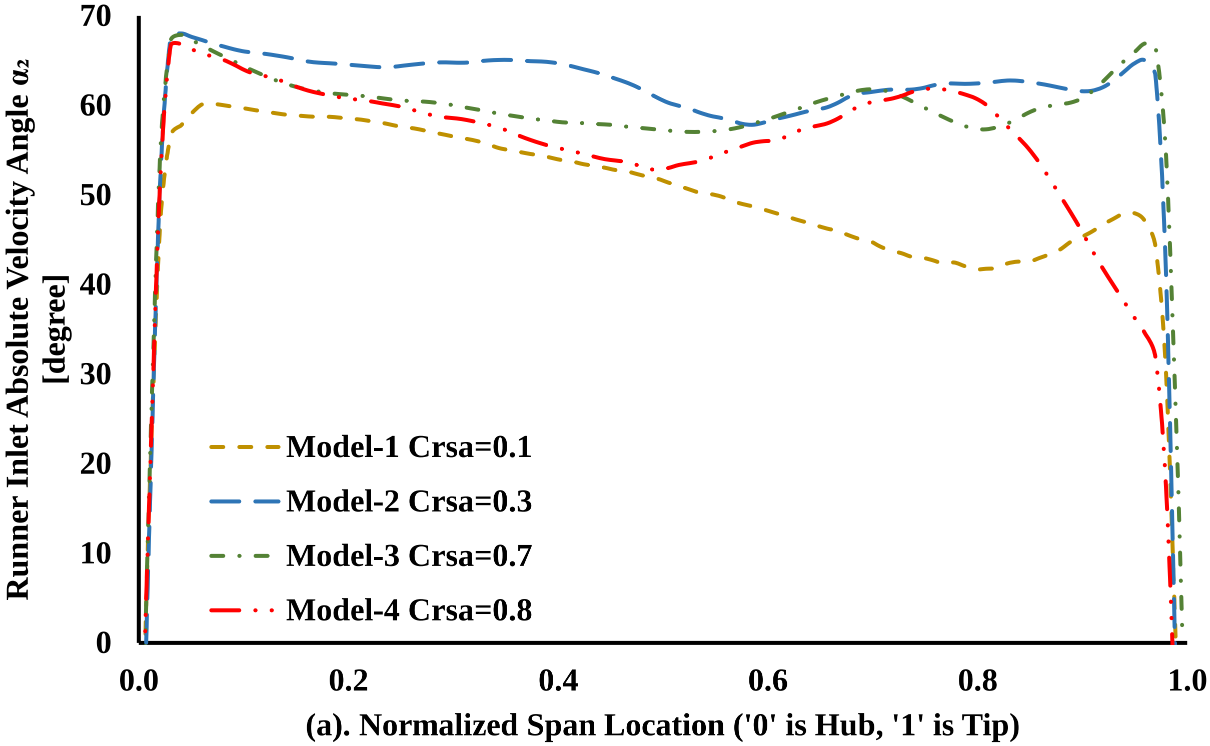

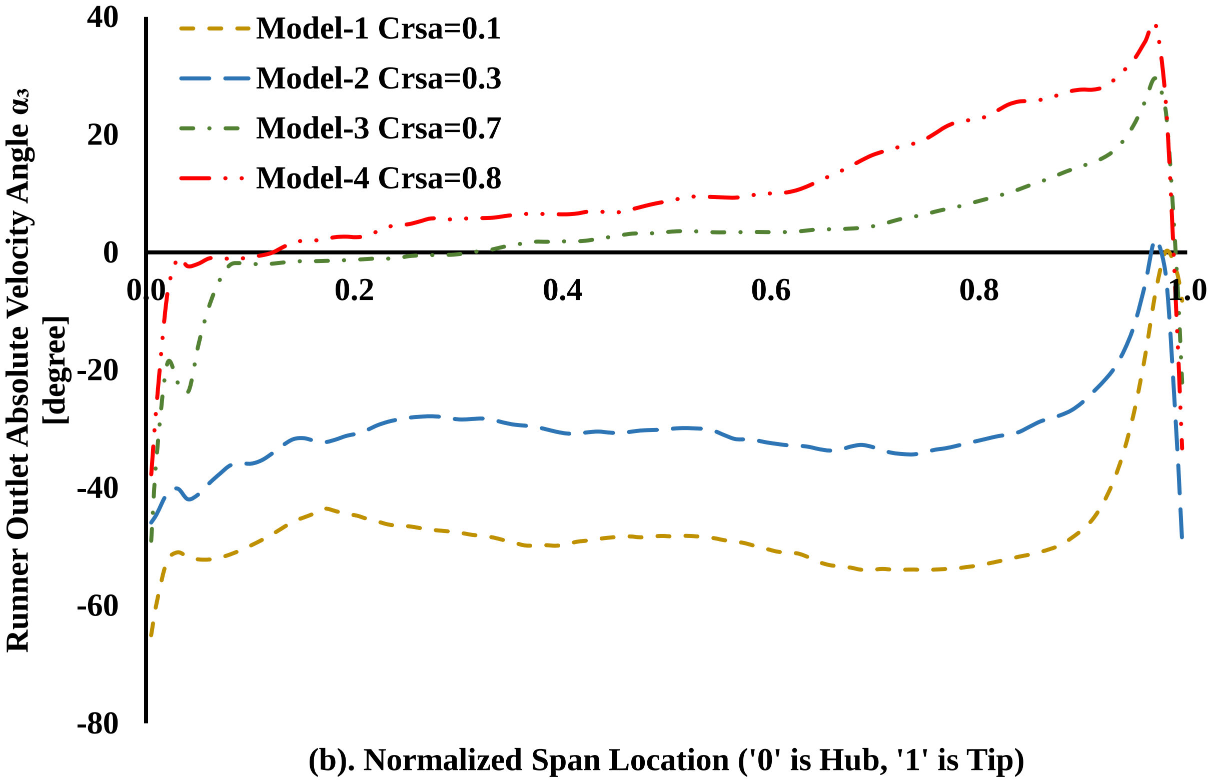

Figure. Appendix H.31. *Runner-blade absolute velocity angle (α) distribution at (a). Runner Inlet (α_2); (b). Runner Outlet (α_3), for the four selected models*

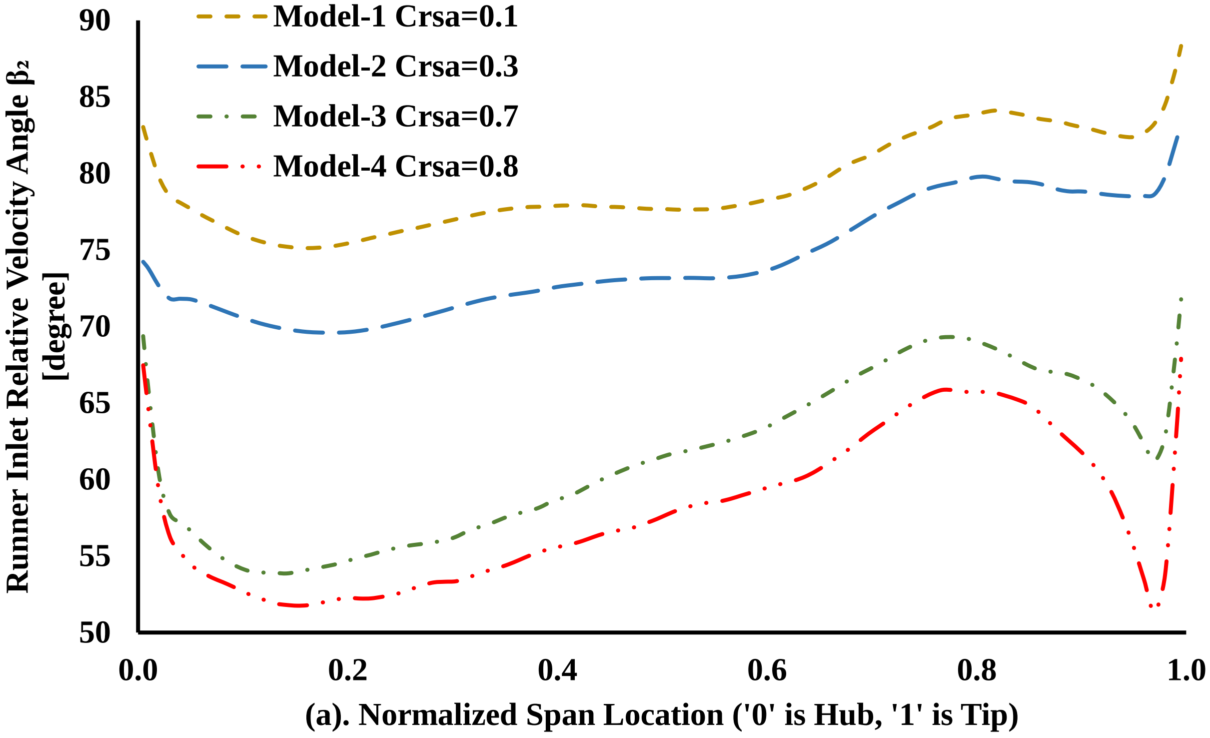

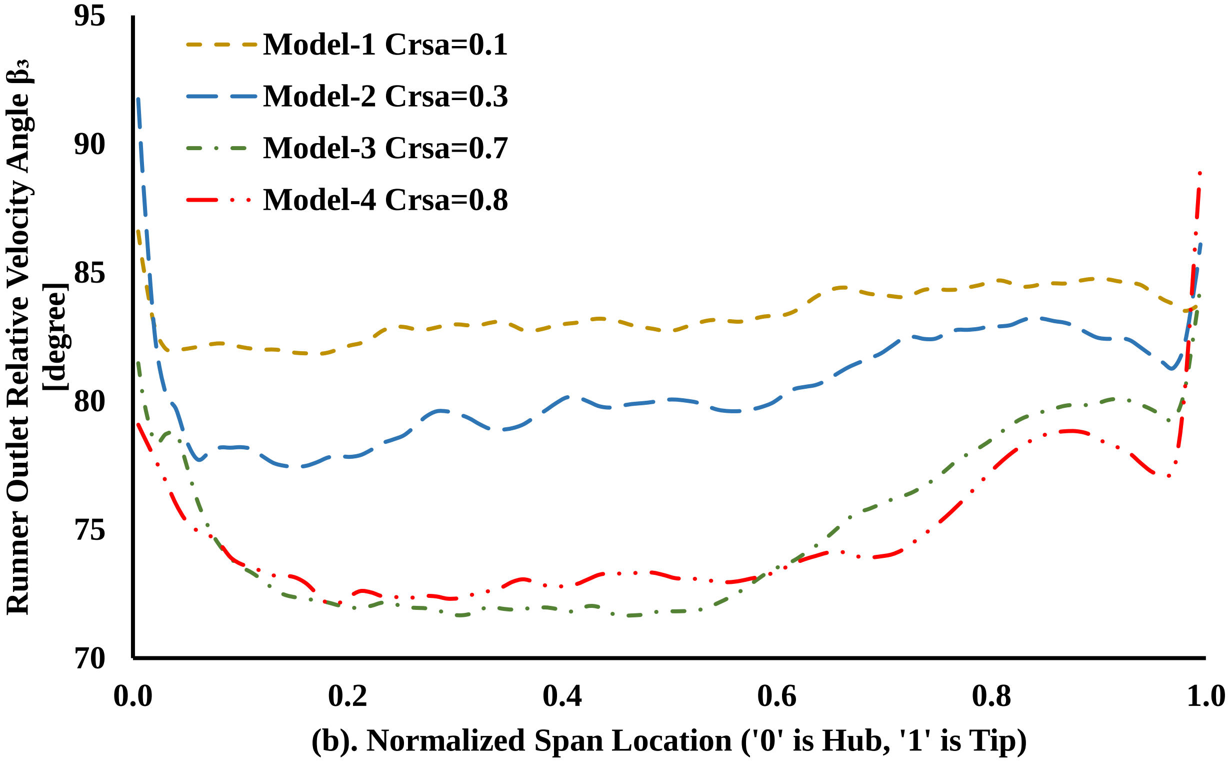

Figure. Appendix H.32. *Runner-blade relative velocity angle (β) distribution at (a). Runner Inlet (β_2); (b). Runner Outlet (β_3), for the four selected models*

APPENDIX I: Additional results and plots for runner-blade solidity considerations

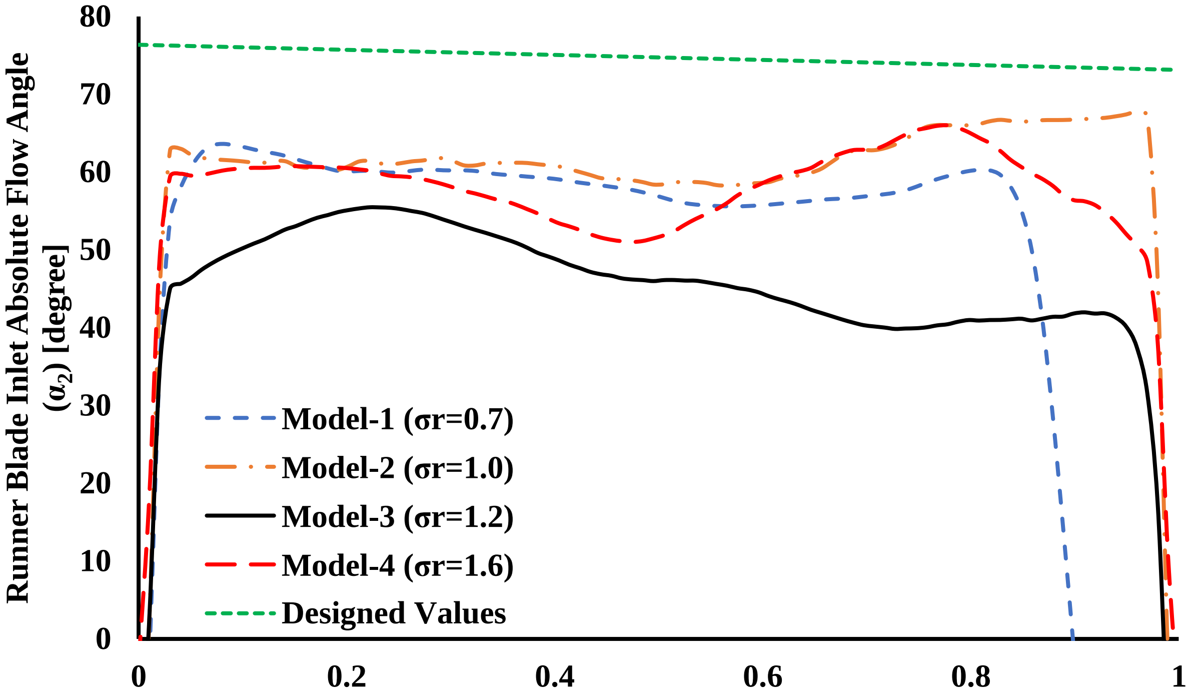

(a). Normalized Span Location ('0' is Hub, '1' is Tip)

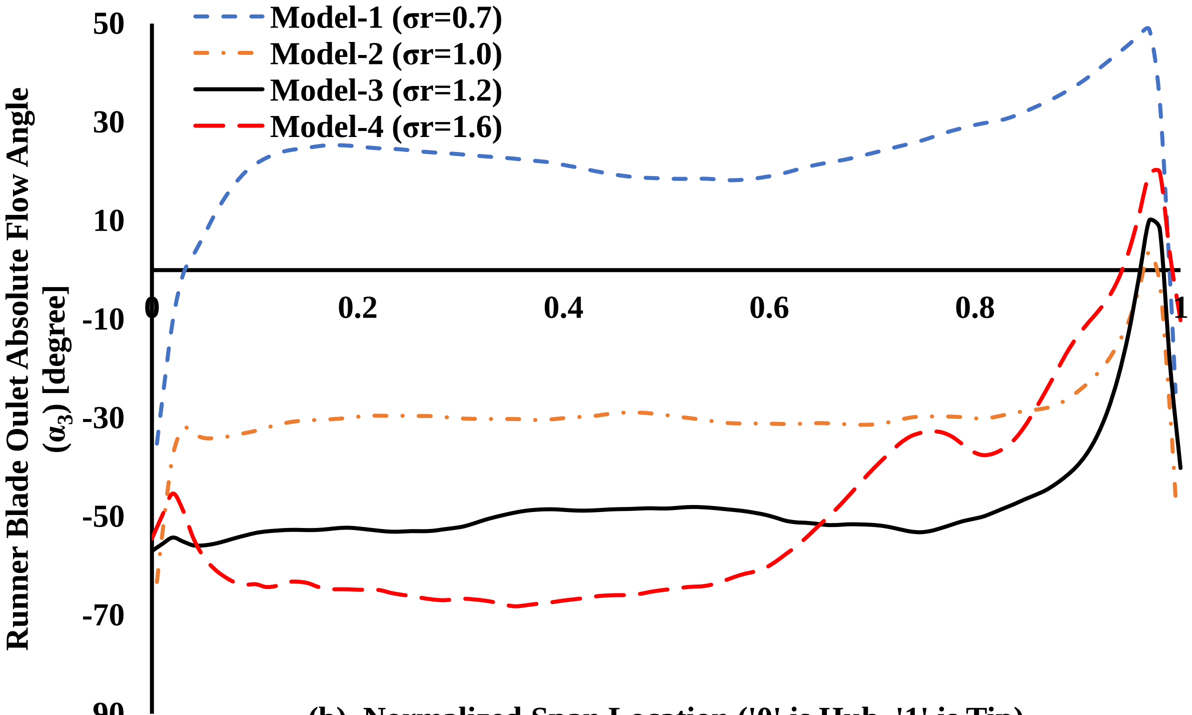

(b). Normalized Span Location ('0' is Hub, '1' is Tip)

Figure. Appendix I.33. *Runner-blade absolute velocity angle (α_3) distribution at (a). Runner Inlet; (b). Runner Outlet; for the four selected models*

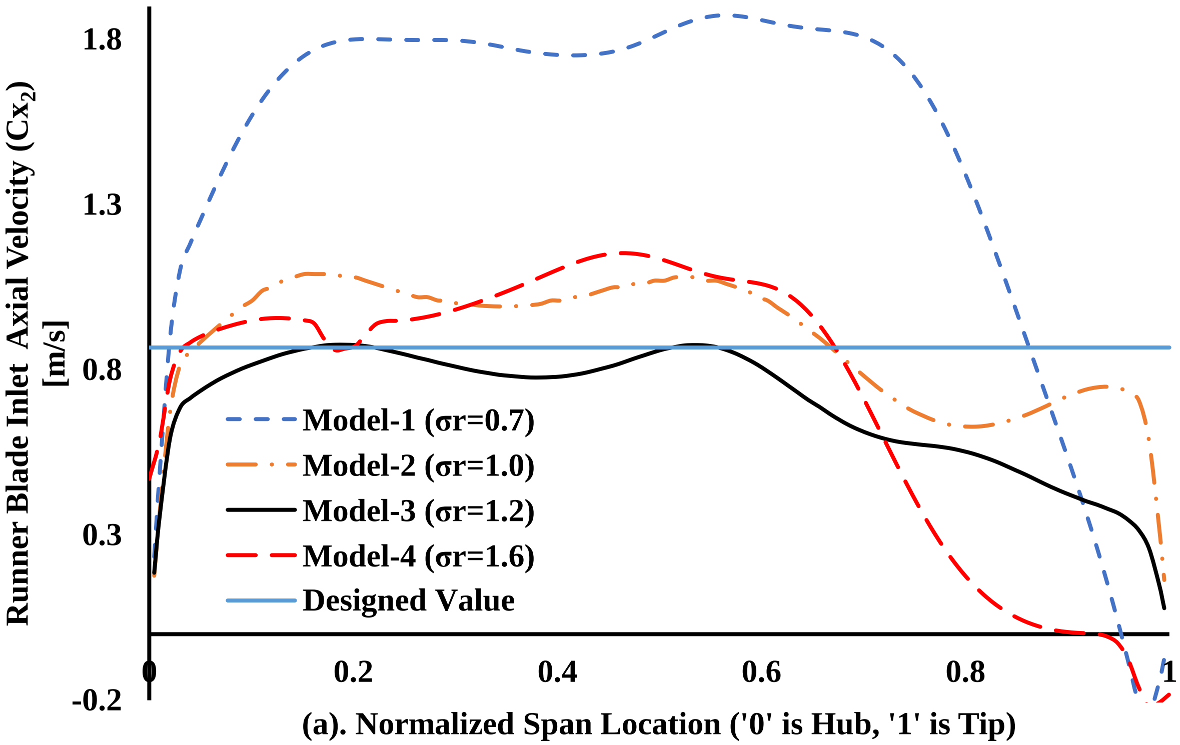

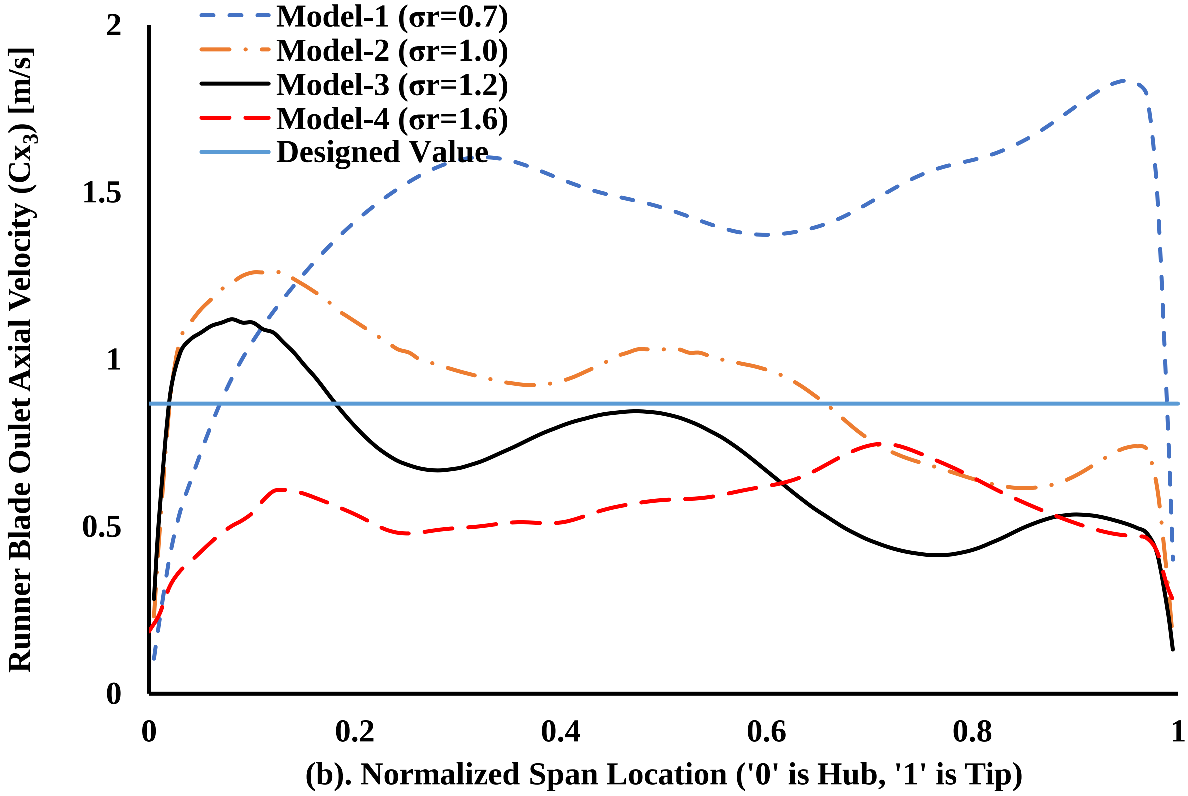

Figure. Appendix I.34. *Runner-blade Axial velocity (C_x) distribution at (a). Runner Inlet; (b). Runner Outlet; for the four selected models*

APPENDIX J: Additional results and plots for runner-blade thickness considerations

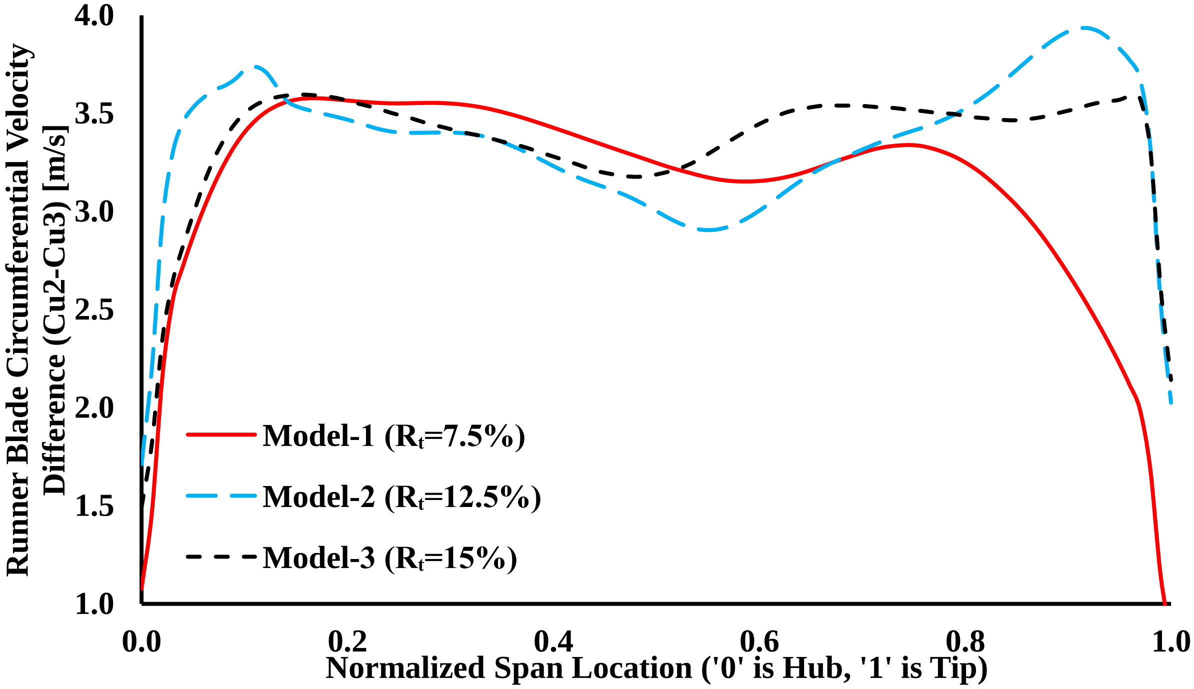

Figure. Appendix J.35. *The circumferential velocity difference (C_{u2}-C_{u3}) distribution plots from hub to tip for the three selected models*

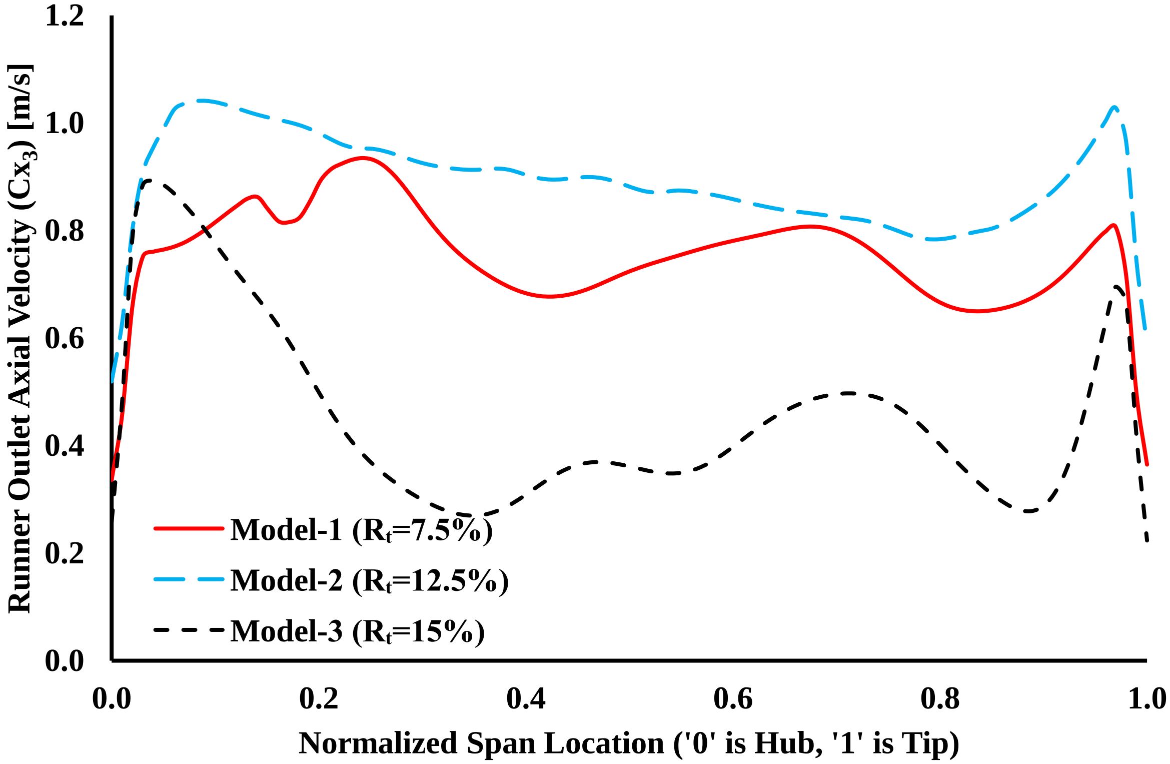

Figure. Appendix J.36. *The axial velocity distribution (C_{x3}) at runner outlet for the three selected models*

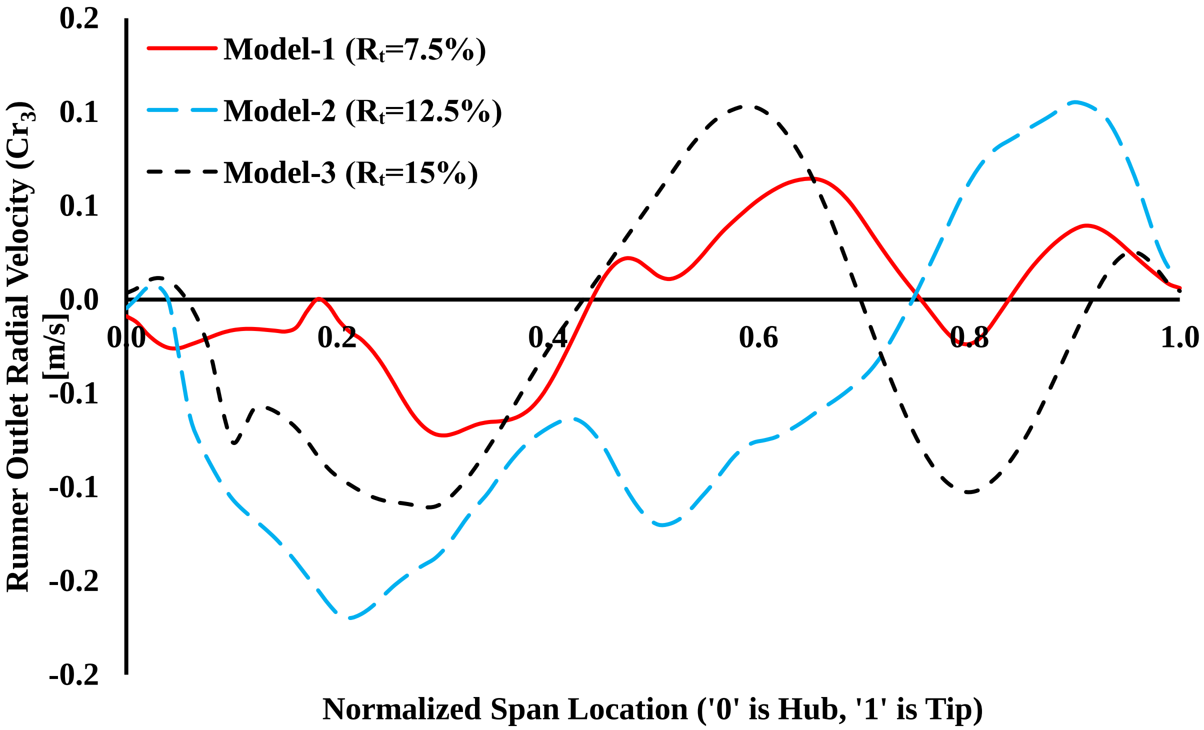

Figure. Appendix J.37. *The radial velocity distribution (C_{r3}) at runner outlet for the three selected models*

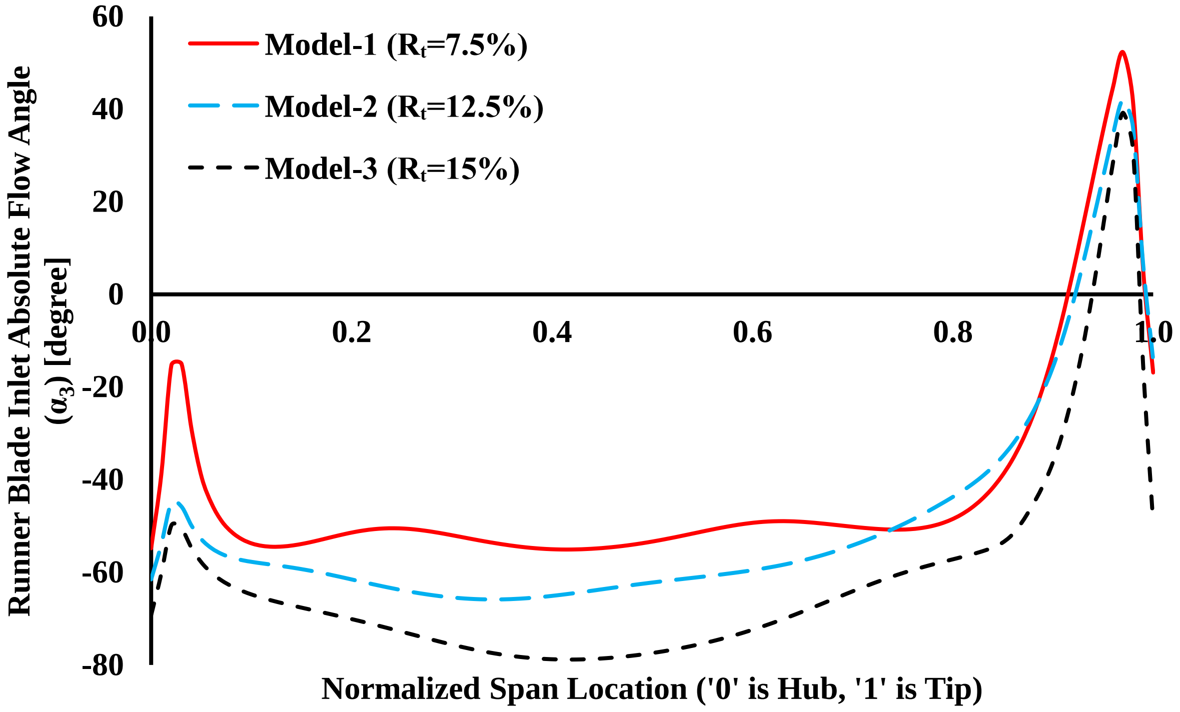

Figure. Appendix J.38. *The runner outlet absolute flow angle (α_3) distribution at runner outlet for the three selected models*

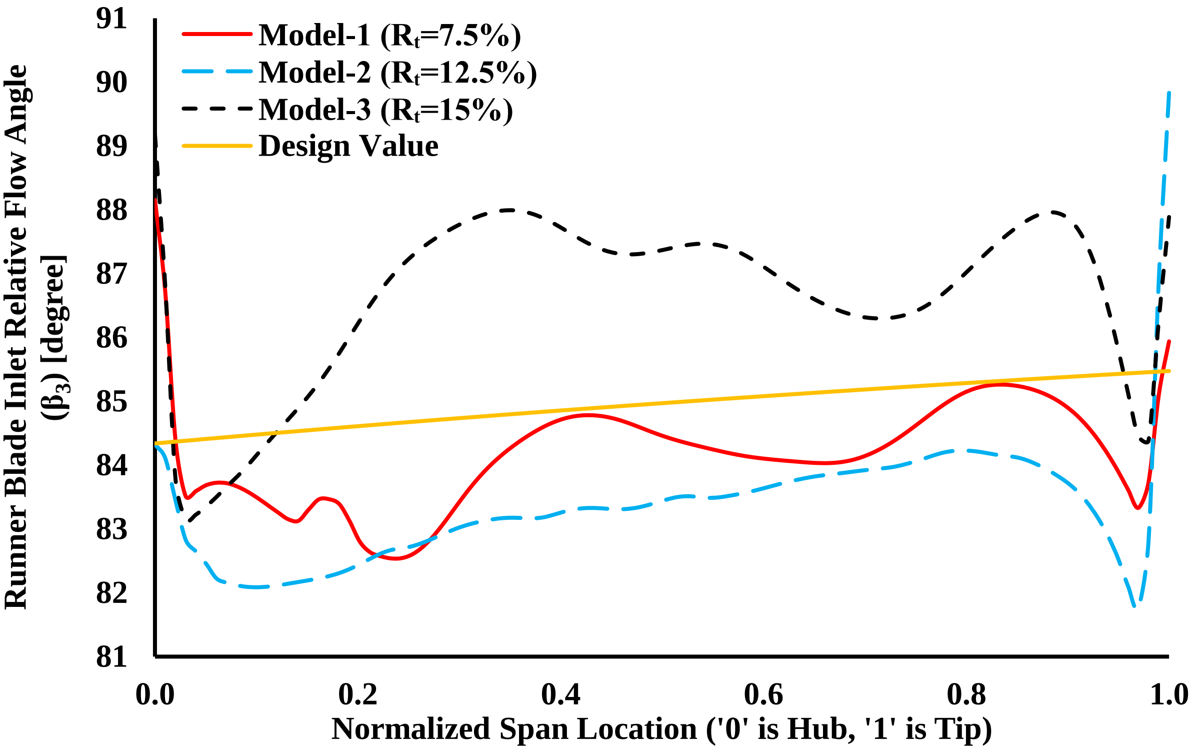

Figure. Appendix J.39. *The runner outlet relative flow angle (β_3) distribution at runner outlet for the three selected models*

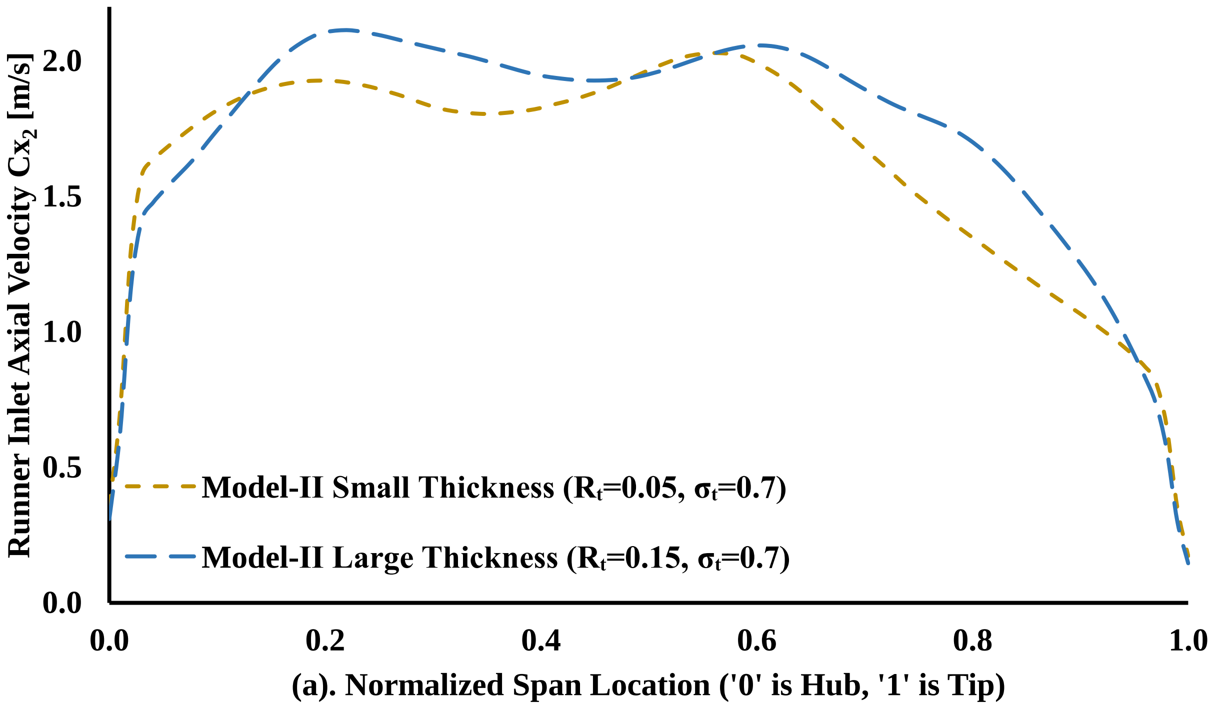

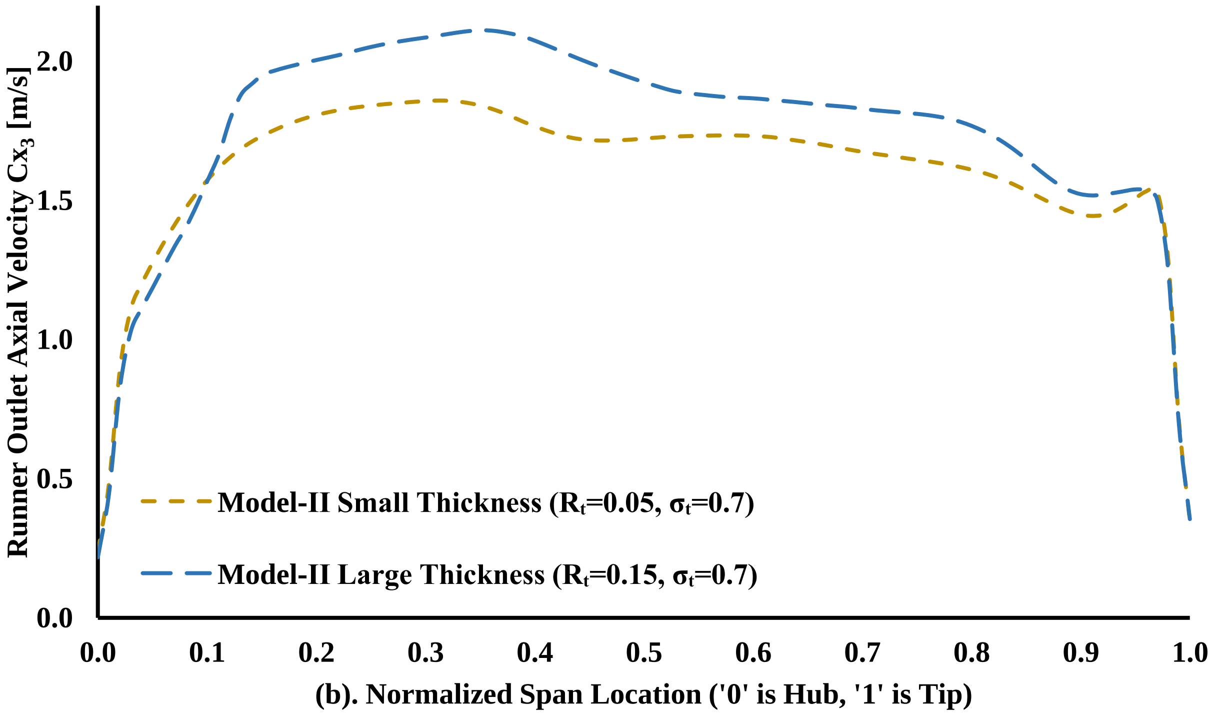

Figure. Appendix J.40*. Runner-blade Axial velocity (C_x) distribution at (a). Runner Inlet; (b). Runner Outlet; for the two different runner-blade thickness models at Low Solidity Condition σ_r=0.7*

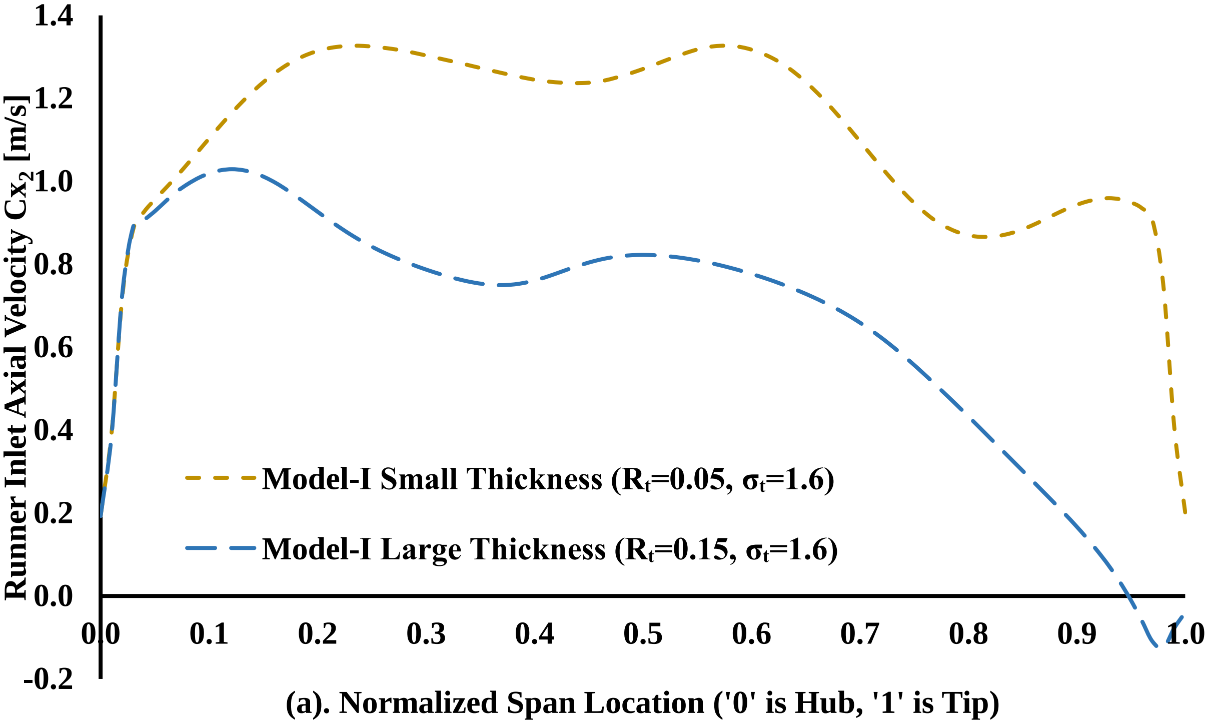

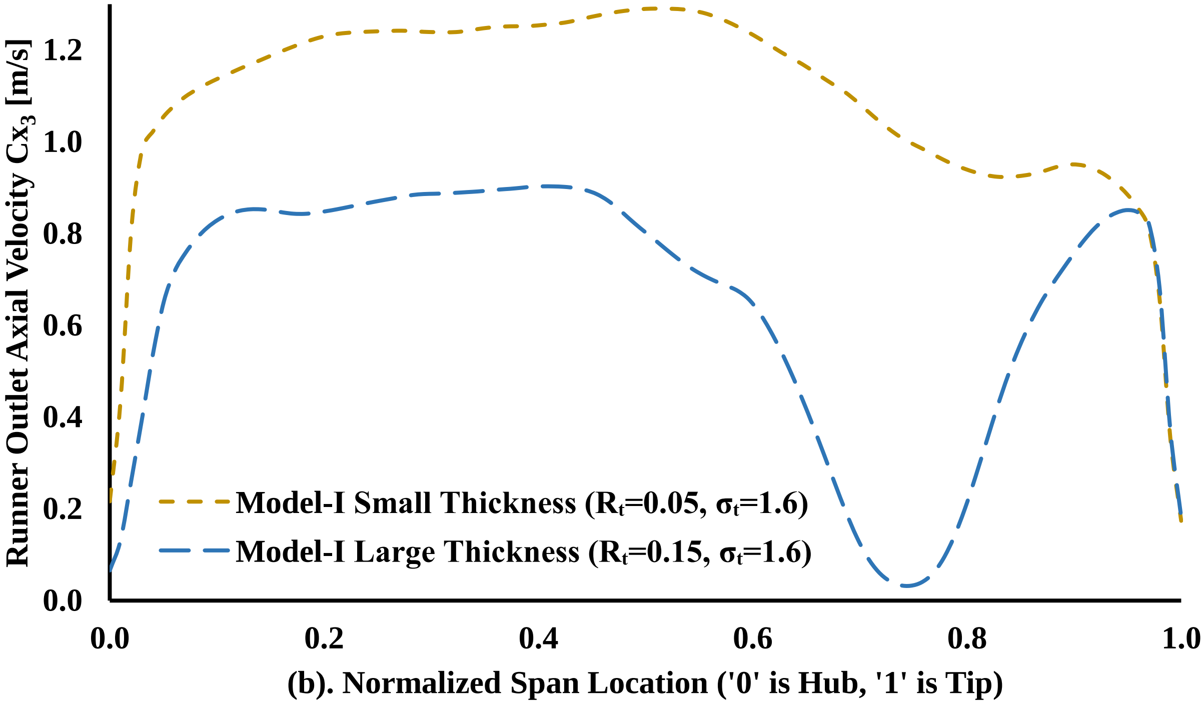

Figure. Appendix J.41. *Runner-blade Axial velocity (C_x) distribution at (a). Runner Inlet; (b). Runner Outlet; for the two different runner-blade thickness models at High Solidity Condition σ_r=1.6*

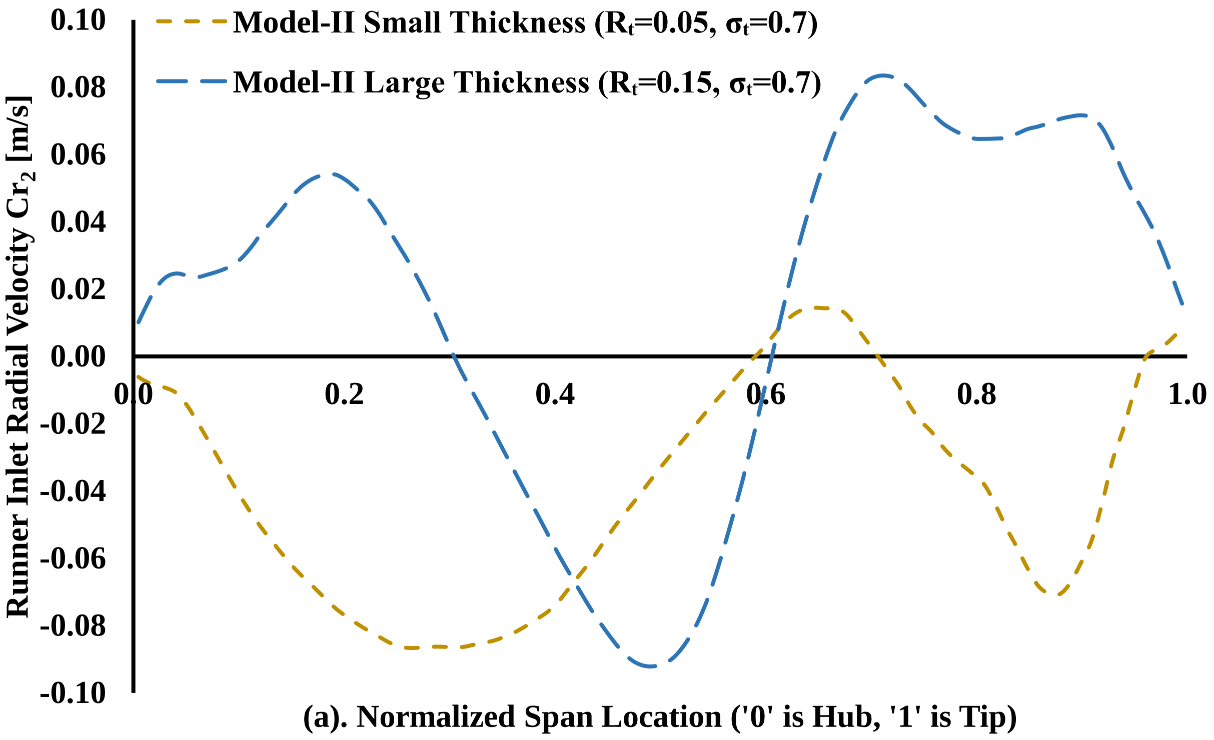

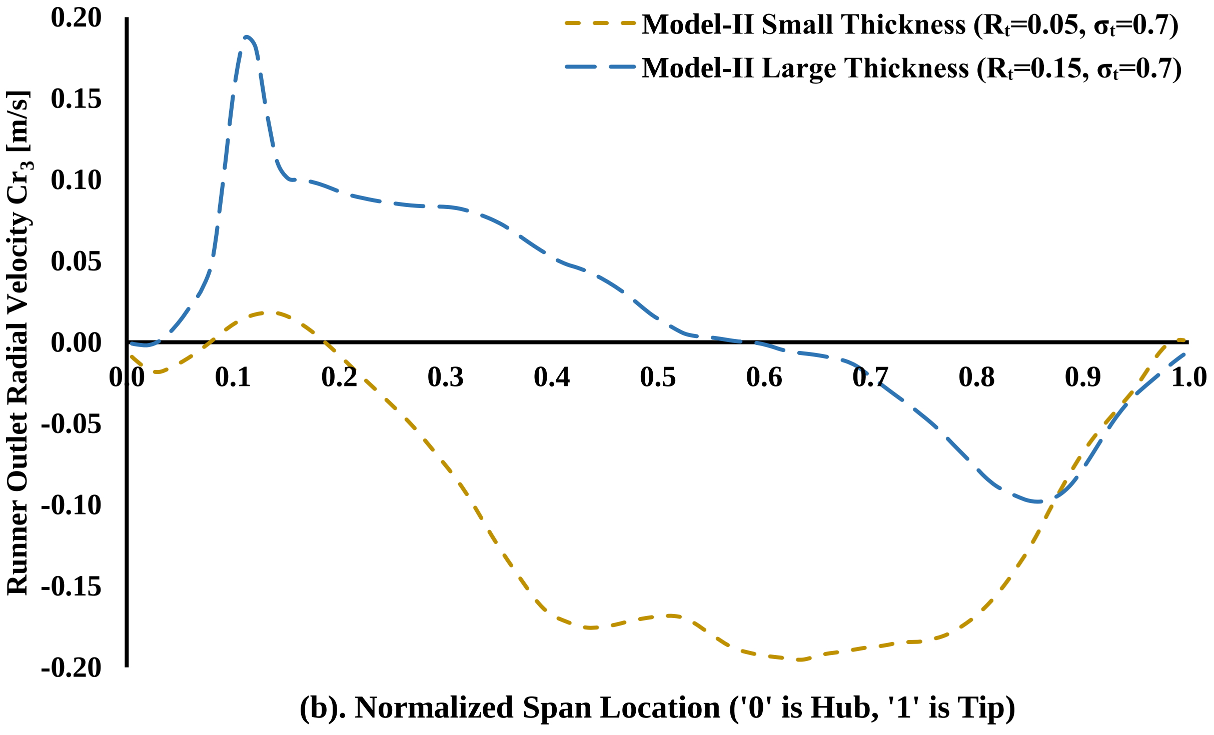

***Figure. Appendix J.42**. Runner-blade Radial velocity (C_r) distribution at (a). Runner Inlet; (b). Runner Outlet; for the two different runner-blade thickness models at Low Solidity Condition σ_r=0.7*

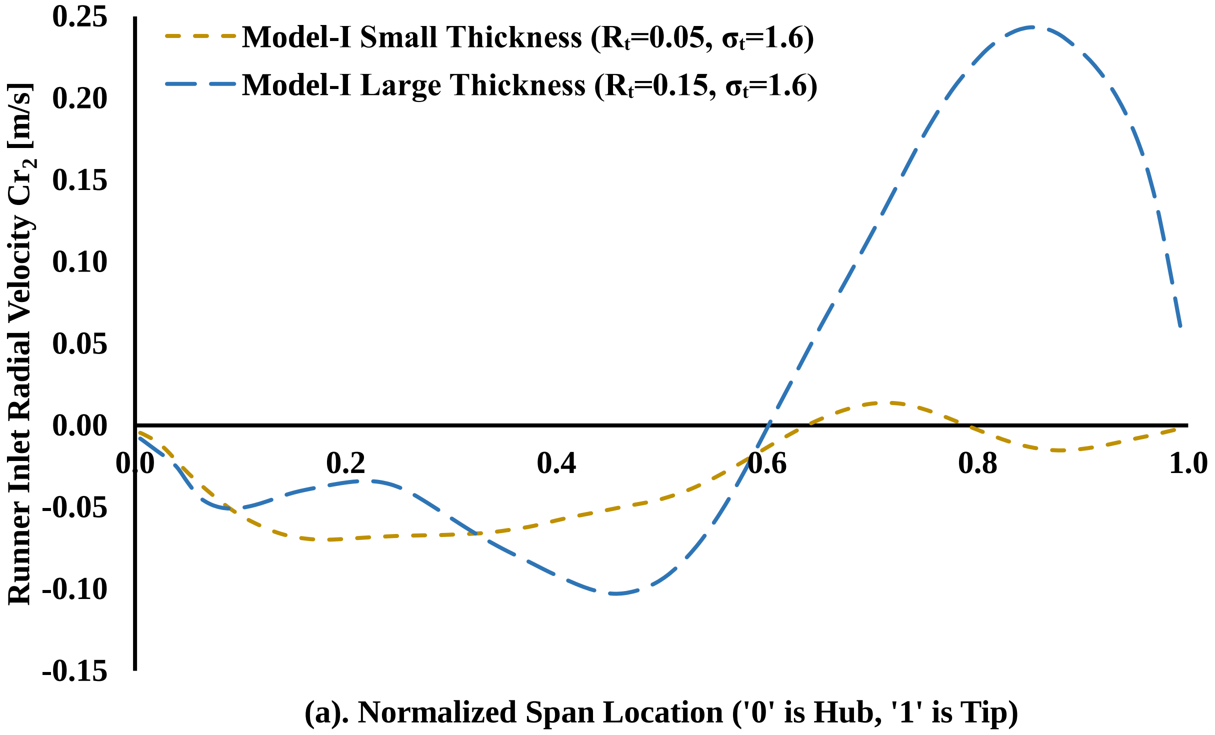

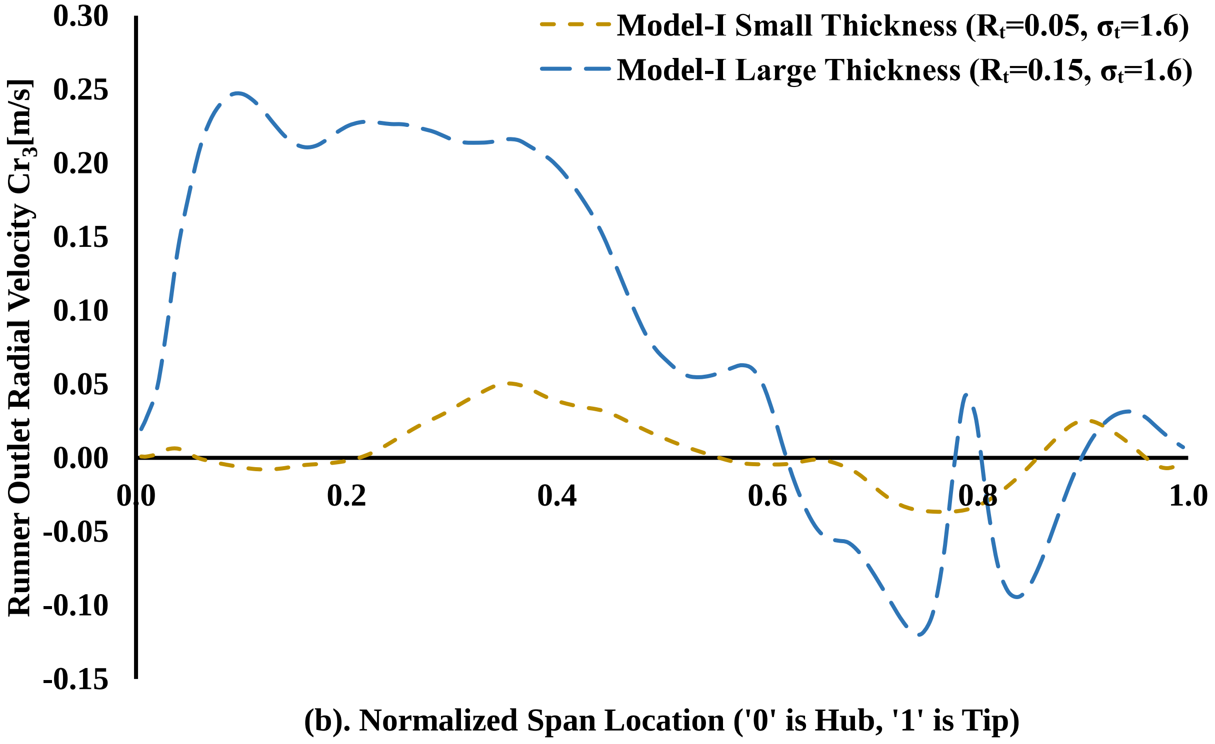

Figure. Appendix J.43. *Runner-blade Radial velocity (C_r) distribution at (a). Runner Inlet; (b). Runner Outlet; for the two different runner-blade thickness models at High Solidity Condition σ_r=1.6*

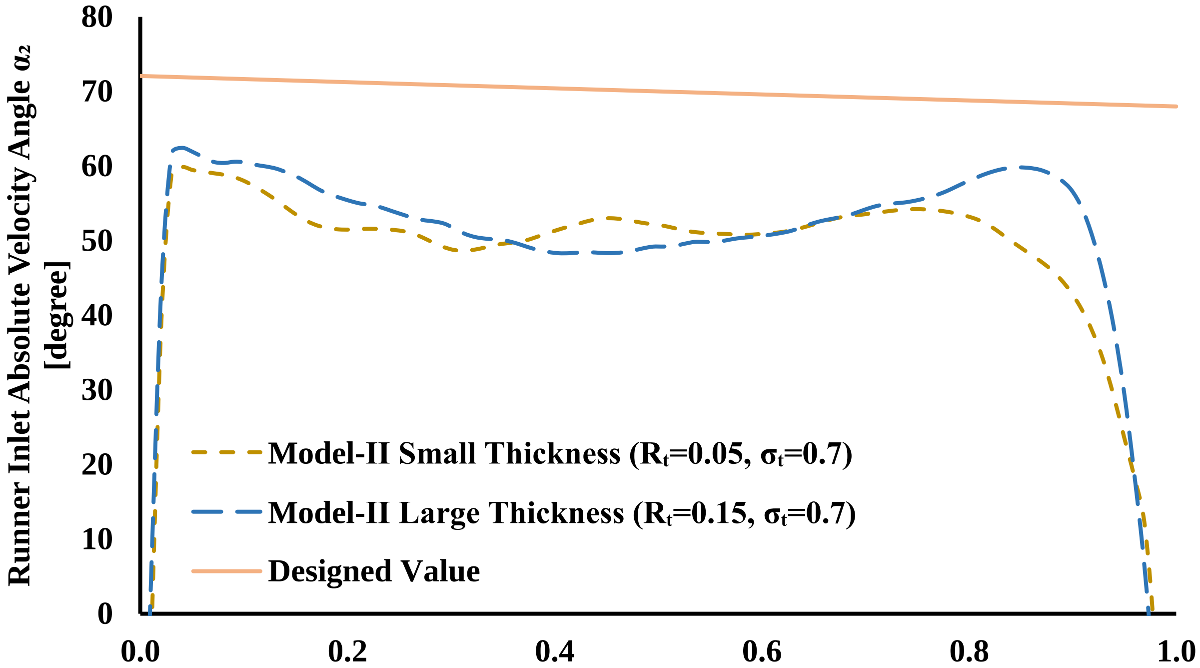

(a). Normalized Span Location ('0' is Hub, '1' is Tip)

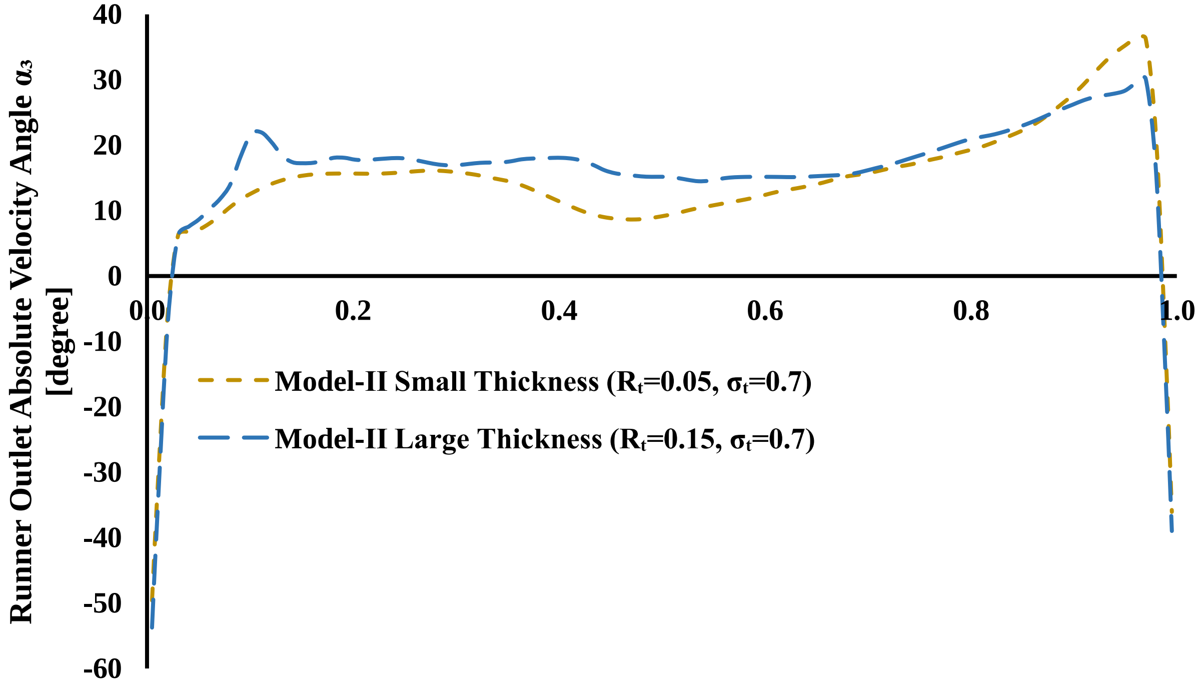

(b). Normalized Span Location ('0' is Hub, '1' is Tip)

Figure. Appendix J.44. *Runner-blade Absolute velocity angle (α) distribution at (a). Runner Inlet; (b). Runner Outlet; for the two different runner-blade thickness models at Low Solidity Condition* σ_r*=0.7, with comparison to the designed values [The designed value for* α_3 *is* 0° *across all span locations, which is not shown.]*

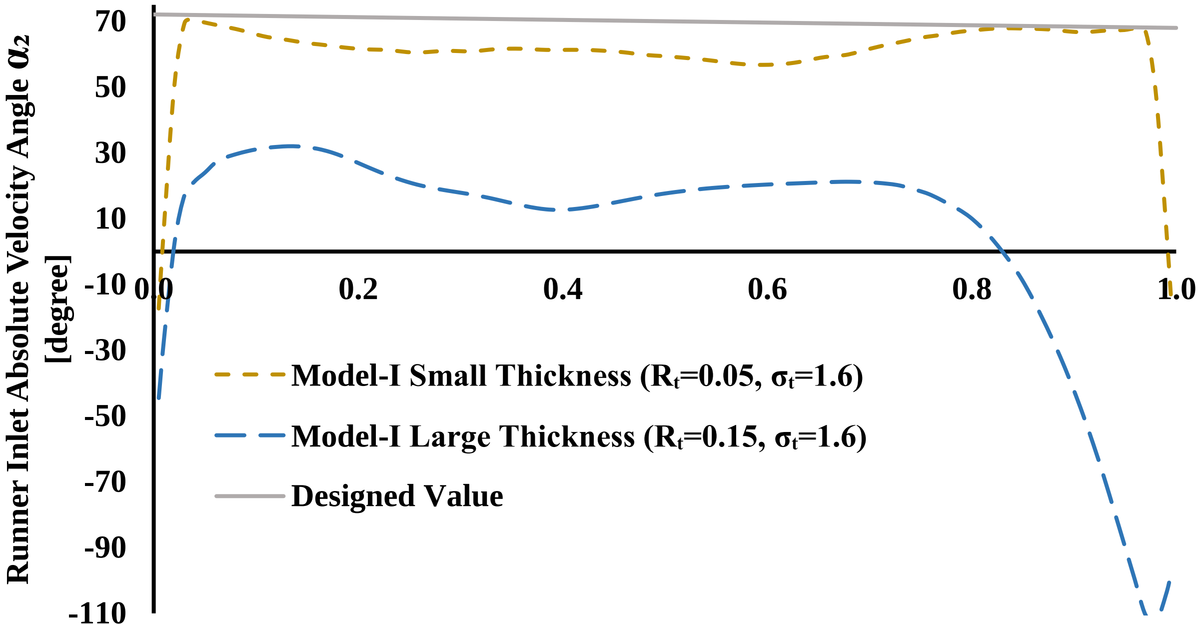

(a). Normalized Span Location ('0' is Hub, '1' is Tip)

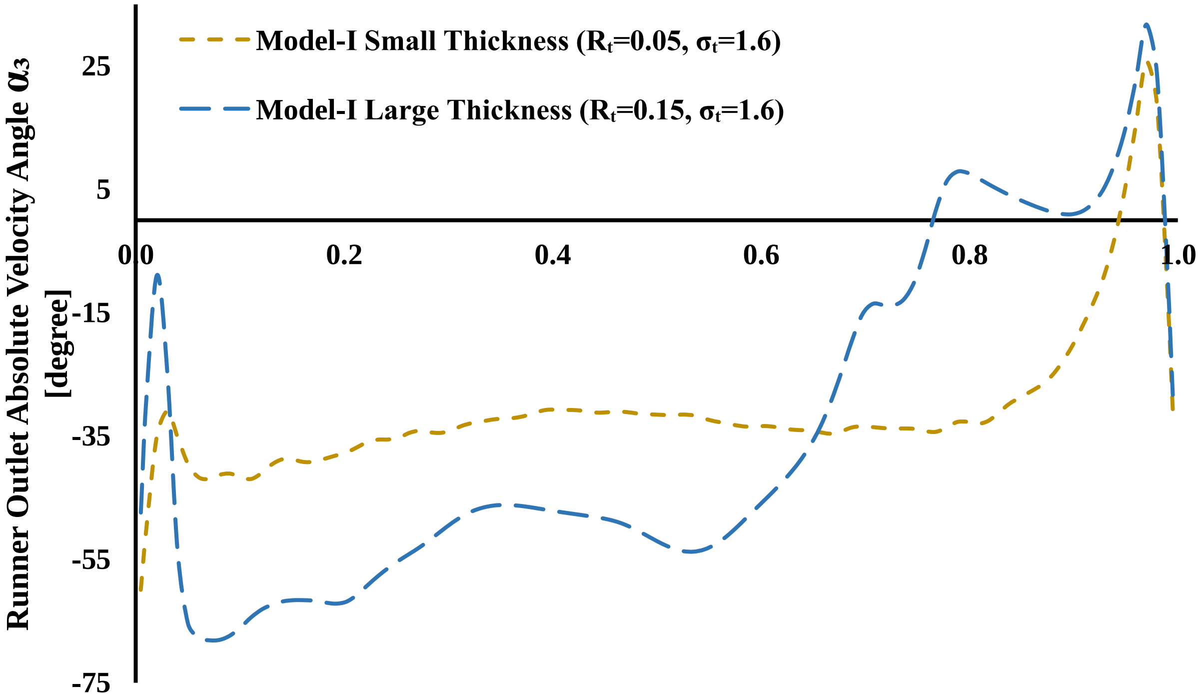

(b). Normalized Span Location ('0' is Hub, '1' is Tip)

Figure. Appendix J.45. *Runner-blade Absolute velocity angle (α) distribution at (a). Runner Inlet; (b). Runner Outlet; for the two different runner-blade thickness models at High Solidity Condition* σ_r*=1.6, with comparison to the designed values [The designed value for* α_3 *is* 0° *across all span locations, which is not shown.]*

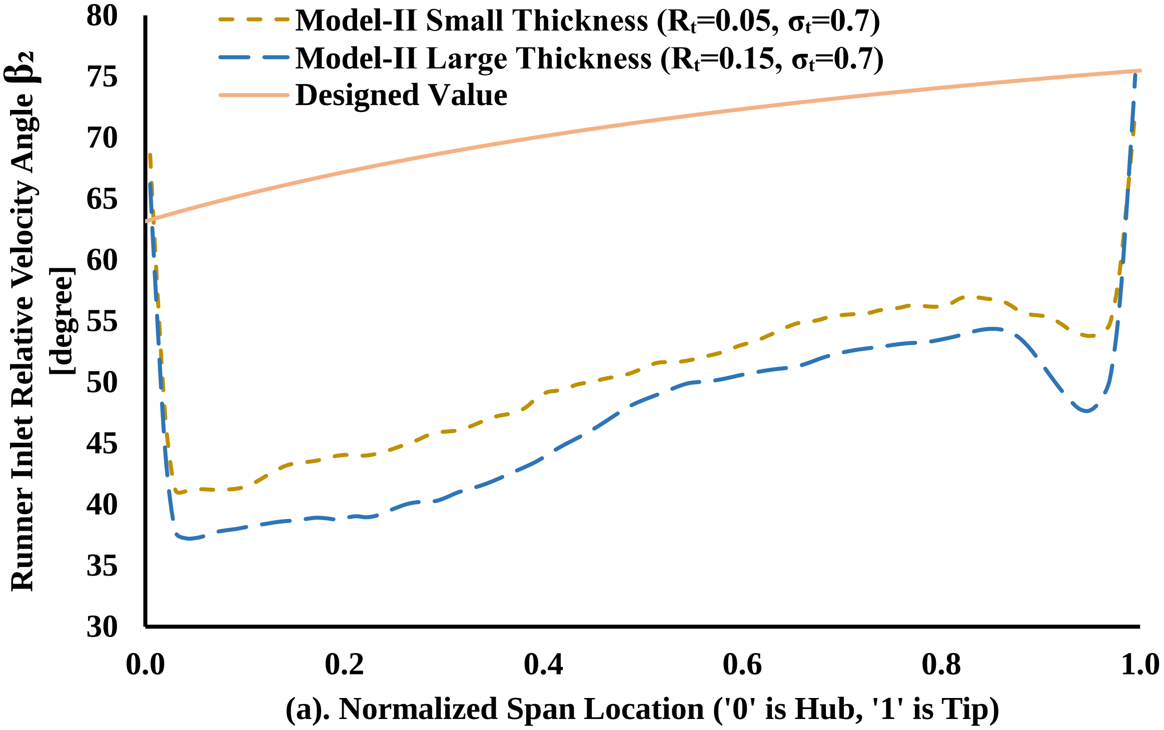

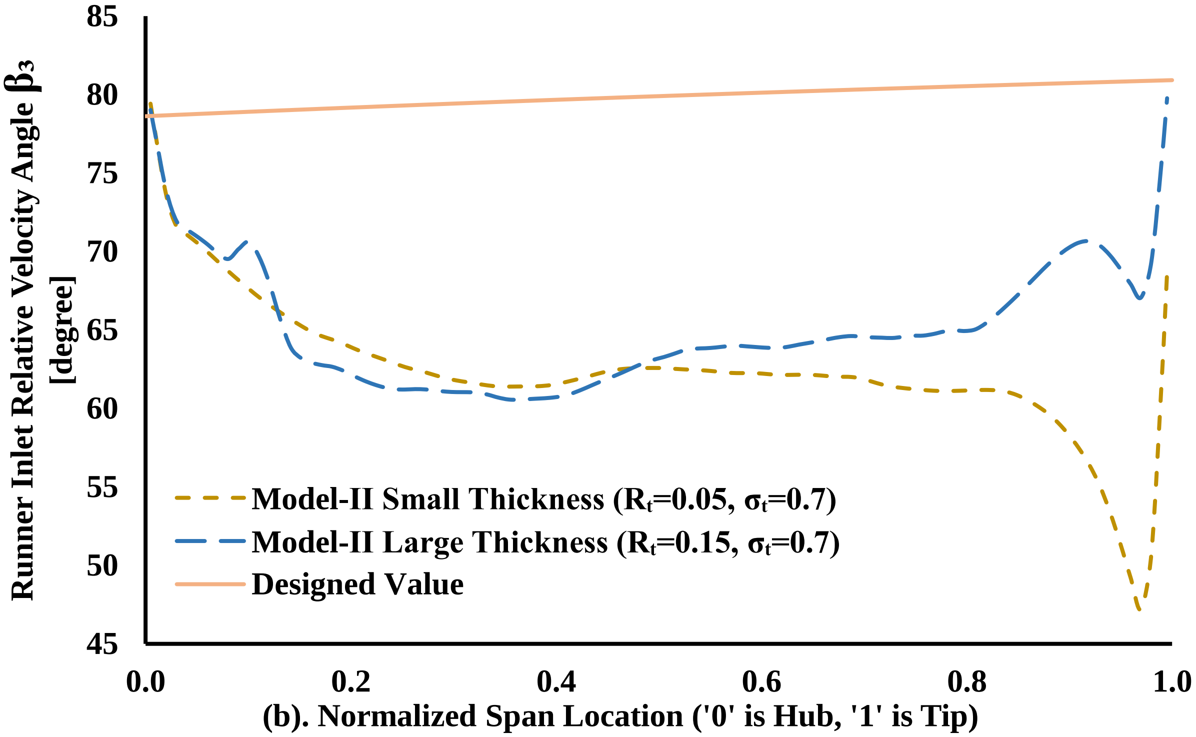

Figure. Appendix J.46. *Runner-blade Relative velocity angle (β) distribution at (a). Runner Inlet; (b). Runner Outlet; for the two different runner-blade thickness models at Low Solidity Condition σ$_r$=0.7, with comparison to the designed values*

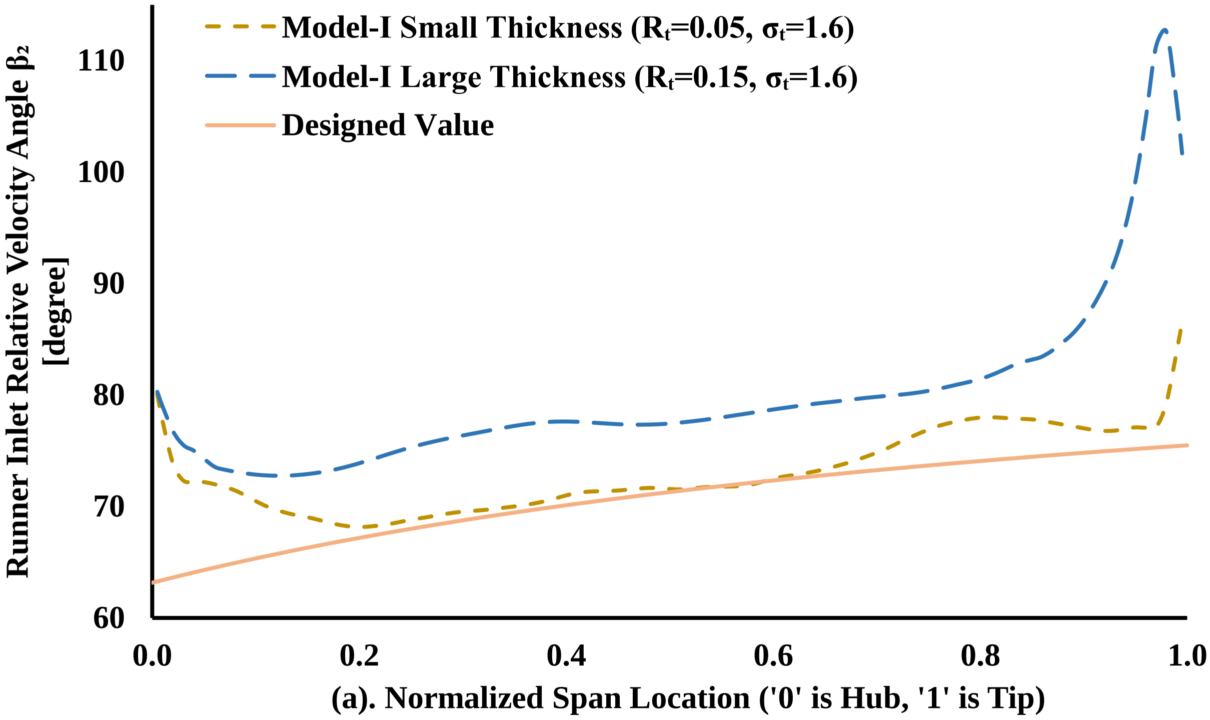

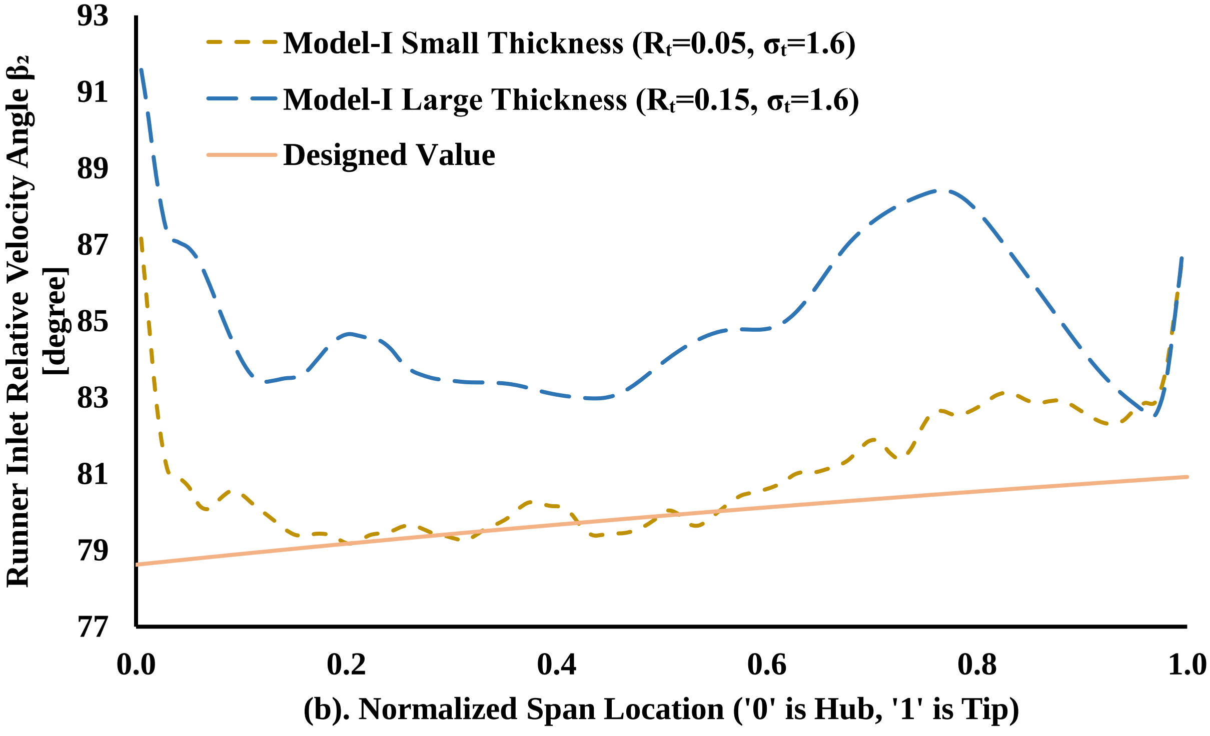

***Figure. Appendix J.47**. Runner-blade Relative velocity angle (β) distribution at (a). Runner Inlet; (b). Runner Outlet; for the two different runner-blade thickness models at High Solidity Condition σ_r=1.6, with comparison to the designed values*

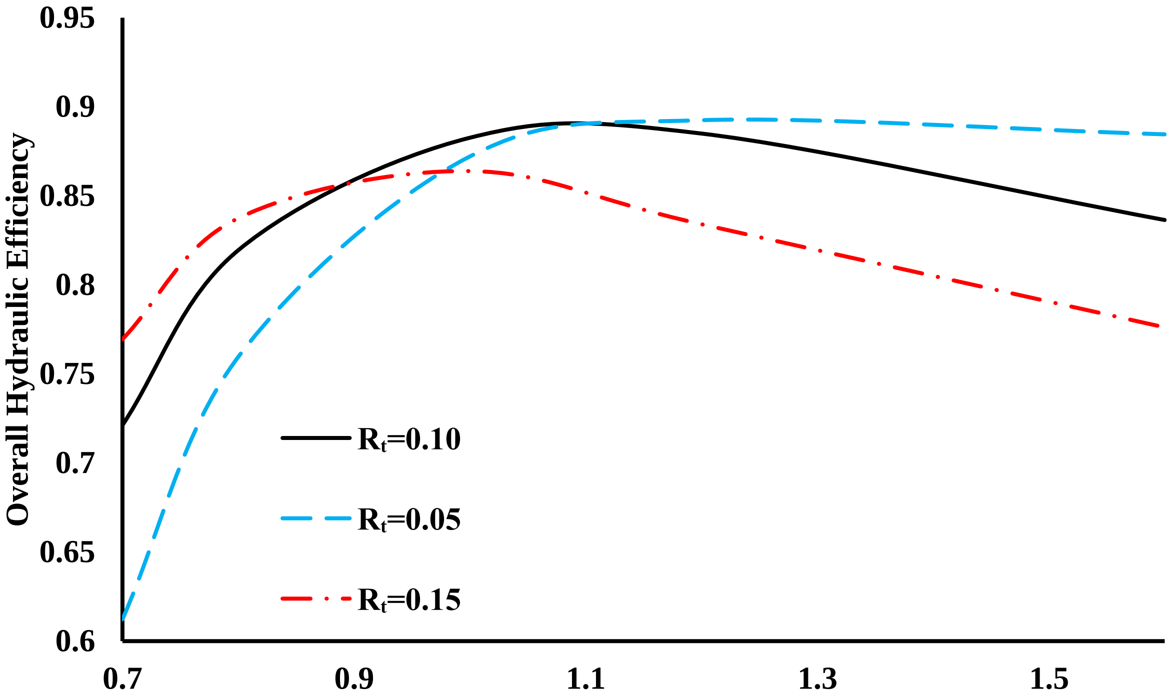

(a). Runner Blade Solidity (σ_R)

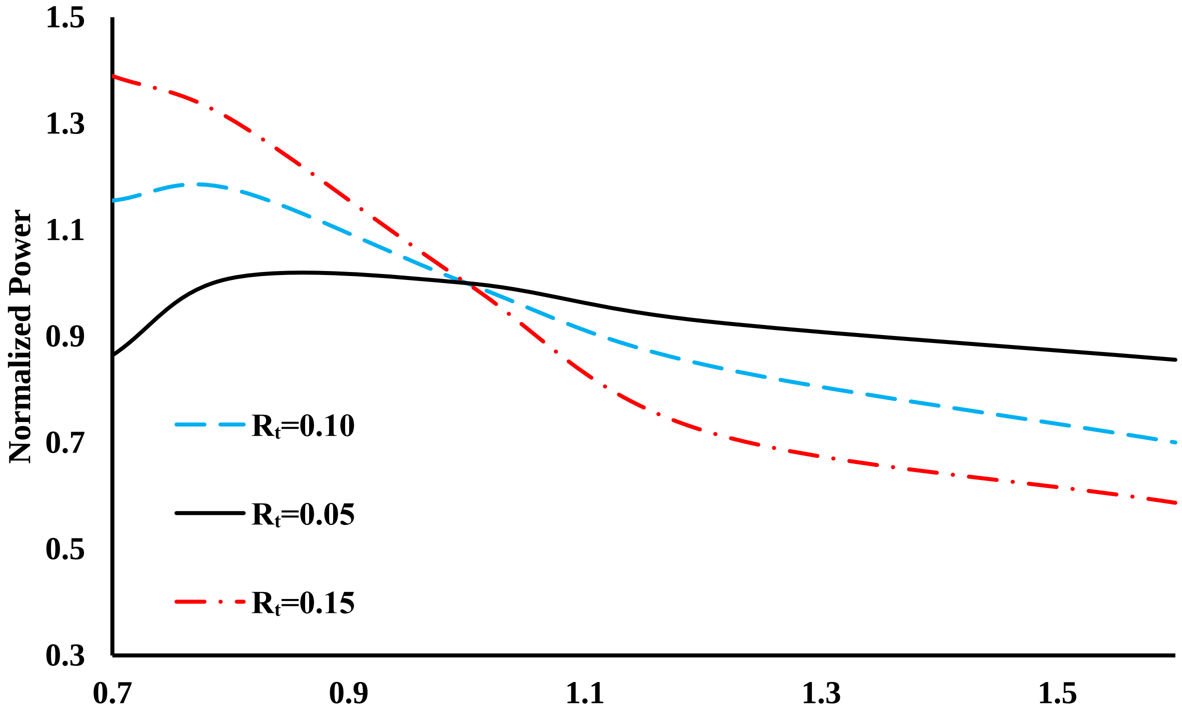

(b). Runner Blade Solidity (σ_R)

Figure. Appendix J.48. *The relation between runner-blade solidity with (a). Overall hydraulic efficiency and (b). Normalized shaft power for three runner-blade thickness conditions at one flow rate condition (Q_{11}=0.207), 6-blades configuration*

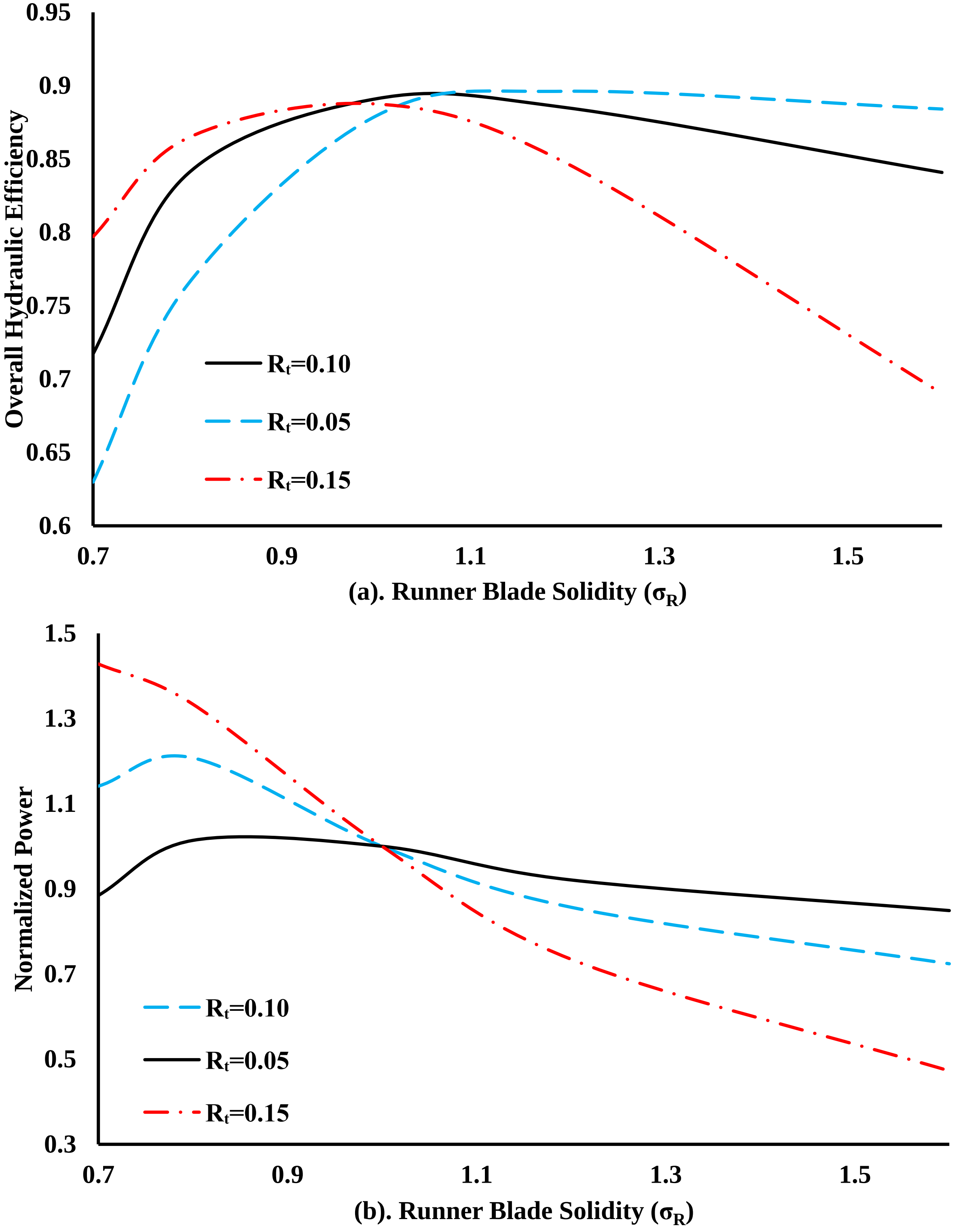

Figure. Appendix J.49. *The relation between runner-blade solidity with (a). Overall hydraulic efficiency and (b). Normalized shaft power for three runner-blade thickness conditions at one flow rate condition (Q_{11}=0.207), 10-blades configuration*

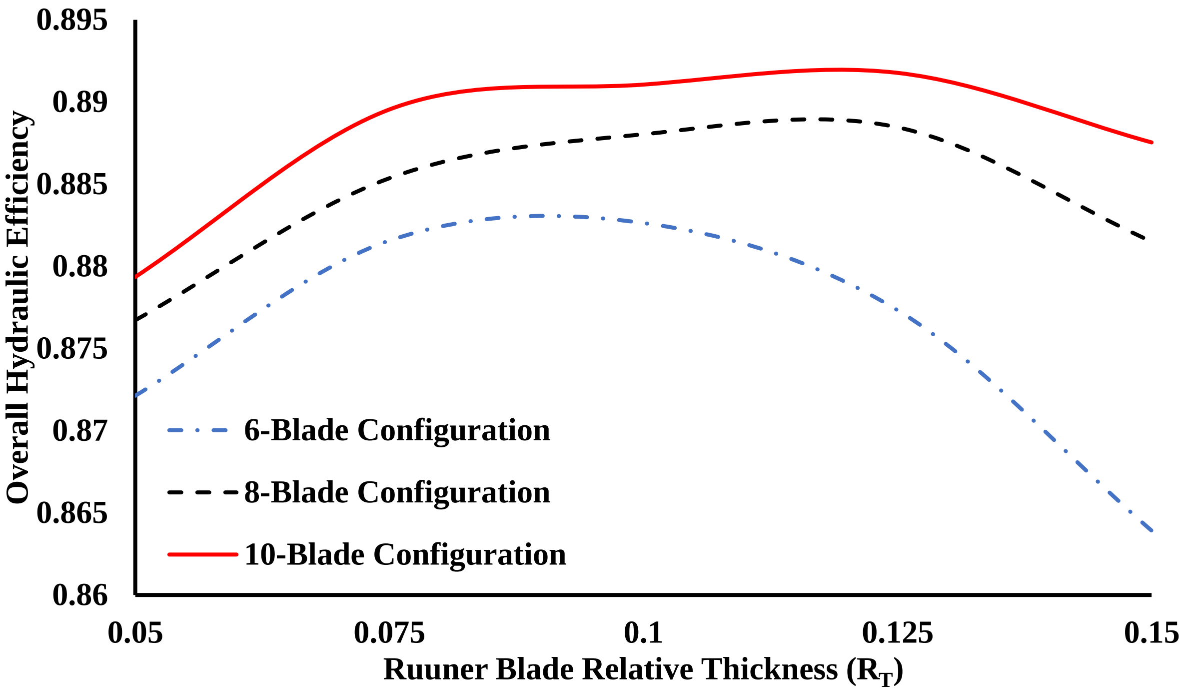

Figure. Appendix J.50. *The relation between runner-blade relative thickness with the Overall hydraulic efficiency for all three runner-blade number conditions at one solidity condition (*σ_r*=1)*

BIBLIOGRAPHY

BIBLIOGRAPHY

[1] Dixon, S. Larry, and Cesare Hall. Fluid mechanics and thermodynamics of turbomachinery. Butterworth-Heinemann, 2013.

[2] Williamson, S. J., B. H. Stark, and J. D. Booker. "Low head pico hydro turbine selection using a multi-criteria analysis." Renewable Energy 61 (2014): 43-50.

[3] World Energy Council. Survey of Energy Resources, 19th Ed. London, UK: World Energy Council, Regency House; 2001.

[4] Cleveland, Cutler J., and Christopher G. Morris. Handbook of energy: chronologies, top ten lists, and word clouds. Elsevier (2013): 79–102.

[5] Elbatran, A. H., et al. "Operation, performance and economic analysis of low head micro-hydropower turbines for rural and remote areas: A review." Renewable and Sustainable Energy Reviews 43 (2015): 40-50.

[6] Mohibullah, Mohd Amran, Mohd Radzi, Mohd Iqbal, Abdul Hakim. Basic design aspects of micro-hydro power plant and its potential development in Malaysia. In: Proceedings of the national power and energy conference 2004, PECON, IEEE 0-7803-8724-4; 29–30 November 2004.

[7] Dilip Singh. Micro hydropower resource assessment handbook. Prepared for APCTT Asian and Pacific Centre for Transfer of Technology of the United Nations – Economic and Social Commission for Asia and the Pacific (ESCAP), September 2009.

[8] Teuteberg BH. Design of a pump-as-turbine for an abalone farm, final report for mechanical project 878. Department of Mechanical and Mechatronic Engineering, Stellenbosch University; March 2010.

[9] Yaakob, O. B., et al. "A review on micro hydro gravitational vortex power and turbine systems." Jurnal Teknologi 69.7 (2014): 1-7.

[10] Paish, Oliver. "Micro-hydropower: status and prospects." Proceedings of the Institution of Mechanical Engineers, Part A: Journal of Power and Energy 216.1 (2002): 31-40.

[11] Derakhshan, Shahram, and Ahmad Nourbakhsh. "Experimental study of characteristic curves of centrifugal pumps working as turbines in different specific speeds." Experimental thermal and fluid science 32.3 (2008): 800-807.

[12] Laghari, J. A., et al. "A comprehensive overview of new designs in the hydraulic, electrical equipments and controllers of mini hydro power plants making it cost effective technology." Renewable and Sustainable Energy reviews 20 (2013): 279-293.

[13] Paish, Oliver. "Small hydropower: technology and current status." Renewable and sustainable energy reviews 6.6 (2002): 537-556.

[14] Wallace, A. R., and H. W. Whittington. "Performance prediction of standardized impulse turbines for micro-hydro." Sutton., Int. Water Power & Dam Construction (2008).

[15] Energy systems and design Ltd. ⟨http://www.microhydropower.com/our-pro ducts/stream-engine/⟩. [Accessed 08/21/13].

[16] Williamson, S. J., B. H. Stark, and J. D. Booker. "Performance of a low-head pico-hydro Turgo turbine." Applied Energy 102 (2013): 1114-1126.

[17] Williamson, S. J., B. H. Stark, and J. D. Booker. "Experimental optimization of a low-head pico hydro Turgo turbine." 2012 IEEE Third International Conference on Sustainable Energy Technologies (ICSET). IEEE, 2012.

[18] Voith hydro Pelton turbines ⟨http://voith.com/en/products- services/hydropower/turbines/ Pelton-turbines-563.html⟩. [Accessed 08/10/13].

[19] U.S. Department of Energy, Energy efficiency and renewable energy, Small hydropower systems, FS217; July 2001.

[20] Ghosh, Tushar K., and Mark A. Prelas. Energy resources and systems: volume 2: renewable resources. Vol. 2. Springer Science & Business Media, 2011.

[21] Ossberger GmbH Co. The Ossberger turbine. Bayern, Germany. ⟨http://www. ossberger.de/cms/en/hydro/the-ossberger-turbine-for-asynchronous-andsynchronous-water-plants/⟩; 2011. [Accessed 01/20/17].

[22] Jiménez, Edy E. "Final study report, achievable renewable energy targets for Puerto Rico's renewable energy portfolio standard. Puerto Rico: Puerto Rico's energy affairs administration; 2009."

[23] The encyclopedia of alternative energy and sustainable living. <https://www.daviddarling.info/encyclopedia/T/AE_Turgo_turbine.html>. [Accessed 1/24/17]

[24] Voith Hydro Pelton turbines. < https://www.voith.com/ca-en/Voith_Pelton_turbines.pdf >. [Accessed 1/22/20]

[25] Small-hydropower-systems DOE/GO-102001-1173, FS217, 2001. < https://www.nrel.gov/docs/fy01osti/29065.pdf>. [Accessed 1/22/20]

[26] Ossberger GmbH Co. (2011) The Ossberger turbine. Bayern, Germany. <http://www.ossberger.de/cms/en/hydro/the-ossberger-turbine-for-asynchronous-and-synchronous-water-plants/>. [Accessed 1/24/17]

[27] Miller, Gabriel, et al. "A study of an axial-flow turbine for kinetic hydropower generation." Energy 12.2 (1987): 155-162.

[28] Voith-Siemens (2011) Francis turbines, Hydropower generation, Voith-Siemens, Heidenheim. <http://www.voithhydro.com/media/t3339eFrancis72dpi.pdf>. [Accessed 1/25/17]

[29] Free Flow Power Corporation (2008) Hydrokinetics. <http://www.free-flow-power.com/index.php?id=10>. [Accessed 1/25/17].

[30] Western renewable energy. <http://www.westernrenew.co.uk/wre/hydro_basics/machines/archimedes_screw_turbines> [Accessed 01/25/17].

[31] Landustries Landy hydropower screw. <http://www.landustrie.nl/fileadmin/files/Folders/Landy%20hydropower%20screws.pdf>. [Accessed 01/25/17].

[32] Saroinsong, Tineke, et al. "The effect of head inflow and turbine axis angle towards the three-row bladed screw turbine efficiency." International Journal of Applied Engineering Research 10.7 (2015): 16977-16984.

[33] Bulb/pit/S-turbines, Voith-Siemens hydropower generation. <http://voith.com/corp-en/BulbPitS-Turbines_Generators.pdf>. [Accessed 01/22/20].

[34] Kydd P (2009) Severn tidal power, Overview and implications of tidal power technologies, Severn tidal power feasibility study

[35] Hydroelectric design center, Portland district, US Army Corps of Engineers. https://www.nwp.usace.army.mil/HDC/edu genexcit.asp. [Accessed 1/26/17]

[36] Gordon, J. L., and P. Eng. "Turbine selection for small low-head hydro developments." Proc. Waterpower XII, Buffalo (2003).

[37] Loots, I., et al. "A review of low head hydropower technologies and applications in a South African context." Renewable and Sustainable Energy Reviews 50 (2015): 1254-1268.

[38] DOE’s 2016 Hydropower Vision Report: <https: //www.energy.gov /eere /water/downloads/hydropower-vision-report-full-report>. [Accessed 1/22/20]

[39] Witt, Adam, et al. "Exemplary Design Envelope Specification for Standard Modular Hydropower Technology: Draft for Public Comment.", 2016.

[40] Brown Kinloch, David. Demonstration of variable speed permanent magnet generator at small, low-head hydro site. No. Final Report: DOE-WEISENBERGER-EE0005429-1. Weisenberger Mills, Inc., Midway, KY (United States), 2015.

[41] Johnson, Megan, Rocio Uria-Martinez, and Patrick O'Connor. 2016 Hydropower Market Report Update Metadata. Oak Ridge National Lab. (ORNL), Oak Ridge, TN (United States), 2017.

[42] Lewis, R. I. Turbomachinery performance analysis. Butterworth-Heinemann, 1996.

[43] Albuquerque, R. B. F., N. Manzanares-Filho, and W. Oliveira. "Conceptual optimization of axial-flow hydraulic turbines with non-free vortex design." Proceedings of the Institution of Mechanical Engineers, Part A: Journal of Power and Energy 221.5 (2007): 713-725.

[44] Horlock, John Harold. Axial flow turbines: fluid mechanics and thermodynamics. Krieger Pub Co, 1973.

[45] Božić, Ivan. "Determination of hydraulic losses in the flow passage between the guide vanes and runner of the Kaplan turbine." Journal of Hydraulic Research 55.3 (2017): 349-361.

[46] Zhou, Daqing, and Zhiqun Daniel Deng. "Ultra-low-head hydroelectric technology: A review." Renewable and Sustainable Energy Reviews 78 (2017): 23-30.

[47] Gordon, J. L., and P. Eng. "Turbine selection for small low-head hydro developments." Proc. Waterpower XII, Buffalo(2003).

[48] Korpela, Seppo A. Principles of turbomachinery. Hoboken, New Jersey: Wiley, 2011.

[49] De Siervo, F., and F. De Leva. "Modern trends in selecting and designing Kaplan turbines." Water power and dam construction 30.1 (1978): 28-35.

[50] Odeh, Mufeed. "A summary of environmentally friendly turbine design concepts." US Department of Energy Idaho Operations Office (1999).

[51] Muis, Abdul, and Priyono Sutikno. "Design and simulation of very low head axial hydraulic turbine with variation of swirl velocity criterion." International Journal of Fluid Machinery and Systems7.2 (2014): 68-79.

[52] Ferro, L. M. C., L. M. C. Gato, and A. F. O. Falcão. "Design of the rotor blades of a mini hydraulic bulb-turbine." Renewable Energy 36.9 (2011): 2395-2403.

[53] Sutikno, Priyono, and Ibrahim Khalil Adam. "Design, simulation and experimental of the very low head turbine with minimum pressure and free vortex criterions." International Journal of Mechanical and Mechatronics Engineering 11.1 (2011): 9-16.

[54] Anagnostopoulos, John S., and Dimitrios E. Papantonis. "Flow modeling and runner design optimization in Turgo water turbines." World Academy of Science, Engineering and Technology 28 (2007): 206-211.

[55] Höfler, Edvard, Janez Gale, and Anton Bergant. "Hydraulic design and analysis of the Saxo-type vertical axial turbine." Transactions of the Canadian Society for Mechanical Engineering 35.1 (2011): 119-143.

[56] Schobeiri, Meinhard. Turbomachinery flow physics and dynamic performance. Heidelberg: Springer, 2005.

[57] Mu, Jie Gang, et al. "Response of Blade Thickness to Hydraulic Performance of Stamping and Welding Multistage Centrifugal Pump." Applied Mechanics and Materials. Vol. 229. Trans Tech Publications Ltd, 2012.

[58] Shigemitsu, Toru, Junichiro Fukutomi, and Kensuke Kaji. "Influence of blade outlet angle and blade thickness on performance and internal flow conditions of mini centrifugal pump." International Journal of Fluid Machinery and Systems 4.3 (2011): 317-323.

[59] Tao, Yi, et al. "Influence of blade thickness on transient flow characteristics of centrifugal slurry pump with semi-open impeller." Chinese Journal of Mechanical Engineering 29.6 (2016): 1209-1217.

[60] Kim, Seung-Jun, et al. "Effect of blade thickness on the hydraulic performance of a Francis hydro turbine model." Renewable energy 134 (2019): 807-817.

[61] Tucker, P. G. "Computation of unsteady turbomachinery flows: Part 1—Progress and challenges." Progress in Aerospace Sciences 47.7 (2011): 522-545.

[62] Guide, ANSYS FLUENT User'S. "Release 17.0." Ansys Inc (2016).

[63] Kalitzin, Georgi, et al. "Near-wall behavior of RANS turbulence models and implications for wall functions." Journal of Computational Physics 204.1 (2005): 265-291.

[64] Menter, Florian R. "Two-equation eddy-viscosity turbulence models for engineering applications." AIAA Journal 32.8 (1994): 1598-1605.

[65] Jones, W. P., and BEi Launder. "The prediction of laminarization with a two-equation model of turbulence." International journal of heat and mass transfer 15.2 (1972): 301-314.

[66] ANSYS, Release. "Documentation for ANSYS, SAS IP." (18)

[67] Adhikari, Ram. Design improvement of crossflow hydro turbine. Diss. University of Calgary, 2016.